RECENT ADVANCES in CIRCUITS, SYSTEMS and CONTROL

Proceedings of the 2014 International Conference on Circuits, Systems and Control (CSC 2014)

Interlaken, Switzerland
February 22-24, 2014

RECENT ADVANCES in CIRCUITS, SYSTEMS and CONTROL

Proceedings of the 2014 International Conference on Circuits, Systems and Control (CSC 2014)

Interlaken, Switzerland
February 22-24, 2014

Copyright © 2014, by the editors

All the copyright of the present book belongs to the editors. All rights reserved. No part of this publication may be reproduced, stored in a retrieval system, or transmitted in any form or by any means, electronic, mechanical, photocopying, recording, or otherwise, without the prior written permission of the editors.

All papers of the present volume were peer reviewed by no less than two independent reviewers. Acceptance was granted when both reviewers' recommendations were positive.

Recent Advances in Electrical Engineering Series – 31

ISSN: 1790-5117
ISBN: 978-1-61804-216-3

RECENT ADVANCES in CIRCUITS, SYSTEMS and CONTROL

Proceedings of the 2014 International Conference on Circuits, Systems and Control (CSC 2014)

Interlaken, Switzerland
February 22-24, 2014

Organizing Committee

General Chairs (EDITORS)

- Professor Maria Isabel García-Planas,
  Universitat Politècnica de Catalunya,
  Spain
- Professor George Vachtsevanos,
  Georgia Institute of Technology,
  Atlanta, Georgia,
  USA
- Professor Gen Qi Xu
  Department of Mathematics
  Tianjin University
  Tianjin, China

Senior Program Chair

- Professor Philippe Dondon
  ENSEIRB
  Rue A Schweitzer 33400 Talence
  France

Program Chairs

- Professor Filippo Neri
  Dipartimento di Informatica e Sistemistica
  University of Naples "Federico II"
  Naples, Italy
- Prof. Constantin Udriste,
  University Politehnica of Bucharest,
  Bucharest,
  Romania
- Professor Sandra Sendra
  Instituto de Inv. para la Gestión Integrada de Zonas Costeras (IGIC)
  Universidad Politécnica de Valencia
  Spain

Tutorials Chair

- Professor Pradip Majumdar
  Department of Mechanical Engineering
  Northern Illinois University
  Dekalb, Illinois, USA

Special Session Chair

- Professor Claudio Talarico,
  Gonzaga University, Spokane,
  USA

Workshops Chair

- Professor Ryszard S. Choras
  Institute of Telecommunications
  University of Technology & Life Sciences
  Bydgoszcz, Poland

Local Organizing Chair

- Professor Jan Awrejcewicz,
  Technical University of Lodz,
  Lodz, Poland

Publication Chair

- Professor Vincenzo Niola
  Departement of Mechanical Engineering for Energetics
  University of Naples "Federico II"
  Naples, Italy

Steering Committee

- Professor Aida Bulucea, University of Craiova, Romania
- Professor Zoran Bojkovic, Univ. of Belgrade, Serbia
- Professor Claudio Talarico, Gonzaga University, Spokane, USA
- Professor Imre Rudas, Obuda University, Budapest, Hungary

Program Committee

Prof. Bimal Kumar Bose (Life Fellow IEEE), The University of Tennessee, Knoxville, USA
Prof. Wasfy B. Mikhael, IEEE Fellow, Vice President IEEE Circuits and Systems, University of Central Florida, Orlando, USA
Prof. Pierre Borne, IEEE France Section Chair, IEEE Fellow, IEEE/SMC Past President, Ecole Centrale de Lille, France
Prof. Yuriy S. Shmaliy (IEEE Fellow), Universidad de Guanajuato, MEXICO
Prof. D. Subbaram Naidu (Fellow IEEE), Idaho State University, USA
Prof. Tadeusz Kaczorek (Fellow IEEE), Warsaw University of Technology, Poland
Prof. Irwin Sandberg (IEEE Fellow, University of Texas at Austin, USA),
Prof. Narsingh Deo, IEEE Fellow, ACM Fellow, AAAS Fellow, ICA Fellowm Orlando, Florida, USA
Prof. George Vachtsevanos, Georgia Institute of Technology, Atlanta, Georgia, USA
Prof. Panagiotis Agathoklis, University of Victoria, British Columbia, Canada
Prof. Imre J. Rudas, Óbuda University, Budapest, Hungary
Prof. Jiri Hrebicek, Masaryk University, Brno, Czech Republic
Prof. Gen Qi Xu, Tianjin University, Tianjin, China
Prof. Brett Nener, The University of Western Australia, Australia
Prof. Maria Isabel García-Planas, Universitat Politècnica de Catalunya, Spain
Prof. Branimir Reljin, University of Belgrade, Serbia
Prof. Humberto Varum, University of Aveiro, Aveiro, Portugal
Prof. Ronald Tetzlaff, Technical University Dresden, Germany
Prof. Peter Szolgay, Pazmany Peter Catholic University, Hungary
Prof. Xiang Bai, Huazhong University of Science and Technology, China
Prof. Alexander Gegov, University of Portsmouth, UK
Prof. Jan Awrejcewicz, Technical University of Lodz, Lodz, Poland
Prof. Carla Pinto, Polytechnic of Porto, Porto, Portugal
Prof. Hung-Yuan Chung, National Central University, Taiwan
Prof. Elbrous M. Jafarov, Istanbul Technical University, Istanbul, Turkey
Prof. Dimitrios A. Karras, Sterea Hellas Institute of Technology, Greece
Prof. Sorinel Oprisan, College of Charleston, Charleston, South Carolina, USA

Prof. Lotfi Zadeh (IEEE Fellow,University of Berkeley, USA)
Prof. Leon Chua (IEEE Fellow,University of Berkeley, USA)
Prof. Michio Sugeno (RIKEN Brain Science Institute (RIKEN BSI), Japan)
Prof. Dimitri Bertsekas (IEEE Fellow, MIT, USA)
Prof. Demetri Terzopoulos (IEEE Fellow, ACM Fellow, UCLA, USA)
Prof. Georgios B. Giannakis (IEEE Fellow, University of Minnesota, USA)
Prof. Brian Barsky (IEEE Fellow, University of Berkeley, USA)
Prof. Aggelos Katsaggelos (IEEE Fellow, Northwestern University, USA)
Prof. Leonid Kazovsky (Stanford University, USA)
Prof. Anastassios Venetsanopoulos (Fellow IEEE, University of Toronto, Canada)
Prof. Steven Collicott (Purdue University, West Lafayette, IN, USA)
Prof. Nikolaos G. Bourbakis (IEEE Fellow, Wright State University, USA)
Prof. Michael Sebek (IEEE Fellow, Czech Technical University in Prague, Czech Republic)
Prof. Hashem Akbari (University of California, Berkeley, USA)
Prof. Lei Xu (IEEE Fellow, Chinese University of Hong Kong, Hong Kong)
Prof. M. Pelikan (UMSL, USA)
Prof. Patrick Wang (MIT, USA)
Prof. Sunil Das (IEEE Fellow, University of Ottawa, Canada)
Prof. Panos Pardalos (University of Florida, USA)
Prof. Nikolaos D. Katopodes (University of Michigan, USA)
Prof. Janusz Kacprzyk (IEEE Fellow, Polish Academy of Sciences, Poland)
Prof. Sidney Burrus (IEEE Fellow, Rice University, USA)
Prof. Biswa N. Datta (IEEE Fellow, Northern Illinois University, USA)
Prof. Mihai Putinar (University of California at Santa Barbara, USA)
Prof. Wlodzislaw Duch (Nicolaus Copernicus University, Poland)
Prof. Michael N. Katehakis (Rutgers, The State University of New Jersey, USA)
Prof. Dimitri Kazakos, Dean, (Texas Southern University, USA)
Prof. Ronald Yager (Iona College, USA)
Prof. Argyris Varonides (Univ. of Scranton, USA)
Prof. Alexey L Sadovski (IEEE Fellow, Texas A&M University, USA)
Prof. Ryszard S. Choras (University of Technology and Life Sciences Bydgoszcz, Poland)
Prof. Remi Leandre (Universite de Bourgogne, Dijon, France)
Prof. Alexander Zemliak (Puebla Autonomous University, Mexico)
Prof. Alexander Grebennikov (Autonomous University of Puebla, Mexico)
Prof. Guennadi A. Kouzaev (Norwegian University of Science and Technology, Norway)
Prof. Weilian Su (Naval Postgraduate School, USA)
Prof. Jiri Klima (Technical Faculty of CZU in Prague, Czech Republic)

Additional Reviewers

Matthias Buyle	Artesis Hogeschool Antwerpen, Belgium
Lesley Farmer	California State University Long Beach, CA, USA
Deolinda Rasteiro	Coimbra Institute of Engineering, Portugal
Sorinel Oprisan	College of Charleston, CA, USA
Santoso Wibowo	CQ University, Australia
Yamagishi Hiromitsu	Ehime University, Japan
Kei Eguchi	Fukuoka Institute of Technology, Japan
Shinji Osada	Gifu University School of Medicine, Japan
Tetsuya Yoshida	Hokkaido University, Japan
Xiang Bai	Huazhong University of Science and Technology, China
Philippe Dondon	Institut polytechnique de Bordeaux, France
José Carlos Metrôlho	Instituto Politecnico de Castelo Branco, Portugal
João Bastos	Instituto Superior de Engenharia do Porto, Portugal
Takuya Yamano	Kanagawa University, Japan
Hessam Ghasemnejad	Kingston University London, UK
Konstantin Volkov	Kingston University London, UK
Eleazar Jimenez Serrano	Kyushu University, Japan
Jon Burley	Michigan State University, MI, USA
Manoj K. Jha	Morgan State University in Baltimore, USA
Frederic Kuznik	National Institute of Applied Sciences, Lyon, France
Stavros Ponis	National Technical University of Athens, Greece
Ole Christian Boe	Norwegian Military Academy, Norway
Imre Rudas	Obuda University, Budapest, Hungary
Masaji Tanaka	Okayama University of Science, Japan
Francesco Rotondo	Polytechnic of Bari University, Italy
George Barreto	Pontificia Universidad Javeriana, Colombia
Dmitrijs Serdjuks	Riga Technical University, Latvia
Andrey Dmitriev	Russian Academy of Sciences, Russia
Tetsuya Shimamura	Saitama University, Japan
Francesco Zirilli	Sapienza Universita di Roma, Italy
Minhui Yan	Shanghai Maritime University, China
Valeri Mladenov	Technical University of Sofia, Bulgaria
Jose Flores	The University of South Dakota, SD, USA
James Vance	The University of Virginia's College at Wise, VA, USA
Genqi Xu	Tianjin University, China
Zhong-Jie Han	Tianjin University, China
Kazuhiko Natori	Toho University, Japan
Moran Wang	Tsinghua University, China
M. Javed Khan	Tuskegee University, AL, USA
Bazil Taha Ahmed	Universidad Autonoma de Madrid, Spain
Alejandro Fuentes-Penna	Universidad Autónoma del Estado de Hidalgo, Mexico
Miguel Carriegos	Universidad de Leon, Spain
Angel F. Tenorio	Universidad Pablo de Olavide, Spain
Abelha Antonio	Universidade do Minho, Portugal

Table of Contents

ISBN: 978-1-61804-216-3

ISBN: 978-1-61804-216-3

ISBN: 978-1-61804-216-3

Plenary Lecture 1

Discrete Lyapunov Controllers for an Actuator in Camless Engines

Professor Paolo Mercorelli
Leuphana University of Lueneburg
Germany
E-mail: mercorelli@uni.leuphana.de

Abstract: This paper deals with a hybrid actuator composed by a piezo and a hydraulic part controlled using two cascade Lyapunov controllers for camless engine motor applications. The idea is to use the advantages of both, the high precision of the piezo and the force of the hydraulic part. In fact, piezoelectric actuators (PEAs) are commonly used for precision positionings, despite PEAs present nonlinearities, such as hysteresis, satura- tions, and creep. In the control problem such nonlinearities must be taken into account. In this paper the Preisach dynamic model with the above mentioned nonlinearities is considered together with cascade controllers which are Lyapunov based. The sampled control laws are derived using the well known Backward Euler method. An analysis of the Backward and Forward Euler method is also presented. In particular, the hysteresis effect is considered and a model with a switching function is used also for the controller design. Simulations with real data are shown.

Brief Biography of the Speaker: Paolo Mercorelli received the (Laurea) M.S. degree in Electronic Engineering from the University of Florence, Florence, Italy, in 1992, and the Ph.D. degree in Systems Engineering from the University of Bologna, Bologna, Italy, in 1998. In 1997, he was a Visiting Researcher for one year in the Department of Mechanical and Environmental Engineering, University of California, Santa Barbara, USA. From 1998 to 2001, he was a Postdoctoral Researcher with Asea Brown Boveri, Heidelberg, Germany. From 2002 to 2005, he was a Senior Researcher with the Institute of Automation and Informatics, Wernigerode, Germany, where he was the Leader of the Control Group. From 2005 to 2011, he was an Associate Professor of Process Informatics with Ostfalia University of Applied Sciences, Wolfsburg, Germany. In 2010 he received the call from the German University in Cairo (Egypt) for a Full Professorship (Chair) in Mechatronics which he declined. In 2011 he was a Visiting Professor at Villanova University, Philadelphia, USA. Since 2012 he has been a Full Professor (Chair) of Control and Drive Systems at the Institute of Product and Process Innovation, Leuphana University of Lueneburg, Lueneburg, Germany.
Research interests: His current research interests include mechatronics, automatic control, signal processing, wavelets; sensorless control; Kalman filter, camless control, knock control, lambda control, robotics.

The full paper of this lecture can be found on page 19 of the present volume, as well as in the CD-ROM proceedings.

ISBN: 978-1-61804-216-3

Plenary Lecture 2

EMG-Analysis for Intelligent Robotic based Rehabilitation

Professor Thomas Schrader
University of Applied Sciences Brandenburg
Germany
E-mail: thomas.schrader@computer.org

Abstract: The establishment of wireless sensor network (WSN) technology in physiotherapy and rehabilitation is a clue for improvement of the thera- peutic process, quality assessment and development of supporting tech- nologies such as robotics. Especially for complex therapeutic interventions such as sensorimotor training, a continuous monitoring during the ther- apy as well as for all sessions would be quite useful. For the usage of robotic support in rehabilitation various input informa- tion about the status of patient and his/her activity status of various muscles have to be detected and evaluated. The critical point for robotic intervention is the response time. Under physiotherapeutic and rehabilita- tion conditions, the robotic device should be able to react differently and in various patterns. A complex analysis procedure of input signals such as EMG is essential to ensure an effective response of the robot. However sensor nodes in a wireless (body) area network have limited resources for calculating and storage processes. A stepwise procedure with distributed analysis tasks is proposed. Electromyogram (EMG) measurements of eight muscles were collected and evaluated in an experimental setting of a sensorimotor training using different types of balance boards. Fast and easy methods for detection of activity and rest states based on time domain analysis using low pass IIR filter und dynamic threshold adaption. These procedures can be done on the sensor nodes themselves or special calculation nodes in the network. More advanced methods in frequency domain or analysis of dynamical system behavior request much more system power in calculation as well as storage. These tasks could be done on the level of mobile devices such as mobile phones or tablet computer. A broad range of resources can be provided by cloud/internet. Such level based organization of analysis and system control can be com- pared with biological systems such as human nervous system.

ISBN: 978-1-61804-216-3

Plenary Lecture 3

Atmospheric Boundary Layer Effects on Aerodynamics of NREL Phase VI Windturbine in Parked Condition

Professor Mohammad Moshfeghi
Sogang University, South Korea
E-mail: mmoshfeghi@sogang.ac.kr

Abstract: In a natural condition, the wind is affected by the groundcover and the type of terrains which impose vertical velocity profile to the wind. This wind profile, which is also called atmospheric boundary layer (ABL), dramatically influences the aerodynamic behaviors and loadings of horizontalaxis wind turbines. However, for the sake of simplicity, many numerical simulations only deal with the uniform wind speed. To consider the effects of the ABL, numerical simulations of the two-bladed NREL Phase VI wind turbines aerodynamicat the parked condition are conducted under both uniform and ABL. The Deaves-Harris (DH)model is applied to the ABL. The wind turbine blades are kept at the six o'clock position and are considered at two different pitch angles. The aerodynamic forces and moments of the uniform the DH model are compared.The results show that the pitch angle at which the HAWT is parked plays an important role on the blade loading. Also it is observed that for the fully separated conditions, the Down-blade and the blade in the uniform wind are under approximately similar aerodynamic loadings, while the Up-blade encounters more aerodynamic loads, which is even noticeable value for this small wind turbine. This in turn means that for an appropriate and exact design, effects of ABL should be considered with more care.

Brief Biography of the Speaker: Dr. Mohammad Moshfeghi works in Multi-phenomena CFD Engineerng Research Center (ERC) Sogang University, Seoul, South Korea. He is also Lecturer in Qazvin Azad University. He has a registered patent: "Split-Blade For Horizontal Axis Wind Turbines" (Inventors: Mohammad Moshfeghi, Nahmkeon Hur).

ISBN: 978-1-61804-216-3

Plenary Lecture 4

Laminar and Turbulent Simulations of Several TVD Schemes in Two-Dimensions

Professor Edisson S. G. Maciel
Federal University of Great Dourados, Brazil
E-mail: edisavio@edissonsavio.eng.br

Abstract: This work, first part of this study, describes five numerical tools to perform perfect gas simulations of the laminar and turbulent viscous flow in two-dimensions. The Van Leer, Harten, Frink, Parikh and Pirzadeh, Liou and Steffen Jr. and Radespiel and Kroll schemes, in their first- and second-order versions, are implemented to accomplish the numerical simulations. The Navier-Stokes equations, on a finite volume context and employing structured spatial discretization, are applied to solve the supersonic flow along a ramp in two-dimensions. Three turbulence models are applied to close the system, namely: Cebeci and Smith, Baldwin and Lomax and Sparlat and Allmaras. On the one hand, the second-order version of the Van Leer, Frink, Parikh and Pirzadeh, Liou and Sreffen Jr., and Radespiel and Kroll schemes is obtained from a “MUSCL” extrapolation procedure, whereas on the other hand, the second order version of the Harten scheme is obtained from the modified flux function approach. The convergence process is accelerated to the steady state condition through a spatially variable time step procedure, which has proved effective gains in terms of computational acceleration (see Maciel). The results have shown that, with the exception of the Harten scheme, all other schemes have yielded the best result in terms of the prediction of the shock angle at the ramp. Moreover, the wall pressure distribution is also better predicted by the Van Leer scheme. This work treats the laminar first- and second-order and the Cebeci and Smith second- order results obtained by the five schemes.

Brief Biography of the Speaker: Professor Edisson Sávio de Góes Maciel was born in Recife, Pernambuco, Brazil in 1969, February, 25. He studied in Pernambuco until obtains his Master degree in Thermal Engineering, in 1996, August. With the desire of study aerospace and aeronautical problems using numerical methods as tools, he obtains his Doctor degree in Aeronautical Engineering, in 2002, December, in ITA and his Post-Doctor degree in Aerospace Engineering, in 2009, July, also in ITA. He is currently Professor at UFGD (Federal University of Great Dourados) – Mato Grosso do Sul – Brasil. He is author in 47 papers in international journals, 2 books, 67 papers in international conference proceedings. His research interestes includes a) Applications of the Euler equations to solve inviscid perfect gas 2D and 3D flows (Structured and unstructured discretizations) b) Applications of the Navier-Stokes equations to solve viscous perfect gas 2D and 3D flows (Structured and unstructured discretizations) c) Applications of the Euler and Navier-Stokes to solve magneto gas dynamics flows 2D and 3D; (Structured and unstructured discretizations) d) Applications of algebraic, one-equation, and two-equations turbulence models to predict turbulent effects in viscous 2D flows (Structured and unstructured discretizations), e) Study of artificial dissipation models to centered schemes

ISBN: 978-1-61804-216-3

in 2D and 3D spaces (Structured and unstructures discretizations) f)Applications of the Euler and Navier-Stokes equations to solve reentry flows in the Earth atmosphere and entry flows in Mars atmosphere in 2D and 3D (Structured and unstructured discretizations).

The full paper of this lecture can be found on page 79 of the Proceedings of the 2014 International Conference on Mechanics, Fluid Mechanics, Heat and Mass Transfer, as well as in the CD-ROM proceedings.

ISBN: 978-1-61804-216-3

Plenary Lecture 5

The Flocking Based and GPU Accelerated Internet Traffic Classification

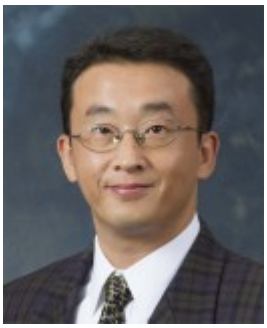

Professor Zhiguang Xu
Valdosta State University
USA
E-mail: zxu@valdosta.edu

Abstract: Mainstream attentions have been brought to the issue of Internet traffic classification due to its political, economic, and legal impacts on appropriate use, pricing, and management of the Internet. Nowadays, both the research and operational communities prefer to classify network traffic through approaches that are based on the statistics of traffic flow features due to their high accuracy and improved robustness. However, these approaches are faced with two main challenges: identify key flow features that capture fundamental characteristics of different types of traffic in an unsupervised way; and complete the task of traffic classification with acceptable time and space costs. In this paper, we address these challenges using a biologically inspired computational model that imitates the flocking behavior of social animals (e.g. birds) and implement it in the form of parallel programs on the Graphics Processing Unit (GPU) based platform of CUDA from NVIDIA™. The experimental results demonstrate that our flocking model accelerated by GPU can not only effectively select and prioritize key flow features to classify both well-known and unseen network traffic into different categories, but also get the job done significantly faster than its traditional CPU-based counterparts due to the high magnitude of parallelism that it exhibits.

Brief Biography of the Speaker: Prof. Zhiguang Xu received his Ph.D. in Computer Science from University of Central Florida, FL, USA in 2001. He is currently Professor of Computer Science in the Department of Math and Computer Science at Valdosta State University, GA, USA. His research and teaching interests include Computer Networking, Artificial Intelligence, Parallel and Distributed Computing, and Computer Science Education. Professor Xu is author or co-author of more than 25 published papers in refereed journals or conference proceedings. He has been awarded many grants from both academic and industrial entities. He is actively serving as committee member, reviewer, or lecturer of many national and international conferences and organizations.

The full paper of this lecture can be found on page 88 of the Proceedings of the 2014 International Conference on Mathematical Methods, Mathematical Models and Simulation in Science and Engineering, as well as in the CD-ROM proceedings.

ISBN: 978-1-61804-216-3

Plenary Lecture 6

The State of Civil Political Culture among Youth: Goals and Results of Education

Professor Irina Dolinina
Perm National Research University, Russia
E-mail: irina_edu@mail.ru

Abstract: Political culture is viewed as a phenomenon of social reality. Attitudes toward it (its meaning or significance) are historically conditioned. This research studies enduring presuppositions about (dispositions toward) society and the state, and how these are reflected in conscious stereotypes and cognitive structures among young people within the sociocultural mechanisms that form and modify the basic characteristics of political culture.

Brief Biography of the Speaker: Prof. Irina Dolinina was born in 1960, in Perm, Russia. She is Team Leader in the Research Project «Formation of the political culture of the students», and Professor of Philosophy and Law of the Faculty of Humanities, Perm National Research Technical University since 2012. She has received a lot of honors and awards (2012 - Diploma of the All-Russian Roswitha fund national education and the Education Committee of the State Duma of the Federal Assembly of the Russian Federation. 2013 - Diploma of the All-Russian Roswitha fund national education and the Education Committee of the State Duma of the Federal Assembly of the Russian Federation. Diploma-Russian contest "Best Science Book in the humanitarian sphere - 2013). Prof. Dolinina has various progessional organizations and activities.
(Expert on the legislative activities of the Council of Federation of Russia. Board member of the Interregional Association "For civic education." Director of the Research Centre of the political culture).

The full paper of this lecture can be found on page 57 of the Proceedings of the 2014 International Conference on Educational Technologies and Education, as well as in the CD-ROM proceedings.

ISBN: 978-1-61804-216-3

Discrete Lyapunov Controllers for an Actuator in Camless Engines

Paolo Mercorelli and Nils Werner

***Abstract*—**This paper deals with a hybrid actuator composed by a piezo and a hydraulic part controlled using two cascade Lyapunov controllers for camless engine motor applications. The idea is to use the advantages of both, the high precision of the piezo and the force of the hydraulic part. In fact, piezoelectric actuators (PEAs) are commonly used for precision positionings, despite PEAs present nonlinearities, such as hysteresis, saturations, and creep. In the control problem such nonlinearities must be taken into account. In this paper the Preisach dynamic model with the above mentioned nonlinearities is considered together with cascade controllers which are Lyapunov based. The sampled control laws are derived using the well known Backward Euler method. An analysis of the Backward and Forward Euler method is also presented. In particular, the hysteresis effect is considered and a model with a switching function is used also for the controller design. Simulations with real data are shown.

***Index Terms*—Lyapunov approach, hybrid actuators.**

I. Introduction

Recently, variable engine valve control has attracted a lot of attention because of its ability to improve fuel economy, reduce NOx emissions and to increase torque performance over a wider range than a conventional spark-ignition engine. In combination with microprocessor control, key functions of the motor management can be efficiently controlled by such mechatronic actuators. For moving distances between 5 and 8 mm, however, there are many actuator types with different advantages and drawbacks. We presented an adaptive PID controller design for a valve actuator control. In [1] a U-magnet structure is considered in which the Maxwell attracting force is quadratic to the current and inversely quadratic to the distance between the valve armature and the electromagnets. Using the topology presented in [1], it is possible to have the availability of a very big force with a small current. Nevertheless, difficulties connected with the control structure and in particular with the control for high cycles of the motor encouraged us to test other topologies. The main idea of this paper is using a hybrid actuator consisting of a piezo and a hydraulic part in order to take advantages of both of them: the high precision and velocity of the piezo and the force of the hydraulic part. Hydraulic actuators have been an attractive field since many years. Recently in [2] a nonlinear model of a hydraulic actuator considering amplitude and rate saturations, identified by an innovative method is proposed. An actuator model is taken into account with a first-order transfer function and nonlinear functions of saturation with unknown parameters. Piezo actuators demonstrate generally less difficulties of electromagnetic compatibility due to the quasi-absence of the inductance effects. The objective of this paper is to show a model of a hybrid actuator and a Lyapunov cascade regulator using, in one case, the Forward Euler discrete approximation, and finally, the case of Backward Euler approximation. The paper is organized with the following sections. Section II is devoted to the model description. After that, in Section III and IV, the control laws are derived. The paper ends with Section V in which simulation results of the proposed valve using real data are presented. After that, the conclusions follow.

Paolo Mercorelli is with the Institute of Product and Process Innovation, Leuphana University of Lueneburg, Volgershall 1, D-21339 Lueneburg, Germany. Phone: +49-(0)4131-677-5571, Fax: +49-(0)4131-677-5300. mercorelli@uni.leuphana.de. Nils Werner is with the Faculty of Automotive Engineering, Ostfalia University of Applied Sciences, Kleiststr. 14-16, D-38440 Wolfsburg, Germany. Phone: +49-(0)5361-831615 Fax. +49-(0)5361-831602. n.werner@ostfalia.de

The main nomenclature

$V_{in}(t)$: input voltage
$V_z(t)$: internal piezo voltage
$i(t)$: piezo input current
R_0: input resistance in the piezo model
R_a: parasite resistance in the piezo model
C_a: parasite capacitance in the piezo model
C_z: internal capacitance in the piezo model
$x_p(t)$: internal position of the piezo part
$x(t) = x_1(t)$: position of the piezo mass
$\dot{x}(t) = x_2(t)$: velocity of the piezo mass
$H(x_p(t), V_{in}(t))$: hysteresis characteristic of the piezo
$M_p/3$: moving piezo mass
K_x: internal spring constant of the piezo
K: spring constant acting on the piezo
D: damping constant acting on the piezo
D_{oil}: damping constant of the oil chamber acting on the piezo
$x_{SK}(t)$: position of the servo piston
$M_{SK}(t)$: mass of the servo piston
$K_{SK}(t)$: spring constant acting on the servo piston
$D_{SK}(t)$: damping constant acting on the servo piston
W: piezo$\rightarrow$ servopiston ratio
Q_{th}: mass flux of the hydraulic part
T_H: time constant of the linear model of the hydraulic part
T_M: time constant of the linear model of the mechanical part
V_H: steady-state factor of the linear model of the hydraulic part
V_M: steady-state factor constant of the linear model of the mechanical part
$K2Lidx$: characteristic value of the velocity-dependent internal leakage
T_s: sampling time

ISBN: 978-1-61804-216-3

II. Modeling of the Piezo Hydraulic Actuator

In the diagram of Fig. 1 the T-A connection links the couple of valves with the tank and the P-B connection links the couple of valves with the pump. In the position of Fig. 1 connections T-A and P-B are maximally open and the couple of valves are closed because point B is under pressure. When the piezo acts its force, the mechanical servo valve moves and begins to close these connections. When the mechanical servo valve is in the middle position, both connections (T-A and P-B) are closed and connections A-P and B-T begin to open. At this position also both motor valves begin to open because point A is under pressure. Figure 1 shows in detail a part of the hybrid structure

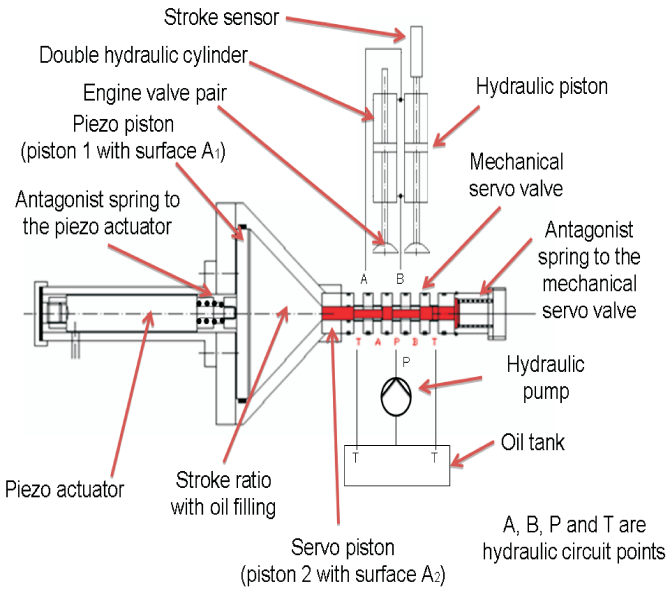

Fig. 1. Scheme of the whole Hybrid Piezo Hydraulic structure

which consists of a piezo actuator combined with a mechanical part. These two parts are connected by a stroke ratio to adapt the stroke length. The proposed nonlinearity model for PEA is quite similar to these presented in [3] and in [4] which show a sandwich model for a PEA. According to this proposed sandwich model, a PEA is constituted like a three layer sandwich. The middle layer is the effective piezo layer (P-layer), and the two outside layers connected to the electrodes are known in the literature as interfacing layers (I-layers). The P-layer is the layer that has the ordinary characteristics of piezo effects but without the nonlinearities of hysteresis and creep so that its behavior can be modeled by an equivalent linear circuitry. In contrast, the I-layers do not contribute any piezo effect; they are just parts of the circuit connecting P-layer to the electrodes in series. In [4] it is hypothesized that each of the I-layers can be equivalently represented by a capacitor and a resistor connected together in parallel. Together with the equivalent circuitry for P-layer, Fig. 2 shows the equivalent circuitry for a PEA with the I-layer nonlinearities of hysteresis and creep, in which two I-layers are combined together as C_a and R_a. The I-layer capacitor, C_a, is an ordinary one, which might be varied slightly with some factors, but here it would be assumed constant first for simplicity. The I-

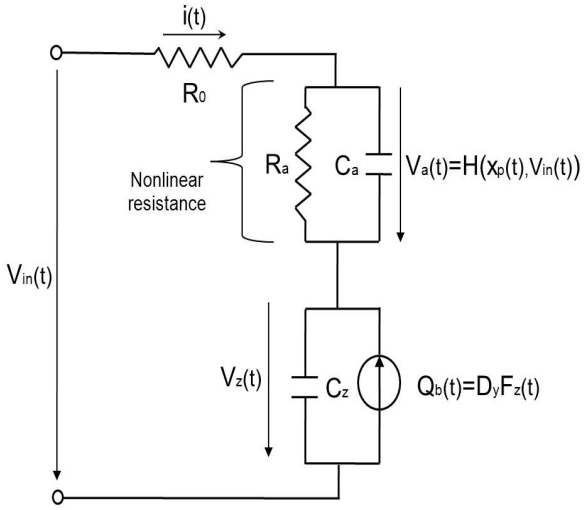

Fig. 2. Electrical part of the model

layer resistor, R_a , however, is really an extraordinary one with a significant nonlinearity. The resistance is either fairly large, say $R_a > 10^6\ \Omega$, when the voltage $\|V_a\| < V_h$, or is fairly small, say $R_a < 1000$, when $\|V_a\| > V_h$. In [4], the threshold voltage, V_h, is defined as the hysteresis voltage of a PEA. The authors in [4] gave this definition due to the observation that there is a significant difference and an abrupt change in resistance across this threshold voltage and it is this resistance difference and change across V_h that introduces the nonlinearities of hysteresis and creep in a PEA. The hysteresis effect could be seen as a function of input $V_{in}(t)$ and output $y(t)$ as follows: $H(y(t), V_{in}(t))$, see Fig. 3. According to this model, if $V_h = 0$, then the hysteresis will disappear, and if $R_a = \infty$ when $\|V_a\| < V_h$, then the creep will also disappear. Based on this proposed sandwich model and the equivalent circuitry as shown in Fig. 2, we can further derive the state model as follows:

$$\dot{V}_a(t) = -\Big(\frac{1}{R_a}+\frac{1}{R_o}\Big)\frac{V_a(t)}{C_a} - \frac{V_z(t)}{C_aR_o} + \frac{V_{in}(t)}{C_aR_o} \quad (1)$$

$$\dot{V}_z(t) = \frac{\dot{Q}_b}{C_z} + \frac{1}{C_z}\Big(-\frac{V_a(t)}{R_o} - \frac{V_z(t)}{R_o} + \frac{V_{in}(t)}{R_o}\Big), \quad (2)$$

where $Q_b = D_y F_z(t)$ is the "back electric charge force" (back-ecf) in a PEA, see [4]. According to [4] and the notation of Fig. 4, it is possible to write:

$$F_z(t) = M_p/3\ddot{x}(t) + D\dot{x}(t) + Kx(t) + K_x x(t). \quad (3)$$

K and D are the elasticity and the friction constant of the spring which is antagonist to the piezo effect and is incorporated in the PEA. C_z is the total capacitance of the PEA and R_o is the contact resistance. For further details on this model see [4]. Considering the whole system described in Fig. 4 with the assumptions of incompressibility of the oil, the whole mechanical system can be represented by a spring mass structure as shown in the conceptual scheme of Fig. 4. In this system the following notation is adopted: K_x

ISBN: 978-1-61804-216-3

is the elasticity constant factor of the PEA. In the technical literature, factor $D_x K_x = T_{em}$ is known with the name "transformer ratio" and states the most important characteristic of the electromechanical transducer. $M_p/3$ is, in our case, the moving mass of the piezo structure which is a fraction of whole piezo mass, M_{SK} is the sum of the mass of the piston with the oil and the moving actuator and M_v is the mass of the valve. It is possible to notice that the moving mass of the piezo structure is just a fraction of the whole piezo mass. The value of this fraction is given by the constructer of the piezo device and it is determined by experimental measurements. K_{SK} and D_{SK} are the characteristics of the antagonist spring to the mechanical servo valve, see Fig. 4. D_{oil} is the friction constant of the oil. Moreover, according to [4], motion $x_p(t)$ of diagram in Fig. 3 is:

$$x_p(t) = D_x V_z(t). \tag{4}$$

According to diagram of Fig. 2, it is possible to write as follows:

$$V_z = V_{in}(t) - R_0 i(t) - H(x_p(t), V_{in}(t)), \tag{5}$$

where R_0 is the connection resistance and $i(t)$ is the input current as shown in Fig. 2. $H(x_p(t), V_{in}(t))$ is the function which describes the hysteresis effect mentioned above and shown in the simulation of Fig. 3. Considering the whole

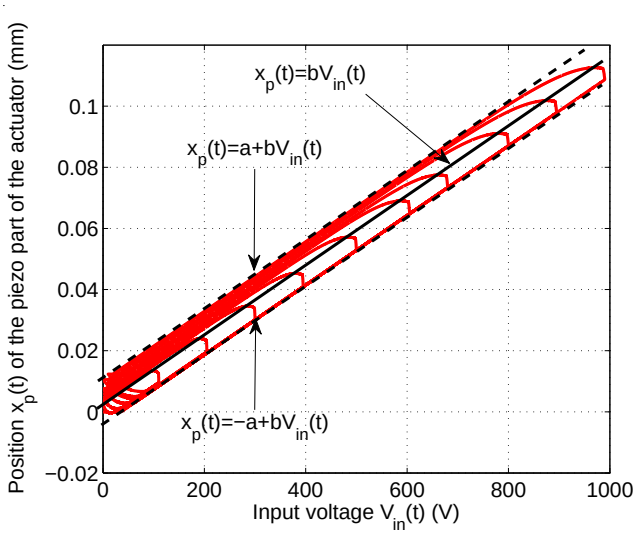

Fig. 3. Simulated Hysteresis curve of the piezo part of the actuator: $H(x_p(t), V_{in}(t))$

system described in Fig. 4, the electrical and mechanical systems described in Figs. 2, 3 and 4 can be represented by the following mathematical expressions:

$$\frac{M_p}{3}\ddot{x}(t) + M_{SK}\ddot{x}_{SK}(t) + Kx(t) + D\dot{x}(t) + K_{SK}x_{SK}(t) + D_{SK}\dot{x}_{SK}(t) + D_{oil}\dot{x}_{SK}(t) + K_x\Big(x(t) - \Delta x_p(V_{in}(t))\Big) = 0, \tag{6}$$

where $\Delta x_p(t)$ represents the interval function of $x_p(t)$ as shown in Fig. 3 which, according to equation (4), can be expressed as:

$$\Delta x_p(t) = D_x \Delta V_z(t). \tag{7}$$

Finally, using equations (5) and (7),

$$K_x \Delta x_p(t) = K_x D_x\big(V_{in}(t) - R_0 i(t) - H(\Delta x_p(t), V_{in}(t))\big), \tag{8}$$

which represents the interval force generated by the piezo device. Equation (6) can be expressed in the following way:

$$\frac{M_p}{3}\ddot{x}(t) + M_{SK}\ddot{x}_{SK}(t) + Kx(t) + D\dot{x}(t) + K_{SK}x_{SK}(t) + D_{SK}\dot{x}_{SK}(t) + D_{oil}\dot{x}_{SK}(t) + K_x x(t) = K_x \Delta x_p(V_{in}(t)). \tag{9}$$

It is to be noticed that under quasi-static conditions (low velocity ranges) the following relation holds:

$$x_{SK}(t) \approx W x(t), \tag{10}$$

where W is the position ratio above defined and it states the incompressibility of the oil in the conic chamber. $F_d(t)$ is the combustion back pressure in terms of force. According to Fig.

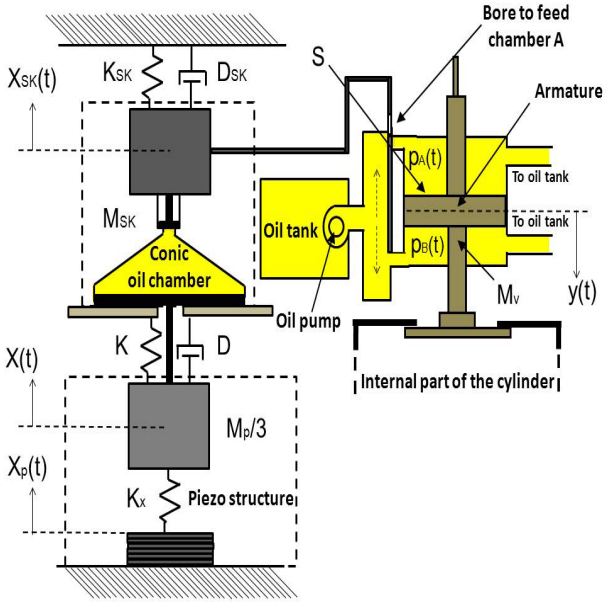

Fig. 4. Mass spring model of the whole actuator

3 in which an upper bound and a lower bound of the hysteresis curve are indicated, it is possible to write that:

$$\Delta x_p(V_{in}(t)) = [-a \quad a] + bV_{in}(t), \tag{11}$$

with $a \in \mathbb{R}$ and $b \in \mathbb{R}$ two positive constants are indicated. In particular,

$$\underline{\Delta} x_p(V_{in}(t)) = -a + bV_{in}(t), \tag{12}$$

and

$$\overline{\Delta} x_p(V_{in}(t)) = a + bV_{in}(t). \tag{13}$$

Considering this notation, the system represented in (6) can be split into the following two models:

$$\frac{M_p}{3}\ddot{x}(t) + M_{SK}\ddot{x}_{SK}(t) + Kx(t) + D\dot{x}(t) + K_{SK}x_{SK}(t) + D_{SK}\dot{x}_{SK}(t) + D_{oil}\dot{x}_{SK}(t) + K_x x(t) = \underline{\Delta} x_p(V_{in}(t)), \tag{14}$$

and

$$\frac{M_p}{3}\ddot{x}(t)+M_{SK}\ddot{x}_{SK}(t)+Kx(t)+D\dot{x}(t)+K_{SK}x_{SK}(t)+ D_{SK}\dot{x}_{SK}(t)+D_{oil}\dot{x}_{SK}(t)+K_x x(t)=\overline{\Delta}x_p(V_{in}(t)), \quad (15)$$

III. Control of the piezo mechanical part of the actuator

If $x(t)=x_1(t)$, then:

$$\begin{aligned}\dot{x}_1(t) &= x_2(t) \quad (16)\\ \dot{x}_2(t) &= \frac{-Dx_2(t)-W(D_{SK}+D_{oil})x_2(t)}{\frac{M_p}{3}+M_{SK}W}+ \frac{-(K+K_x+K_{SK}W)x_1(t)}{\frac{M_p}{3}+M_{SK}W}+ \frac{3K_xbV_{in}(t)+(-1)^q a}{\frac{M_p}{3}+M_{SK}W}, \quad (17)\end{aligned}$$

where $q=1,2$. If it is assumed that $V_{in}(t)=V_z(t)$, then

$$\begin{bmatrix}\dot{x}_{1_{SK}}(t)\\ \dot{x}_{2_{SK}}(t)\end{bmatrix}=\begin{bmatrix}0 & 1\\ -\frac{c_n}{a_n} & -\frac{b_n}{a_n}\end{bmatrix}\cdot\begin{bmatrix}x_1(t)\\ x_2(t)\end{bmatrix}+ \begin{bmatrix}0\\ \frac{3K_xb}{a_n}\end{bmatrix}\cdot\left[V_z(t)+\frac{a(-1)^q}{3K_xb}\right], \quad (18)$$

where

$$a_n=\frac{M_P}{3}+M_{SK}\cdot W \quad (19)$$

$$b_n=D+D_{SK}\cdot W \quad (20)$$

$$c_n=K_x+K+K_{SK}\cdot W. \quad (21)$$

To sum up, it is possible to write the following general expression for the dynamics of the piezo part of the actuator:

$$\dot{\mathbf{x}}(t)=\mathbf{A}_n\cdot\mathbf{x}(t)+\mathbf{B}_n\cdot\left[V_z(t)+\frac{a(-1)^q}{3K_xb}\right]. \quad (22)$$

To obtain the servo piston position it is enough to remember that in quasi-static conditions the following expressions hold: $x_{SK}(t)\approx Wx_1(t)$ and $\dot{x}_{SK}(t)\approx Wx_2(t)$.

A. A Lyapunov based controller for the piezo mechanic actuator

For designing a controller for the piezo mechanical part of the actuator, it is to consider that, according to the real data which we have, the piezo part of the model results to be more than 10 times faster than the mechanical part. This allows us to consider just the mechanical model in order to conceive a possible control law. Considering $\mathbf{K}_i(t)=\mathbf{e}(t)=\mathbf{x}_d(t)-\mathbf{x}(t)$, in which $\mathbf{x}_d(t)$ represents the desired state vector (position and velocity) of the servo mechanical piston. Defining

$$\mathbf{V}(\mathbf{K}_i)=\frac{\mathbf{K}_i^2(t)}{2}, \text{then it follows that:} \quad (23)$$

$$\dot{\mathbf{V}}(\mathbf{K}_i)=\mathbf{K}_i(t)\dot{\mathbf{K}}_i(t). \quad (24)$$

In order to find a stabile solution, it is possible to choose the following function:

$$\dot{\mathbf{V}}(\mathbf{K}_i)=-\eta(t){\mathbf{K}_i}^2(t), \quad (25)$$

with η a positive definite diagonal matrix is indicated. Comparing (24) with (25), the following relationship is obtained:

$$\mathbf{K}_i(t)\dot{\mathbf{K}}_i(t)=-\eta\mathbf{K}_i^2(t), \quad (26)$$

and finally

$$\mathbf{K}_i(t)\big(\dot{\mathbf{K}}_i(t)+\eta\mathbf{K}_i(t)\big)=0. \quad (27)$$

The no trivial solution follows from the condition

$$\dot{\mathbf{K}}_i(t)+\eta\mathbf{K}_i(t)=0, \quad (28)$$

which can be rewritten as:

$$\dot{\mathbf{x}}_d(t)-\dot{\mathbf{x}}(t)+\eta\big(\mathbf{x}_d(t)-\mathbf{x}(t)\big)=0. \quad (29)$$

Considering Eq. (22) the following expression is obtained:

$$\dot{\mathbf{x}}_d(t)-\mathbf{A}_n\cdot\mathbf{x}(t)+\mathbf{B}_n\cdot\left[V_z(t)+\frac{a(-1)^q}{3K_xb}\right]+ \eta\big(\mathbf{x}_d(t)-\mathbf{x}(t)\big)=0, \quad (30)$$

it follows that:

$$V_z(t)=pinv(\mathbf{B}_n)\cdot \Big(\mathbf{A}_n\cdot\mathbf{x}(t)-\dot{\mathbf{x}}_d(t)-\eta\big(\mathbf{x}_d(t)+\mathbf{x}(t)\big)\Big)-\frac{a(-1)^q}{3K_xb}, \quad (31)$$

where Moore-Penrose Pseudoinverse of matrix $\mathbf{B}_n$ is used. Considering that the model of Eq. (22) is a minimum phase model, then signal $V_z(t)$ is a limited one. Using the control of Eq. (31), the following error dynamics is obtained:

$$\dot{\mathbf{e}}(t)+\eta\mathbf{e}(t)=0. \quad (32)$$

If a non exact cancellation is considered, then:

$$\dot{\mathbf{e}}(t)+\eta\mathbf{e}(t)=\mathbf{\Delta}(\mathbf{x}_d(t),\mathbf{x}(t)), \quad (33)$$

where $\mathbf{\Delta}(\mathbf{x}_d(t),\mathbf{x}(t))$ represents the cancellation error which can be assumed to be limited because of model of Eq. (22) being a minimum phase one. Considering the Forward Euler sampling approximation, Eq. (33) becomes:

$$\mathbf{e}(k)-\mathbf{e}(k-1)+T_s\eta\mathbf{e}(k-1)=T_s\mathbf{\Delta}(\mathbf{x}_d(k-1),\mathbf{x}(k-1)), \quad (34)$$

where T_s equals the sampling time. It is well known that in order to obtain the asymptotic stability it must be $\eta < diag(2/T_s)$, but in this case parameter η does not influence the reduction of the error. In fact, we can write the following relation:

$$\mathbf{e}(k)=(\mathbf{I}-T_s\eta)\mathbf{e}(k-1)+T_s\mathbf{\Delta}(\mathbf{x}_d(k-1),\mathbf{x}(k-1)). \quad (35)$$

If Backward Euler sampling approximation is considered, then Eq. (33) becomes:

$$\mathbf{e}(k)-\mathbf{e}(k-1)+T_s\eta\mathbf{e}(k)=T_s\mathbf{\Delta}(\mathbf{x}_d(k),\mathbf{x}(k)), \quad (36)$$

and in case of no exact cancellation through parameter η it is possible to control the error: the bigger parameter η is, the smaller the error becomes. In fact, we can write the following relation:

$$\mathbf{e}(k)=(\mathbf{I}+T_s\eta)^{-1}\mathbf{e}(k-1)+ (\mathbf{I}+T_s\eta)^{-1}T_s\mathbf{\Delta}(\mathbf{x}_d(k-1),\mathbf{x}(k-1)). \quad (37)$$

ISBN: 978-1-61804-216-3

If the Backward Euler sampling method is considered for the control law of Eq. (31), then:

$$V_z(k) = pinv(\mathbf{B}_n) \cdot \Big(\mathbf{A}_n \cdot \mathbf{x}(k) - \frac{\mathbf{x}_d(k) - \mathbf{x}_d(k-1)}{T_s} - \eta\big(\mathbf{x}_d(k) + \mathbf{x}(k)\big)\Big) - \frac{a(-1)^q}{3K_x b}, \quad (38)$$

where Moore-Penrose Pseudoinverse of $\mathbf{B}_n$ is used.

IV. Modelling and Control of the Hydraulic Part of the Actuator

In Fig. 5 a possible linear model often utilised in practical applications is presented. The model was presented in [5] and it is a possible linear approximation utilized in many industrial applications, see the industrial cases presented in [5]. In Fig. 5 this model in which, the following parameters are visible, is represented: T_H which represents the time constant of the hydraulic part, T_M which represents the time constant of the mechanic part. V_H and V_M represent the steady state factors of the hydraulic and mechanical transfer function respectively. The other parameter which characterises the hydraulic-mechanical model is $K2Lidx$. In fact, parameter $K2Lidx$ is a characteristic value of the velocity-dependent internal leakage. This parameter multiplied by the velocity of the valve states a loosing force as represented in the block diagram of Fig. 5. Parameter A_{AK} is the surface of the moving part (servo piston). Observing Fig. 5 and considering that

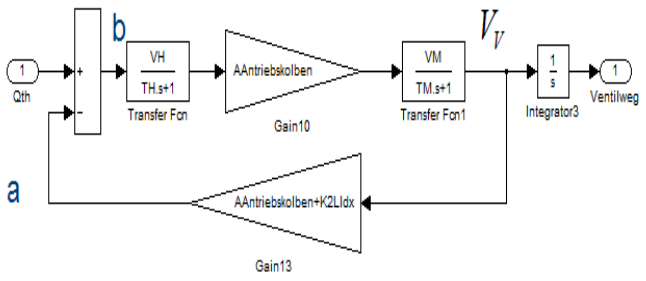

Fig. 5. Hydraulic model structure

variable Q_{th} is the mass flux involved in the hydraulic actuator, the following calculations are derived:

$$b_m = Q_{th}(s) - a_m \quad (39)$$

$$V_V(s) = b_m \cdot \frac{V_H \cdot V_M \cdot A_{AK}}{(T_H \cdot s + 1) \cdot (T_M \cdot s + 1)} \quad (40)$$

$$V_V(s) = b_m \cdot \frac{V_H \cdot V_M \cdot A_{AK}}{T_H \cdot T_M \cdot s^2 + (T_H + T_M) \cdot s + 1} \quad (41)$$

$$a_m = V_V(s) \cdot (A_{AK} + K2Lidx), \quad (42)$$

$$b_m = Q_{th}(s) - V_V(s) \cdot (A_{AK} + K2Lidx), \quad (43)$$

$$V_V(s) = (Q_{th}(s) - V_V(s) \cdot (A_{AK} + K2Lidx)) \cdot \frac{V_H \cdot V_M \cdot A_{AK}}{T_H \cdot T_M \cdot s^2 + (T_H + T_M) \cdot s + 1} \quad (44)$$

Considering the transfer function, then:

$$\frac{V_V(s)}{Q_{th}(s)} = \frac{d_m}{a_m \cdot s^2 + b_m \cdot s + c_m}, \quad (45)$$

where:

$$a_m = T_H \cdot T_M, \quad (46)$$

$$b_m = (T_H + T_M), \quad (47)$$

$$c_m = 1 + V_H \cdot V_M \cdot A_{AK} \cdot (A_{AK} + K2Lidx), \quad (48)$$

$$d_m = V_H \cdot V_M \cdot A_{AK}, \quad (49)$$

$$a_m \cdot s^2 \cdot V_V(s) + b \cdot s \cdot V_V(s) + c \cdot V_V(s) - d_m \cdot Q_{th}(s) = 0. \quad (50)$$

Considering the back Laplace transform, then:

$$a_m \cdot \ddot{V}_V(t) + b \cdot \dot{V}_V(t) + c \cdot V_V(t) - d_m \cdot Q_{th}(t) = 0. \quad (51)$$

If the following positions are considered:

$$x_1(t) = V_V(t) \quad (52)$$

$$x_2(t) = \dot{x}_1(t) \quad (53)$$

then:

$$\dot{x}_1(t) = x_2(t) \quad (54)$$

$$\dot{x}_2(t) = \frac{1}{a_m} \cdot (d_m \cdot Q_{th}(t) - b_m \cdot x_2(t) - c_m \cdot x_1(t)) \quad (55)$$

and

$$\begin{bmatrix} \dot{x}_1(t) \\ \dot{x}_2(t) \end{bmatrix} = \begin{bmatrix} 0 & 1 \\ -\frac{c_m}{a_m} & -\frac{b_m}{a_m} \end{bmatrix} \cdot \begin{bmatrix} x_1(t) \\ x_2(t) \end{bmatrix} + \begin{bmatrix} 0 \\ \frac{d_m}{a_m} \end{bmatrix} \cdot Q_{th}(t). \quad (56)$$

It is possible to write the following general equation:

$$\dot{\mathbf{x}}(t) = \mathbf{A}_m \cdot \mathbf{x}(t) + \mathbf{B}_m \cdot Q_{th}(t). \quad (57)$$

Concerning the control aspects, similar considerations as for the piezo mechanical part of the actuator can be done and the following sampled control law can be derived using Backward Euler sampling method, the following final inverse equation is obtained:

$$Q_{th}(k) = pinv(\mathbf{B}_m) \cdot \Big(\mathbf{A}_m \cdot \mathbf{x}(k) - \frac{\mathbf{x}_d(k) - \mathbf{x}_d(k-1)}{T_s} - \eta\big(\mathbf{x}_d(k) + \mathbf{x}(k)\big)\Big), \quad (58)$$

where Moore-Penrose Pseudoinverse of $\mathbf{B}_m$ is used.

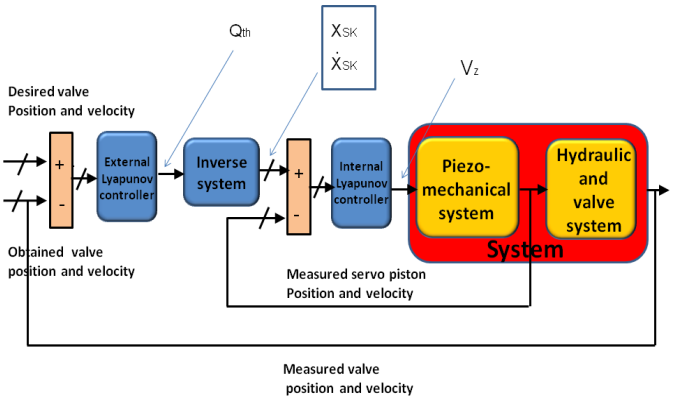

Fig. 6. Control scheme

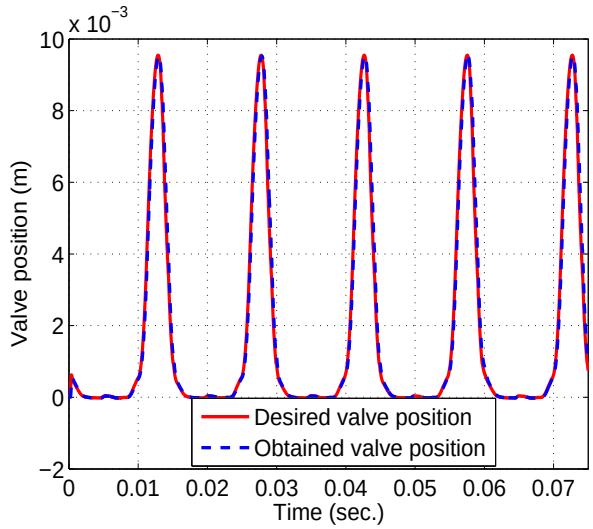

Fig. 7. Desired and obtained valve positions corresponding to 8000 rpm

V. Simulation Results

The control scheme is shown in Fig. 6 in which the control laws of equations (38) and (58) are inside the internal and external Lyapunov blocks. After the external Lyapunov block an inversion block is put to state the algebraic relation between variable Q_{th} and variable x_{SK}. Figure 7 shows the final results concerning the tracking of a desired position of an exhaust valve with 8000 rpm. Figure 8 shows the final results concerning the tracking of a desired velocity of an exhaust valve with 8000 rpm. Concerning the force acting directly on the valve at the opening time which has a peak value equal to 700 N circa and it is reduced to a few Newton acting on the piezo part thanks to the decoupling structure of the hybrid actuator. This is one of the greatest advantages of these hybrid actuators. The model of such kind of a disturbance is obtained as an exponent function of the position of the valve. The digital controller is set to work with a sampling time equal to 20×10^{-6} s, according to the specifications of the Digital Signal Processor which we are intended to test the system with.

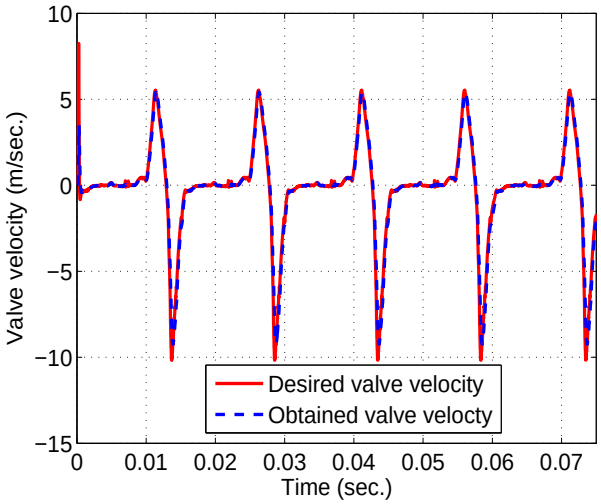

Fig. 8. Desired and obtained valve velocity considering 8000 rpm

VI. Conclusions and Future Objectives

A. Conclusions

This paper deals with a hybrid actuator composed by a piezo and a hydraulic part and its control structure for camless engine motor applications. The idea is to use the advantages of both, the high precision of the piezo and the force of the hydraulic part. The proposed control scheme considers two Laypunov based controllers. Backward and Forward Euler sampling methods are compared. Simulations with real data of a motor and of a piezo actuator are shown for the controller realized by Backward Euler method.

References

[1] P. Mercorelli. An anti-saturating adaptive pre-action and a slide surface to achieve soft landing control for electromagnetic actuators. *IEEE/ASME Transactions on Mechatronics*, 17(1):76–85, 2012.

[2] P. Sarhadi, N.O. Ghahramani, and I. Shafeenejhad. Identification of a non-linear hydraulic actuator considering rate saturation using particle swarm optimisation algorithm. *In Int. J. of Modelling, Identification and Control, Inderscience publishers*, 18(2):136–145, 2013.

[3] H.J.M.T.A. Adriaens, W.L. de Koning, and R. Banning. Modeling piezoelectric actuators. *IEEE/ASME Transactions on Mechatronics*, 5(4):331–341, 2000.

[4] Y.-C. Yu and M.-K. Lee. A dynamic nonlinearity model for a piezo-actuated positioning system. In *Proceedings of the 2005 IEEE International Conference on Mechatronics, ICM* 10^{th}-12^{th} *July*, Taipei, 2005.

[5] H. Murrenhoff. *Servohydraulik*. Shaker Verlag, Aachen, 2002.

ISBN: 978-1-61804-216-3

FPGA Implementation of a Memory-Efficient Stereo Vision Algorithm Based on 1-D Guided Filtering

Yuki Sanada, Katsuki Ohata, Tetsuro Ogaki, Kento Matsuyama, Takanori Ohira, Satoshi Chikuda, Masaki Igarashi, Tadahiro Kuroda, Masayuki Ikebe, Tetsuya Asai and Masato Motomura

***Abstract*—** This paper presents an FPGA implementation of a memory-efficient stereo vision algorithm. Recently, a hardware-oriented stereo vision algorithm using 1-D guided filtering was proposed [1]. Our architecture is based on this algorithm and calculates the depth map in 1-D space, and therefore, the required amount of memory is significantly reduced. To realize high speed processing, we apply a full-pipeline and highly parallel structure. Implemented on FPGA, our design uses an 89 kb memory and achieves a 188 frame per second rate for 384×288 stereo images. The accuracy of the disparity map is not satisfactory; however, it can be improved by a small amount of software processing (8.6 ms) [1]. This result shows that the proposed architecture is highly efficient in terms of the required memory, and its processing speed and accuracy is the same as that of other methods.

***Index Terms*—**Stereo Vision, Guided Filter, FPGA

I. INTRODUCTION

STEREO matching is a method for estimating a depth map from a stereo image pair. It is desirable to calculate a depth map in real time so that it can be applied for tracking objects, surveillance, pedestrian detection, and so on. Therefore, many researchers have proposed high speed and high accuracy stereo matching methods, and an FPGA or GPU is often used as an accelerator.

GPU-based methods yield high accuracy disparity information, since they employ a complex algorithm. Recently, several methods that employ an edge-preserving filter, such as a guided filter [2], bilateral filter [3], and domain transform filter [4], have been proposed. The method proposed in [5] provides the best accuracy of all the high-speed methods. It achieves a speed that is close to real-time, and holds the second place in the Middlebury stereo evaluation ranking [6].

FPGA-based methods achieve a very high processing speed for a large image having dense disparity. Correlation-based algorithms (SSD, CENSUS) and dynamic programming are often employed ([7],[8]). The objective of some research studies was to achieve an implementation that requires only a small amount of resources. For example, the method presented in [9] reduces the required memory size to 0.9 Mb. However, in these studies, the error rates that were obtained were high or were not evaluated numerically. Meanwhile, Jin and Maruyama presented a system that is, to the best of our knowledge, state of the art [10]. It maintains an accuracy that places in the middle of the Middlebury stereo evaluation ranking and achieves 199.7 fps for an image size of 1024×768.

These methods are satisfactory in terms of both processing speed and accuracy. However, in terms of their application in mobile devices, there is room for improvement. A small device cannot be equipped with a high-end GPU, since it consumes a large amount of energy and uses a large space. Jin and Maruyama's method, which achieves the best performance in FPGA, requires a memory size of 7 Mb. In cases where only on-chip or limited off-chip memory can be used to create a compact package, 7 Mb is too large a memory size.

In this paper, we propose a memory-efficient stereo vision architecture for implementation in mobile device applications. Our algorithm is based on 1-D guided filtering and calculates the disparity map using 1-D information only. Our designed architecture employs a 1-D guided filter in parallel and applies a full pipeline structure. Therefore, it achieves both a reduction in the required amount of memory and high speed processing. On the other hand, the error rate is quite high, because 2-D information is missing. However, by applying simple 2-D software processing to the 1-D hardware output, the error rate can be reduced. When realized in an Altera Stratix II device, our circuit required 89 kb of memory and achieved a rate of 188 fps at 20 MHz for producing a 384×288 disparity map.

The rest of this paper is organized as follows. In Section II, we introduce our stereo matching algorithm and 2-D-software refinement processing. Then, the details of our designed architecture are described in Section III. In Section IV, the experimental results for FPGA implementation are given. Finally, in Section V we present our conclusions.

II. ALGORITHM AND 2-D SOFTWARE REFINEMENT

In general, a local stereo matching algorithm is divided into four steps: i) Cost calculation: a cost map is calculated for each disparity according to the similarities of the corresponding pixels in the stereo image; ii) Cost aggregation: cost maps are filtered to suppress noise; iii) Disparity computation: disparity for each pixel, usually that with the lowest cost, is selected; iv) Disparity refinement: errors in the depth map are detected and fixed.

Our algorithm is based on that presented in [2], and thus, the processes in steps i), iii), and iv) remain the same. The

Y. Sanada is with the Graduate School of Information Science and Technology, Hokkaido University, Kita 14, Nishi 9, Kita-ku, Sapporo 060–0814, Japan (e-mail: sanada@lalsie.ist.hokudai.ac.jp).

K. Ohata, T. Ogaki and T. Kuroda are with the Faculty of Science and Technology, Keio University Hiyoshi 3-14-1, Kouhokuku, Yokohama 223–8522, Japan.

K. Matsuyama, T. Ohira, S. Chikuda, M Igarashi, M. Ikebe, T. Asai and M. Motomura are with the Graduate School of Information Science and Technology, Hokkaido University, Kita 14, Nishi 9, Kita-ku, Sapporo 060–0814, Japan.

ISBN: 978-1-61804-216-3

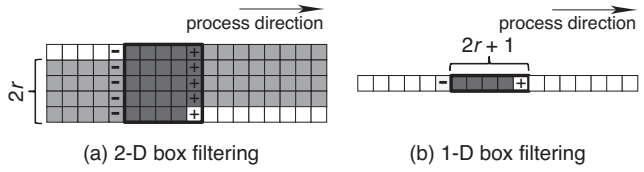

(a) 2-D box filtering (b) 1-D box filtering

Fig. 1: Comparison of the buffer size. The black frame of pixels are used in the calculation. In a 2-D process, the gray pixels outside the black frame must be conserved.

difference is in the cost aggregation step (ii). We applied gray-scale and one-dimensional filtering to 2-D guided filtering to reduce the required amount of memory. 2-D software processing, which improves a 1-D disparity map, is also a characteristic of our system.

A. 1-D Cost Aggregation

Rheman *et al.* employed a guided filter in cost aggregation [2]. The given input image is a pixel $I(x, y)$; the equations are

$$A(y,x) = \frac{\overline{I(y,x)C(y,x)} - \overline{I(y,x)}\ \overline{C(y,x)}}{\overline{I(y,x)^2} - \overline{I(y,x)}\ \overline{I(y,x)} + \epsilon} \tag{1}$$

$$B(y,x) = \overline{C(y,x)} - A(y,x)\overline{I(y,x)} \tag{2}$$

$$C'(y,x) = \overline{A(y,x)}I(y,x) - \overline{B(y,x)} \tag{3}$$

where $\overline{X(y,x)}$ denotes the mean of X in the window centered at position (y, x), and ϵ denotes a regularizing parameter. This filter smooths the cost C using I, and outputs C'.

In our method, we adopted a 1-D process and gray scale for guided filtering. If the input image is given by a raster scan, calculating $\overline{X}$ in 2-D space requires a large amount of memory. Using a fast calculation algorithm [11], 2-D box filtering requires $2r$ line buffers (Fig. 1(a)). Here, r is a filter radius. On the other hand, calculating $\overline{X}$ in 1-D space reduces the required memory size to $2r + 1$ (Fig. 1(b)). The amount of calculation required using the formulae (1) to (3) is six times greater, and thus, a 1-D method can greatly reduce the required memory size. Gray scale guided filtering is also memory efficient. The amount of information contained in the RGB scale is three times that in the gray scale, and therefore, gray scale calculating reduces the memory size by 1/3. It should be noted that the accuracy of the disparity map does not deteriorate significantly, since the RGB information is already contained in the initial cost.

The 1-D process increases the error rate but it can be refined to some degree by adopting a variable filter size. In our system, since there is no correlation between different rows, the filter radius can be assigned to each row independently. The filter radius is determined by tendency T of texture continuity:

$$T(y,x) = \sum_{x} |I^f_{r\mathrm{large}}(y,x) - I^f_{r\mathrm{small}}(y,x)| \tag{4}$$

where I^f_r is the gray scale image 1-D box filtered with radius r. If the values of both inputs are close, it is considered that the textures repeat a similar pattern. The filter size of each line processing is selected using the tendency and thresholds. In our experiment, two threshold values, θ_1 and $\theta_2(= 2\theta_1)$, and three approximate radius values,r_s, $r_m(= r_s + r_{\mathrm{step}})$, and $r_m(= r_s + 2r_{\mathrm{step}})$, were determined. We confirmed that the error rate is improved by approximately 0.18%.

B. 2-D Software Refinement

2-D software processing consists of preprocessing, error correction, and applying a median filter.

Before completing the refinement, the error detection and noise reduction is preprocessed. The 1-D hardware output does not consider the vertical connections of disparities, and errors occur as horizontal streaks. In error detection, the vertical gradient of the target pixel (x, y) and $(y \pm 1, x)$ is used for labeling. The labeled pixel contains streak errors or correct edge information. In noise reduction, if the disparity of the upper and lower pixel is equal, the center pixel is corrected to the same value.

Error correction is performed according to the five nearest non-labeled pixels above and below the target pixel. The mode disparity of a 5-pixel set whose colors are closer to that of the target pixel is used for the correction.

2-D refinement is completed with a 5×5 median filter for denoising. The details of 2-D software refinement are described in [1]. Figure 2 shows a comparison of the 1-D hardware and 2-D software outputs.

In this study, the entire 2-D refinement algorithm is processed by software, but the preprocessing can be implemented on hardware equipped with a 3-line buffer. On the other hand, the error correction must be executed by software. This requires a vertical direction process, and means that a frame-size memory is necessary for the hardware implementation.

III. FPGA IMPLEMENTATION

The solid blocks of Fig. 3 show the block diagram of our architecture. The depth resolution ($\equiv 2^N$) determines the degree of the parallelism, where the output latency increases as N increases, while the throughput is constant for different N values. Since our circuit is fully pipelined, each pixel of the left and right image ($H \times W$) is input and 1 disparity pixel is output in every clock cycle. Therefore, a latency of about $4 \times W$ clock cycles is required, but the frame rate is determined by the clock frequency f and the image size.

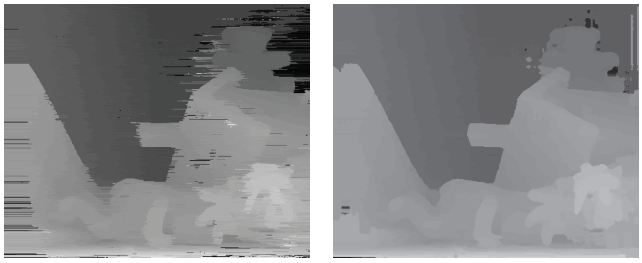

Fig. 2: Example of the Teddy dataset. Left: 1-D hardware output. Right: Processed 2-D software refinement.

ISBN: 978-1-61804-216-3

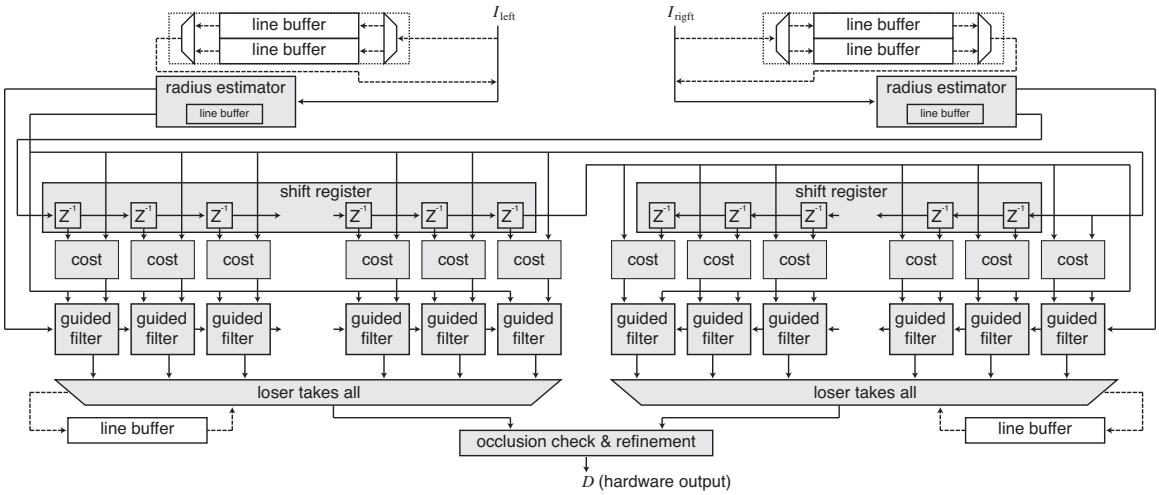

Fig. 3: Block diagram of proposed parallel stereo-matching architecture

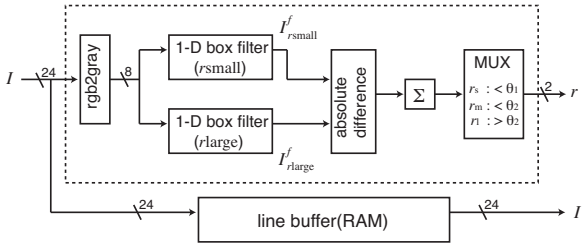

Fig. 4: Block diagram of radius estimator

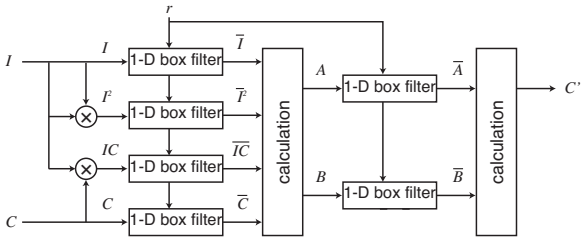

Fig. 5: Block diagram of 1-D-guided filter

The system consists of two radius estimators for left and right sequential images, $2^{N+1}-1$ delay registers (Z^{-1}) for generating binocular disparity, 2^{N+1} cost estimators, 2^{N+1} guided filters, two loser-takes-all circuits to find the minimum costs for the left and right blocks, and an occlusion-check and refinement circuit.

A. Radius Estimator

The given input (sequential) left and right image are first sent to the radius estimator (Fig. 4), which outputs the radius values for the subsequent guided filters. Since the radius estimator employs gray-scale information, an RGB 24 bit pixel is converted to a gray-scale 8 bit pixel. Then, the sum of the absolute difference of $I^f_{r\text{large}}$ and $I^f_{r\text{small}}$ is calculated, and the filter radius is determined by comparing this value with the threshold θ. The bandwidth of the output is sufficient to use 2 bits as a control signal.

The radius values are obtained after reading one line of input images. Therefore, the input image sequences are delayed by the line buffers, as shown in Fig. 4.

B. Cost Estimator

After the radius estimation step, the delayed image sequences arrive as inputs at the shift register (leftmost and rightmost of Z^{-1} in Fig. 3), which gives the pixel values shifted from 0 to 2^N-1 pixels in both the left and right

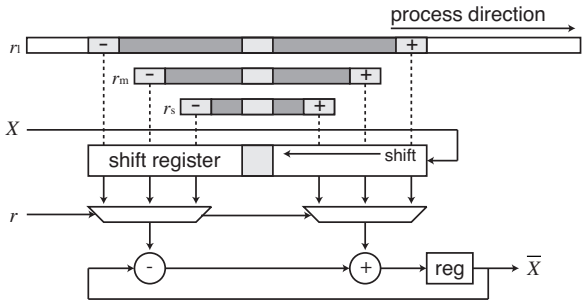

Fig. 6: Block diagram of 1-D box filter

direction. The cost estimator receives both shifted and non-shifted pixel values and accumulates the cost between them in parallel. The disparity between the left and right images is equivalent to the number of shifts. In the cost estimator, the cost map C for each disparity d is calculated using

$$\begin{aligned} C_d(y,x) = \min[|I_{\text{left}}(y,x) - I_{\text{right}}(y,x-d)|, \tau_1] \\ +\gamma \min[|\nabla_x I_{\text{left}}(y,x) - \nabla_x I_{\text{right}}(y,x-d)|, \tau_2] \end{aligned} \quad (5)$$

where ∇_x is the gradient of the x direction, α is the parameter to balance the effect of color and gradient, and $\tau_{1,2}$ are threshold values. The color cost employs the RGB channel, and the gradient cost employs gray scale.

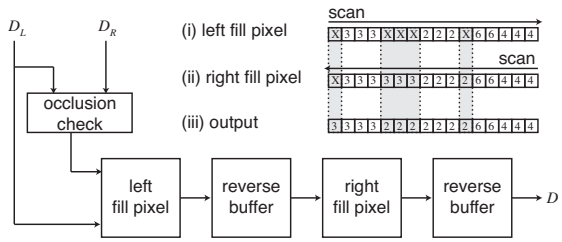

Fig. 7: Block diagram of occlusion check and refinement circuit

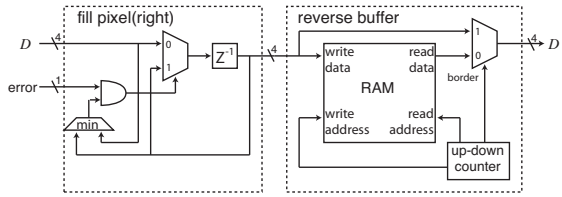

Fig. 8: Fill pixel circuits and reverse buffer

C. 1-D Guided Filter

The calculated cost maps C are then smoothed, using the edge of the gray scale image I, by parallel guided filters. As shown in Fig. 5, our 1-D guided filter circuit consists of six 1-D box filters and associated combinational arithmetic circuits, which calculate formulas (1), (2), and (3). The radius of the 1-D box filter circuits is variable, and can be set at three different values.

The 1-D box filter is based on a fast calculation algorithm [11], and is shown in Fig. 6. A register keeps the summed values of the filter kernel. When the kernel slides to the next pixel, a new summed value is given by (old summed value) + (rightmost pixel value of the target box) - (leftmost pixel value of the box). Therefore, the shift register is required to preserve the leftmost pixel value. The 1-D box filter shares a shift register with a different radius value, because equipping the system with several shift registers is a waste of cost. Note that the center of different filter kernel is matched. In this method, regardless of different radius values, the output timing is constant.

It should be noted that, in practical implementation, one may remove two box filters and one multiplier from the 1-D guided filter, because the values of $\bar{I}$ and $\bar{I^2}$ in Fig. 5 are common over the line.

D. Occlusion Check and Refinement

Among the smoothed cost maps, the minimum values for left and right views are selected by loser-takes-all circuits, and the corresponding disparity values are passed to an occlusion check and refinement circuit.

In the occlusion check, the calculated disparity map is checked using left and right consistency. Disparities that satisfy $D_L(y,x) \neq D_R(y, x - D_L(y,x))$ are detected as an error.

The error is corrected by using the disparity values on the border of the error region. This requires bidirectional scanning, which we realized in the following method (Fig. 7, (i, ii and iii)): i) The error region is filled by the disparity values on the left border; ii) The flow direction of the disparity sequences is inverted, and the resulting error region is filled by the smallest disparity values among the filled values in i) and the disparity values on the right border; iii) The flow direction is further inverted; the inverted flow represents the refined disparity output. Figure 7 shows a block diagram of processes i) to iii), where the left and right fill pixel blocks represent the disparity filling circuits consisting of combinational circuits, and the reverse buffers invert the signal flows. The advantage of this scheme is that the disparity filling circuits consist of very simple logic elements (Fig. 8). As shown in Fig. 9, the reverse buffer is constructed using a one line-size RAM and one up-down counter only. The read address precedes the write address operation, and both addresses are given by the same up-down counter. In the count-up operation, the input sequence is written from 0 to W addresses sequentially. In the count-down operation, the output sequence is read in the order of addresses from W to 0, and thus, the signal flows are inverted. At the same time, the input sequences are written from W to 0 addresses, sequentially. Returning to the count-up operation, the output sequence is read in the order of addresses 0 from W, and thus, the signal flows are similarly inverted.

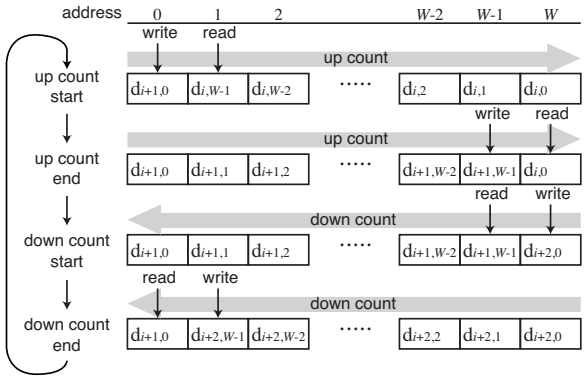

Fig. 9: Reverse buffer operation

After the errors have been corrected, the hardware processing is complete, and the disparity map is transmitted to the CPU.

IV. EXPERIMENTAL RESULTS

A. Hardware Experiments

The proposed system was implemented on a commercial FPGA board (MMS Co., Ltd., Power Medusa MU200-SXII with Altera Stratix II and onboard SRAMs). The system was coded by Verilog HDL, and the RTL model was synthesized by Quartus II. Because the number of logic elements was limited, N was set at 3 (depth resolution is 2^3), and, because of this reduction, the original image was shrunk to 192×144 pixels. Table I summarizes the implementation and performance. The parameters used for cost calculation and aggregation are $\{\tau_1, \tau_2, \gamma\} = \{41, 2, 12\}$, $\{\epsilon, w_{r\mathrm{large}}, w_{r\mathrm{small}}, \theta_1, w_s, w_d\} = \{2, 8, 6, 330, 5, 9\}$.

Figure 10 shows the estimated depth results for three different samples produced by the FPGA. Although the precision

ALUT	Register	Block memory	DSP block 9-bit	Input Res. & Depth	Output Res. & Depth	FPGA CLK
36,969	35,360	32,451	504	192×144 (24-bit rgb)	192×144 (3-bit)	20 MHz

TABLE I: Implementation and performance summary

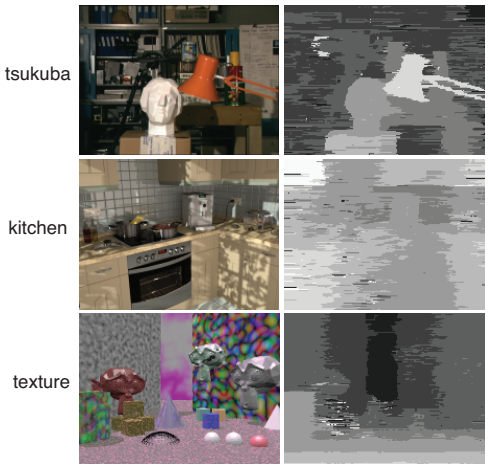

Fig. 10: Experimental results(192×144 pixels, 3-bit depth)

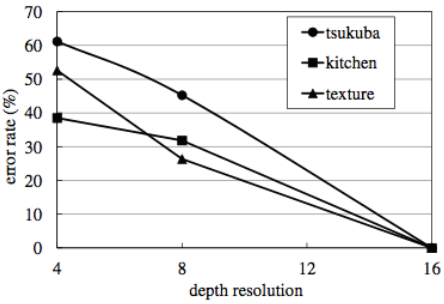

Fig. 11: Error rate vs. implemented depth resolution

of the depth values is degraded because of the reduction in depth resolution, the FPGA could generate an approximate depth map. It should be noted that this is certainly due to the limited number of logic elements in Stratix II, because our RTL results perfectly matched the numerical results at any depth resolution, and the RTL results with the 3-bit depth map matched the FPGA results as well. We also compared the error rates of the original 4-bit depth map and the degraded 2- and 3-bit depth map, as shown in Fig. 11.

These results indicate that the proposed architecture is not nominal, but can be synthesized and operated with acceptable clocks and number/scale of hardware resources. To compare our method with that presented in [10], we compiled and estimated a method using an image size of 1024×768(Table II). When we compiled the method, the depth resolution was reduced to 16 in order to achieve successful compilation. Using the compilation results, we estimated the hardware specification at a depth resolution of 64. Since 52% of RAM is depth resolution-dependent, doubling the depth resolution to 32 increases the total size of RAM to 152% of that of the compiled result. When extending the depth resolution from 32 to 64, doubling the size of RAM again results in an

	[10]	Ours	Estimated
Disparity range	60	16	64
LUTS	122 k	111 k	202 k
RAM	7189 k	89 k	266 k
CLK	318.3 M	20.0 M	40.0 M
FPS	199.7	25.4	25.4

TABLE II: Comparison of the hardware specifications for Jin and Maruyama's method and our method for an image size of 1024×768. Because of lack of resources, our method was only compiled, and not implemented.

enormous FPGA size. Instead, we doubled the CLK of the radius generators and guided filters. Thirty two guided filters are operated twice and generate 64 filtered costs. Thus, the additional circuits shown inside the dotted box in Fig. 3 are needed. They are: (i) four line buffers to hold the left and right lowest cost and its disparity; and (ii) two RGB line buffers for the left and right input image, which have a total size of 130 kb. As a result, the estimated size of RAM for a depth resolution of 64 was 266 kb, which is only 3.7% of that of the system proposed in [10]. Therefore, we can say our method is a low-memory method.

B. Software Experiments

The measurement of the software was conducted on an Intel Core i3 2.53GHz PC, using C++ and four Middlebury stereo pairs. The threshold value was set to 40. The output is shown in Fig. 12. The Middlebury stereo evaluation ranking of our method is listed in Table III. The average processing time was 56.6 ms for a 1024×768 image and 8.6 ms on average for the Middlebury dataset stereo pairs, which are 400×380. When the size of the Middlebury dataset is used, a significant amount of time remains to place the depth-aided application.

V. CONCLUSIONS

This paper presented an FPGA implementation of a memory-efficient stereo vision algorithm. The most significant element of the memory reduction was adapting the 1-D process and gray scale to guided filtering. The proposed architecture employs 1-D guided filters in parallel and a full-pipeline

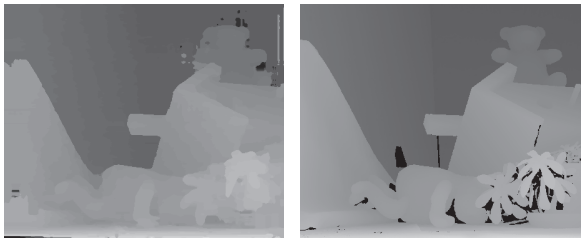

Fig. 12: Left: Results of the Middlebury data set. Right: Ground truth

ISBN: 978-1-61804-216-3

	Tsukuba			Venus			Teddy			Cones			
Method	nonocc	all	disc	nonocc	all	disc	nonocc	all	disc	nonocc	all	disc	average
CostFilter[2]	1.51	1.85	7.61	0.20	0.39	2.42	6.16	11.8	16.0	2.71	8.24	7.66	5.55
Fast[10]	1.38	1.84	7.36	0.30	0.48	2.09	7.41	12.7	17.5	3.44	9.19	9.90	6.13
Ours	2.25	2.81	9.45	1.23	1.76	6.83	4.84	10.5	13.0	3.54	8.90	9.83	6.24
RealTimeBP[12]	1.49	3.40	7.87	0.77	1.90	9.00	8.72	13.2	17.2	4.61	11.6	12.4	7.69
RealTimeDP-Tree[13]	1.49	2.51	6.60	2.37	2.97	13.1	8.11	13.6	15.5	8.12	13.8	16.4	8.71

TABLE III: Middlebury evaluation of previous methods and our method

structure to achieve high speed processing. The results of the FPGA implementation showed that our design performs at a rate of 188 fps and requires only an 89 kb bit memory for a 384×288 image. Moreover, the disparity map, which is improved by a small amount of software processing (8.6 ms), maintained sufficient accuracy. Owing to the use of Middlebury datasets, the average percentage of bad pixels is 6.24%. Our architecture is targeted at applications for mobile devices. The results that we obtained for the speed, accuracy, and cost of the processing are satisfactory.

ACKNOWLEDGMENT

The authors would like to thank Semiconductor Technology Academic Research Center (STARC), Japan, for funding this research project.

REFERENCES

[1] K. Ohata, Y. Sanada, T. Ogaki, K. Matsuyama, T. Ohira, S. Chikuda, M. Igarashi, M. Ikebe, T. Asai, M. Motomura, and T. Kuroda, "Hardware-oriented stereo vision algorithm based on 1-D guided filtering and its FPGA implementation," in *Proc. IEEE International Conference on Electronics, Circuits, and Systems(ICECS)*, Dec. 2013. pp. 169-172.

[2] C. Rhemann, A. Hosni, M. Bleyer, C. Rother, and M. Gelautz, "Fast cost-volume filtering for visual correspondence and beyond," in *Proc. IEEE Conference on Computer Vision and Pattern Recognition(CVPR)*, Jun. 2011. pp. 3017-3024.

[3] Q. Yang, "Recursive bilateral filtering," in *Proc. 12th European Conference on Computer Vision(ECCV)*, Oct. 2012. part I, pp. 399-413.

[4] C. Pham and J. Jeon, "Domain transformation-based efficient cost aggregation for local stereo matching," *IEEE Trans. CSVT*, Vol. 23, Issue 7, pp. 1119-1130. Jul. 2013.

[5] X. Mei, X. Sun, M. Zhou, S. Jiao, H. Wang, and X. Zhang, "On building an accurate stereo matching system on graphics hardware," in *Proc. International Conference on Computer Vision (ICCV) Workshops*, Nov. 2011. pp. 467-474.

[6] D. Scharstein and R. Szeliski, "Middlebury stereo evaluation," `http://vision.middlebury.edu/stereo/`

[7] K. Ambrosch, M. Humenberger, and W. Kubinger, "SAD-based stereo matching using FPGAs," in *Embedded Computer Vision, Advances in Pattern Recognition, Springer*, 2009, pp. 121-138.

[8] S. Jin, J. Cho, X. D. Pham, K. M. Lee, S.-K. Park, M. Kim, and J. W. Jeon, "FPGA design and implementation of a real-time stereo vision system," *IEEE Trans. CSVT*, Vol. 20, Issue 1, pp. 15-26. Jan. 2010.

[9] Y. Shan, Z. Wang, W. Wang, Y. Hao, Y. Wang, K. Tsoi, W. Luk, and H. Yang, "FPGA based memory efficient high resolution stereo vision system for video tolling," in *Proc. International Conference on Field-Programmable Technology (FPT)*, Dec. 2012. pp. 29-32.

[10] M. Jin and T. Maruyama, "A fast and high quality stereo matching algorithm on FPGA," in *Proc. International Conference on Field Programmable Logic and Applications (FPL)*, Aug. 2012. pp. 507-510.

[11] M. J. McDonnell, "Box-filtering techniques," *Computer Graphics and Image Processing*, vol. 17, pp. 65-70, 1981.

[12] Q. Yang, L. Wang, R. Yang, S. Wang, M. Liao, and D. Nister, "Real-time global stereo matching using hierarchical belief propagation," in *Proc. British Machine Vision Conference(BMVC)*, Sep. 2006. vol. 2. pp. 989-998.

[13] M. Jin and T. Maruyama, "A real-time stereo vision system using a tree-structured dynamic programming on fpga," in *Proc. ACM/SIGDA International Symposium on Field Programmable Gate Arrays(FPGA)*, Feb. 2012. pp. 21-24.

Study dynamics of systems with multiple eigenvalues of state matrix

Taalaybek Akunov, Natalya Dudarenko, Nina Polinova, Anatoly Ushakov

Abstract – The steady aperiodic continuous system with state matrix has real spectrum of the multiple eigenvalues which multiplicity is equal to dimension of its state vector is considered. Is shown that if the eigenvalues modulus is less than unit, in free transient motion of system on norm of state vector the oscillativity which become apparent by initial overshoot, being replaced by monotonous movement to quiescent state is found. It is established that the size of overshoot is more, than it is less the modulus of eigenvalue and more its multiplicity.

Key-Words – eigenvalues, multiplicity, free transient motion, norm, overshoot

I. INTRODUCTION. PROBLEM FORMULATION

The task is to research the influence of the multiplicity and the absolute value of the eigenvalues of the state matrix on the free motion steady continuous multidimensional linear dynamic system in the norm of the state vector. It is assumed that the multiplicity of the eigenvalue equal to the dimension of the state vector. As will be shown, we have to state systemic phenomenon, which consists in the fact that in the aperiodic system at a multiplicity of eigenvalues greater than one, and absolute value of the eigenvalues less than one there is the possibility of appreciable overshoot of the norm of the state vector in free motion. Found that the value of overshoot increases with the decrease in the absolute value of the eigenvalues and with increase their multiplicity. Moreover, there is an opportunity to "exchange" absolute value of the eigenvalues for their multiplicity in the class of systems with fixed value of overshoot. At first the problem is solved for the case of a state matrix representation in the Jordan canonical form, and then research activities are carried on an arbitrary case.

II. ANALYTICAL RESEARCHES

Consider the linear continuous Hurwitz multidimensional dynamical system given by [2,3] in the vector - matrix form

$$\dot{x}(t) = Fx(t), x(t)\big|_{t=0} = x(0), \tag{1}$$

where $x(0), x(t)$ is vector of initial and current states of the system respectively; F is state matrix; $x(0), x(t) \in R^n; F \in R^{n\times n}$. Matrix F of system (1) given in a random basis, such that it has the following characteristic polynomial $D(\lambda)$ representation

$$D(\lambda) = det(\lambda I - F) = \\ = \left\{ (\lambda - \alpha)^n = \lambda^n + \sum_{i=1}^{n} (-1)^i C_n^i \alpha^i \lambda^{n-i}; \alpha : Jm(\alpha) = 0 \right\} \tag{2}$$

Eigenvalues spectrum of matrix *F*:

$$\sigma\{F\} = \left\{ \lambda_i = \arg[det(\lambda I - F) = 0] : \lambda_i = \alpha; i = \overline{1,n} \right\} \tag{3}$$

Defect of characteristic matrix of matrix [1] *F:*

$$def\,(\lambda I - F) = 1 \tag{4}$$

From (3), (4) it follows [1] that canonical form of matrix is $(n\times n)$-Jordan block $J(\alpha)$. It's represented in the following form

$$J(\alpha) = \begin{bmatrix} \alpha & 1 & 0 & \dots & 0 \\ 0 & \alpha & 1 & \dots & 0 \\ \vdots & \vdots & \vdots & \dots & \vdots \\ 0 & 0 & 0 & \dots & 1 \\ 0 & 0 & 0 & \dots & \alpha \end{bmatrix}. \tag{5}$$

Matrix in Jordan form $J(\alpha)$ generates an autonomous dynamical system of the type (1), defined in the Jordan canonical basis

$$\dot{\tilde{x}}(t) = J(\alpha)\tilde{x}(t), \tilde{x}(t)\big|_{t=0} = \tilde{x}(0). \tag{6}$$

Vector $\tilde{x}$ and matrix $J(\alpha)$ are related with vector x and matrix *F* by the following vector – matrix ratios

$$x = S\tilde{x},\ SJ(\alpha) = FS \tag{7}$$

where $S - (n\times n)$ is the non-singular similarity transformation matrix , allowing representation of the matrix in the form of

$$F = SJ(\alpha)S^{-1}. \tag{8}$$

In turn, Jordan matrix $J(\alpha)$ (5) can be decomposed in a following additive form

$$J(\alpha) = diag\left\{\lambda_i = \alpha; i = \overline{1,n}\right\} + J(0) = \alpha I + J(0) \tag{9}$$

where $J(0)$ is nilpotent matrix [1] with the index $\nu = n$.

Now, the task is to the research of the free motion of the system (6) in its state vector in a scalar form. The solution of the system (6) is [1]–[3]

$$\tilde{x}(t) = \tilde{x}(t, \tilde{x}(0)) = exp\{J(\alpha)t\}\tilde{x}(0). \tag{10}$$

We will do scalarization of vector process (10), based on the use of consistent [1] vector and matrix norms. As a result, on the basis of (9), we obtain the sequence of ratios

$$\|\tilde{x}(t)\| = \|exp\{J(\alpha)t\}\tilde{x}(0)\| \le \|exp\{J(\alpha)t\}\| \cdot \|\tilde{x}(0)\| = \\ = e^{\alpha t}\|exp\{J(0)t\}\| \cdot \|\tilde{x}(0)\| \quad (11)$$

where

$$exp\{J(0)t\} = \exp\left\{\begin{bmatrix} 0 & 1 & 0 & \dots & 0 \\ 0 & 0 & 1 & \dots & 0 \\ \vdots & \vdots & \vdots & \dots & \vdots \\ 0 & 0 & 0 & \dots & 1 \\ 0 & 0 & 0 & \dots & 0 \end{bmatrix} t\right\} = \\ = \begin{bmatrix} 1 & t & (2)^{-1}t^2 & \dots & [(\mu-1)!]^{-1}t^{\mu-1} \\ 0 & 1 & t & \dots & [(\mu-2)!]^{-1}t^{\mu-2} \\ \vdots & \vdots & \vdots & \dots & \vdots \\ 0 & 0 & 0 & \dots & t \\ 0 & 0 & 0 & \dots & 1 \end{bmatrix}. \quad (12)$$

From (12) it follows that the column norm $\|exp\{J(0)t\}\|_1$, the row norm $\|exp\{J(0)t\}\|_\infty$ and the spectral norm $\|exp\{J(0)t\}\|_2$ are the same. And they are defined by the following majorizing inequality

$$\|exp\{J(0)t\}\|_p = 1 + t + (1/2)t^2 + \dots + (1/(\mu-1)!)t^{\mu-1} = \\ = \sum_{k=0}^{\mu-1}(1/k!)t^k, (p = 1,2,\infty). \quad (13)$$

Thus, norm of the matrix exponential satisfy the following relation:

$$\|exp\{J(\alpha)t\}\| = e^{\alpha t}\sum_{k=0}^{\mu-1}(1/(k!))t^k. \quad (14)$$

From (11) and (14) it follows:

$$\|\tilde{x}(t)\| = \|exp\{J(\alpha)t\}\| \cdot \|\tilde{x}(0)\|_{\|\tilde{x}(0)\|=1} = e^{\alpha t}\sum_{k=0}^{\mu-1}(1/(k!))t^k. \quad (15)$$

Now, the task is to evaluation sign of the velocity change of norm $\|\tilde{x}(t)\|$ at time $t = 0$. We are fixing multiplicity $\mu = n$ eigenvalue $\lambda = \alpha$. We differentiate equation (15) on time:

$$\frac{d}{dt}\|\tilde{x}(t)\| = \frac{d}{dt}\left\{e^{\alpha t}\sum_{k=0}^{\mu-1}(1/(k!))t^k\right\}\Big|_{t=0} = \\ = \left\{\alpha e^{\alpha t}\sum_{k=0}^{\mu-1}(1/(k!))t^k + e^{\alpha t}\sum_{k=0}^{\mu-2}(1/(k!))t^k\right\}\Big|_{t=0} = \alpha + 1. \quad (16)$$

Relation (16) allows us to separate the processes by their quality in the system (6) as a function of multiplicity eigenvalue $\lambda = \alpha$. Clear is that processes in the system (6) are convergent for any negative value $\lambda = \alpha$ and any multiplicity, because the multiplicative term $e^{\alpha t}$ in (16) for $\|\tilde{x}(t)\|$ has an infinite number of elements of the expansion in powers of t, and the term $\sum_{k=0}^{\mu-1}(1/(k!))t^k$ has a finite number elements.

Consequently, there is always a moment of time $t = t^*$, at which the dominance of the exponential multiplier $e^{\alpha t}$ begins to emerge. Now, we consider the following situations.

Situation 1: $\alpha < 0, |\alpha| > 1$, $\left\{\frac{d}{dt}\|\tilde{x}(t)\|\right\}\Big|_{t=0} < 0$, process $\|\tilde{x}(t)\|$ converges to zero, and is majorized by an exponent in the form $\|\tilde{x}(t)\| \le e^{(\alpha+1)t}\|\tilde{x}(0)\|$.

Situation 2: $\alpha = -1, \left\{\frac{d}{dt}\|\tilde{x}(t)\|\right\}\Big|_{t=0} = 0$, the initial velocity is zero, but at $t > 0$ by (16) is set to a negative velocity. It is defined by the following relations

$$\frac{d}{dt}\|\tilde{x}(t)\| = \left\{\alpha e^{\alpha t}\sum_{k=0}^{\mu-1}(1/(k!))t^k + e^{\alpha t}\sum_{k=0}^{\mu-2}(1/(k!))t^k\right\}\Big|_{\alpha=-1} = \\ = -(1/(\mu-1)!)e^{-t}t^{(\mu-1)}. \quad (17)$$

The velocity of change norm $\|\tilde{x}(t)\|$ on the system trajectories is characterized by the extremum, which is observed at time t_m. It is defined by (15) the following relations

$$t_m = arg\left\{\frac{d^2}{dt^2}\|\tilde{x}(t)\| = 0\right\} = \\ = arg\left\{\frac{d}{dt}\left(e^{-t}t^{(\mu-1)}\right) = 0\right\} = \mu - 1 \quad (18)$$

And the Velocity of change norm $\|\tilde{x}(t)\|$ is determined by the relation

$$\max_t\left(\frac{d}{dt}\|\tilde{x}(t)\|\right) = -\frac{(\mu-1)^{(\mu-1)}}{(\mu-1)!}e^{-(\mu-1)}. \quad (19)$$

The process $\|\tilde{x}(t)\|$ converges to zero by (15). The process is majorized by an exponential function so that the following inequality

$$\|\tilde{x}(t)\| \le \rho e^{\gamma t}\|\tilde{x}(0)\| \quad (20)$$

where

$$(\rho,\gamma) = \\ = arg\left\{\begin{array}{l} \min_{\rho,\gamma}\|\tilde{x}(t)\| - \rho e^{\gamma t}\|\tilde{x}(0)\| \,\&\, \left(\frac{d}{dt}\left(\rho e^{\gamma t}\|\tilde{x}(0)\|\right)\right)\Big|_{t=(\mu-1)} = \\ = -\frac{(\mu-1)^{(\mu-1)}}{(\mu-1)!}e^{-(\mu-1)} \,\&\, \rho \ge 1 \end{array}\right\}.$$

Situation 3 (the subject of the paper): $\alpha < 0, |\alpha| < 1$, $\left\{\frac{d}{dt}\|\tilde{x}(t)\|\right\}\Big|_{t=0} > 0$. The process $\|\tilde{x}(t)\|$ at the initial

interval time diverges, reaching a maximum at the time t_M. It is defined by the following relations

$$t_M = arg\left\{\frac{d}{dt}\|\tilde{x}(t)\| = 0\right\} = \quad (21)$$
$$arg\left\{(1+\alpha)\sum_{k=0}^{\mu-2}(1/k!)t^k + \alpha(1/(\mu-1)!)t^{(\mu-1)} = 0\right\}$$

And further process $\|\tilde{x}(t)\|$ converges to zero. Thus, the process $\|\tilde{x}(t)\|$ on the trajectories of free motion of aperiodic system detects overshoot. It is numerically determined by value $\alpha:(\alpha<0,|\alpha|<1)$ of the multiple eigenvalue and value μ of its multiplicity. The obvious property of process $\|\tilde{x}(t)\|$: the smaller the value $|\alpha|<1$ and the more its multiplicity μ, the greater the value of its overshoot over the level $\|\tilde{x}(0)\|$. To illustrate this result, we perform the calculation of the time t_M by (21) and overshoot to the curve $\|\tilde{x}(t)\|$ aperiodic systems for time $t=t_M$ by (15) for different values of $\alpha:(\alpha<0,|\alpha|<1)$ and multiplicity μ. The calculation results are shown in Tables 1 and 2.

μ	2	3	4	5	10
α	t_M				
-0.2	4	8.9	13.9	18.8	43.8
-0.02	49	99	149	199	449

Table1.Values of moments overshoot to curve $\|\tilde{x}(t)\|$

μ	2	3	4	5	10
α	$\max_t(\|\tilde{x}(t)\|)=\|\tilde{x}(t_M)\|$				
-0.2	2.25	8.3	34.7	151.6	$3.32\cdot10^5$
-0.02	18.8	690	$2.86\cdot10^4$	$1.25\cdot10^6$	$2.72\cdot10^{14}$

Table 2. Values of overshoot $\max_t(\|\tilde{x}(t)\|)=\|\tilde{x}(t_M)\|$ to curve $\|\tilde{x}(t)\|$

Now, we return to the original system (1) with the state matrix F, defined in an arbitrary basis. Then, by analogy with (10), using (8) we can write the following

$$x(t)=x(t,x(0))=\exp\{Ft\}x(0)= \quad (22)$$
$$=S\exp\{J(\alpha)t\}S^{-1}x(0).$$

If in (22) we will proceed to scalarized vector processes in the state vector norm of system (1), we obtain using (14), the following sequence of relations

$$\|x(t)\| = \left\|S\exp\{J(\alpha)t\}S^{-1}x(0)\right\| \le$$
$$\le \|S\|\left\|\exp\{J(\alpha)t\}\right\|\left\|S^{-1}\right\|\|x(0)\| = \quad , \quad (23)$$
$$= c\{S\}e^{\alpha t}\sum_{k=0}^{\mu-1}(1/(k!))t^k\|x(0)\|$$

where $c\{S\}=\|S\|\cdot\|S^{-1}\|$ is condition number of the matrix S, $1\le c\{S\}<\infty$ [4].

The values of $\|x(t)\|$ will be $c\{S\}$ times greater than value of $\|\tilde{x}(t)\|$, keeping the same dependence on absolute value $|\alpha|$ of the eigenvalue $\lambda=\alpha$ and its multiplicity μ.

III. COMPUTER SIMULATIONS

Computer simulation the processes in the norm $\|\tilde{x}(t)\|$ as a function of eigenvalue $\lambda=\alpha$ and its multiplicity $\mu=n$ was conducted in accordance with the ratio of $\|\tilde{x}(t)\|=\|exp\{J(\alpha)t\}\tilde{x}(0)\|\le\|exp\{J(\alpha)t\}\|\cdot\|\tilde{x}(0)\|$ on his majorizing part. This research was carried out in Matlab. The results of the simulation of processes in the form of $\|\tilde{x}(t)\|$ for a single set of multiplicity $\mu=n=2;3;5;10$ and values $\lambda=\alpha=-2;-0.2;-0.02$ are presented in the figures below.

Figure 1 shows the curves for the case $\lambda=\alpha=-2$. Processes $\|\tilde{x}(t)\|$ converge monotonically with no overshoots (look situation 1). The left curve corresponds to the case $\mu=n=2$, and the right curve corresponds to the case $\mu=n=10$.

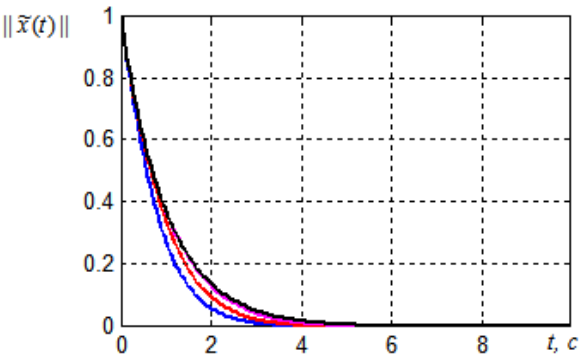

Fig.1. Curves of processes $\|\tilde{x}(t)\|$ for $\lambda=\alpha=-2;$ and $\mu=n=2;3;5;10$

Figure 2 shows the curves for the case $\lambda=\alpha=-0.2$. Processes $\|\tilde{x}(t)\|$ detect overshoots that increase with increasing $\mu=n$ (look situation 3).

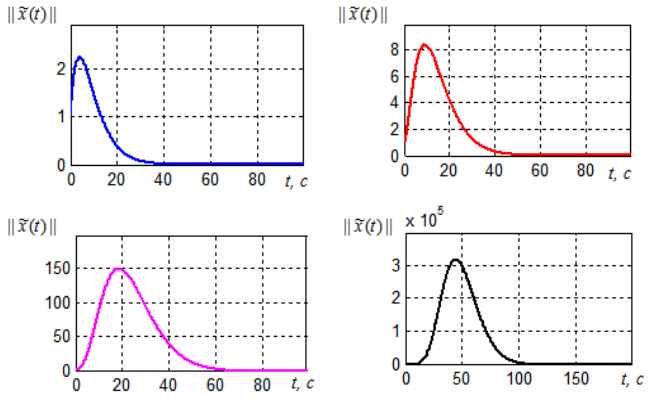

Fig.2. Curves of processes $\|\tilde{x}(t)\|$ for $\lambda = \alpha = -0.2;$ and $\mu = n = 2;3;5;10$

Figure 3 shows the curves for the case $\lambda = \alpha = -0.02$. Processes $\|\tilde{x}(t)\|$ detect the notable overshoots that increase with increasing $\mu = n$ (look situation 3).

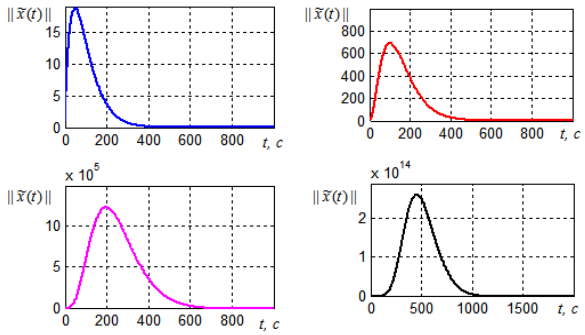

Fig.3. Curves of processes $\|\tilde{x}(t)\|$ for $\lambda = \alpha = -0.02;$ and $\mu = n = 2;3;5;10$

Fig.4 shows the curves of constant values of $\max_t(\|\tilde{x}(t)\|) = \|\tilde{x}(t_M)\| = \text{const}$ in the plane «$\mu - \lambda$». They illustrate the possibility of «exchange» multiplicity to the value of a multiple eigenvalue of the task at hand.

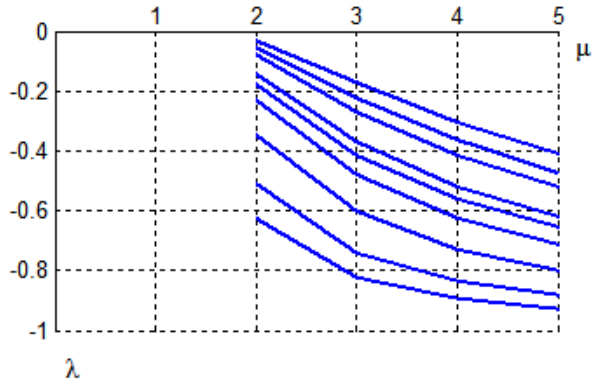

Fig.4. Curves of constant values of $\max_t(\|\tilde{x}(t)\|) = \|\tilde{x}(t_M)\| = \text{const}$

Figure 5 shows the curves for $\lambda = \alpha = -0.2$ for the case of system (1) with the matrix F is specified in the accompanying row form (frobenius form), and for the case of system (6). Processes $\|x(t)\|$ correspond with the curves $\|\tilde{x}(t)\|$, but each time $\|x(t)\|$ exceed $\|\tilde{x}(t)\|$ in $c\{S\}$ times.

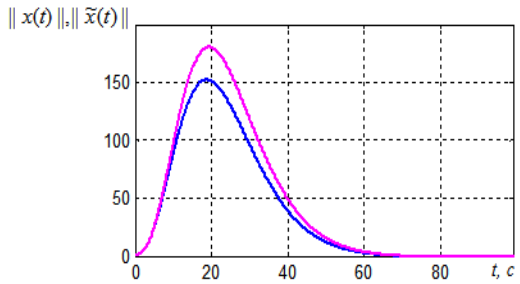

Fig.5. Curves of processes $\|x(t)\|$ (top) and $\|\tilde{x}(t)\|$ for $\lambda = \alpha = -0.2;$ and $\mu = n = 5$

Finally, it should be noted that if the spectrum of eigenvalues of the matrix F has several multiples eigenvalues

$$\sigma\{F\} = \left\{ \lambda_i = \alpha_j : i = \overline{1,\mu_j};\ j = \overline{1,q};\ \sum_{j=1}^{q} \mu_j = n \right\},$$ the canonical representation F in the Jordan form will contain q Jordan blocks of $(\mu_j \times \mu_j)$-dimension each. Then for this case, relation (11) takes the following form

$$\|\tilde{x}(t)\| = \left\| diag\left\{ exp\{J(\alpha_j)t\};\ j = \overline{1,q} \right\} \tilde{x}(0) \right\| \le$$

$$\le e^{\bar{\alpha}t} \left\| exp\{J_{(\bar{\mu}\times\bar{\mu})}(0)t\} \right\| \cdot \|\tilde{x}(0)\|,$$

where $\bar{\alpha} = \max_j \{\alpha_j : \alpha_j < 0 \ \&\ |\alpha_j| < 1;\ j = \overline{1,q}\}$, $\bar{\mu} = \max_j \{\mu_j;\ j = \overline{1,q}\}$

IV CONCLUSION

The is found that multiplicity of the eigenvalues of state matrix of stable aperiodic continuous systems and the structure of eigenvectors of state matrix [5] is an important factor in the system, endowing a dynamic system processes of specific properties that may lead to undesirable consequences of a destructive nature. In order to prevent the discovered effect "multiplicity of eigenvalues" in the synthesis of modal control methods [3] state matrix *F* should be given the spectrum of eigenvalues not contain multiple elements.

REFERENCES

[1] F. R. Gantmaher, *Matrix Theory*, FIZMATLIT,2004.
[2] Andreev J.N. Control of finite dimensional linear plants. Science, 1976 (in Russian).
[3] Dudarenko N.A., Slita O.V., Ushakov A.V. Mathematical base of modern theory of control: the space states method. Tutorial. – SPb: SPbSU ITMO, 2008 (in Russian).
[4] Golub, Gene H., van Loan, Charles F., Matrix Computations, MIR, 1999
[5] N. Dudarenko, A. Ushakov, Eigenvectors structure of state matrices in multichannel systems as a degeneration factor, Scientific and Technical Journal of Information Technologies, Mechanics and Optics, №5 (81), 2012, pp.52–58.

High Output Impedance Current-mode Multifuntions Filter Using CDCTAs

K. Pitaksuttayaprot, and W. Jaikla

***Abstract*—** This article presents a three-inputs single-output biquadratic filter performing completely standard functions: low-pass, high-pass, band-pass, band-reject and all-pass functions, based on current differencing cascaded transconductance amplifiers (CDCTA). The quality factor and pole frequency can be electronically/independently tuned via the input bias current. The proposed circuit uses 2 CDCTAs and 2 grounded capacitors without external any resistors which is very suitable to further develop into an integrated circuit. The filter does not require double input current signal. Each function response can be selected by suitably selecting input signals with digital method. Moreover, the circuit possesses high output impedance which would be an ideal choice for current-mode cascading. The PSPICE simulation results are included to verify the workability of the proposed filter. The given results agree well with the theoretical anticipation.

***Keywords*—** Analog filter, CDCTA, Current-mode, Multiple input-Single output..

I. Introduction

RECENTLY, current-mode circuits have been receiving considerable attention due to their potential advantages such as inherently wide bandwidth, higher slew-rate, greater linearity, wider dynamic range, simpler circuitry and lower power consumption [1]. With this potential, a number of papers have been published dealing with the realization of current-mode circuits [2-4]. One of the standard research topics in current-mode circuit design is an analog filter. This circuit is important in electrical and electronic applications, widely used for continuous-time signal processing. It can be found in many fields: including, communications, measurement, instrumentation, and control systems [5-6]. One of most popular analog current-mode filters is a multiple-input single-output biquadratic filter (MISO) which different output filter functions can be realized simply by different combinations of switching on or off the input currents where the selection can be done digitally using a microcontroller or microcomputer. Moreover, the high-output impedance of current-mode filters are of great interest because they make it easy to drive loads and they facilitate cascading without using a buffering device [7-8].

From our survey, it is found that several implementations of MISO current-mode filters have been reported [9-27]. Unfortunately, these reported circuits suffer from one or more of following weaknesses:

- Non independent control of the pole frequency and quality factor [9,10, 11, 12, 13, 14,15, 17, 18, 27, 25, 26, 27].
- Excessive use of the passive elements, especially external resistors [9,12, 14, 15, 16, 19, 21, 22, 23].
- Requirement of double input current signal to realize all the responses [13, 14, 20, 21, 24].
- Lack of electronic adjustability [9, 12, 14, 15, 19, 21, 22].
- Requirement of changing circuit topologies to achieve several functions [9, 21].
- Requirement of element-matching conditions [9, 11, 15, 19, 21, 26].
- Use of floating capacitor which is not desirable for IC implementation [9, 15].

The aim of this paper is to propose a current-mode biquadratic filter, emphasizing on use of CDCTA[28]. The features of proposed circuit are that: the proposed universal filter can provide completely standard functions (low-pass, high-pass, band-pass, band-reject and all-pass) without changing circuit topology: the circuit description is very simple, it uses only 2 CDCTAs and 2 grounded capacitors, which is suitable for fabricating in monolithic chip or off-the-shelf implementation: quality factor and pole frequency can be independently adjusted. The performances of proposed circuit are illustrated by PSPICE simulations, they show good agreement as mentioned.

II. THEORY AND PRINCIPLE

A. CDCTA Overview

The characteristics of the ideal CDCTA are represented as the following hybrid matrix.

$$\begin{bmatrix} I_z, I_{zc} \\ I_{x1}, I_{x1c} \\ I_{x2}, I_{x2c} \\ V_{x2} \end{bmatrix} = \begin{bmatrix} 1 & -1 & 0 & 0 \\ 0 & 0 & g_{m1} & 0 \\ 0 & 0 & 0 & g_{m2} \\ 0 & 0 & 0 & 0 \end{bmatrix} \begin{bmatrix} I_p \\ I_n \\ V_z \\ V_{x1} \end{bmatrix}, \qquad (1)$$

K. Pitaksuttayaprot is with Department of Technology Electronic, Phetchabun Rajabhat University, Sadeang Phetchabun, 67000, Thailand (e-mail: koson@pcru.ac.th).

W. Jaikla is with Department of Engineering Education, King Mongkut's Institute of Technology Ladkrabang, Bangkok, 10520, Thailand (e-mail: kawinai@kmitl.ac.th).

where g_m is the transconductance of the CDCTA. This g_m can be adjusted by external input bias current I_B . For bipolar junction transistor CDCTA, the transconductances can be shown in Eq. (2) and (3) . The symbol and the equivalent circuit of the CDCTA are illustrated in Fig. 1 .

$$g_{m1} = \frac{I_{B1}}{2V_T}, \tag{2}$$

and

$$g_{m2} = \frac{I_{B2}}{2V_T}. \tag{3}$$

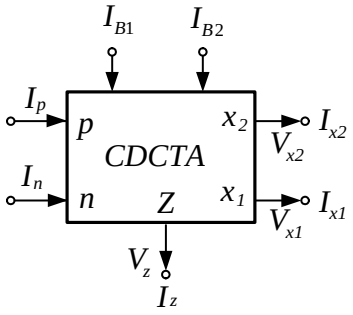

(a)

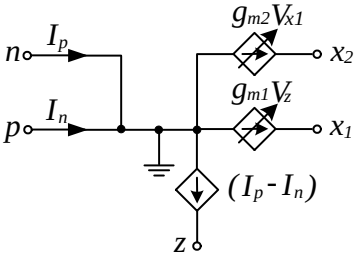

(b)

Fig. 1. CDCTA (a) Symbol (b) Equivalent circuit.

B. Proposed MISO Current-mode Filter

The proposed multiple input single output current-mode biquadratic filter is shown in Fig. 2. By routine analysis of the circuit in Fig. 2, the output current can be obtained to be

$$I_{Out} = k\left(\frac{-I_{in1}\frac{sg_{m1}}{C_1} + I_{in2}\frac{g_{m1}g_{m2}}{C_1C_2} - I_{in3}\left(s^2 + \frac{g_{m1}g_{m2}}{C_1C_2}\right)}{s^2 + \frac{sg_{m1}k}{C_1} + \frac{g_{m1}g_{m2}}{C_1C_2}}\right). \tag{4}$$

where $k = g_{m4}/g_{m3}$. From Eq. (4), I_{in1}, I_{in2} and I_{in3} can be chosen as in Table I to obtain a standard function of the 2^{nd}–order network without requirement of double input current signal(s). Moreover, it is found in Table I that each function response can be selected by digital method. The pole frequency (ω_0) and quality factor (Q_0) of each filter response can be expressed to be

$$\omega_0 = \sqrt{\frac{g_{m1}g_{m2}}{C_1C_2}}, \tag{5}$$

and

$$Q_0 = \frac{1}{k}\sqrt{\frac{C_1g_{m2}}{C_2g_{m1}}}. \tag{6}$$

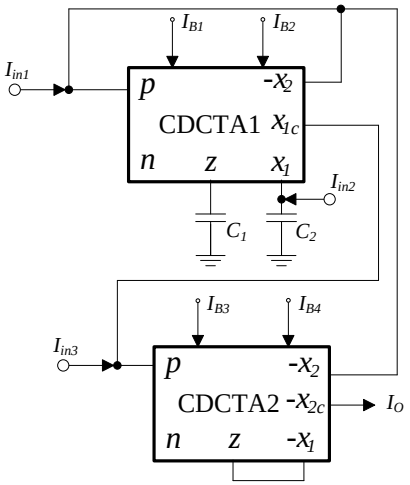

Fig. 2. Proposed MISO current-mode filter.

TABLE I. THE I_{IN1}, I_{IN2} AND I_{IN3} VALUES SELECTION FOR EACH FILTER FUNCTION RESPONSE.

Filter Responses	Input selections		
I_O	I_{in1}	I_{in2}	I_{in3}
BP	I_{in}	0	0
HP	0	I_{in}	I_{in}
BR	0	0	I_{in}
AP	I_{in}	0	$-I_{in}$
LP	0	I_{in}	0

If g_{m1} and g_{m2} are equal to Eq. (2) and (3), the pole frequency and quality factor of the proposed circuit are written as

$$\omega_0 = \frac{1}{2V_T}\sqrt{\frac{I_{B1}I_{B2}}{C_1C_2}}, \tag{7}$$

and

$$Q_0 = \frac{I_{B3}}{I_{B4}}\sqrt{\frac{C_1I_{B2}}{C_2I_{B1}}}. \tag{8}$$

From Eqs. (7) and (8), it is found that the quality factor can be adjusted independently from the pole frequency by varying I_{B3} or I_{B4}. Another advantage of the proposed circuit is that the high Q_0 circuit can be obtained by setting I_{B3} more greater than I_{B4} without effecting pole frequency.

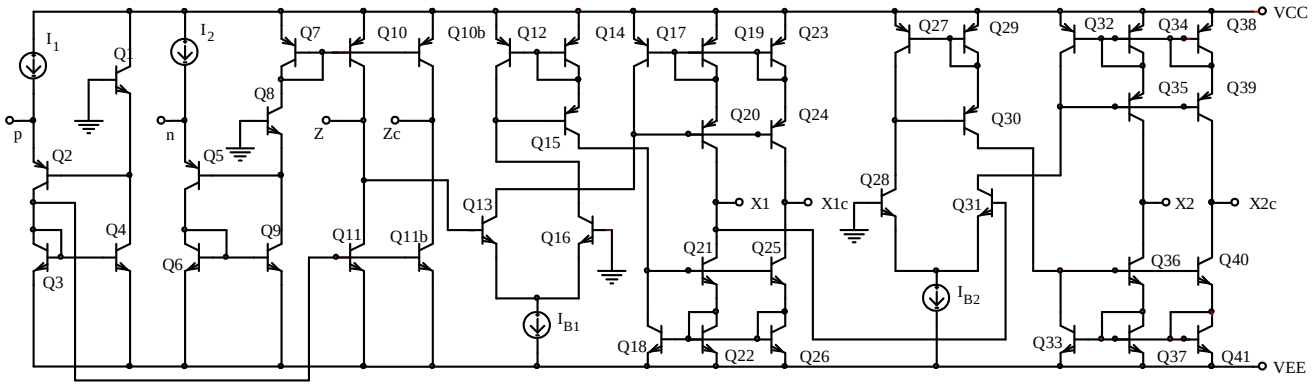

Fig. 3. Internal construction of CDCTA

Furthermore, it can be remarked that if $I_{B1}=I_{B2}=I_B$ and $C_1=C_2$, this can be achieved by using current mirror copying the current I_B to terminals I_{B1} and I_{B2} of CDCTA1, respectively. The pole frequency and quality factor can be expressed as

$$\omega_0 = \frac{I_B}{2CV_T}, \tag{9}$$

and

$$Q_0 = \frac{I_{B3}}{I_{B4}}. \tag{10}$$

From Eqs. (9) and (10), it should be remarked that the pole frequency can be electronically adjusted by I_B without disturbing the quality factor.

C. Relative Sensitivities

The relative sensitivities of the proposed circuit can be found as

$$S_{I_{B1}}^{\omega_0} = S_{I_{B2}}^{\omega_0} = \frac{1}{2};\ S_{C_1}^{\omega_0} = S_{C_2}^{\omega_0} = -\frac{1}{2};\ S_{V_T}^{\omega_0} = -1, \tag{11}$$

and

$$S_{I_{B2}}^{Q_0} = S_{C_1}^{Q_0} = \frac{1}{2}; S_{I_{B1}}^{Q_0} = S_{C_2}^{Q_0} = -\frac{1}{2}; S_{I_{B3}}^{Q_0} = 1; S_{I_{B4}}^{Q_0} = -1. \tag{12}$$

Therefore, all the active and passive sensitivities are equal or less than unity in magnitude.

III. RESULTS OF COMPUTER SIMULATION

To prove the performances of the proposed circuit, the PSPICE simulation program was used for the examinations. The PNP and NPN transistors employed in the proposed circuit were simulated by respectively using the parameters of the PR200N and NR200N bipolar transistors of ALA400 transistor array from AT&T [29]. The CDCTA has been simulated using the bipolar technology structure [30] of Fig. 3. The capacitors: $C_1=C_2=3$nF, $I_{B1}=I_{B2}=105$µA, $I_{B3}=I_{B4}=100$µA are chosen. It yields the pole frequency of 100kHz and Q=1, while calculated value of pole frequency from Eq. (7) is 107.12kHz (deviated by 6.65%). The results shown in Fig. 4 are the gain and phase responses of the proposed filter obtained from Fig. 2. It is clearly seen that the proposed filter can provide low-pass, high-pass, band-pass, band-reject and all-pass functions, dependent on digital selection as shown in table I, without modifying circuit topology. Fig. 5 and Fig.6 display gain responses of band-pass function for different I_{B3} and I_{B4} values. It is shown that the quality factor can be adjusted by I_{B3} and I_{B4}, as depicted in Eq. (8) without affecting the pole frequency. Fig. 7 shows the gain responses of the band-pass function while setting I_B to 50µA, 75µA, and 100µA, respectively. This result shows that the pole frequency can be adjusted without affecting the quality factor, as described in Eqs. (9) and (10).

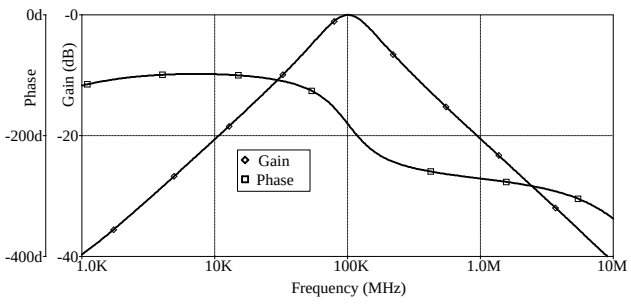

(a) BP

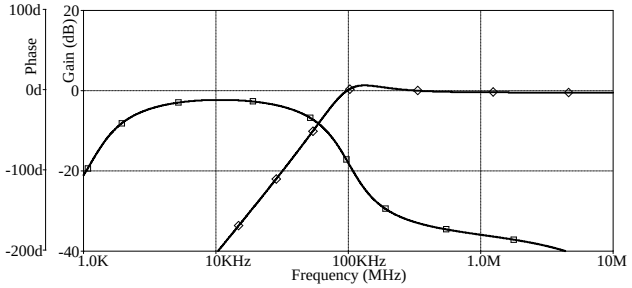

(b) HP

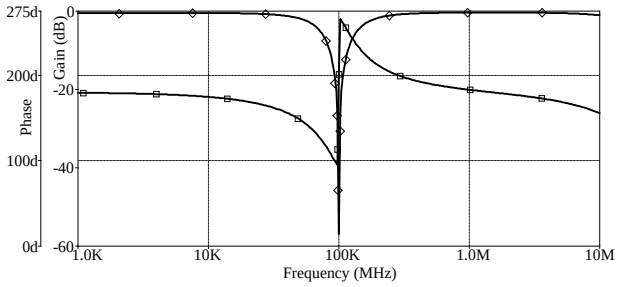

(c) BR

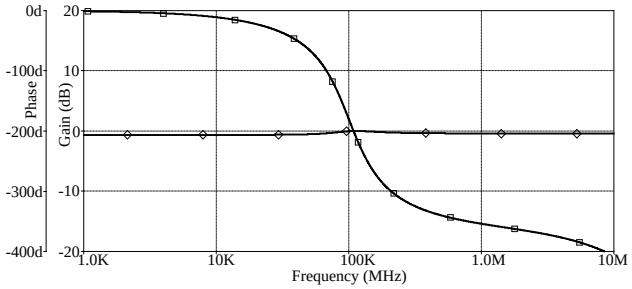

(d) AP

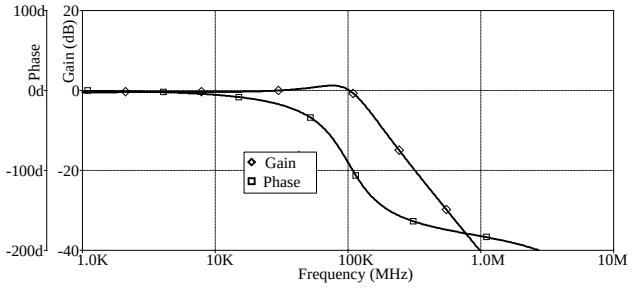

(e) LP

Fig. 4. Gain and phase responses of the proposed filter.

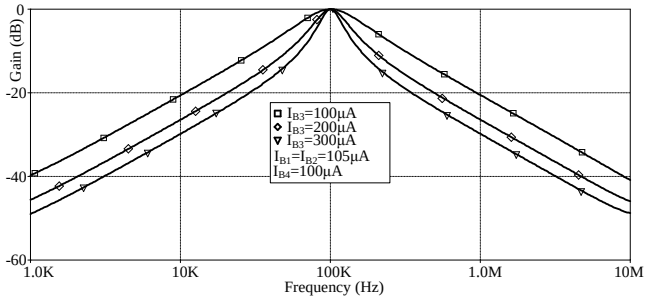

Fig. 5. Band-pass responses at different values of I_{B3}

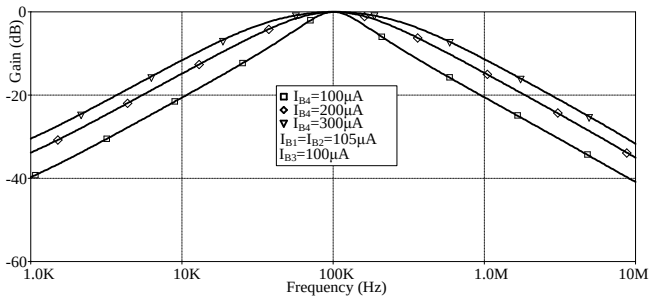

Fig. 6. Band-pass responses at different values of I_{B4}

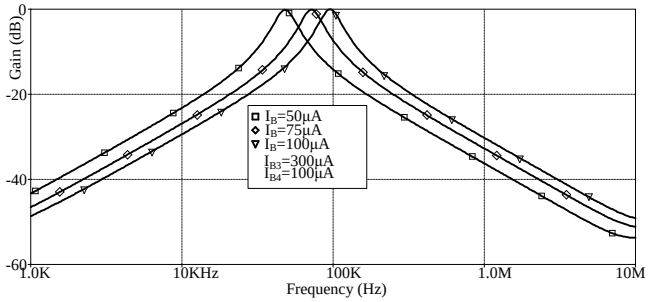

Fig. 7. Band-pass responses for different values of I_B

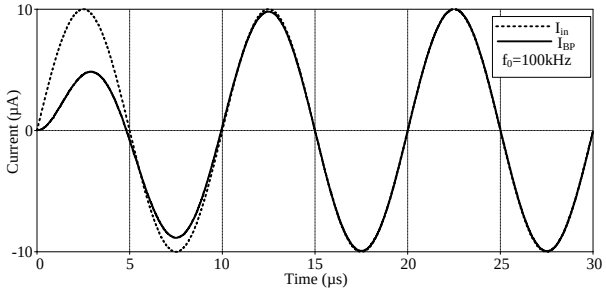

Fig. 8. Transient response at center frequency of 100kHz obtained from the proposed filter for BP function.

IV. CONCLUSION

The digitally controllable current-mode multi-function filter has been presented. The advantages of the proposed circuit are that: it performs low-pass, high-pass, band-pass, band-reject

and all-pass functions from the same circuit configuration without component matching conditions: the quality factor and the pole frequency can be independently controlled. The circuit description comprises only 2 CDCTAs, and 2 grounded capacitors, which is attractive for either IC implementation.

REFERENCES

[1] C. Toumazou, F. J. Lidgey, D. G. Haigh, Analogue IC Design: The Current-Mode Approach, Peter Peregrinus, Stevenage, 1990.

[2] W. Jaikla, A. Noppakarn, S. Lawanwisut, "New gain controllable resistor-less current-mode first order allpass filter and its application," Radioengineering, vol. 21, no. 1, pp. 312-316, 2012.

[3] J. Bajer, A. Lahiri, D. Biolek, "Current-mode CCII+ based oscillator circuits using a conventional and a modified wien-bridge with all capacitors grounded," Radioengineering, vol. 20, no. 1, pp. 245-250, 2011.

[4] Y. Li, "Current-mode sixth-order elliptic band-pass filter using MCDTAs," Radioengineering, vol. 20, no. 3, pp. 645-649, 2011.

[5] M. A. Ibrahim, S. Minaei, H. A. Kuntman, "A 22.5 MHz current-mode KHN-biquad using differential voltage current conveyor and grounded passive elements," International Journal of Electronics and Communication (AEU), vol. 59, pp. 311-318, 2005.

[6] A. S. Sedra, K. C. Smith, Microelectronic circuits, 3rd ed., Florida: Holt, Rinehart and Winston, 1991.

[7] W. Tangsrirat, W. Surakampontorn, "Systematic realization of cascadable current-mode filters using CDTAs," Frequenz, , vol. 60, pp. 241-245, 2006.

[8] A. M. Soliman, "New current mode filters using current conveyors," International Journal of Electronics and Communication (AEU), vol. 51, pp. 275-278, 1997.

[9] E. Arslan, B. Metin, O. Ciekoglu, "Multi-input single-output cacadable current-mode universal filter topology with a single current conveyor," Proceedings of the Third IASTED International Conference Circuits, Signals, and Systems, pp. 62-66, 2005.

[10] S. V. Singh, S. Maheshwari, D. S. Chauhan, "Single MO-CCCCTA-based electronically tunable current/trans-impedance-mode biquad universal filter," Circuits and Systems, vol. 2, pp. 1-6, 2011.

[11] C.-N. Lee, "Multiple-mode OTA-C universal biquad filters," Circuits System and Signal Processing, vol. 29, pp. 263–274, 2010.

[12] J-W. Horng, "Current-mode universal biqudaratic filter with five inputs and one output using tree ICCIIs," Indian Journal of Pure & Applied Physics, vol. 49, pp. 214-217, 2011.

[13] M. Siripruchyanun, W. Jaikla, "Electronically controllable current-mode universal biquad filter using single DO-CCCDTA," Circuits System Signal Processing, vol. 27, no. 1, pp. 113-122, 2008.

[14] V. Sawangarom, T. Dumawipata, W. Tangsrirat, W. Surakampontorn, "Cascadable three-input single-output current-mode universal filter using CDBAs," The 2007 ECTI International Conference, pp. 53-56, 2007.

[15] S. Özcan, H. Kuntman, O. Çiçekoglu, "A novel multi-input single-output filter with reduced number of passive elements using single current conveyor," Proceedings of 43rd IEEE Midwest Symp. on Circuits and Systems, pp. 1-3, 2000.

[16] A. Chunhuw, L. Haiguang, Z. Yan, "Universal current-mode filter with multiple inputs and one output using MOCCII and MO-CCCA," International Journal of Electronics and Communication (AEU), vol. 63, pp. 448-453, 2009.

[17] S. V. Singh, S. Maheshwari, D. S. Chauhan, "Electronically tunable current-mode SIMO/MISO universal biquad filter using MO-CCCCTAs," International J. of Recent Trends in Engineering and Technology, vol. 3, no. 3, pp. 65-70, 2010 .

[18] N. Pandey, S. K. Paul, "VM and CM universal filters based on single DVCCTA," Active and Passive Electronic Components, Article ID 929507, 2011.

[19] R. Senani, K. K. Abdalla, D. R. Bhaskar, "A state variable method for the realization of universal current-mode biquads," Circuits and Systems, vol. 2, pp. 286-292, 2011.

[20] M. Kumngern, "Multiple-input single-output current-mode universal filter using translinear current conveyors," Journal of Electrical and Electronics Engineering Research, vol. 3, pp. 162-170, 2011.

[21] [21] N. Pandey, S. K. Paul, "Multi-input single-output universal current mode biquad," Journal of Active and Passive Electronic Devices, vol. 1, pp. 229-240, 2006.

[22] J.-W. Horng, "High output impedance current-mode universal biquadratic filters with five inputs using multi-output CCIIs," Microelectronics Journal, doi:10.1016/j.mejo.2011.02.007, 2011.

[23] W. Tangsrirat, T. Pukkalanun, "Structural generation of two integrator loop filters using CDTAs and grounded capacitors," International Journal of Circuit Theory and Applications, vol. 39, pp. 31- 45, 2011.

[24] W. Tangsrirat, T. Dumawipata, W. Surakampontorn, "Multiple-input single-output current-mode multifunction filter using current differencing transconductance amplifiers," International Journal of Electronics and Communication (AEU), vol. 61, pp. 209-214, 2007.

[25] W. Tangsrirat, "Cascadable current-controlled current-mode universal filters using CDTAs and grounded capacitors," Journal of Active and Passive Electronic Devices, vol. 4, pp. 135–145, 2009.

[26] W. Tangsrirat, W. Surakampontorn, "Electronically tunable current-mode universal filter employing only plus-type current-controlled conveyors and grounded capacitors," Circuits System Signal and Processing, vol. 27, no. 6, pp. 701-713, 2006.

[27] O. Channumsin, T. Pukkalanun, W. Tangsrirat, "Universal current-mode biquad with minimum components," Proceedings of the 2011 International Multi-Conference of Engineering and Computer Scientists, 2011.

[28] X. Jun, W. Chunhua, and J. Jie, "Current Differencing Cascaded Transconductance Amplifier (CDCTA) and Its Applications on Current-Mode nth-Order Filters," Circuits,System, and Signal Processing, Springer Science+Business Media New York 2013.Frey D., Log-domain filtering: an approach to current-mode filtering, IEE Proceedings-Circuits, Devices and Systems, pp. 406-416, 1993.

[29] W. Tangsirrat and w. Tanjaroen,"Current-mode sinusoidal quadrature oscillator with independent control of oscillation frequency and condition using CDTAs," Indian Journal of Pure &Applied Physics,vol48, ,pp.363-366, May, 2010.R. J. Vidmar. (1992, August). On the use of atmospheric plasmas as electromagnetic reflectors. *IEEE Trans. Plasma Sci.* [Online]. *21(3).* pp. 876—880. Available: http://www.halcyon.com/pub/journals/21ps03-vidmar

First A. Author (M'76–SM'81–F'87) and the other authors may include biographies at the end of regular papers. Biographies are often not included in conference-related papers. This author became a Member (M) of **EUROPMENT** in 1976, a Senior Member (SM) in 1981, and a Fellow (F) in 1987. The first paragraph may contain a place and/or date of birth (list place, then date). Next, the author's educational background is listed. The degrees should be listed with type of degree in what field, which institution, city, state or country, and year degree was earned. The author's major field of study should be lower-cased.

The second paragraph uses the pronoun of the person (he or she) and not the author's last name. It lists military and work experience, including summer and fellowship jobs. Job titles are capitalized. The current job must have a location; previous positions may be listed without one. Information concerning previous publications may be included. Try not to list more than three books or published articles. The format for listing publishers of a book within the biography is: title of book (city, state: publisher name, year) similar to a reference. Current and previous research interests ends the paragraph.

The third paragraph begins with the author's title and last name (e.g., Dr. Smith, Prof. Jones, Mr. Kajor, Ms. Hunter). List any memberships in professional societies other than the **EUROPMENT**. Finally, list any awards and work for **EUROPMENT** committees and publications. If a photograph is provided, the biography will be indented around it. The photograph is placed at the top left of the biography. Personal hobbies will be deleted from the biography.

Sliding mode control with Bond graph modeling applied on a robot leg

Alexandru I. Gal, Luige Vladareanu*

***Abstract*—** In this paper we use the bond graph modeling to control a mobile walking robots' leg. The legs' structure presents 2DOF for an easy understanding of the control laws' behavior. Along with this approach we used the sliding mode control method, which is a dynamic position control method, to achieve the reference tracking control. Also, a fuzzy control law was added to the main feedback loop, to improve the tracking speed and to lower the time needed by the legs' foot to reach the desired reference position. Compared to others, we achieved to eliminate override, a better time in reaching the desired position and a lower error rate..

***Keywords*—**Bond Graph, Dynamic Control, Fuzzy Control, Sliding Mode Control.

I. Introduction

A functional representation of a system is a representation that describes how the system works, or how it should work. This representation can be used in simulating and verifying the system, and to generate diagnostics by using many simulation environments like Matlab Simulink or Bond Graph modeling[1,2].

Robots are well-known as nonlinear systems that include a strong coupling between their dynamics (Craig, 1996). These characteristics along with structured and unstructured uncertainties cause by model imprecision and un-modeled dynamics make the motion control a difficult problem (Spong & Vidiasagar, 1989) that can be reduced by using the bond graph modeling approach. Modeling a system is based on its decomposition. This is why the solution of the majority of complex problems consists in modeling. A model simplifies the problem by abstracting certain subsets of its observable attributes. Thus, we can emphasis on the problems' relevant points and we can exclude for the respective problem the irrelevant ones [3, 5, 13].

A well-known approach, which was made to model the interaction between physical systems, is the bond graph method, designed by Henry Paynter in 1959 and Damic and Montgomery in 2003[5]. This method uses the analogy effort-flow to describe the physical processes. These processes are graphical represented like elementary components with one or multiple ports. These ports represent the places where the systems interact with each other [7, 8]. By using this type of modeling allowed by the bond graphs, we made a virtual system that is a model of, and simulates, a walking robots' leg with 2 degrees of freedom. This was conducted in the Bond Graph simulation environment 20-Sim. By using this virtual system we could test a dynamic control law based on Sliding Control Method [2]. This type of simulation represents a new method of approaching the design and control of walking robots that are controller through a dynamic control method. The Sliding Mode Control (SMC) is used because its dynamic behavior can be modified according to specific options [2, 12] and because its closed loop response is undisturbed for a certain group of uncertainties (Lin et. all, 1998 [6]).

In this paper, we'll present a modified dynamic control SMC, developed with the help of bond graphs and for which we used a fuzzy control law to amplify the command signal for each joint/motor. The purpose of this paper is to improve a walking robot movement control on unstructured and bumped surfaces and to achieve improved tracking performances of position reference.

II. The Dynamic Control Using Sliding Control Method

For the control system used, we have the main dynamic relation below:

$$H(q)\ddot{q} + C(q,\dot{q})\dot{q} + G(q) + \tau_d = \tau \quad (1)$$

where, H is the inertial matrix, the vectors q, $\dot{q}$, $\ddot{q}$ are the position, speed and angular acceleration within the robots joints. The matrix C represents the Coriolis and centrifugal forces, and G is the gravitational vector. Also, τ_d represents the vector of disturbances and the dynamics that are not computed, and τ is the desired torque. Knowing that the system error is:

$$e = q_d - q \quad (2)$$

we chose the sliding surface as given in relation (3) (as shown by S.E. Shafiei in [4]). This value of s tends to 0 when the error e also tends to 0, meaning that lim(s)=0 when e->0.

By using the relation (3) we can rewrite the equation (1) and obtain equation (4), by replacing the value of q with the sum

Alexandru I. Gal is with the Institute of Solid Mechanics of Romanian Academy, Str. Constantin Mille 15, Sector 1, Bucharest, Romania (corresponding author to provide phone: +4 021 3157478; e-mail: galexandru2003@yahoo.com).

*Luige Vladareanu, Institute of Solid Mechanics of Romanian Academy, Str. Constantin Mille 15, Sector 1, Bucharest, Romania (corresponding author to provide phone: +4 021 3157478; e-mail: luigiv2007@yahoo.com.sg).

$q+s$, which will have the value of the desired value of qd when s equals zero. The value of q becomes qd because we need to calculate the torque of a desired angular position.

$$s = \dot{e} + \lambda_1 e + \lambda_2 \int_0^t e dt \tag{3}$$

$$H(q)(\ddot{q} + \dot{s}) + C(q, \dot{q})(\dot{q} + s) + G(q) + \tau_d = \tau \tag{4}$$

By replacing the terms of equations (3) and (4) we get:

$$H\dot{s} = -Cs + f + \tau_d - \tau \tag{5}$$

Results, that we can compute the torque:

$$\tau = \hat{f} + K_v s + K \cdot sat(s) \tag{6}$$

where,

$$\hat{f} = \hat{H}\left(\ddot{q}_d + \lambda_1 \dot{e} + \lambda_2 e\right) + \hat{C}\left(\dot{q}_d + \lambda_1 e + \lambda_2 \int_0^t e dt\right) + \hat{G} \tag{7}$$

Equation (6) presents the force estimation, and $\boldsymbol{s}$ is the exterior PID tracking loop, Kv,K are positive diagonal matrix and are built so that the stability conditions are fulfilled, and $\hat{f}$ is an estimation of f. The lambda 1 and 2 matrices were adjusted to get the best results. The *sat(s)* function used is the saturation function, in which φ is a constant that defines an area around the sliding surface in which the control parameter K is lowered proportional to the constant φ:

$$sat\left(\frac{s}{\varphi}\right) = \begin{cases} -1, & s \le -\varphi \\ \dfrac{s}{\varphi}, & -\varphi < s < \varphi \\ 1, & \varphi \le s \end{cases} \tag{8}$$

$$K = N \cdot K_{fuzzy},\ K_V = N_V \cdot K_{fuzzy} \tag{9}$$

To calculate the two matrices K and Kv we use a fuzzy control law and two constant matrices, N and Nv. To calculate the K_{fuzzy} gain matrix [7, 11], we need two inputs, s and $\dot{s}$ for which we have the membership functions in figure 1a and figure 1b. The abbreviation from figure 1a and figure 1b stands for: N=Negative, Z=Zero, P=Positive, V=Very, B=Big, M=Medium, S=Small. The control diagram used in the Sliding Control Simulation is the one presented in figure 2, in which we can observe two main parts: the Sliding Control area and the Internal Motors control for the two controlled joints. The diagram has three function blocks that can be attributed to the sliding control method. The first block is the one that computes the value of $\hat{f}$ from the relation (7). This block uses the values that were computed by many blocks: the reference generation blocks for each joint; the error computation bock; the function block that computes the dynamic matrix named "*Calculate H, C, G"*.

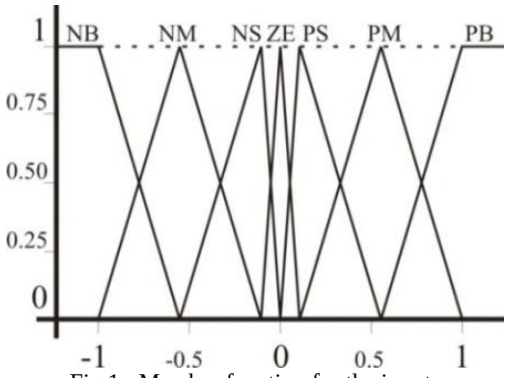

Fig.1a-Member function for the input s

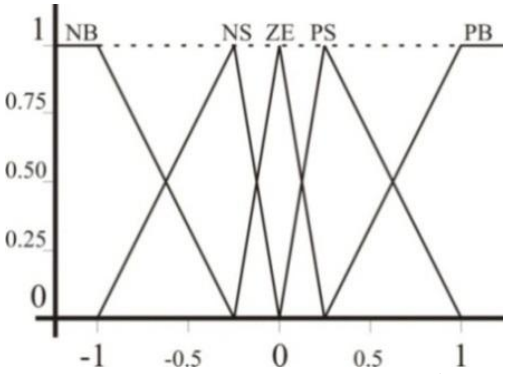

Fig.1b-Member function for the input $\dot{s}$

The second block called *Sliding Surface* that forms the Sliding Mode Control Method is the block that computes the value of $\boldsymbol{s}$ according to relation (3) and it contains the PID computation of the error e, relation (2).

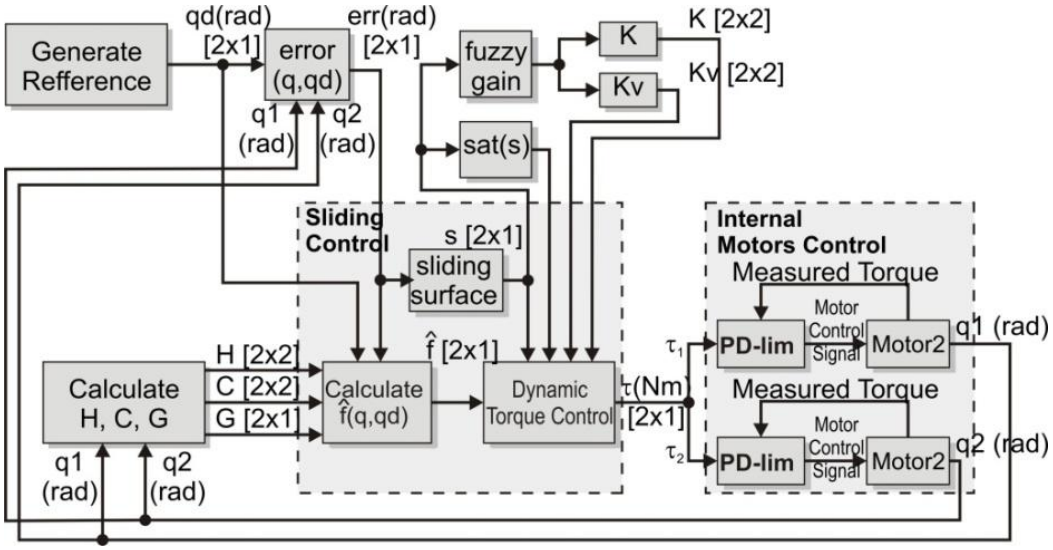

Fig. 2 – The control diagram of the Dynamic Leg Control using Sliding Control

Using these control blocks, we have made an internal torque control feedback loop and an external joint position feedback loop control, by using a dynamic approach along with the Sliding Control Method and the Fuzzy adjustment law.

III. CASE STUDY ACCOMPLISHED BY USING BOND GRAPHS

Bond graphs are mainly used in modeling different mechatronic/electrical/hydraulically systems because this component part of the system is the most difficult to simulate. Thus, we could simulate the behavior of a joint's motor used in figure 3 to develop the robot joint system. The control system was applied to a walking robot leg that has 2 degrees of freedom with rotating joints. This system is presented in figure 2 [7, 9]. The kinematic structure from figure 4 corresponds to the equations system in relation (10).

$$\begin{bmatrix} x_M \\ y_M \end{bmatrix} = \begin{bmatrix} l_2 \sin\theta_1 + l_3 \sin\theta_2 \\ l_1 + l_2 \cos\theta_1 + l_3 \cos\theta_2 \end{bmatrix} \quad (10)$$

Also, we need the numerical values of the physical characteristics of the robot to test the control system.

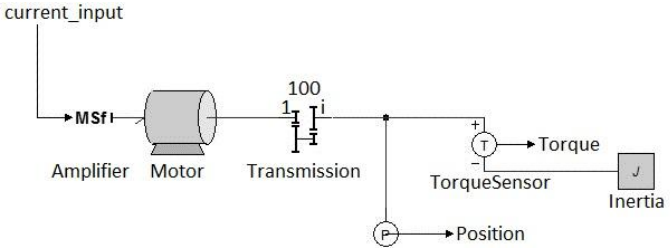

Fig. 3 – Bond Graph of the Robot Joint System

Thus, in Table 1, these values are presented and are chosen closer to reality [2].

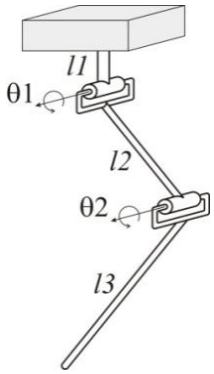

Fig. 4 – The robot leg structure

Table 1

Parameter	Value	Type
m1	0,04	Kg
m2	0,44	Kg
m3	0,22	Kg
l1	0,1	m
l2	0,5	m
l3	0,7	m
g	9,8	m/s^2

In order to implement the sliding mode control method we need to define the dynamic parameters that are used in relation (7), where *H* is the inertial matrix, *C* is the matrix of Coriolis effect and centrifugal forces, and *G* is the matrix of gravity tensor:

$$H(q)=\begin{bmatrix}(m_2+m_3)l_2^2+m_3l_3^2+2m_3l_2l_3\cos q_2 & m_3l_3^2+m_3l_2l_3\cos q_2\\ m_3l_3^2+m_3l_2l_3\cos q_2 & m_3l_3^2\end{bmatrix} \quad (11)$$

$$C(q,\dot{q})=\begin{bmatrix}-m_3l_2l_3\dot{q}_2\sin q_2 & -m_3l_2l_3(\dot{q}_1+\dot{q}_2)\sin q_2\\ m_3l_2l_3\dot{q}_1\sin q_2 & 0\end{bmatrix} \quad (12)$$

$$G(q)=\begin{bmatrix}(m_2+m_3)l_2^2\dfrac{g}{l_2}\cos q_1+m_3l_2l_3\dfrac{g}{l_2}\cos(q_1+q_2)\\ m_3l_2l_3\dfrac{g}{l_2}\cos(q_1+q_2)\end{bmatrix} \quad (13)$$

Table 2 - Fuzzy rule for adjusting Kfuzzy

s / $\dot{s}$	NB< -3	-3<=NM NM<-1.5	-1.5<=NS NS<0	Z=0	0<PS PS<=1.5	1.5<PM PM<=3	3<PB
NB< -20	400	400	250	150	50	15	50
NS= -10	400	250	150	50	15	50	150
Z= 0	250	150	50	15	50	150	250
PS= 10	150	50	15	50	150	250	400
PB> 20	50	15	50	150	250	400	400

The presented control method uses a fuzzy logic gain to better control the approach of the robot foot to the sliding surface. The values of the fuzzy membership functions (figures 1a and 1b) are presented in table 2, values which were found by trial and error.

Also, we need to define the constants that were used in the sliding mode control combined with the fuzzy logic [4]. Besides the adjustments of parameters to achieve a better positioning error, the main variation from the classic SMC is the fuzzy control. In order to reduce the positioning error, we added a constraint to the sliding parameter ***s***. This constraint removes the integral value from the sliding parameter calculation when its value is below a certain threshold.

By using all of these parameters and functions, we have made an internal torque control feedback loop and an external joint position feedback loop control. Also, by using a dynamic approach along with the Sliding Control Method and the Fuzzy adjustment law, through the bond graph simulation method, we could achieve a better control law.

$$s=\begin{cases}\dot{e}+\lambda_1 e+\lambda_2\int_0^t edt, & \int_0^t edt<threshold\\ \dot{e}+\lambda_1 e, & \int_0^t edt\geq threshold\end{cases} \quad (14)$$

IV. Results and Conclusions

The control system was made and simulated with the help of the 20-Sim modeling environment which has the possibility of using bond graphs. To test the control system, we chose 2 sinusoidal signals of 2 and 2.5 radians amplitude.

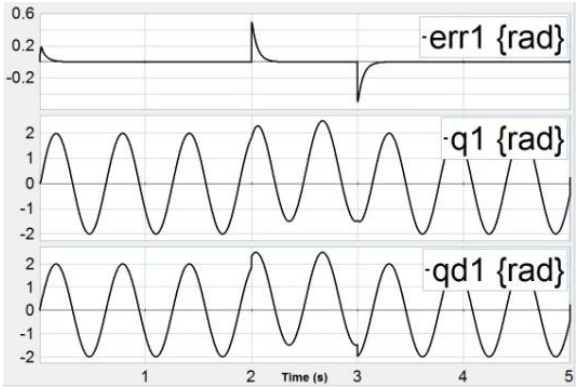

Fig. 5 – Joint 1: a) Error, b) Tracking Position, c) Reference Position

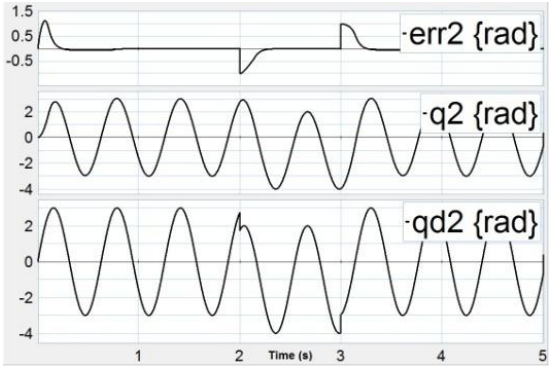

Fig. 6 – Joint 2: a) Error, b) Tracking Position, c) Reference Position

In figure 5 and figure 6 we presented the obtained results according to the simulation. In these two figures, the bottom diagram represents the angular reference for each joint (figure 5 and respectively figure 6). The middle diagrams represent the system tracking signal, and the top diagram has the angular error signal for the two joint motors. By watching these diagrams one can observe that after 2 seconds and respectively 3 seconds, the reference signals have a sudden increase/decrease respectively decrease/increase in value, to test the system response to rapid change in the reference signal.

Compared with the results presented by S.E. Shafiei in [4], we achieved a better overall positioning error and a faster positioning when the signal abruptly changes. Besides the fact that our control system has better tracking capabilities, ours removes the overrides of the system along with a faster time in which the system reaches its goal position. Of course that the overrides eliminated are the ones that are very large, but the only ones that remain are those due to the system oscillation around its target, as one can see in the figures 7 and 8, which shows the magnified positioning errors of joint 1 and 2.

Figure 7 and figure 8 respectively, represent the angular error, which has been zoomed in to better observe the error variations. One can observe that in the case of joint number 1, the system reaches faster the reference signal, under 0.25 seconds, to an angular error lower than +/- 0.002 radians, meaning 0.11 degrees, after which the system starts to oscillate around the reference position due to the sinusoidal shape of the reference signal. In the case of joint number 2, the system reaches in the first 0.75 seconds from the disturbance (the sudden increase/decrease in reference value) a +/- 0.005 radians error meaning 0.28 degrees, after which the system starts to oscillate around the reference position due to the sinusoidal shape of the reference signal.

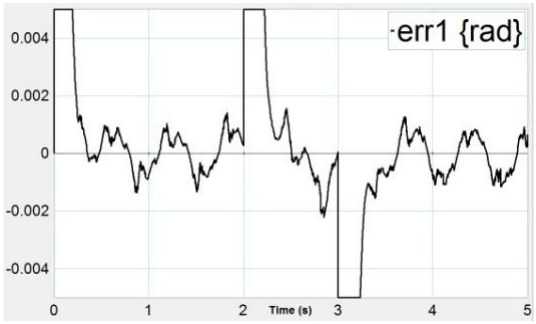

Fig. 7 – Joint 1 - Angular Error (rad)

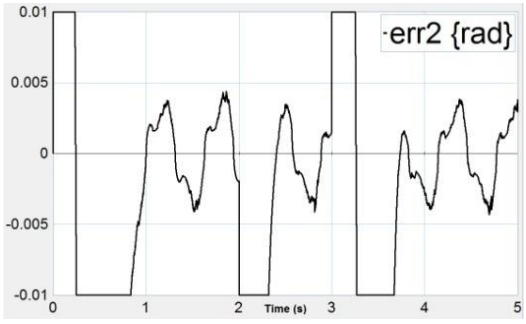

Fig. 8 – Joint 2 - Angular Error (rad)

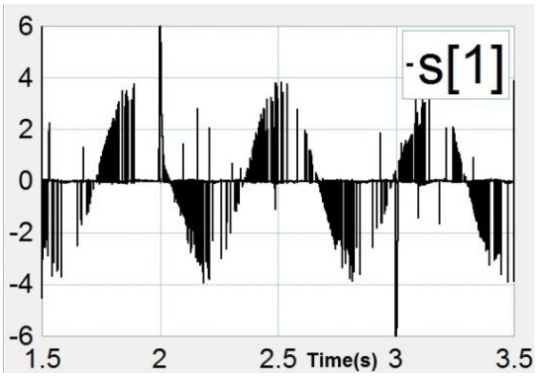

Fig. 9 – Joint 1 with value of s

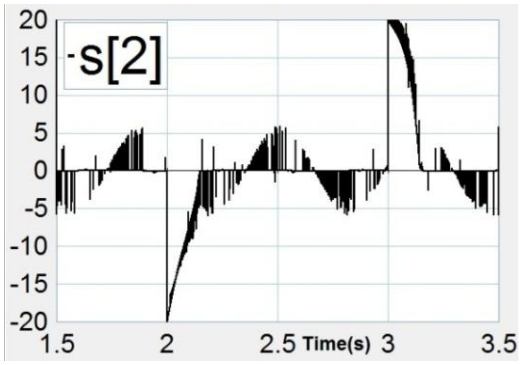

Fig. 10 – Joint 2 with value of s

To be able to analyze the sliding control method, we presented the values of ***s*** during the simulation. Figure 9 and 10 presents the value of ***s***. Thus, one can observe how the sliding control method really works, by noticing how the computed value of the PID that returns the ***s*** value oscillates for different values of the reference signal. One can observe in figure 9 and 10 that when the two disturbances appear (at second 2 and 3), the value of ***s*** has really big amplitude peaks (over 30), due to its derivative part which has a punctual high value. As a difference between the two signals (joint 1 and joint 2) one can observe that in joint 2, the disturbance signal also records a big peak but it maintains a high value (over +/-10 rad) for another 0.125 seconds, where the signal of joint 1 presents only a peak at the moment of the disturbance and after a very short time (under 0.05 seconds) the signal lowers in value.

Because the Sliding Control is known for having a chattering problem we solved the issue by using a saturation function instead of a sign function and it can be seen that the output signal does not present this effect. The main observed conclusion is that this kind of control is one that tracks very well a uniform reference signal where other control methods like the simple PID controllers tend to overrides and in some cases to become instable if the PID gains are not correctly chosen. Also, the use of the fuzzy control method to adjust the output gain provides a better tracking error than the use of a PID control as shown by Vicente in 2003[10, 14].

ISBN: 978-1-61804-216-3

In this paper, we designed the sliding mode control method through intelligent approaches that include sliding mode control, fuzzy control and bond graph modeling. This method uses the modeling approach of bong graphs used in designing and testing mechatronic systems but combined with the dynamic properties of the sliding mode control and fuzzy methods. Thereby, we showed a new method of robot walking control that improves the real time tracking control and we applied it on a 2 DOF mobile walking leg control. Compared to the conventional sliding mode control method, our system is 4 times faster and 10 times more accurate in tracking the position reference and can also compensate disturbances that may appear on the sliding surface. Comparing to other methods[4,13], which also uses a fuzzy based controller, our system has a better tracking error and much more, it can overcome uncertainties in a much shorter time with fewer error oscillations, resulting a robust controller with a predictive behavior.

The main performance demonstrates that using the sliding control method and a fuzzy adjustment law to calculate the gain matrix, removes the overrides and has better tracking capabilities, behaving like a predictive system, using the reference speed and acceleration and also the error speed so the robot can track and reach the reference position as smoothly as possible. By modeling the control system through Bond Graphs we could show more clearly the interaction between the components of the dynamic control system and also the electric motors, which can mimic the behavior of real life systems. Through simulation and modeling, and by using Bond Graphs, this paper develops a new research method that can analyze real time control and complex systems, specifically for the intelligent systems of which the mobile walking robots are part of.

The experimental results of the sliding mode control method which was used along with a fuzzy adjustment law in order to improve the performance of the robot dynamic control have proved that the studied robot system behaves very well when walking on an unstructured and bumped surface, because on encountering a sudden change in reference signal, the system is stable and compensates very well the disturbance.

ACKNOWLEDGMENT

This work was supported in part by the Romanian Academ and the FP7 IRSES RABOT project no. 318902/2012-2016 (sponsor and financial support acknowledgment goes here).

REFERENCES

[1] V Damic, J Montgomery, *Bond Graph Based Automated Modelling Approach to Functional Design of Engineering Systems*, Proceedings of the International Conference Mechanics in Design'98 / Gentle, C.R. ; Hull, J.B. (ed). - Nottingham, GB 1998, 377-386.

[2] Gal A., Vladareanu L., Munteanu M. S., Melinte O., *PID sliding motion control by using fuzzy adjustment*, SISOM 2012, Bucharest 25-26 May 2012

[3] Vladareanu L., Capitanu L., *Hybrid Force-Position Systems with Vibration Control for Improvment of Hip Implant Stability*, Journal of Biomechanics, vol. 45, S279, Elsevier, 2012

[4] SeyedEhsanShafiei (Editor):*Advanced Strategies for Robot Manipulators*, ISBN 978-953-307-099-5, Published by JanezaTrdine, pp. 135-172, Croația, 2010

[5] V. Damic, J. Montgomery,*Mechatronics by Bond Graphs: An Object-Oriented Approach to Modelling*, Springer-Verlag, Berlin-Heidelberg,pp 71-97, 2003.

[6] Lin F.J., Wai R.J., Kuo R.H., Liu D. C.:*A comparative study of sliding mode and model reference adaptive observers for induction motor drive*. Electr. Power Syst. Res. 44, 163–174, 1998

[7] Vladareanu L., Melinte D.O., *Dynamic Force-Position Control of the Walking Robots Motion on Slope*, Applied Mechanics and Materials Journal, vol. 186, Trans Tech Pub, Switzerland, pg.98-104, ISSN: 1662-7482, 2012

[8] Octavian Melinte, Alexandru Gal: *Bond graph modeling for haptic interface robot control*, The European Computing Conference, Paris, 2011, pg. 364-369, ISBN: 978-960-474-297-4

[9] Vladareanu L., A.Curaj, R.I.Munteanu, *Complex Walking Robot Kinematics Analysis And Plc Multi-Tasking Control*, Revue Roumaine des Sciences Techniques – Série Électrotechnique et Énergétique, Vol. 57, no. 1, pg.90-99, 2012, ISSN 0035-4066

[10] Vicente Parra-Vega, SuguruArimoto, Yun-Hui Liu, Gerhard Hirzinger, *Dynamic Sliding PID Control for Tracking of Robot Manipulators: Theory and Experiments*, IEEE Transactions On Robotics And Automation, Vol. 19, No. 6, December 2003

[11] Abdelfettah Kerboua, Mohamed Abid, *Hybrid Fuzzy Sliding Mode Control of a Doubly-Fed Induction Generator in Wind Turbines*, Revue Roumaine des Sciences Techniques – SérieÉlectrotechnique et Énergétique, Vol. 57, no. 4, pg. 412 - 421, 2012, ISSN 0035-4066

[12] Utkin, V. I.,*Sliding Modes and their Application in Variable Structure Systems*, MIRPublishers, Moscow, 1978.

[13] Boscoianu M, Axente C., Pahonie R, *Some aspects regarding the cooperative control problem for flying wing air vehicles*, in Computational Methods and Intelligent Systems, Sofia, Bulgaria, May 2-4, 2008, ISSN 1790-5117, ISBN 978-960-6766-60-2

[14] Kaynak, O.,ErbaturK.,E.M., *The Fusion of Computationally Intelligent Methodologies and Sliding-Mode Control*, IEEE Trans. on IndustrialElectronics, vol. 48, no. 1, pp. 4-17, 2001.

Design of Third Order Current-mode Quadrature Sinusoidal Oscillator with High Output Impedances

Kritphon Phanrattanachai and Winai Jaikla

***Abstract*—**This article presents a current-mode quadrature oscillator using differential different current conveyor (DDCC) and voltage differencing transconductance amplifier (VDTA) as active elements. The proposed circuit is realized from a non-inverting lossless integrator and an inverting second order low-pass filter. The oscillation condition and oscillation frequency can be electronically/orthogonally controlled via input bias currents. The circuit description is very simple, consisting of merely 1 DDCC, 1VDTA, 1 grounded resistor and 3 grounded capacitors. Using only grounded elements, the proposed circuit is then suitable for IC architecture. The proposed oscillator has high output impedance which is easy to cascade or dive the external load without the buffer devices. The PSPICE simulation results are depicted, and the given results agree well with the theoretical anticipation. The power consumption is approximately 1.76mW at ±1.25V supply voltages.

***Keywords*—**Current-mode, Oscillator, Integrated circuit, DDCC, VDTA.

I. Introduction

An oscillator is an important basic building block, which is frequently employed in electrical engineering applications. Among the several kinds of oscillators, a quadrature oscillator is widely used because it can offer sinusoidal signals with 90° phase difference, for example, in telecommunications for quadrature mixers and single-sideband [1].

Several implementations of second order quadrature oscillators using different high-performance active building blocks, such as, OTAs [2], current conveyors [3], four-terminal floating nullors (FTFN) [4-5], current follower [6], current differencing buffered amplifiers (CDBAs) [7], current differencing transconductance amplifiers (CDTAs) [8], fully-differential sec-ond-generation current conveyor (FDCCII) [9], and differencing voltage current conveyor (DVCCs) [10], have been reported. Recently, it has been proved that the third order oscillator provides good characteristic with lower distortion than second order oscillator [11-12]. From our literature found that the third order oscillator employing CCCIIs [11], OTAs [12-13], CDTAs [14], have been proposed.

The aim of this paper is to propose a third order current-mode oscillator, based on DDCC and VDTA. The features of the proposed circuits are that: the oscillation condition can be adjusted independently from the oscillation frequency by electronic method. The circuit construction consists of 1 DDCC, 1VDTA, 1 grounded resistor and 2 grounded capacitors. The PSPICE simulation results are also shown, which are in correspondence with the theoretical analysis.

K. Phanrattanachai is with the Electronics Technology Program, Faculty of Industrial Technology, PhetchabunRajabhat University,Phetchabun, 67000, Thailand (e-mail: kritphon@pcru.ac.th).

W. Jaikla is with the Department of Engineering Education, Faculty of Industrial Education, King Mongkut's Institute of Technology Ladkrabang, Bangkok, 10520, Thailand (e-mail: winai.ja@hotmail.com).

II. Theory and Principle

A. Basic concept of DDCC

The electrical behaviors of the ideal DDCC are represented by the following hybrid matrix [15]:

$$\begin{bmatrix} V_X \\ I_{Y1} \\ I_{Y2} \\ I_{Y3} \\ I_Z \end{bmatrix} = \begin{bmatrix} 0 & 1 & -1 & 1 & 0 \\ 0 & 0 & 0 & 0 & 0 \\ 0 & 0 & 0 & 0 & 0 \\ 0 & 0 & 0 & 0 & 0 \\ 1 & 0 & 0 & 0 & 0 \end{bmatrix} \begin{bmatrix} I_X \\ V_{Y1} \\ V_{Y2} \\ V_{Y3} \\ V_Z \end{bmatrix}. \quad (1)$$

The symbol and the equivalent circuit of the DDCC are illustrated in Figs. 1(a) and (b), respectively.

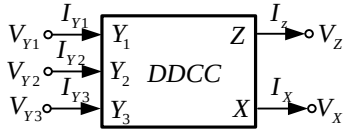

(a)

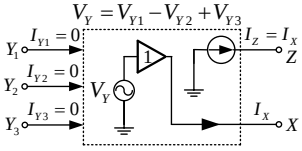

(b)

Fig. 1. DDCC (a) Symbol (b) Equivalent circuit

B. Basic Concept of VDTA

The circuit symbol of VDTA is shown in Fig. 2, where V_P and V_N are the input terminals, Z and Xare the output ones. Hence, Z is the current output terminal; current through Z terminal follows the difference of the voltages at V_P and V_N terminals by transconductances g_{m1}. The voltage v_Z on Z terminal is transferred into current using transconductance g_{m2}, which flows into output terminal X. The g_{m1} and g_{m2} are tuned by I_{B1} and I_{B2}, respectively. In general, CDTA can contain an arbitrary number of x terminals, providing currents I_X of both

directions. All terminals of VDTA exhibit high impedance values [17]. The characteristics of the ideal VDTA are represented by the following hybrid matrix:

$$\begin{bmatrix} I_Z \\ I_{X+} \\ I_{X-} \end{bmatrix} = \begin{bmatrix} g_{m1} & -g_{m1} & 0 \\ 0 & 0 & g_{m2} \\ 0 & 0 & -g_{m2} \end{bmatrix} \begin{bmatrix} V_P \\ V_N \\ V_Z \end{bmatrix}. \quad (2)$$

If the VDTA is realized using CMOS technology, $g_{m1}$and g_{m2} can be respectively written as

$$g_{m1} = \sqrt{kI_{B1}}\,, \quad (3)$$

and

$$g_{m2} = \sqrt{kI_{B2}}\,. \quad (4)$$

Here k is the physical transconductance parameter of the CMOS transistor. I_{B1} and I_{B2} are the bias current used to control the g_{m1} and g_{m2}, respectively.

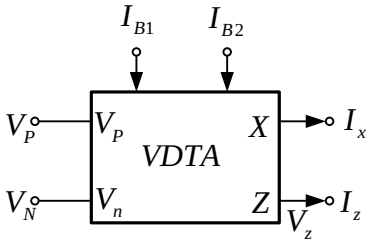

Fig. 2. The circuit symbol of VDTA

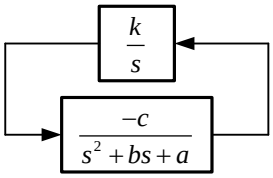

Fig. 3. Block diagram for design of proposed oscillator

C. General structure of 3rd oscillator

The oscillator is designed by cascading an inverting second order low-pass filter and the lossless integrators as systematically shown in Fig. 3 [13]. From block diagram in Fig. 3, we will receive the characteristic equation as

$$s^3 + bs^2 + as + ck = 0\,. \quad (5)$$

From Eq. (5), the condition of oscillation (OC) and frequency of oscillation (FO) can be written as

$$OC: ab = ck\,, \quad (6)$$

and

$$\omega_{osc} = \sqrt{a}\,. \quad (7)$$

From Eq. (5), if $a = c$, the oscillation condition and oscillation frequency can be adjusted independently, which are the oscillation condition can be controlled by *b* and *k*, while the oscillation frequency can be tuned by *a*.

D. Proposed oscillator

The completed 3rd current-mode quadrature oscillator is shown in Fig. 4. The condition of oscillation and frequency of oscillation can be written as

$$\frac{1}{C_1 R} = \frac{g_{m2}}{C_3}\,, \quad (8)$$

and

$$\omega_{osc} = \sqrt{\frac{g_{m1}}{C_1 C_2 R}}\,. \quad (9)$$

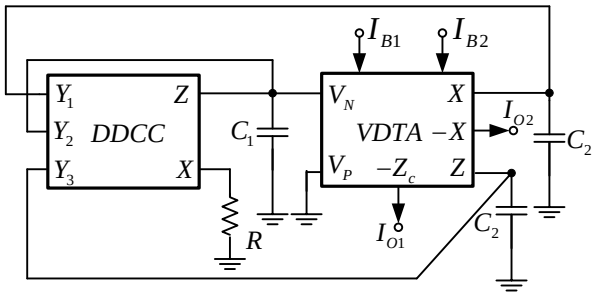

Fig. 4. Proposed current-mode oscillator

If $g_{m1} = \sqrt{kI_{B1}}$, $g_{m2} = \sqrt{kI_{B2}}$ and $C_1 = C_2 = C_3 = C$, the condition of oscillation and frequency of oscillation can be rewritten as

$$\frac{1}{R} = \sqrt{kI_{B2}}\,, \quad (10)$$

and

$$\omega_{osc} = \frac{1}{C}\sqrt{\frac{(kI_{B1})^{\frac{1}{2}}}{R}}\,. \quad (11)$$

It is obviously found that, the condition of oscillation and frequency of oscillation can be adjusted independently, which are the oscillation of oscillation can be controlled by setting I_{B2}, while the frequency of oscillation can be tuned by setting I_{B1}. From the circuit in Fig. 4, the current transfer function from I_{o1} to I_{o2} is

$$\frac{I_{o2}(s)}{I_{o1}(s)} = \frac{g_{m1}}{sC_2}\,. \quad (12)$$

For sinusoidal steady state, Eq. (12) becomes

$$\frac{I_{o2}(j\omega)}{I_{o1}(j\omega)} = \frac{g_{m1}}{\omega C_2} e^{-j90^\circ}\,. \quad (13)$$

ISBN: 978-1-61804-216-3

The phase difference ϕ between I_{o1} and I_{o2} isϕ = -90°ensuring that the currents I_{o2} and I_{o1} are in quadrature.

III. Results of Computer Simulation

The working of the proposed oscillator has been verified in PSpice simulation.Internal constructions of DDCC and VDTA used in simulation are respectively shown in Figs. 5 and 6. The PMOS and NMOS transistors have been simulated by respectively using the parameters of a 0.25µm TSMC CMOS technology [16]. The transistor aspect ratios of PMOS and NMOS transistor are indicated in Table I. The circuit was biased with ±1.25V supply voltages, V_{BB}=-0.55V, C_1=C_2=C_3=50pF, I_{B1}=I_{B2}=60µAand R=3.5kΩ. This yields simulated oscillation frequency of 1MHz. Fig. 7 shows simulated quadrature output waveforms. Fig. 8 shows the simulated output spectrum, where the total harmonic distortion (THD) is about 2.95%. The quadrature relationship between the generated waveforms has been verified using Lissagous figure and shown in Fig. 9.The power consumption is approximately 1.76mW.

TABLE I. Dimensions of the Transistors

Transistor	W (µm)	L (µm)
M_1-M_4	3	0.25
M_5-M_8	1	0.25
M_9-M_{10}	10	0.25
M_{11}-M_{12}, M_{13}-M_{16}	5	0.25
M_{17}-M_{20}	8	0.25

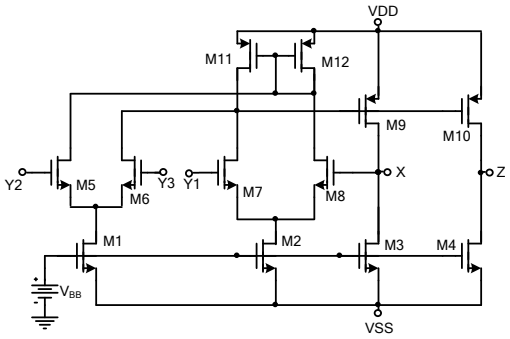

Fig. 5. Internal construction of the CMOSDDCC

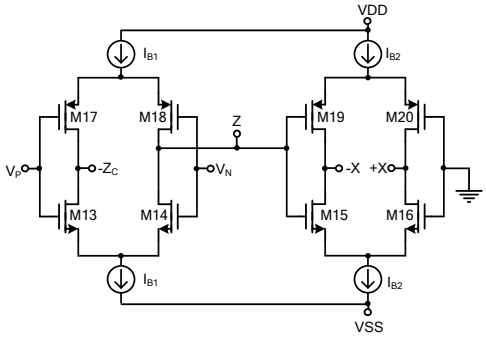

Fig. 6. Internal construction of the CMOSVDTA [17]

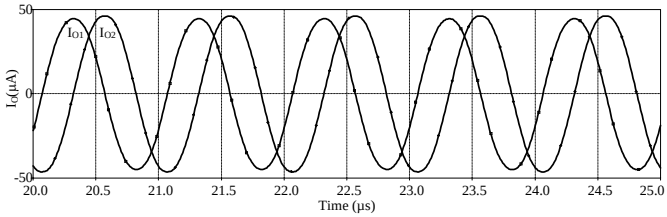

Fig. 7. The simulation result of quadrature outputs

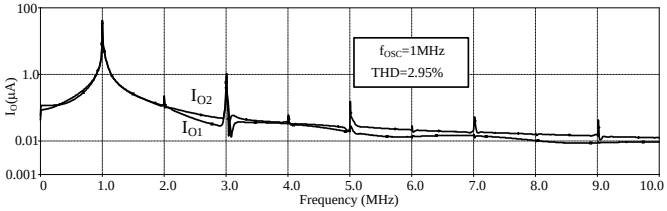

Fig. 8. Frequency spectrum of signal in Fig. 7

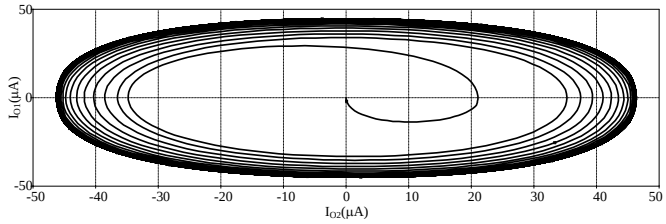

Fig. 9. Relative of the output waveform

IV. Conclusion

A 3rd current-mode quadrature sinusoidal oscillator based on DDCC and VDTA has been presented. The features of the proposed circuit are that: oscillation frequency an oscillation condition can be orthogonally adjusted via input bias current; it consists of 1 DDCC, 1 VDTA, 1 grounded resistor and 3 grounded capacitors, which is convenient to fabricate. The PSPICE simulation results agree well with the theoretical anticipation

References

[1] I. A. Khan and S. Khawaja, An integrable gm-C quadrature oscillator. Int. J. Electronics, 2000, 87(1): 1353-1357.

[2] K. Kumwachara and W. Surakampontorn, An integrable temperature-insensitive gm–RC quadrature oscillator. International Journal of Electronics, 2003, 90(1): 599-605.

[3] M. T. Abuelma'atti and A. A. Al-Ghumaiz, Novel CCI-based single-element-controlled oscillators employing grounded resistors and capacitors. IEEE Transaction on Circuits and Systems-I, 1996, 43: 153-155.

[4] M. T. Abuelma'atti and H. A. Al-Zaher, Current-mode sinusoidal oscillators using single FTFN. IEEE Transaction on Circuits and Systems-II, 1999: 46, 69-74.

[5] U. Cam, A. Toker, O. Cicekoglu, and Kuntman, Current-mode high output impedance sinusoidal oscillator configuration employing single FTFN. Analog Integrated Circuits and Signal Processing, 2000, 24: 231-238.

[6] M. T. Abuelma'atti, Grounded capacitor current-mode oscillator using single current follower. IEEE Transaction Circuits and Systems-I, 1992, 39: 1018-1020.

[7] R. Nandi, P. Venkateswaran, Soumik Das and M. Kar, CDBA-based electronically tunable filters and sinusoid quadrature oscillator. Journal of Telecommunication, 2010, 4(1): 35-41.

ISBN: 978-1-61804-216-3

[8] A. Lahiri, New current-mode quadrature oscillators uisng CDTA. IEICE Electronics Express, 2009, 6(3): 135-140.

[9] J. W. Horng, C. L. Hou, C. M. Chang, H. P. Chou, C. T. Lin, and Y. H. Wen, Quadrature oscillators with grounded capacitors and resistors using FDCCIIs. ETRI Journal, 2006, 28: 486-494.

[10] J. W. Horng, Current-mode quadrature oscillator with grounded capacitors and resistors using two DVCCs. IEICE Transaction Fundamentals of Electronics, Communications and Computer Sciences, 2003, E86-A: 2152-2154.

[11] S. Maheshwari, and I. A. Khan, Current controlled third-order quadrature oscillator. IEE Proceeding on Circuits Devices Systems, 2005, 152: 605-607.

[12] P. Prommee, K. Dejhan, An integrable electronic-controlled quadrature sinusoidal oscillator using CMOS operational transconductance amplifier. International Journal of Electronics, 2002, 89: 365-379.

[13] T. Tsukutani, Y. Sumi, and Y. Fukui, Electronically controlled current-mode oscillators using MO-OTAs and grounded capacitors. Frequenz, 2006, 60: 220-223.

[14] J. W. Horng, Current-mode third-order quadrature oscillator using CDTAs, Active and Passive Electronic Components, 2009, Article ID 789171, doi:10.1155/2009/789171.

[15] W. Chiu, S. I. Liu, H. W. Tsao and J. J. Chen, COMS differential difference current conveyors and their applications. IEE Proceedings—Circuits Devices and Systems, 1996, 143: 91–96.

[16] P. Prommee, K. Angkeaw, M. Somdunyakanok, K. Dejhan. CMOS-based near zero-offset multiple inputs max–min circuits and its applications. Analog Integr. Circuits Signal Process, 2009, 61: 93–105.

[17] A. Yeşil, F. Kacar ; H. Kuntman, "New simple CMOS realization of voltage differencing transconductance amplifier and its RF filter application" Radioengineering, vol. 20, no. 3, pp. 632-637, 2011.

Optimization by genetic algorithm for synthesize a robust stabilizer PSS applied to power system *(application under GUI/MATLAB)*

GHOURAF Djamel Eddine
Department of Electrical Engineering University of SBA
IRECOM Laboratory
BP 98 22000 Algeria
E-mail: jamelbel22@yahoo.fr

NACERI Abdellatif
Department of Electrical Engineering University of SBA
IRECOM Laboratory
BP 98 22000 Algeria
E-mail : abdnaceri@gmail.com

DERRAR Amina
Department of Electrical Engineering University of SBA
IRECOM Laboratory
BP 98 22000 Algeria
E-mail: gh.mohamed22@gmail.com

***Abstract*— This paper presents the use of genetic algorithms (GA) to synthesize the optimal parameters of Power System Stabilizer (PSS),this later is used as auxiliary of turbo generator excitation system in order to damp electro mechanicals oscillations of the rotor (inductor),and consequently ,improve the Electro Energetic System (EES).in this study, we started with the linearization of a system around the operating point ,than, we analyzed its stability in slight movement, after that, we have optimized the PSS parameters using the Genetic Algorithms (G.A).The obtained results have proved that (G.A) are a powerful tools for optimizing the PSS parameters, and more robustness for the studied PS . Our present study was performed using a GUI realized under MATLAB in our work.**

Keywords*— *AVR-PSS, Electric power system, genetic algorithm, GUI-MATLAB, powerful synchronous generators , stability and robustness.

I. INTRODUCTION

The electric power system (EPS) stability is viewed as the most necessary condition to regular operating electrical network control systems are required to ensure this stability by identifying the main factors that influence on this one. The Classical controllers AVR and PSS [1,2] (PI or PID) have a leading role in increasing static and dynamic stability degree, and damping electro mechanicals oscillations generated by the rotor (the inductor).However ,a robustness test (a disturbance injected on the EPS) showed that PID -AVR and PSS are hardly robust ,so ,in order to improve their efficiency (robustness),we used the (G.A) for the optimization and the adjusting of PSS parameters [3,4].

The genetic algorithms is a global research technical and an optimization procedure based on natural inspired operators such as crossing, and selection [5,6].unlike other optimization methods, the (G.A) operate under several encodings parameters (binary, ternary, real…),to be optimized and not the parameters themselves .in addition, to better guide the AVR-PSS optimal parameters search ,the (G.A) use a performanced index to approach this solution [6].

II. DYNAMIC POWER SYSTEM MODEL:

In this paper the dynamic model of an IEEE - standard of power system, namely, a single machine connected to an infinite bus system (SMIB) was considered [4]. It consists of a single synchronous generator (turbo-Alternator) connected through a parallel transmission line to a very large network approximated by an infinite bus as shown in figure 1.

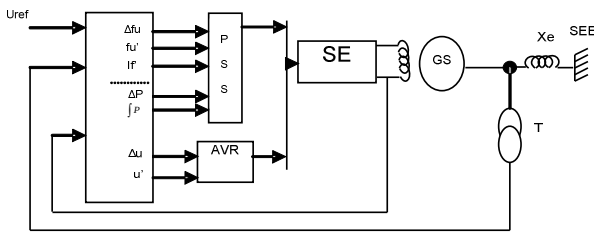

Fig. 1. Standard system IEEE type SMIB with excitation control of powerful synchronous generators

The AVR (Automatic Voltage Regulator), is a controller of the SG voltage that acts to control this voltage, thought the exciter .Furthermore, the PSS was developed to absorb the generator output voltage oscillations [5].

In our study the synchronous machine is equipped by a voltage regulator model "IEEE" type – 5 [7, 8], as is shown in Figure 2.

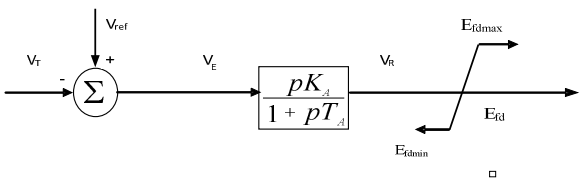

Fig. 2. A simplified " IEEE type-5" AVR

$$V_R = \frac{K_A V_E - V_R}{T_A} \quad , \quad V_E = V_{ref} - V_F \tag{1}$$

About the PSS, considerable's efforts were expended for the developpement of the system. The main function of a PSS is to modulate the SG excitation to [1, 2, 4].

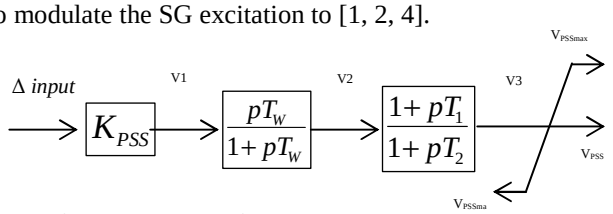

Fig. 3. A functional diagram of the PSS used [8]

In this paper the PSS signal used, is given by:[14]

$$\dot{V}_1 = \frac{V_2 - V_1}{T_1} + \frac{T_2}{T_1}\dot{V}_2 \quad ;$$
$$\dot{V}_2 = \frac{V_3 - V_2}{T_2} + \frac{T_3}{T_2}\dot{V}_2 \quad ;$$
$$\dot{V}_3 = \frac{V_3}{T_W}\dot{V}_1 ; \dot{V}_1 = K_{PSS}.\Delta input$$

$$\Delta input = \begin{cases} \Delta P \ , \int p \\ or \\ \Delta\omega = \omega_{mach} - \omega_0 \\ and \\ \Delta I_f = I_f - I_{f0} \\ and \\ \Delta U_f = U_f - U_{f0} \end{cases} \tag{2}$$

III. THE GENETICS ALGORITHMS THEORY

A. Introduction

Overall, a Genetic Algorithm handles the potential solutions of a given problem, to achieve the optimum solution, or a solution considered as satisfactory .the algorithm is organized into several steps and works iteratively. The figure 4 shows the most simple genetic algorithm introduced by Holland [6].

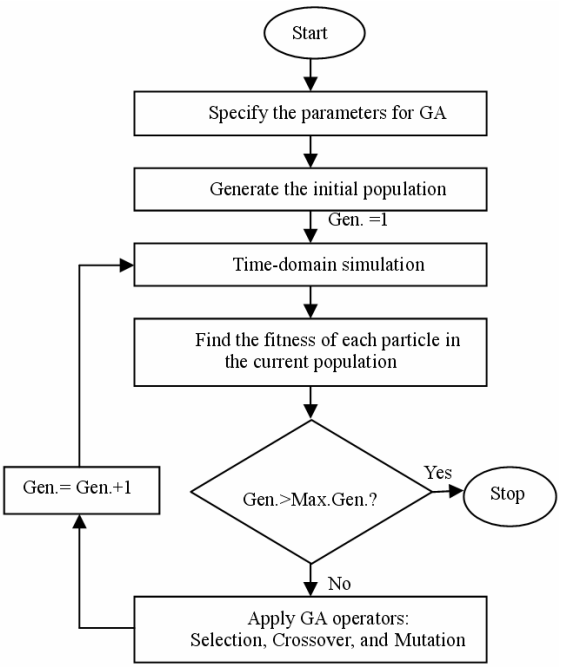

Fig. 4. The genetic algorithm organization

B. The genetic algorithm steps description

In what follows, we will describe in more detail the various steps of a simple genetic algorithm Figure 4

1) Coding and initialization [9]

The first step is the problem parameters coding in order to constitute the chromosomes. The most used type of coding is the binary one, but other coding can be also used for example: ternary, integer, real…the passage from the actuar representation to the coded one is done through encoding and decoding functions.

2) Evaluation

It's to measure the performance of each individual in the population; this is done using a function directly related to the objective function which is called "fitness function". This is positive real function that reflects the strength of the individual. An individual with a high fitness value is a good solution to the problem, whereas individual with low fitness value represents a worse solution.

3) Selection

Selection in genetic algorithms plays the same role as natural selection. It follows the survivals Darwinian principle of those most adapted, it decide what are the individuals that survive and which ones disappear ,this selection is according to their fitness functions. a Population called intermediate is then formed by selected individuals.

There are several methods of selection. We mention two of the best known:

- Lottery roulette Méthod ;
- Tournement Method.

4) Crossover

Crossing enables a pair of individuals among those selected, to share their genetic information e. d. their genes. Its principle is simple: two individuals are randomly taken, and they are called "parents", then we draw a random"P" number in the interval [0, 1], after that it will be compared to some crossing probability "Pc".

- If P>Pc, there will be no crossing, and the parents are copied into a new generation.
- If else; P≤ Pc, crossing occurs and the chromosomes parents are crossed to produce tow children replacing their parents in the next generation.

There are different crossing types, the most known are:

- The multipoint crossover
- The uniforme crossover

5) Mutation

The mutation operator enables to explore new points in the search space and ensures the possibility to leave local optima; mutation applies to each individual gene with a mutation probability (Pm) following the same crossing principle.

ISBN: 978-1-61804-216-3

- If P> Pm, there will be no mutation will and the gene remains as it is.
- If P ≤ Pm mutation occurs, and the gene will replaced with another gene randomly drawn among the possible values. In the case of a binary coding, it is simply to replace a"0" by a "1" and vice versa.

6) Terminaison criteria

As in any iterative algorithm, we must define a stopping criteria, this can be formulated in various ways, among which we can mention:

- Stop the algorithm when the result reached a satisfactory solution;
- Stop if there is no improvement for some number of generations;
- Stop if a certain number of generations is exceeded.

Example:

We consider the simple case of function with one variable "x" belonging to the natural numbers set:

Maximise $F_{obj} = 15\,x - x$

Subject to $0 > x \geq 15$

The used parameters:

- A 8 bits binary encoding ;
- The search interval [0,15] ;
- A Lottery roulette Method;
- A simple crossing (to one point),with crossing probability Pc=0.7 ;
- A mutation probability Pm=0.1.

To run and view the various steps of genetic algorithm, we created and developed a "GUI" (Graphical User Interfaces) in MATLAB software, this latter allows:

- To calculate and display the AG operations (Coding and initialization, Evaluation, Selection, Crossing and mutation);
- To display graphically the problem solution, as is shown in figure 5.

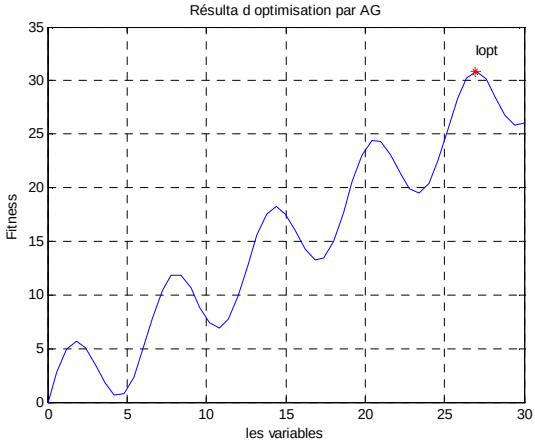

Fig. 5. Optimization result by AG

The problem solution:

x= 26.9412. $F(x)$ = 30.8288

The various operations are developed by the realized "GUI" (shown in figure 6).

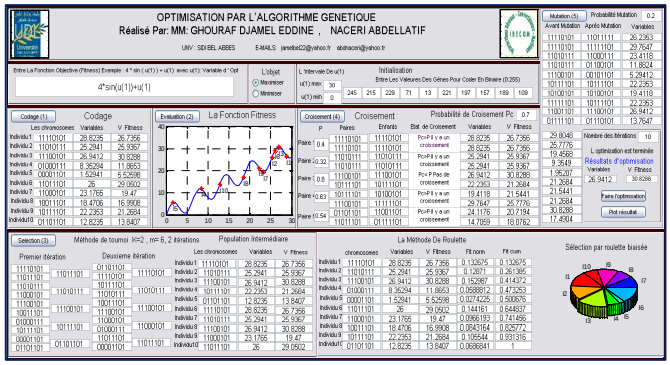

Fig. 6. The genetic algorithm operting developped under GUI / MATLAB

IV. Application of the Algorithm Genetic to Optimezed AVR-PSS

A) The Linear System Stability -analytical study

Recall that the damping factor ζ of method represented by its complex eigenvalue "λ" is given by:

$$\zeta = \frac{-\sigma}{\sqrt{\sigma^2 + \omega^2}} \quad (3)$$

With $\lambda = \sigma \pm j\omega$ (4)

A damping factor ζ leads to a significant well-damped dynamic response, all eigenvalues must be located in the left area of the complex plane defined by two half-lines. For a critical value of the damping factor ζcr: we impose a relative stability margin [10].

The real part of the eigenvalue σ determines the rapid decay / growth exponential dynamic response of the component system. Thus, σ very negative results in a fast dynamic response. To do this, all the eigenvalues must be located in the left area of the complex plane defined by a vertical through a critical value of the portion real (σ_{cr}: we defined as the absolute stability margin when setting the parameters of PSS, it is desirable that these two criteria are taken into account for proper regulation. The combination between these two criteria leads to an area called D; stability area [11], show in figure 7. Moving eigenvalues in this area ensures robust performance for a large number of points operated [12].

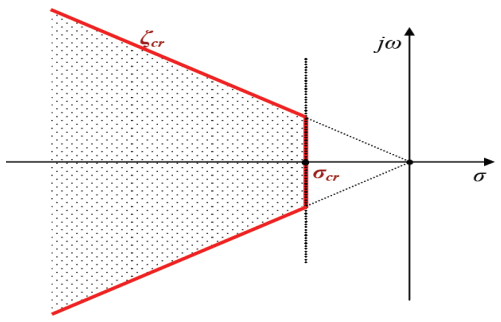

Fig. 7. D. Stability area

ISBN: 978-1-61804-216-3

B) objective function

The purpose of the PSS use is to ensure satisfactory oscillations damping, and ensure the overall system stability to different operation points. To meet this goal, we using a function composed of two multi-objective functions [13]. This function must maximize the stability margin by increasing damping factors while minimizing the system real eigenvalues . Therefore, all eigenvalues are in the D stability area, the multi-objective function calculating steps are:

1-formulate the linear system in an open –loop (without PSS);

2-locate the PSS and its parameters initialized by the G.A through an initial population;

3- Calculate the closed loop system eigenvalues and take only the dominant modes: $\lambda = \sigma \pm j\omega$

4- Find the system eigenvalues real parts (σ) and damping factor ζ;

5- Determine the (ζ) minimum value and the (- σ) maximum value, which can be formulated respectively as: (minimum (ζ)) and (maximum - (σ));

6- Gather both objective functions in a multi-objective function F as follows:

$F_{obj} = -\max(\sigma) + \min(\zeta)$

7- Return this Multi-objective function value the to the AG program to restart a new generation.

Figure 8 shows the proposed in this paper the GA for the AVR-PSS parameters optimization.

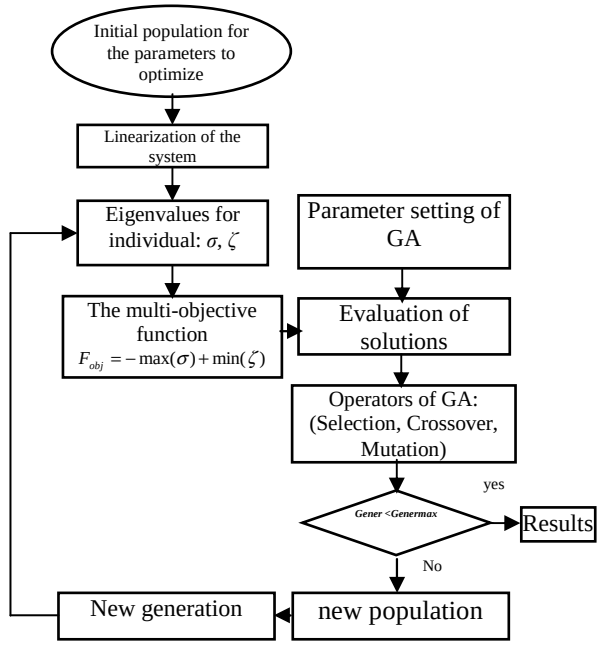

Fig. 8. The multi-objective function and AG program Flowchart for the PSS

Table 1 give a simulation result optimized PSS parameters with different SG

The optimized parameters for PSS are: K_{PSS}, T_W, T_1, and T_2

With

$5 \le K_{PSS} \le 150$

$0.01 \le T_w \le 0.05$

$0.01 \le T_1 \le 0.06$

$0.01 \le T_2 \le 0.065$

Number of Individuals = 120

Maximum Generation = 100

A crossing probability Pc = 0.7

A mutation probability Pm = 0.01

TABLE I. THE PSS OPTIMIZED PARAMETERS

parameters	TBB-200	TBB-500	BBC-720	TBB-1000
T_W	0.0321	0.029	0.0445	0.0234
T_1	0.054	0.0322	0.0356	0.0214
T_2	0.074	0.011	0.034	0.0142
K_{PSS}	51.43	15.45	100.548	15.506

V. THE SIMULATION RESULT UNDER GUI/ MATLAB

A) Creation of a calculating code under MATLAB / SIMULINK

The "SMIB" system used in our study includes:

- A synchronous generator (SG) ;
- Tow voltage regulators: AVR and AVR-PSS connected to;
- A Power Infinite network line

We used for our simulation in this paper, the SMIB mathematical model based on permeances networks model culled Park-Gariov [14], and shown in Figure 9 [14].

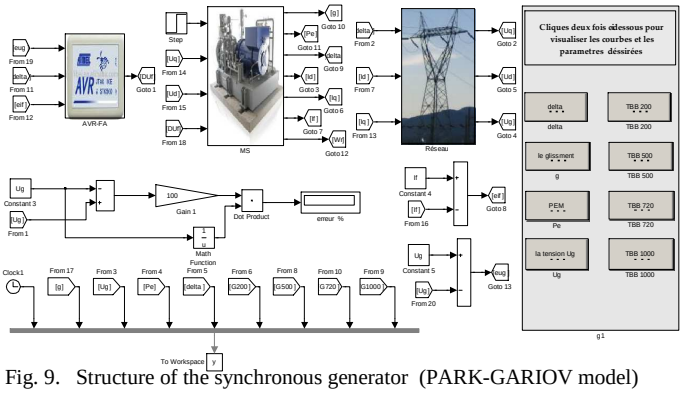

Fig. 9. Structure of the synchronous generator (PARK-GARIOV model) with the excitation controller under [14].

B) A Created GUI/MATLAB ….. Optimization using GA

To analyzed and visualized the different dynamic behaviors we have creating and developing a "GUI" (Graphical User Interfaces) under MATLAB .This GUI allows as to:

- Perform control system from PSS controller;
- To optimized the controller parameters by Genetic Algorithm;
- View the system regulation results and simulation;

ISBN: 978-1-61804-216-3

- Calculate the system dynamic parameters ;
- Test the system stability and robustness;
- Study the different operating regime (under-excited, rated and over excited regime).

The different operations are performed from GUI realized under MATLAB and shown in Figure 10.

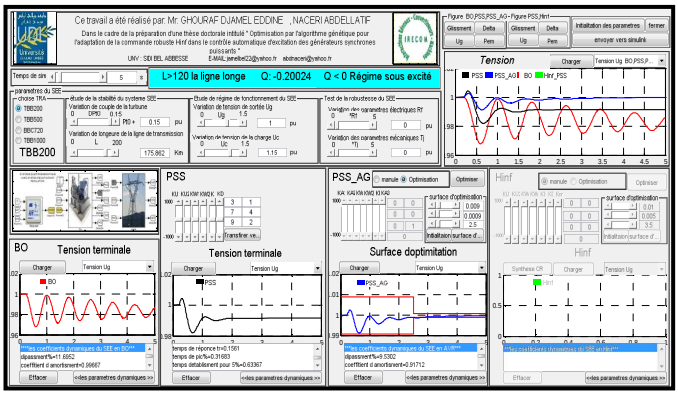

Fig. 10. The realised GUI / MATLAB

C) Simulation result and discussion

The following results (Table 2 and Figure 11, 12) were obtained by studying the "SMIB" static and dynamic performances in the following cases:

1. SMIB in open loop (without regulation) (OL)
2. Closed Loop System with the regulator AVR and conventional stabilizer PSS-FA [14].
3 - Optimization of Regulators PSS-AVR using genetic algorithm (PSS-OPT) parameters.

We simulated three operating: the under-excited, the rated and the over-excited.

Our study is interested in the Powerful Synchronous Generators of type: TBB-200, TBB-500 BBC-720, TBB-1000 (parameters in Appendix 2) [14].

Table 2 shows the dominant modes eigenvalues , for more details about the calculating parameters see GUI-MATLAB in the Appendix 3 created.

Table 3 presents the TBB -200 static and dynamic performances results in (OL) and (CL) with PSS and PSS-optimized, for an average line (Xe = 0.3 pu), and an active power P=0.85 p.u.

Where: α: Damping coefficient ε %: the static error, d%: the maximum overshoot, t_s: the setting time

TABLE II. THE EIGENVALUES OFF THIS SYSTEM

eigenvalues			
Q	**λ OL**	**λ PSS**	**λ PSS-OPT**
-0.1372	**instable**	**-1.6201 ± 4.3629i**	**-2.3283 ± 3.3747i**
-0.4571	**instable**	**-1.6503 ± 4.3582i**	**-2.3463 ± 3.9866i**
0.1896	**-0.0813 ± 7.2567i**	**-1.6865 ± 5.2802i**	**-2.3906 ± 2.9698i**
0.3908	**-0.1271 ± 7.9143i**	**-1.5379 ± 5.9476i**	**-2.3906 ± 2.9698i**
0.5078	**-0.1451 ± 8.2203i**	**-0.9432 ± 5.0531i**	**-1.9582 ± 3.2602i**
0.6356	**-0.1588 ± 8.5134i**	**-0.9283 ± 5.3747i**	**-1.9803 ± 3.5592i**

TABLE III. THE "SMIB "STATIC AND DYNAMIC PERFORMANCES

Damping coefficient α					**the static error**			
Q	**OL**	**AVR**	**PSS**	**PSS-OPT**	**OL**	**AVR**	**PSS**	**PSS-GA**
-0.1372	**Unstable**	**-0.709**	**-1.6201**	**-2.3283**	**instable**	**-2.640**	**-1.620**	**-1.234**
-0.4571	**Unstable**	**-0.708**	**-1.6503**	**-2.3463**	**instable**	**-2.673**	**-1.629**	**-1.241**
0.1896	**-0.0813**	**-0.791**	**-1.6865**	**-2.3906**	**-5.038**	**-2.269**	**-1.487**	**-1.267**
0.3908	**-0.1271**	**-0.634**	**-1.5379**	**-2.3906**	**-5.202**	**-1.807**	**-1.235**	**-1.129**
0.5078	**-0.1451**	**-0.403**	**-0.9432**	**-1.9582**	**-3.777**	**-0.933**	**-0.687**	**-0.604**
0.6356	**-0.1588**	**-0.396**	**-0.9283**	**-1.9803**	**-3.597**	**-0.900**	**-0.656**	**-0.567**
the setting time for 5%					**the maximum overshoot %**			
Q	**OL**	**AVR**	**PSS**	**PSS-OPT**	**OL**	**AVR**	**PSS**	**PSS-GA**
-0.1372	**Unstable**	**4,231**	**1,704**	**1,349**	**9.572**	**9,053**	**7,892**	**7,237**
-0.4571	**Unstable**	**4,237**	**1,713**	**1,323**	**9.487**	**9,036**	**7,847**	**7,219**
0.1896	**-**	**3,793**	**1,617**	**1,408**	**10,959**	**9,447**	**8,314**	**7,928**
0.3908	**-**	**4,732**	**1,706**	**1,630**	**10,564**	**8,778**	**7,883**	**7,659**
0.5078	**14,320**	**7,444**	**2,041**	**1,877**	**9,402**	**6,851**	**6,588**	**6,269**
0.6356	**14,423**	**7,576**	**2,080**	**1801**	**9,335**	**6,732**	**6,463**	**6,012**

In the Figures 11 and 12 show an example of simulation result with respectively 'Ug' the stator terminal voltage; 'Pe' the electromagnetic power system, 's' variable speed, 'delta' The internal angle TBB200 of Turbo-generator with P = 0.85, Xe = 0.5, Q1 = -0.1372 (pu)

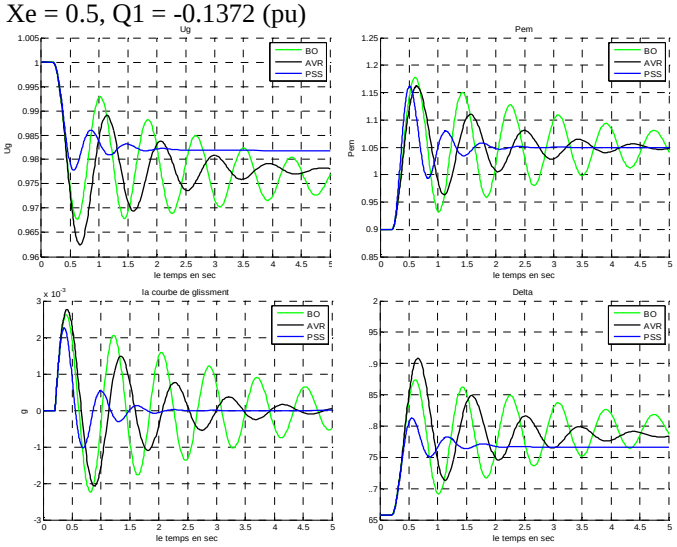

Fig. 11. functioning system in the under-excited of TBB 200 connected to a long line with AVR ,OL and PSS

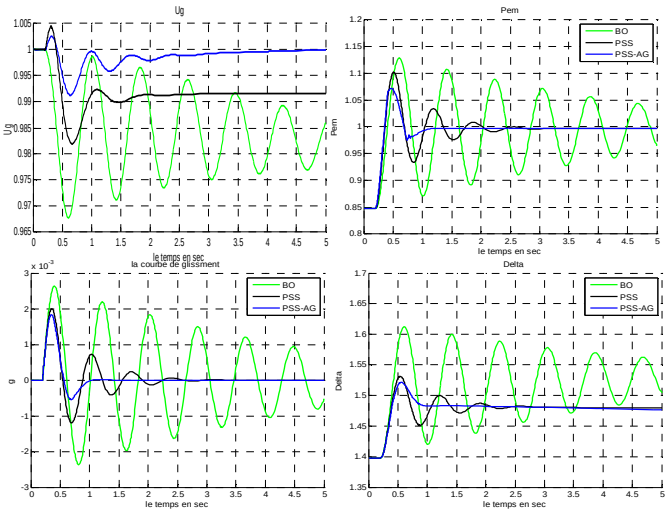

Fig. 12. functioning system in the under-excited used of TBB 200 connected to a long line with PSS , PSS- AG and OL

From the simulation results, it can be observed that the use of PSS optimized by AG improves considerably the dynamic performances (static errors negligible so better precision, and very short setting time so very fast system., and we found that after few oscillations, the system returns to its equilibrium state even in critical situations (specially the under-excited regime) and granted the stability and the robustness of the studied system.

VI. CONCLUSION

In this article, we have optimized the PSS parameters by genetic algorithms; these optimized PSS are used for powerful synchronous generators exciter voltage control in order to improve static and dynamic performances of power system.

This technique (GA) allows us to obtain a considerable improvement in dynamic performances and robustness stability of the SMIB studied.

All results are obtained by using our created GUI/MATLAB.

REFERENCES

[1] LA. GROUZDEV, A.A. STARODEBSEV, S.M. OUSTINOV "Conditions d'application des meilleurs amortissements des processus transitoires dans les systèmes énergétiques avec optimisation numérique des paramètres du régulateur AVR-FA" Energie -1990-N°ll-pp.21-25 (traduit du russe).

[2] DeMello F.P., Flannett L.N. and Undrill J.M., « Practical approach to supplementary stabilizing from accelerating power », *IEEE Trans.*, vol. PAS-97, pp, 1515-1522, 1978.

[3] Demello F.P. and Concordia C., « Concepts of synchronous machine stability as affected by excitation control », *IEEE Trans. on PAS*, vol. PAS-88, pp. 316–329, 1969.

[4] S. V. SMOLOVIK "Méthodes de modélisation mathématique des processus transitoires des générateurs synchrones plus usuels et non traditionnels dans les systèmes électro -énergétiques"Thèse doctorat d'état, Institut polytechnique de Leningrad, 1988 (traduit du Russe).

[5] P. KUNDUR, "Definition and Classification of power System Stability", Draft 2, 14 January,2002

[6] J.H. Holland, Adaptation in Natural and Artificial Systems, University of Michigan Press, 1975.

[7] P.M. ANDERSON, A. A. FOUAD "Power System control and Stability", IEE Press, 1991.

[8] Hong Y.Y. and Wu W.C., « A new approach using optimization for tuning parameters of power system stabilizers », IEEE Transactions on Energy Conversion, vol. 14, n°. 3, pp. 780–786, Sept. 1999.

[9] R. Asgharian "Asymptomatic approach to performance weights sélection in design of robust H∞PSS using genetic algorithms", IEEE trans. on EC, vol 11, No 21, September 1996, pp.111-11

[10] Allenbach J.M., Systèmes Asservis, Volume 1, Asservissements linéaires classiques, Ecole d'Ingénieurs de Genève, 2005.

[11] Yee S.K. and Milanović J.V., « Comparison of the optimisation and linear sequential method for tuning of multiple PSSs ». *IEEE Power Engineering Society, General Meeting Denver*, CO, June. 2004.

[12] Singh R., A Novel Approach for Tuning of Power System Stabilizer Using Genetic Algorithm, Ph.D. Thesis, Faculty of Engineering, Indian Institute of Science, Bangalore, July 2004.

[13] Hasan ALKHATIB ''ETUDE DE LA STABILITE AUX PETITES PERTURBATIONS DANS LES GRANDS RESEAUX ELECTRIQUES : OPTIMISATION DE LA REGULATION PAR UNE METHODE METAHEURISTIQUE'' Thèse doctorat d'état, UNIVERSITE PAUL CEZANNE D'AIX-MARSEILLE, 2008 .

[14] GHOURAF.D.E"Exploitation des techniques fréquentielles avancées dans le contrôle automatique d'excitation des machines synchrones" mémoire Magister ETT, op. convertisseur électromécanique, Dept. ETT, université SBA, 2009-20110 (Encadré par . Mr. NACERI).

APPENDIX

1. The PSS-AVR model

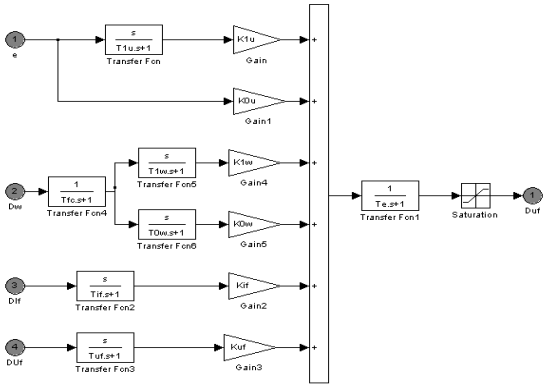

2. Parameters of the used Turbo –Alternators

Parameters	*TBB-200*	*TBB-500*	*BBC-720*	*TBB1000*	Units of measure
power nominal	**200**	**500**	**720**	**1000**	**MW**
Factor of power nominal	**0.85**	**0.85**	**0.85**	**0.9**	**p.u.**
X_d	**2.56**	**1.869**	**2.67**	**2.35**	**p.u.**
X_q	**2.56**	**1.5**	**2.535**	**2.24**	**p.u.**
X_s	**0.222**	**0.194**	**0.22**	**0.32**	**p.u.**
X_f	**2.458**	**1.79**	**2.587**	**2.173**	**p.u.**
X_{sf}	**0.12**	**.115**	**0.137**	**0.143**	**p.u.**
X_{sfd}	**0.0996**	**0.063**	**0.1114**	**0.148**	**p.u.**
X_{sf1q}	**0.131**	**0.0407**	**0.944**	**0.263**	**p.u.**
X_{sf2q}	**0.9415**	**0.0407**	**0.104**	**0.104**	**p.u.**
R_a	**0.0055**	**0.0055**	**0.0055**	**0.005**	**p.u.**
R_f	**0.000844**	**0.000844**	**0.00176**	**0.00132**	**p.u.**
R_{1d}	**0.0481**	**0.0481**	**0.003688**	**0.002**	**p.u.**
R_{1q}	**0.061**	**0.061**	**0.00277**	**0.023**	**p.u.**
R_{2q}	**0.115**	**0.115**	**0.00277**	**0.023**	**p.u.**

3. Dynamics parameters calculated through GUI-MATLAB

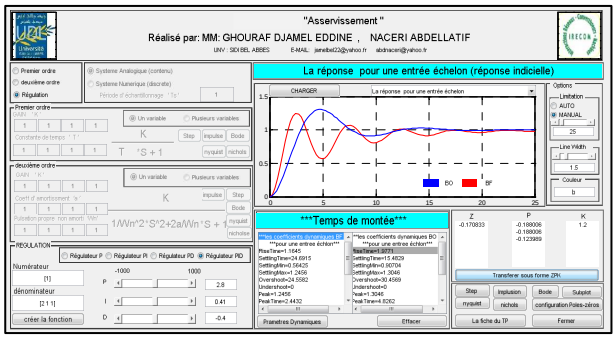

4. Power System model:

Currants equations:

$$I_d = \frac{U_q - E_q^{''}}{X_d^{''}} \quad I_d = \frac{-\left(U_d - E_d^{''}\right)}{X_q^{''}} \quad I_f = \frac{\left(\Phi_f - \Phi_{ad}\right)}{X_{sr}}$$

$$I_{1d} = \frac{\left(\Phi_{1d} - \Phi_{ad}\right)}{X_{srd}} \quad I_{1q} = \frac{\left(\Phi_{1q} - \Phi_{aq}\right)}{X_{sr1q}} \quad I_{2q} = \frac{\left(\Phi_{2q} - \Phi_{aq}\right)}{X_{sr2q}}$$

$$E_q^{''} = \frac{1/X_{sf} \cdot \frac{X_f}{X_{ad}} E_q^{'} + 1/X_{sfd} \cdot \frac{X_{fd}}{X_{ad}} E^{'}_{fq}}{\frac{1}{X_{ad}} + \frac{1}{X_{sf}} + \frac{1}{X_{sfd}}} \quad E_d^{''} = \frac{1/X_{sfq} \cdot \frac{X_{fq}}{X_{aq}} E^{'}_{fd}}{\frac{1}{X_{ad}} + \frac{1}{X_{sfq}}}$$

Flow equations:

$$\Phi_{ad} = E_q^{''} + \left(X_d^{''} - X_s\right) I_d \; ; \; \Phi_{aq} = E_d^{''} + \left(X_q^{''} - X_s\right) I_q$$

$$\Phi_{1q} = \omega_s \int_0^{\Phi_{1q}} \left(-R_{1q} I_{1q}\right) dt \quad \Phi_{2q} = \omega_s \int_0^{\Phi_{2q}} \left(-R_{2q} I_{2q}\right) dt$$

$$\Phi_f = \omega_s \int_0^{\Phi_f} \left(-R_f I_f + U_{f0}\right) dt \quad \Phi_{1d} = \omega_s \int_0^{\Phi_{1d}} \left(-R_{1d} I_{1d}\right) dt$$

Mechanical equations

$$d\delta = \left(\omega - \omega_s\right) dt \;\; , \;\; s = \frac{\omega - \omega_s}{\omega_s}$$

$$M_T + M_j + M_e = 0 \qquad \text{With} \quad \left(M_j = -j \frac{d\omega}{dt}\right)$$

$$T_j \frac{d}{dt} s + \left(\Phi_{ad} . I_q - \Phi_{aq} . I_d\right) = M_T \quad \text{ou} \quad T_j \frac{d}{dt} s = M_T - M_e$$

ISBN: 978-1-61804-216-3

Experimental Implementation of Encrypted Audio Messages in Real-Time

A. Arellano-Delgado*, C. Cruz-Hernández‡, R.M. López-Gutiérrez†, and O.R. Acosta-Del Campo*
*Information and Communication Technologies, Technological University of Tijuana (UTT)
Tijuana, BC, México 22253 Email: adrian.arellano@uttijuana.edu.mx, oscar.acosta@uttijuana.edu.mx
†Engineering, Architecture and Design Faculty, Baja California Autonomous University (UABC)
Ensenada, BC, México, 22860 Email: roslopez@uabc.edu.mx
‡Electronics and Telecommunications Department, Scientific Research and Advanced Studies of Ensenada (CICESE)
Ensenada, BC, México, 22860 Email: ccruz@cicese.mx
Tel.: +52 646 1750500; fax: +52 646 1750554.

***Abstract*—This work presents the experimental implementation of encrypted messages in real-time. Particularly, we use the Hénon chaotic map. Synchronization is implemented to achieve secure transmission and reception of confidential audio messages in real-time.**

***Keywords*—Synchronization, encryption, real-time systems, chaos, discrete-time systems, secure communications.**

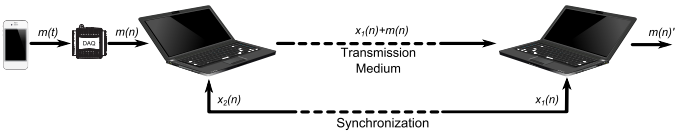

Fig. 1. Diagram of a communications system.

I. Introduction

In past decades, chaotic synchronization has received a tremendous increasing interest, see e.g. [1]-[7] and references therein. This property is supposed to have interesting applications in different fields, particularly to design private/secure communication systems, see e.g. [4], [5], [7]-[16]; in which the confidential information is encrypted into the transmission chaotic signal by direct modulation, masking, or another technique. At the receiver end, if chaotic synchronization can be achieved, then it is possible to extract the hidden information from the transmitted signal. Discrete systems are ideal candidates for experimental realization in secure communications. Particularly interesting is the scenario where the connected nodes have chaotic behavior. Synchronization in complex dynamical networks has direct applications in different fields, see e.g. [11], [17]. Promising results on synchronization of coupled chaotic nodes in different topologies are reported in [7], [11], [17]. However, synchronization in two coupled systems has direct application in communications, where is possible to transmit information from a single transmitter to single receiver.

The purpose of this experimental implementation is transmit a message (audio) in real-time through a public channel and prevent that intruders can decipher it. In other words, we want to send a message through a public channel securely in real-time. Fig. 1 shows the diagram of a communications system with a transmitter and a receiver, where the encrypted message is sent via a transmission medium which may be a public channel.

At the transmitter, the message is introduced to the PC through data acquisition card. Inside the computer, the encrypted message is obtained by summing the audio message to one state of the chaotic system, which is developed in Labview. To recover the encrypted message, the transmitter and receiver must be synchronized unidirectionally or bidirectionally. Once synchronization is achieved, we can send the encrypted message via the public channel. At the receiver, the recovered message is reproduced or stored in a unit.

This implementation has potential application in telecommunications, mainly in where security is required for the transmission of audio messages (civilian and military).

In this work, we concentrate on experimental synchronization of two linearly coupled identical discrete systems, using techniques reported in [19], [20] where synchronization in complex networks is shown analytically. The main goal of this work is the experimental implementation of encrypted audio messages in real-time by using two Hénon maps operating in chaotic regime. We have constructed two scenarios: (i) to obtain network synchronization of two coupled chaotic Hénon maps, considering a bidirectional coupling. This objective is achieved by using recent results from complex systems theory. In addition, (ii) to transmit encrypted confidential (audio) messages from a transmitter to receiver in real-time. Both goals are achieved with experimental implementation by using the software Labview.

II. Preliminaries

In this section, we give a brief review on complex dynamical networks, in particular of discrete systems and its synchronization.

A. Synchronization of complex networks

We consider a complex network composes of N identical nodes, linearly and diffusively coupled through the first state of each node. In this network, each node constitutes a m-dimensional dynamical system, described as follows

ISBN: 978-1-61804-216-3

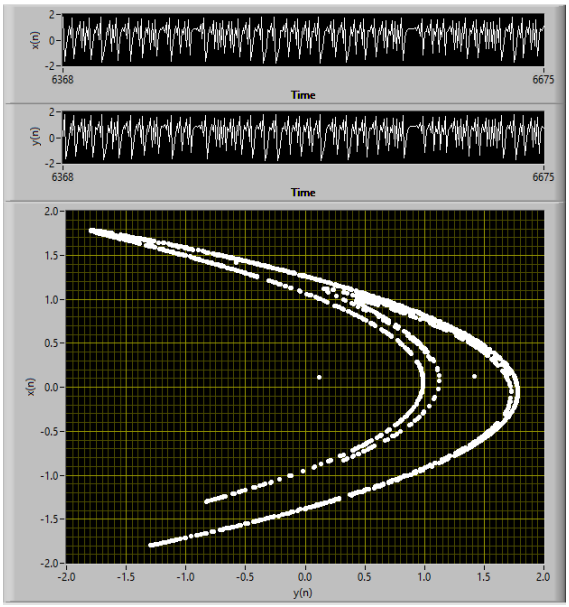

Fig. 2. Temporal dynamics and chaotic attractor of Hénon map.

$$
\begin{aligned}
x_{i1}(n+1) &= f_1(\mathbf{x}_i(n)) + c\sum_{J=1}^{N}(a_{ij}x_{j1}^2(n)), \quad i = 1, 2, ..., N,\\
x_{i2}(n+1) &= f_2(\mathbf{x}_i(n)),\\
&\vdots\\
x_{im}(n+1) &= f_k(\mathbf{x}_i(n)),
\end{aligned} \tag{1}
$$

where $\mathbf{x}_i(n) = (x_{i1}(n), x_{i2}(n), ..., x_{im}(n))^T \in R^m$ are the state variables of the node i, the constant $c > 0$ represents the coupling strength among the discrete nodes and $\mathbf{A} = (a_{ij})_{N\times N}$ is the coupling matrix, which represents the coupling topology of the complex network. If there is a connection between node i and node j, then $a_{ij} = 1$; otherwise, $a_{ij} = 0$ for $i \neq j$. The complex network (1) is said to achieve (asymptotically) synchronization, if [18]:

$$
\mathbf{x}_1(n) = \mathbf{x}_2(n) = \ ... \ = \mathbf{x}_N(n), \ \text{as}\, n \to \infty. \tag{2}
$$

B. Hénon map like node

In this section, we describe the Hénon map used like transmitter and receiver to construct the experimental implementation. The objective of this work is to achieve experimental synchronization with the purpose of implement a chaotic communication system in real-time. The Hénon map difference equations used in the implementation are described by [21]

$$
\begin{aligned}
x(n+1) &= \alpha + \beta y(n) - x^2(n),\\
y(n+1) &= x(n).
\end{aligned} \tag{3}
$$

In order to generate chaotic dynamics in Eq. (3), the parameter values are; $\alpha = 1.4$ and $\beta = 0.3$ and initial conditions, $x(0) = 0.11$ and $y(0) = 0$, the chaotic dynamics and chaotic attractor are shown in Fig. 2. In Fig. 3 we can observe the block diagram for the realization of graphs in Fig. 2.

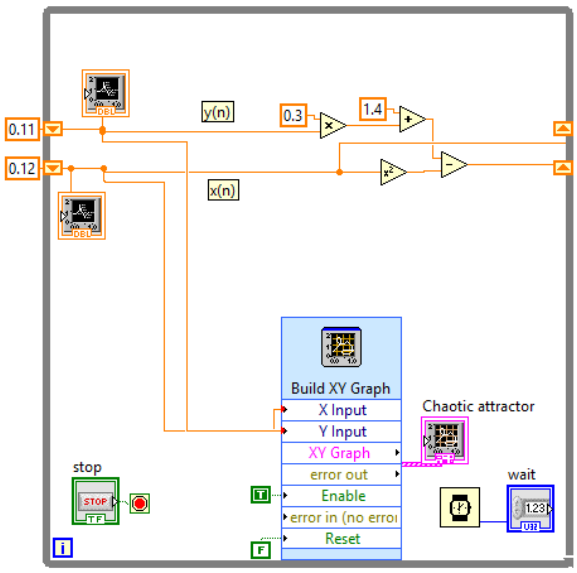

Fig. 3. Block diagram for implementation of a Hénon map as isolated node.

Fig. 4. Two Hénon maps nodes bidirectionally coupled.

III. Synchronization of two Hénon maps

In this section, we describe the synchronization of two Hénon maps. The two coupled Hénon maps takes the following form according to Eq. (1). The first node N1 in the coupling is described as follows,

$$
\begin{aligned}
x_1(n+1) &= \alpha + \beta y_1(n) - x_1^2(n) + c(2x_1^2(n) - x_2^2(n)),\\
y_1(n+1) &= x_1(n),
\end{aligned} \tag{4}
$$

the second node N2 is given by

$$
\begin{aligned}
x_2(n+1) &= \alpha + \beta y_2(n) - x_2^2(n) + c(2x_2^2(n) - x_1^2(n)),\\
y_2(n+1) &= x_2(n),
\end{aligned} \tag{5}
$$

Now, by using Eqs. (4) and (5) as chaotic nodes, we have constructed the network with two Hénon maps nodes to be synchronized according to Fig. 4. Fig. 5 shows synchronization between node N1 and node N2 choosing a coupling force $c = 0.8$ arbitrary according by [22]. We can observe a transient error of approximately 0.1 seconds in $x_1(n) - x_2(n)$ since the initial conditions of the two Hénon maps are different. The parameter values, $\alpha = 1.4$ and $\beta = 0.3$ are the same for two Hénon maps but initial conditions for node N1 are $x_1(0) = 0.11$ and $y_1(0) = 0$ and for node N2 are $x_2(0) = 0.12$ and $y_2(0) = 0$.

IV. Experimental implementation of real-time encryption

This section presents the experimental implementation for encryption of audio messages in real-time.

ISBN: 978-1-61804-216-3

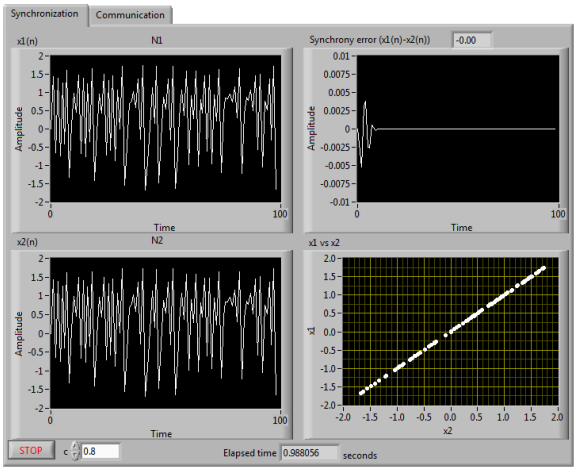

Fig. 5. Synchronization between two Hénon maps with coupling strength $c = 0.8$, $x_1(n)$, $x_2(n)$, synchrony error $x_1(n) - x_2(n)$ and phase diagram x_1 *vs* x_2.

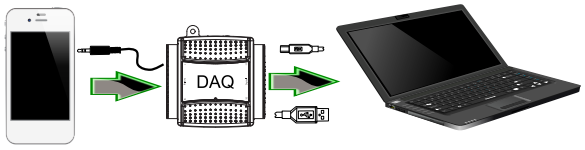

Fig. 6. Schematic diagram of the implementation for the encryption of audio messages in real-time.

A. *Implementation details*

In the experimental implementation, we used the following devices; data acquisition card NI DAQ 6009, computer with AMD A4 processor quad core with 4 Gb of RAM, mobile device (we can use any device that generates an audio signal to 3.5mm TRS connector) and Labview software. Fig. 6 shows the block diagram of the experimental implementation, where we get an audio signal from the mobile device denoted m which can be, stored music, prerecorded message, or a conversation made in this moment (in this experimental implementation, we use an instrumental music portion like audio message) which is sent to the computer using the DAQ. Once in the computer, the confidential information m is encrypted by direct modulation with the chaotic signal and is transmitted by a public channel, arrives at the receiver and is decrypted by calculating the difference $x_2 - x_1 + m$. For illustrative purposes, the recovered message m' is obtained inside the same computer (we are working on the step of sending to different computers). Fig. 7 shows the graphs of the message to encrypt m, encrypted message $x_1 + m$, recovered message $m' = x_2 - x_1 + m$ and the error between messages sent and recovered $m - m'$. Moreover, Fig. 8 shows the block diagram of the experimental implementation of encrypted audio messages in real-time.

V. Conclusion

We have presented experimental network synchronization between two chaotic Hénon maps using Labview programming software. Synchronization was obtained by using complex systems theory and was applied to encrypt audio messages from chaotic transmitter to a receiver; for this purpose, we have used the NI DAQ 6008 for adequate the signal m and

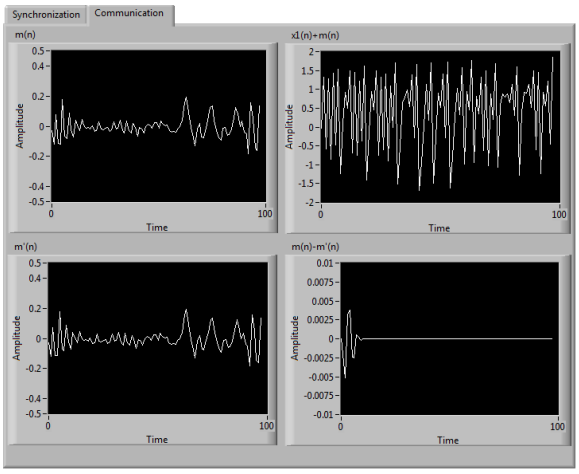

Fig. 7. Message to encrypt $m(n)$, encrypted message $x_1(n) + m(n)$, recovered message $m'(n)$, and error between $m(n)$ and $m'(n)$.

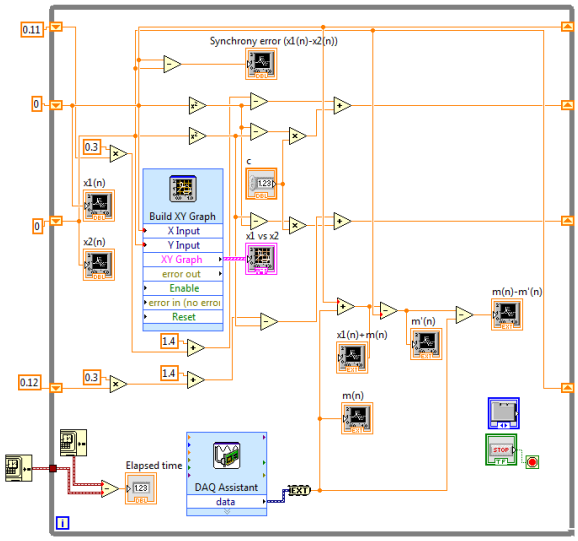

Fig. 8. Block diagram of the implementation for the encryption of audio messages in real-time.

be able to send to the computer. The obtained experimental results (for only illustrative purposes) have shown that it is possible networks synchronization, encrypted, transmission, and recovery of encrypted audio messages in real-time by using the software Labview.

Acknowledgment

This work was supported by the CONACYT, Mexico under Research Grant No. 166654.

References

[1] L.M. Pecora, T.L. Carroll, Synchronization in chaotic systems, *Phys. Rev. Lett.* 64 (1990) 821-824.

[2] C. Cruz-Hernández, H. Nijmeijer, Synchronization through filtering, Int. J. Bifurcat. Chaos 10 (4) (2000) 763-775.

[3] H. Sira-Ramírez, C. Cruz-Hernández, Synchronization of chaotic systems: a generalized Hamiltonian systems approach, *Int. Bifurcat. Chaos* 11 (5) (2001) 1381-1395.

[4] D. López-Mancilla, C. Cruz-Hernández, Output synchronization of chaotic systems: model matching approach with application to secure communication, *Nonlinear Dyn. Syst. Theory* 5 (2) (2005) 141-156.

[5] U. Feldmann, M. Hasler, W. Schwarz, Communication by chaotic signals: the inverse system approach, *Int. J. Circ. Theory Appl.* 24 (5) (1996) 551-579.

[6] H. Nijmeijer, I.M.Y. Mareels, An observer looks at synchronization, *IEEE Trans. Circ. Syst.* I 44 (10) (1997) 882-890.

[7] C. Cruz-Hernández, A.A. Martynyuk, Advances in Chaotic Dynamics with Applications, vol. 4, *Cambridge Scientific Publishers*, London, 2010.

[8] K.M. Cuomo, A.V. Oppenheim, Circuit implementation of synchronized chaos with applications to communications, *Phys. Rev. Lett.* 71 (1993) 65-68.

[9] C. Cruz-Hernández, D. López-Mancilla, V. García, H. Serrano, R. Núñez, Experimental realization of binary signal transmission using chaos, *J. Circ. Syst. Comput.* 14 (3) (2005) 453-468.

[10] C. Cruz-Hernández, Synchronization of time-delay Chua's oscillator with application to secure communication, *Nonlinear Dyn. Syst. Theory* 4 (1) (2004) 1-13.

[11] C. Posadas-Castillo, R.M. López-Gutiérrez, C. Cruz-Hernández, Synchronization of chaotic solid-state Nd:YAG lasers: application to secure communication, *Commun. Nonlinear Sci. Numer. Simul.* 13 (8) (2008) 1655-1667.

[12] L. Gámez-Guzmán, C. Cruz-Hernández, R.M. López-Gutiérrez, E.E. García-Guerrero, Synchronization of Chua's circuits with multi-scroll attractors: application to communication, *Commun. Nonlinear Sci. Numer. Simul.* 14 (6) (2009) 2765-2775.

[13] C. Cruz-Hernández, N. Romero-Haros, Communicating via synchronized timedelay Chua's circuits, *Commun. Nonlinear Sci. Numer. Simul*. 13 (3) (2008) 645-659.

[14] K. Kusumot, J. Ohtsubo, 1.5-GHz message transmission based on synchronization of chaos in semiconductor lasers, *Opt. Lett*. 27 (2002) 989- 991.

[15] M.W. Lee, J. Paul, S. Sivaprakasam, K.A. Shore, Comparison of closed-loop and open-loop feedback schemes of message decoding using chaotic laser diodes, *Opt. Lett.* 28 (2003) 2168 2170.

[16] J. Paul, S. Sivaprakasam, K.A. Shore, Dual-channel chaotic optical communications using external-cavity semiconductor lasers, *J. Opt. Soc. Am. B* 21 (2004) 514-521.

[17] X.F. Wang, G. Chen, Synchronization in small-world dynamical networks, *Int. J. Bifurcat. Chaos* 12 (1) (2002) 187-192.

[18] X.F. Wang, Complex networks: topology, dynamics and synchronization, *Int. J. Bifurcat. Chaos* 12 (5) (2002) 885-916.

[19] V. Spirin, C.A. López-Mercado, S.V. Miridonov, L. Cardoza-Avendaño, R.M. López-Gutiérrez, C. Cruz-Hernández, Elimination of low-frequency fluctuations of backscattered Rayleigh radiation from optical fiber with chaotic lasers, *Opt. Fiber Technol.* 17 (2011) 258-261.

[20] C. Posadas-Castillo, C. Cruz- Hernández, R.M. López-Gutiérrez, Experimental realization of synchronization in complex networks with Chua's circuits like nodes, *Chaos Solitons Fractals* 40 (4) (2009) 1963-1975

[21] Dmitriev A. S., G. A. Kassian, Khilinsky A. D. "Chaotic synchronization of Hénon mappings: the information approach", *Technical Physics Letters* 28 (2002) 5.

[22] T. Kreuz, F. Mormann, R.G. Andrzejak. "Measuring synchronization in coupled model systems: A comparison of different approaches", *Physica D* 225 (2007) 2942.

Substrate Integrated Waveguide (SIW) to Microstrip Transition at X-Band

Muhammad Imran Nawaz, Zhao Huiling
Northwestern Polytechnical University
Xi'an, Shaanxi, China.

Muhammad Kashif
NESCOM
Islamabad, Pakistan

***Abstract*— Substrate integrated waveguide (SIW) is a new form of transmission line. It facilitates the realization of non-planar (waveguide based) circuits into planar form for easy integration with other planar (microstrip) circuits and systems. This paper describes the design of an SIW to microstrip transition. The transition is broadband covering the frequency range of 8 – 12GHz. The measured in-band insertion loss is below 0.6dB while the return loss is less than 10dB. The circuit is simulated in HFSS and results are measured on vector network analyzer (VNA).**

***Keywords*— Microstrip; Substrate Integrated Waveguide; Transition**

I. INTRODUCTION

Substrate Integrated Waveguide (SIW) technology has provided a new approach in the design of microwave and millimeter-wave systems. It is replacing the traditional hybrid systems which are combination of both waveguides and stripline circuits. Using SIW, rectangular waveguide based non-planar circuits can be synthesized into planar form with a dielectric substrate having two parallel arrays of via-holes analogous to waveguide metallic side walls. The whole systems, combination of passive components (filters, couplers, diplexers, mixers etc), active elements (amplifiers, oscillators etc) and antennas can be made on same substrate. Two such systems, 24GHz radar and 60GHz active radio front-end are reported in [1]. The SIW based systems have several advantages: 1) Cost effective, 2) Easy to fabricate, 3) No bulky transitions between elements, thus reducing losses and parasitics, 4) Provide inherent shielding from outer environment, and 5) Considerably reduce packaging, EMC/EMI, interconnect and assembly problems that are of major concern in current microwave and millimeter equipment and systems.

In HMICs (hybrid microwave integrated circuits), the transition is an important bridge between non-planar and planar circuits. This transition is often very costly, bulky in size and often requires run-time tuning which is a cumbersome task. The synthesis of a non-planar waveguide in substrate permits the realization of efficient wideband transitions between the synthesized non-planar waveguide and planar circuits such as microstrip and coplanar waveguide (CPW) integrated circuits. With these transitions, the complexity and cost of interconnection between non-planar high-Q circuits and planar circuits are reduced to a minimum [2].

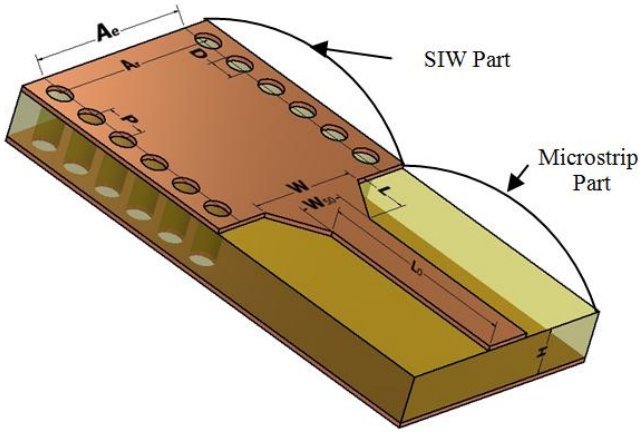

Fig. 1. SIW to Microstrip Transition Design Scheme

This paper presents the design of an SIW to microstrip transition. The desired band of frequencies is X-band. The taper line is utilized as impedance transformation between SIW and 50 ohm microstrip line. The effect of taper line length is observed on circuit performance. Rogers's 4350B substrate having relative permittivity of 3.48, loss tangent 0.0037 and 0.762 mm height is preferred because of its rigidity [8].

The remaining paper is organized as follows. The theoretical design of transition is discussed in section II. In section III modeling and simulation of transition is described while circuit fabrication and results are discussed in section IV. The work is finally concluded in section V.

II. DESIGN DESCRIPTION

The SIW to Microstrip transition consists of two parts; one is SIW part and the other is microstrip part as shown in Fig 1. The design of each part involves specific equations and design criteria which is briefly discussed in the subsequent paragraphs.

A. SIW Design

The substrate integrated waveguide (SIW) is sort of a guided transmission line just like a dielectric filled rectangular waveguide. Its dominant mode cut-off frequency is same as TE_{10} mode of rectangular waveguide. The only difference is that the metallic walls are replaced by two parallel arrays of conductive via holes. The key parameters of SIW design are spacing between the vias "P" also called pitch, diameter of

ISBN: 978-1-61804-216-3

vias "D", central distance between via arrays "A_r" also called integrated waveguide width, and the equivalent SIW width "A_e".

The SIW parameters should be designed carefully. The pitch "P" and diameter "D" control the radiation loss and return loss, while the integrated waveguide width "A_r" determine the cut-off frequency and propagation constant of the fundamental mode [3]. There are two design rules related to the pitch and via diameter as given by [4]:

$$D < \lambda_g / 5 \quad (1)$$

$$P \le 2D \quad (2)$$

Where λ_g is the guide wavelength in the SIW.

The cut-off frequency of an SIW can be determined by [5]:

$$f_c = \frac{c}{2\sqrt{\varepsilon_r}}\left(A_r - \frac{D^2}{0.95P}\right)^{-1} \quad (3)$$

Where c is the speed of light in vacuum and ε_r is the relative permittivity of dielectric material.

The equivalent SIW width "Ae" is the width of rectangular waveguide whose modes exhibit the same propagation characteristics of the SIW modes [5]. It can be found by:

$$A_e = \frac{a}{\sqrt{\varepsilon_r}} \quad (4)$$

Where "a" is the broadside dimension of an air filled rectangular waveguide as shown in Fig.2.

Using (4), integrated waveguide width can be found by [6]

$$A_r = A_e + \frac{D^2}{0.95P} \quad (5)$$

After discussing the design details, next we move onto the design of an X-band SIW. The WR-90 is the standard X-band rectangular waveguide with dimensions:

a= 22.86 mm and b= 10.16mm.

From this using (4), the equivalent SIW width comes out to be 12.25mm on Roger's 4350B substrate. The via diameter is chosen to be 0.61mm and pitch chosen as 1.5*D= 0.91mm following rules (1) & (2).

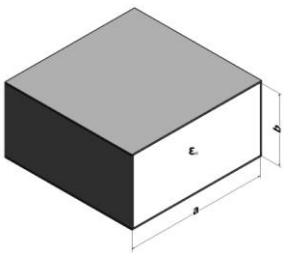

Fig. 2. Standard Rectangular Waveguide

B. Microstrip Part Design

The microstrip portion consists of series combination of quarter-wave tapered transformer and a 50 ohm track as shown in Fig 1. The transformer transforms the SIW impedance to the standard 50 ohm microstrip impedance. The 50 ohm track is added for interconnection of the I/O connectors. The key design parameters in this part are the length of tapered line "L" and width "W" of the taper at SIW end.

The width "W" of taper line can found by solving (6) [7]:

$$\frac{120\pi}{\eta H\left[\frac{W}{H}+1.393+0.667\ln\left(\frac{W}{H}+1.444\right)\right]} = \frac{4.38}{A_e}e^{-0.627\frac{\varepsilon_r}{\frac{\varepsilon_r+1}{2}+\frac{\varepsilon_r-1}{2\sqrt{1+\frac{12H}{W}}}}} \quad (6)$$

Where η is the free space intrinsic impedance having value 377 ohm.

The equation (6) is a complex equation and cannot be solved analytically. However, it can be solved numerically with the aid of some software e.g. Mathematica.

The taper length "L" is given by

$$L = \frac{n\lambda_g}{4}, n = 1,2,3,4..... \quad (7)$$

and

$$\lambda_g = \frac{c}{f\sqrt{\varepsilon_r}} \quad (8)$$

Where f is the design frequency.

Using (6), the width of taper comes out be 3.51mm for 0.762mm height of the substrate while using (7) & (8), taper length is found to be 4.1mm for n=1 at 9.8GHz. The taper length is related to the return loss of the structure which will be discussed in the next section.

III. Modeling and Simulation

Due to un-availability of SIW probes currently, its not possible to test the SIW to microstrip transition. However, if two transitions are joined back to back then the structure can be tested with existing standard instruments. Due to symmetry, the total insertion loss can simply be halved to get insertion loss for one transition. Therefore, based on the calculations in the previous section, a back-back transitions structure is modeled in HFSS software as shown in Fig 3.

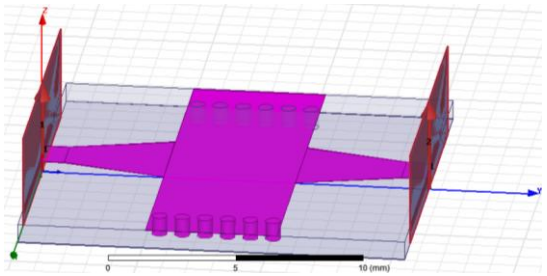

Fig. 3. Back to Back Transitions Simulation Model

ISBN: 978-1-61804-216-3

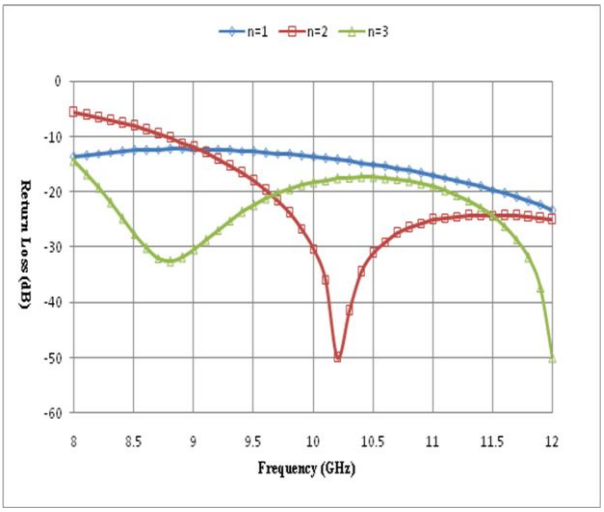

Fig. 4. Return Loss as a function of Taper Length

It is notable that the length of the taper line controls the return loss of the structure. It is already mentioned that the taper length is integer multiple of guided quarter wavelength λ_g. Fig. 4 analyzes the effect of taper length on return loss. It is seen that the return loss improves as the length is 2*quarter wavelength or 3* quarter wavelength. However, the band response becomes narrower for higher integer values, so an optimized value is to be selected according to the requirements.

IV. Fabrication and Results

Fig. 5 shows the picture of the fabricated back-back transitions structure. SMA connectors are used for the input and output ports. The vias are filled using Plated Through Hole (PTH) technique.

The circuit is tested using Vector Network Analyzer (VNA). The measured results are compared with the simulation results as shown in Fig. 6. Overall the measured results are acceptable. The simulated insertion loss for SIW-to- Microstrip transition is below 0.2dB while the measured value is below 0.6dB in the whole X-band i.e. 8 – 12GHz. The measured value of return loss is below 10dB as in simulation, although the two curves do not follow each other exactly.

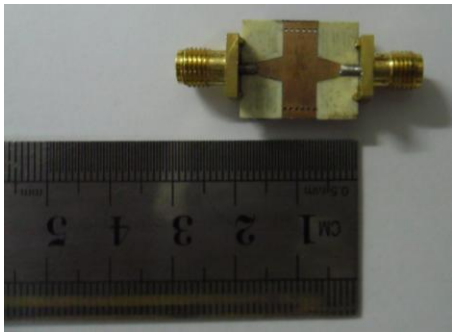

Fig. 5. Fabricated Circuit

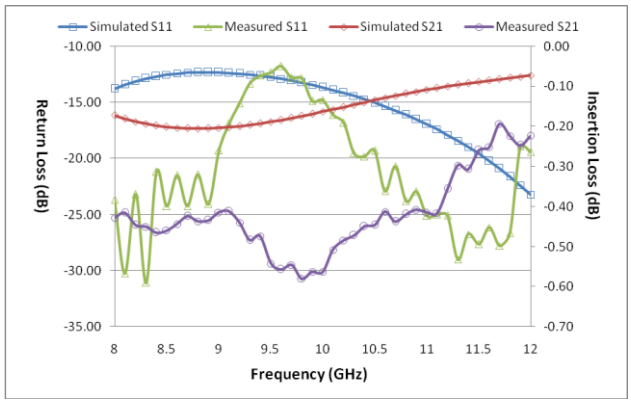

Fig. 6. Comparison of Simulated and Measured S_{11} and S_{21}

The discrepancy in the simulated and measured results can be attributed to the improper filling of via holes, deviation of dielectric loss tangent of the substrate, and, losses from SMA connectors and soldering (not considered in simulation).

V. Conclusions

This paper describes the design of an SIW-to-Microstrip transition at X-band. The tapered microstrip transmission line is utilized for matching purposes. The key design parameters are discussed along with the governing mathematical equations. The measured insertion loss of transition is below 0.6dB and return loss is below 10dB in the whole band. This transition is useful for X-band substrate integrated circuits and systems and also working band can be extended to millimeter wave frequencies as well.

References

[1] Ke Wu, "Substrate Integrated Circuits (SiCs) – A Paradigm for Future Ghz and Thz Electronic and Photonic Systems", IEEE Circuits and Systems Society Newsletter, Volume 3, Issue 2, April 2009.

[2] Maurizio BOZZI , Luca PERREGRINI, Ke WU and Paolo ARCIONI, "Current and Future Research Trends in Substrate Integrated Waveguide Technology", Radio Engineering, Volume 18, No.2, June 2009.

[3] Dominic Deslandes and Ke Wu, "Single-Substrate Integration Technique of Planar Circuits and Waveguide Filter", IEEE Transactions on Microwave Theory and Techniques, VOL. 51, NO. 2, February 2003.

[4] Dominic Deslandes and Ke Wu, "Design Consideration and Performance Analysis of Substrate Integrated Waveguide Components", Microwave Conference, 2002, 32nd European.

[5] Maurizio Bozzi , Feng Xu, Dominic Deslandes and Ke WU, "Modeling and Design Considerations for Substrate Integrated Waveguide Circuits and Components", TELSIKS 2007, Serbia, Nis, September 26-28.

[6] M. Bozzi, A. Georgiadis and K. Wu, "Review of Substrate Integrated Waveguide Circuits and Antennas", Special Issue on RF/Microwave Communication Subsystems for Emerging Wireless Technologies. 2010.

[7] Dominic Deslandes, "Design Equations for Tapered Microstrip-to-Substrate Integrated Waveguide Transitions", IMS 2010.

[8] http://www.rogerscorp.com/documents/726/acm/RO4000-Laminates---Data-sheet.pdf

ISBN: 978-1-61804-216-3

Speech and Sensors in Improving the Guidance of an Electric Wheelchair by Handicapped Persons

Mohamed Fezari and Ibrahiem M. El-Emary

***Abstract*-**Many people with disabilities do not have the necessary ability to control a joystick on an electric wheelchair. Moreover, they have difficulty to avoid obstacles. The aim of this work is to implement a multi-modal system to control the movement of an Electric wheelchair using small vocabulary word recognition system and a set of sensors to detect and avoid obstacles. In this work we adopted the use of a microcontroller , a DSP processor and a hardware speech recognition module for isolated word from a dependent speaker. To give the user more security, we included on the electric wheelchair a set of sensors in order to avoid obstacles. To gain in time design, tests have shown that it would be better to choose a speech recognition kit and to adapt it to the application.

Keywords: Voice command, ultrasonic sensors, microcontroller, wheelchair command, HPEWC (Handicapped Person Electric Wheelchair).

1. INTRODUCTION

Despite rapid scientific and technological progress in assistive devices for people with motor disabilities disciplines, there has been very little innovation in wheelchair design over the last 200 years. The folding wheelchair came in 1933, and powered wheelchair was developed in the early 1970s. New material such as plastics, fiber-reinforced composites and beryllium-aluminum alloys have found their way into the design and manufacture of lighter, stronger and more reliable wheelchair [1]. The wheelchair industry has also benefited from the development of lighter, efficient, durable and reliable motors, better amplifiers and controllers and most important of all superior batteries. In addition, with the exponential increase in computing power and shrinkage of size and cost, the microcontroller is finding its way into every aspect of human life. It's used as examples in a wide spectrum of applications such as auto assembly plant, data handling and acquisition systems, stepper motor control, robotic control, and bio-control systems [2]. However speech recognition has a key role in many application fields [3–6]. Various studies made in the last few years have given good results in both research and commercial applications [7–9].

Mohamed Fezari Author is with Badji Mokhtar Annaba University,Faculty of engineering, bp:12, 23000 Algeria. , Email:mohamed.fezari@uwe.ac.uk
Ibrahim M. M. El-Emary Author is with faculty of IT, King Abdulaziz University, Saudi Arabia, Email: Omary57@hotmal.com

This paper proposes a new approach to the problem of a better control for the electric wheelchair using a speech recognition development kit from "sensory" [10] and implements it for vocal command of a HPEWC (Handicapped Person Electric WheelChair) [11–15]. The study is part of a specific application concerning system control by simple vocal commands. It has to be implemented on a portable system and has to be robust to any background noise confronted by the system. The object of this design is therefore the recognition of isolated words from a limited vocabulary in the presence of background noise. This application is speaker-dependent. It should however, be pointed out that this limit does not depend on the overall approach but only on the method with which the reference patterns were chosen. So leaving the approach unaltered and choosing the reference patterns appropriately can make the application made speaker-independent. To enhance the designed system by avoiding obstacles and secure the wheelchair driver, a set of ultrasonic sensors for obstacle detection were used [16–18].

The application to be integrated in this embedded system is first simulated using MPLAB, then implemented in a RISC architecture microcontroller adapted to a speech recognition development kit "Voice Direct 364" (VD364). Experimental tests showed the validity of the new hardware adaptation. To detect front and each side obstacles, better position for ultrasonic sensors on the wheelchair were found. Implementation tests of the designed system gave good results within the experience area.

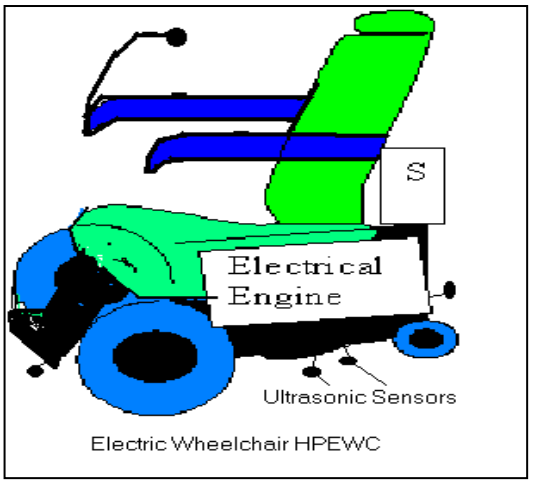

Fig. 1:HPEWC with sensors and mic position

II. GENERAL DESCRIPTION OF THE DESIGNED EMBEDDED SYSTEM

The designed System as shown in Figure 2 is developed around the following components:

- The VR-Stamp based on RSC4128 special processor, which is the heart of the vocal command system [6].
- A DSP TMS320C6711, to eliminate echos and background noises based on Kalman-filter.
- A microcpontroller PIC18F252 as a main processor.
- A special designed keyboard with eleven switches (two for each motor: one for rotation in one direction and the other for the other direction) and one for the stop command.
- Bluetooth module Rok101007 from Ericsson Microelectronics.
- Set of ultrasonic sensors to cover the movement of the electric wheelchair HPEWC.

These components are controlled by a CMOS-RISC microcontroller from Microchip, a new generation of powerful computation, low-cost, low-power microcontrollers. The client-system is fed by a rechargeable Li+ battery as a power supply.

The application is based on the development of a vocal command for HPEWC, by means of simple vocal messages. It therefore involves the recognition of isolated words from a limited vocabulary.

The HPEWC specifications are ten commands that are necessary to control the wheelchair: Switching on and off the engine, forward movement, backward movement, stop engine, turn left, turn right, speed up, speed down, lights on or off and horn on or off.

The vocabulary chosen to control the system contains a total often words. The number of words in the vocabulary was kept to a minimum to make the application simpler and easier for the user. However, this number can be increased if any improvement is necessary such as adding words to control a horn or lights installed on the HPEWC. The selected ten words are from a arabic vocabulary, which is used, in vocal control of an AGV and where the phonemes are quite different from a word to another, this choice will increase teh rate of recognition. These words are:

• “Engine”: To switch the engine on or off. If it is on then the engine will be off and vice versa.
• “Forward”: To keep the movement upward.
• “Backward”: To move backward, this means a turn of 180 degree.
• “Stop”: To stop the movements temporarily ‘pause'.
• “Right”: To make a right turn of 90 degree.
• “Left”: To make a left turn of 90 degree.
• “Speed”: To increase the speed of engine by a step (speed up).
• “Slow”: To reduce the speed of engine by a step (speed down).
• “Light”: To turn lights on or off.
• “Horn”: To turn the horn on or off.

In order to run a wheelchair safely and comfortably by vocal commands, a set of sensors were added to detect obstacles, avoid misleading commands and control the speed of the engine [16–18]. The developed system “S”, the set of sensors and the microphone will be installed as shown in Fig. 1.

3. Details of Main Part

The main part is developed around the VR-Stamp and a DSP processor controlled by the PIC18f252. For best performance, the system gives better results in a quiet environment with the speaker’s mouth in close proximity to the microphone, approximately 5 to 15 cm.

A. DSP processor

A TMS320C6711 DSP processor were used to do two jobs, enhancing the speech signal by reducing the environment noise using ***Kalman Filter*** and reducing the effect of echo. Moreover this unit presents words of the sentence as a set of isolated and filtered words to the speech processor VR-stamp. The TMS320C6711 DSK module was chosen as it provides low cost gateway into real-time implementation of DSP algorithms. This module has the following features: A 150MHz TMS320C6711 DSP capable of executing 1200 Million Instruction Per Second (MIPS), 4M-bytes of 100MHz SDRAM, 128K-bytes of flash memory, a 16-bit audio codec, a parallel port interface to standard parallel port on a host PC. The TMS320C6711 DSK module is accompanied by the Code Composer Studio (CCS) IDE software, developed by Texas Instruments.

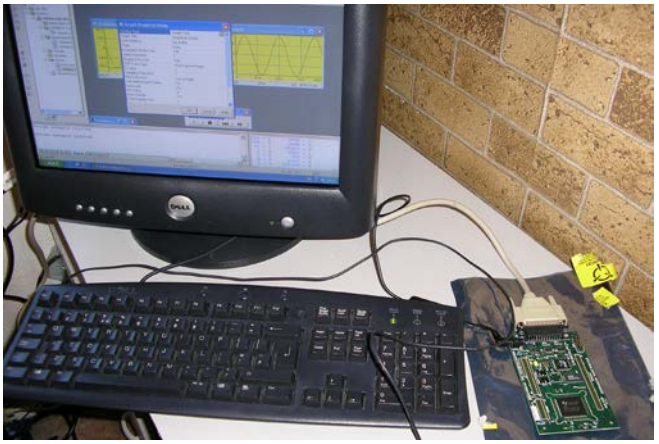

Fig 2 DSP-TMS320c6711 programming using CCS software

B. VR-Stamp (Voice recognition Stamp)

Voice Recognition Stamp is a new component from Sensory inc. It has more capabilities designed for embedded systems. It was designed for consumer telephony products and cost-sensitive consumer electronic applications such as home electronics, personal security, and personal communication because of its performances:-

- Noise-robust Speaker Independent (SI) and Speaker Dependent (SD) recognition.
- Many language models now available for international use.
- High quality, 2.4-7.8 kbps speech synthesis &
- Speaker Verification Word Spot (SVWS) -Noise robust voice biometric security.

The module VR-Stamp is based on the following components: a special microcontroller RSC4128, a

reference word storage 24C65 of EEPROM type that holds the parameters of referenced word produced during the training phase, a Flash program memory of 4 Mega-byte that holds the main program of word recognition, and a parallel interface of 24 lines (divided into 3 by 8-bit ports) to generate the results of recognition or to introduce commands, and audio communication lines for microphone and speakers .

In training phase, the module gets features of the 10 spotted words used in the vocabulary and presented in table 1, among these words, the starting keyword “Lasa” which is the name the laboratory and finishes with the Keyword "Tabek" which means 'execute' the command, so whenever the user wants to submit a voice command the sentence should start with the word “Lasa” and finishes with the word "Tabek". In recognition phase the VR-Stamp should detect some spotted words in the sentence and then submit the code of recognized words to the microcontroller, example: “ Lasa Aswad Yassar tabek”, in this sentence the module will submit the codes: 3 for the robot name and 7 for the action to be taken by that robot, the codes are presented in table 1 with the corresponding words. Figure 3 illustrats the development kit for VR-Stamp , this Kit helped us to simulate the functioning and recognition of words by blinking the corresponding LED.

RSC-4X mikroC is neccessary for developping teh application on VR-Stamp, it needs the binary objects (as FluentChip Library, reference words,…) et directories of included files. For that, we used the folowing repertory : Tools->Options->Project->Search Path, to add the directory of our project and also the FluentChip library from sensory.

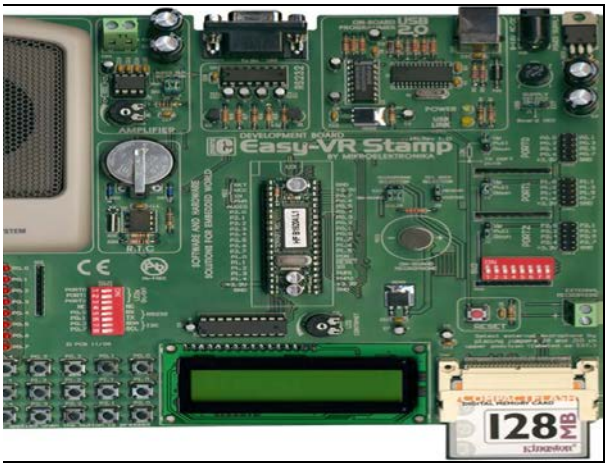

Fig 3: Developed Kit for VR-STAMP

C. The microcontroller PIC18F252

As an interface between the wireless transmission circuit Bluetooth and the vocal module VD364, a microcontroller with at least 16 input/output lines and minimum of 4 kilo instructions is needed. Therefore a better choice was the PIC18F252 from Microchip [17].

The main function of the microcontroller is to get the information from the VR-STAMP and based on the order of the codes it will submit this command to the Bluetooth or signal to the user (client) that an error in recognition or in comprehension: as an error recognition every sentence with no starting word, or non recognised word. As comprehension error, a sentence containing correct spotted words however it does not have a meaning: yade Mikbath Fawk”.

The microcontroller gets also high priority command from special keyboard.

D. Bluetooth wireless communication system

Initially Bluetooth wireless technology was created to solve a problem of replacing cables used for communication between such devices as: laptops, palmtops, personal digital assistant (PDA), cellular phones and other mobile devices [13][14] and [15]. Now Bluetooth enables users to connect to a wide range of computing and telecommunications devices without any need of connecting cables to the devices.

E.. Set of Sensors

In order to avoid and maintain a safe distance from obstacles, a set of ultrasonic sensors are attached in front and at left and right sides of the wheelchair. Finally, to control the HPEWC speed, a speed sensor attached to the wheel is then used. These ultrasonic sensors were chosen because they are readily commercially available as a module to be integrated in the robot base, they are also cheap, and they complied with the requirement specification for HPEWC. With the help of the ultrasonic sensors, HPEWC is able to keep track of the distance between itself and obstacles such as walls. Most distance-measuring ultrasonic systems are based on the time-of-flight method. This method comprises:

(1) Transmitting an ultrasonic pulse, consisting of one or several discrete frequencies, from a suitable ultrasonic transmitter.
(2) Radiating ultrasonic pulses over a certain range.
(3) Receiving the ultrasonic pulses.
(4) Calculating the time between the transmission and the reception of the ultrasonic pulse, where the distance (d) to the object having reflected the ultrasonic pulse can be calculated as:

2*d= v*t

Where :- *v*= velocity of sound and *t*= time between the transmission and the reception of ultrasonic pulse. The time measured can easily be transformed into distance. The ultrasonic signal processing module used in the design is the “UTRl” from LEXTRONIC. It is an interface between the ultrasonic sensors of type UST-40RT and the microcontroller.

IV. SYSTEM OPERATION

External noise affects the system since it is by nature in movement within the wheelchair. In designing the application, account was taken to decrease the affecting noise on the system at various movements. To do so, the external noise was recorded and spectral analysis was performed to study how to limit its effects in the recognition phase. However this is just done within the experience area.

The vocal command system works in two phases: The training phase and the recognition phase or verification phase. In the training phase, the operator will be asked to pronounce a command words one by one. The first word will activate the first output; the second word will activate the second output and so on. During this phase, the operator might be asked to repeat a word many times, especially if the word pronunciation is quite different from time to time. The recognition phase represents the use of the system. In this phase, the system will be in a waiting state, whenever a word is detected. The acquisition step will be activated, and then the parameters of that word are extracted and compared to those of reference words. If there is any matching between a reference word and the user word, the likelihood rate is high, and then the appropriate command will be generated. In addition, the ultrasonic sensors, placed at each side of the wheelchair, generate information on the context. Finally, a decision block produces the appropriate action. The command taken should not put the user in dangerous position. The system might take a proper decision "stopping the wheelchair or reduce the speed" to avoid collisions of the HPEWC as shown in Fig. 4.

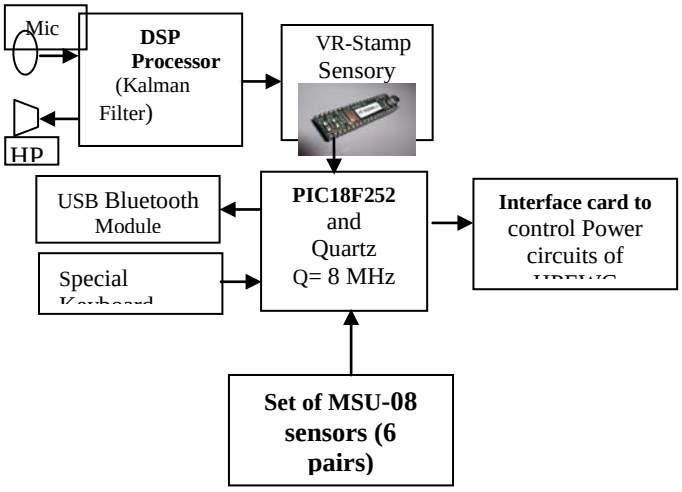

Fig. 4: synoptic of designed module based on multiprocessors

A. Set of sensors

In order to avoid and maintain a safe distance from obstacles, a set of six pairs of ultrasonic sensors type MSU-08 are attached in front and at left and right sides of the wheelchair. Finally, to control the HPEWC speed, a speed sensor attached to the wheel is then used. These ultrasonic sensors were chosen because they are readily commercially available as a module to be integrated in the robot base, they are also cheap, and they complied with the requirement specification for HPEWC. With the help of the ultrasonic sensors, HPEWC is able to keep track of the distance between itself and obstacles such as walls. Most distance-measuring ultrasonic systems are based on the time-of-flight method. This method comprises:

(1) Transmitting an ultrasonic pulse, consisting of one or several discrete frequencies, from a suitable ultrasonic transmitter.

(2) Radiating ultrasonic pulses over a certain range.

(3) Receiving the ultrasonic pulses.

(4) Calculating the time between the transmission and the reception of the ultrasonic pulse, where the distance (d) to the object having reflected the ultrasonic pulse can be calculated as:

$$2*d= v/t$$

where :-

v= velocity of sound and *t*= time between the transmission and the reception of ultrasonic pulse.

The time measured can easily be transformed into distance. The ultrasonic signal processing module used in the design is the "UTRl" from LEXTRONIC. It is an interface between the ultrasonic sensors of type UST-40RT and the microcontroller.

V. NUMERICAL RESULTS OF THE SIMULATION

The PIC18F252 program was simulated by MPLAB, which is a Windows-Based Integrated Development Environment (IDE) for the Microchip Technology Incorporated PIC microcontroller families, under windows XP. For a mono speaker, in the training phase, the speaker repeats two times each word to construct the database of referenced words. In the recognition phase, the application gets the word to be processed, treats it, then takes a decision if the word belongs to the ten command-words (referenced words) or not. If so, then the corresponding bit on the port B of the PIC18F252 is set to one. Otherwise, a bit on port A is set to one, turning on a red LED, which means, "the word is not recognized". Many tests on the developed vocal command were done within the laboratory L.A.S.A (laboratory of Automatic and Signal, Annaba). The VD-364 has been tested and its recognition rate for isolated words is shown in Fig. 5. It is clear that to increase this rate, a set of selected command words where the phonemes are quite different, should be used. Moreover, the training phase should be done within the same environment (noise) and same conditions in which the system would be used.

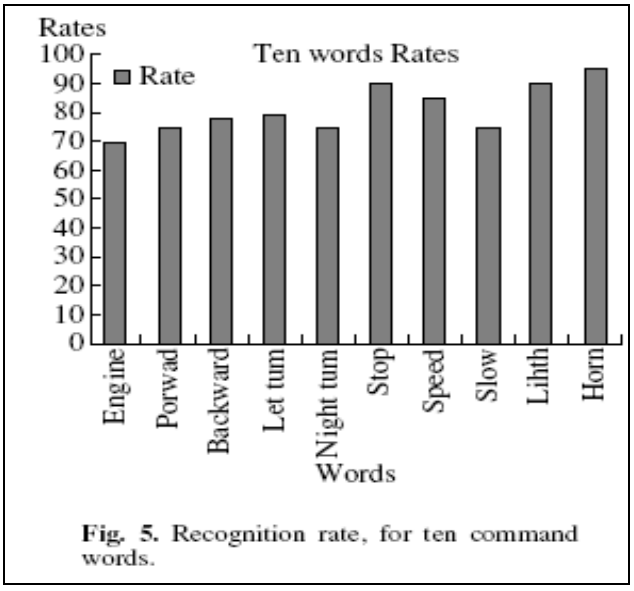

Fig. 5. Recognition rate, for ten command words.

VI.. CONCLUSIONS

In this paper, a hardware design of a special portable vocal command system for a handicapped person
wheelchair is presented. The bulky and complex designs have been overcome by exploring the new speech recognition kits. Interfacing this special vocal microcontroller to the wheelchair was controlled by the PIC16F876. Thus the program memory capacity is improved in order to design more complex controls. The application might be used to enhance AVG in robotics or other type of vocal command. However, in order to optimize sound output from the VR-Stamp, we recommend using the DAC output with an external amplifier. The overall product cost is increased slightly, but the DAC will provide higher quality sound output. In addition, the sensors types can be improved to play a secondary role in sharing the control of the HPEWC such as adding some infrared emitters and detectors [19].

REFERENCES

[1]. McLaurin, C.A. and Axelson P., Wheelchair Standards: An Overview, *Journal of Rehabilitation Research and*
Development , 1990, vol. 27, pp. 100–103.

[2]. Microchip manual, PIC16F87X Data sheet 28/40-Pin 8-bit FLASH Microcontrollers, Microchip Technology Inc. 2001.

[3]. Beritelli, F., Casale, S., and Cavallaro, A., A Robust Voice Activity Detector for Wireless Communications Using Soft Computing, *IEEE Journal on Selected Areas in Communications (JSAC)* , Special issue on Signal Processing for Wireless Communications, 1998, vol. 16, no. 9.

[4]. Mabo, R.I. and Donadson, W.R., Zero Crossing Measurements for Phonetic Recognition of Speech, *IEEEASSP* ,1971, vol. 24, no. 1.

[5]. Schraft, R.D., Schaeffer, C., and May, T., Care-O-bot: The Concept of a System for Assisting Elderly or Disabled Persons in Home Environments, *Proc. of the 24th Annual Conference IECON98* , 1998, vol. 4, pp. 2476–2481.

[6]. Huang, J., Ohnishi, N., and Sugie, N., Sound Localization in Reverberant Environment Based on the Model of the Precedence Effect, *IEEE Trans. on Instrumentation and Measurement* , 1997, vol. 46, pp. 842–846.

[7]. Shlomot, E., Cuperman, V., and Gersho, A., Hybrid Coding of Speech at 4 Kbps, *Proc. IEEE Workshop on Speech Coding* , Pocono Manor, PA, 1997, pp. 37–38.

[8]. Wang, T. and Cuperman, V., Robust Voicing Estimation with Dynamic Time Warping, *Proc. IEEE ICASSP'98* , 1998, pp. 533–536.

[9]. Rao, Rose, K., and Gersho, A., Deterministically Annealed Design of Speech Recognizers and Its Performance on Isolated Letters, *Proc. IEEE ICASSP'98* , 1998, pp. 461–464.

[10]. Sensory, Data sheet for RSC-364, Sensory Inc., 2001.

[11]. Design notes, Selecting an Interactive Speech Chip, 80-0078-C, Sensory, Inc., 2001.

[12]. Graf, B., Reactive Navigation of an Intelligent Robotic Walking Aid, in *Proc. of Roman*, 2001, pp. 353–358.

[13]. Rimon, E. and Koditschek, D.E., Exact Robot Navigation Using Artificial Potential Functions, *IEEE Trans. On Robotics and Automation* , 1992, vol. 8, no. 5, pp. 501–518.

[14]. Mazo, M., Rodriguez, F., Lazaro, J., Urena, J., Garcia, J., Santiso, E., Revenga, P., and Garcia, J., Wheelchair for Physically Disabled People with Voice, Ultrasonic and Infrared Sensor Control, *Autonomous Robots* , 1995, volpp. 203–224.

[15]. Wang, H., Ishimatsu, T., and Mian, J., Self-Localization for an Electric Wheelchair, *JSME International Journal, Series C- Mechanical Systems Machine Elements and Manufacturing* , 1997, vol. 40, no. 3, pp. 433–438.

[16]. Cooper, R.A., Widman, L.M., Jones, D.K., and Robertson, R.N., Force Sensing Control for Electric Powered
Wheelchairs, *IEEE Trans. Control Syst. Technol.* , 2000, vol. 38, pp. 112–117.

[17]. Cooper, R.A., Jones, D.K., Fitzgerald, S., Boninger, M.L., and Albright, S.J., Analysis of Position and Isometric Joysticks for Powered Wheelchair Driving, *IEEE Trans. Biomed. Eng.* , 2000, vol. 47, no. 7, pp. 902–910.

[18]. Wasson, G., Gunderson, J., Graves, S., and Felder, R., Effective Shared Control in Cooperative Mobility Aids, *Proc. of the 14th International Florida Artificial Intelligence Research Society Conference* , Key West, Florida, Menlo Park (CA): AAAI Press, 2001, pp. 509–518.

[19]. Simpson, R.C., Poirot, D., and Baxter, F., The Hephaestus Smart Wheelchair System, *IEEE Trans. on Neural Systems and Rehabilitation Engineering* , 2002, vol. 10, no. 2, pp. 118–122.

Electronically Tunable Current-mode Multiphase sinusoidal Oscillator Employing CDCTA-based Allpass Filters

K. Pitaksuttayaprot, and W. Jaikla

***Abstract*—** An implementation of current-mode multiphase sinusoidal oscillators (MSOs) is presented. The odd and odd/even phase systems can be realised using current differencing cascaded transconductance amplifier (CDCTA)-based all-pass filters. The condition of oscillation and frequency of oscillation can be controlled electronically and independently through adjusting the current of the CDCTA. The high output impedances facilitate easy driving an external load without additional current buffers. The proposed MSOs provide odd or even phase signals that are equally spaced in phase and equal amplitude. The circuit requires one CDCTA, one grounded resistor and one grounded capacitor per phase without additional current amplifier. The results of PSPICE simulations using BJT CDCTA are included to verify theory.

***Keywords*—** Current Differencing Cascaded Transconductance Amplifier; (CDCTA).

I. Introduction

MULTIPHASE sinusoidal oscillator (MSO) is important blocks for various applications. For example, in telecommunications it is used for phase modulators, quadrature mixers [1], and single-sideband generators [2]. In measurement system, MSO is employed for vector generator or selective voltmeters [3]. It can also be utilized in power electronics systems [4]. Recently, current-mode circuits have been receiving considerable attention of due to their potential advantages such as inherently wide bandwidth, lower slew-rate, greater linearity, wider dynamic range, simple circuitry and low power consumption [5]. Many active building blocks (ABBs) have been proposed to realize the current-mode circuit. The interesting active element, called current differencing cascaded transconductance amplifier (CDCTA) [20], is introduced to provide new possibilities in the current-mode circuit. It is really current-mode element whose input and output signal are currents. In addition, output currents of CDCTA can be electronically adjusted.

K. Pitaksuttayaprot is with Department of Technology Electronic, Phetchabun Rajabhat University, Sadeang Phetchabun, 67000, Thailand (e-mail: koson@pcru.ac.th).

W. Jaikla is with Department of Engineering Education, King Mongkut's Institute of Technology Ladkrabang, Bangkok, 10520, Thailand (e-mail: kawinai@kmitl.ac.th).

Several realizations of current-mode MSOs using different active building blocks are available in the literature. These include realizations using current follower (CF) [8], CCCII [9]-[11], CDTA [12]-[14], CDBA [15], CFOA [16], and CCCCTA [17] and CCCDTA [18-19]. The CF-based MSO in [8] requires two current followers, one floating resistor, and one floating capacitor for each phase and thus the circuit is not suitable for monolithic integration. Moreover, it cannot be electronically controlled. The CCCII-based MSOs [9]-[11] enjoy high-output impedances and electronic tunability. However, the first one requires a large number of external capacitors. In addition, the oscillation condition can be provided by tuning the capacitance ratio of external capacitors, which is not easy to implement. The second reported circuit requires additional current amplifiers, which makes the circuit more complicated and increases its power consumption. CDTA-based current-mode MSOs in [12] is based on lossy integrators, where as the circuits in [13] and [14] contain CDTA-based allpass sections. They exhibit good performance in terms of electronic tunability, high-output impedances, and independent control of the oscillation frequency and the oscillation condition. However, MSOs in [12] and [13] require an additional current amplifier, which is implemented by two CDTAs. Moreover, the output currents of the MSO, utilizing the CDTA-based lossy integrators, are of different amplitudes. The MSO employing CDTA-based allpass sections [13] requires two CDTAs in each allpass section, and the circuitry becomes more extensive. While MSO using CDTA-based allpass sections [14] requires floating capacitor. Consequently, it occupies a larger chip area for VLSI design. In addition, its power consumption is also increased.

The purpose of this study is to introduce a new current-mode multiphase sinusoidal oscillator. The features of the proposed circuit are the following: (I) Use of grounded capacitors and identical circuit configuration for each section in the MSO topology. (II) The electronic tunability of oscillation condition and oscillation frequency. (III) High-impedance current outputs. (IV) The possibility of generating multi-phase signals for both an even and odd number of equally-spaced in phases. (V) Independent tuning of the oscillation frequency and the oscillation condition. (VI) Equality of amplitudes of each phase due to utilizing identical

ISBN: 978-1-61804-216-3

sections. (VII) Requirement for only one CDCTA as the active element for each phase without any additional current amplifiers.

II. THEORY AND PRINCIPLE

A. CDCTA Overview

The characteristics of the ideal CDCTA are represented as the following hybrid matrix.

$$\begin{bmatrix} I_z, I_{zc} \\ I_{x1}, I_{x1c} \\ I_{x2}, I_{x2c} \\ V_{x2} \end{bmatrix} = \begin{bmatrix} 1 & -1 & 0 & 0 \\ 0 & 0 & g_{m1} & 0 \\ 0 & 0 & 0 & g_{m2} \\ 0 & 0 & 0 & 0 \end{bmatrix} \begin{bmatrix} I_p \\ I_n \\ V_z \\ V_{x1} \end{bmatrix}, \quad (1)$$

where g_m is the transconductance of the CDCTA. This g_m can be adjusted by external input bias current I_B . For bipolar junction transistor CDCTA, the transconductances can be shown in Eqs. (2) and (3) . The symbol and the equivalent circuit of the CDCTA are illustrated in Fig. 1 .

$$g_{m1} = \frac{I_{B1}}{2V_T}, \quad (2)$$

and

$$g_{m2} = \frac{I_{B2}}{2V_T}. \quad (3)$$

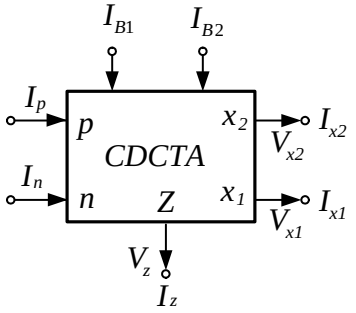

(a)

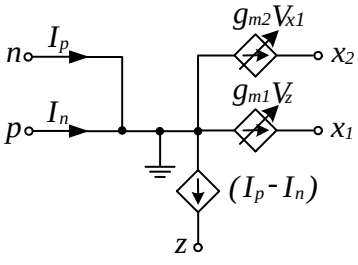

(b)

Fig. 1. CDCTA (a) Symbol (b) Equivalent circuit.

B. Principle of n-cascaded Allpass-based MSO

The generalized structure of MSO by cascading the n identical stages (n≥2) is shown in Fig. 2 which containing the first-order allpass filter for each phase. The output of nth stage is fed back to the input of the first stage, and the signal of the last section is inverted for even phase system and non-inverted for odd phase system. It is found in Fig. 2 that the system can provide one phase per one allpass filterwithout any additional external amplifier. The system loop gain can be written as follows :

$$L(s) = -\left(k\frac{sa-1}{sa+1}\right)^n. \quad (4)$$

where the symbols k is the current gain and a denotes the natural frequency of each allpass section. At the oscillation frequency ω_{osc}, the Barkhausen's condition can be written as

$$L(j\omega_{osc}) = -\left(k\frac{j\omega_{osc}a-1}{j\omega_{osc}a+1}\right)^n = 1. \quad (5)$$

From (5), the magnitude and the phase of the system loop gain can be expressed as follows:

$$\left|L(j\omega_{osc})\right| = 1, \quad (6)$$

and

$$\angle H(j\omega_{osc}) = 2n\phi = 2n\left(\left(-2\tan^{-1}(\omega_{osc}a)\right)\right) = -2\pi. \quad (7)$$

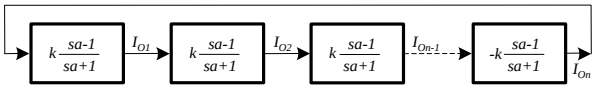

Fig. 2. MSO block diagram for odd/enven phase

Equation (7) shows that for n - phase systems, each phase is shifted by -360 /2n. Hence the oscillation condition (OC) and the oscillation frequency (OF) are given by the formulae

$$\text{OC:} \quad k = 1, \quad (8)$$

and

$$\text{OF:} \quad \omega_{osc} = \frac{1}{a}\tan\left(\frac{\pi}{2n}\right). \quad (9)$$

Considering (8) and (9), the oscillation condition can be controlled independently of the oscillation frequency by the gain k, while the oscillation frequency can be changed by the natural frequency a .

ISBN: 978-1-61804-216-3

C. Proposed Current-mode MSO

As mentioned in the above section, the proposed MSO is based on identical first-order allpass sections. A prospective CDCTA-based implementation is shown in Fig. 3. It is seen that the proposed first-order allpass circuit consists of 1 CDCTA, 1 grounded capacitor and 1 grounded resistor. The current transfer function can be written as follows:

$$L(s) = g_{m2}R\left(\frac{s\frac{C}{g_{m1}}-1}{s\frac{C}{g_{m1}}+1}\right)^n . \quad (10)$$

According to Eqs. (8) and (9), the oscillation condition and oscillation frequency are as follows:

$$\text{OC:} \quad g_{m2}R = 1, \quad (11)$$

and

$$\text{OF:} \quad \omega_{osc} = \frac{g_{m1}}{C}\tan\left(\frac{\pi}{2n}\right). \quad (12)$$

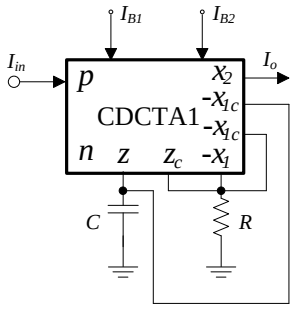

Fig. 3. CDCTA-based allpass filter

From Eqs. (10) and (11), if $g_{m1}=I_{B1}/2V_T$ and $g_{m2}=I_{B2}/2V_T$, theFO and CO is modified as

$$\frac{I_{B2}R}{2V_T} = 1, \quad (11)$$

and

$$\omega_{osc} = \frac{I_{B1}}{2V_T C}\tan\left(\frac{\pi}{2n}\right). \quad (12)$$

From Eqs. (11) and (12), it can be seen that the CO can be adjusted electronically/independently from the FO by varying I_{B2} while the oscillation frequency can be electronically adjusted by I_{B1}. The resulting current-mode MSO is shown in Fig. 4 for odd/even phase system, respectively. It is found from Fig. 4 that the current mirrors are required to split the bias currents I_{B1} and I_{B2} to each allpass section. In addition, it can be seen that the proposed MSOs enjoy high-output impedances which facilitate easy driving an external load without additional current buffers.

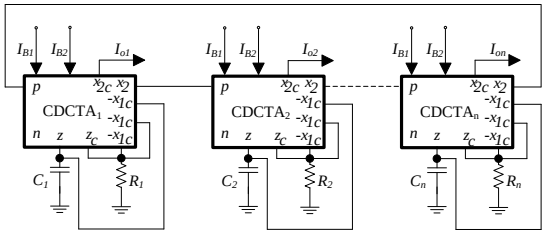

Fig. 4. Proposed current-mode MSO for odd/even phase system

III. RESULTS OF COMPUTER SIMULATION

To prove the performances of the proposed current-mode MSO, the PSpice simulation program was used for the examination. The PNP and NPN transistors employed in the proposed circuit were simulated by using the parameters of the PR200N and NR200N bipolar transistors of ALA400 transistor array from AT&T [21]. The CDCTA has been simulated using the bipolar technology structure [22] of Fig. 5. The circuit was biased with ±2.5V supply voltages. Firstly, an odd three-phase sinusoidal oscillator (n=3) based on the structure in Fig. 2 has been designed on the basis of Fig. 4. The component values are as follows: I_{B1}=100μA, I_{B2}=62μA, C=0.1nF and R=1kΩ. The simulated output waveforms, I_{O1}, I_{O2} and I_{O3} are shown in Fig. 6 and 7. The frequency of oscillation achieved was 2.93MHz. The frequency spectrum of output currents are shown in Fig. 8. The total harmonic distortion is about 2.88%.

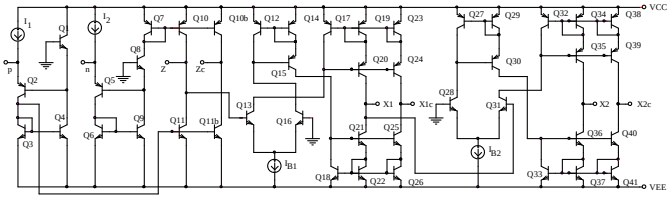

Fig. 5. Internal construction of CDCTA

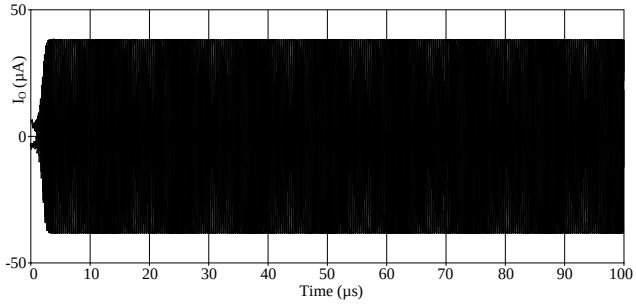

Fig. 6. Output waveforms during initial state (n=3)

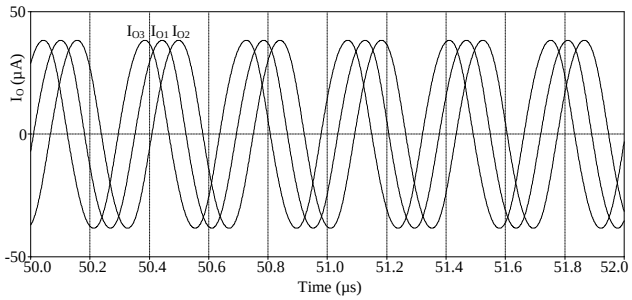

Fig. 7. Current outputs of the proposed MSO (n=3)

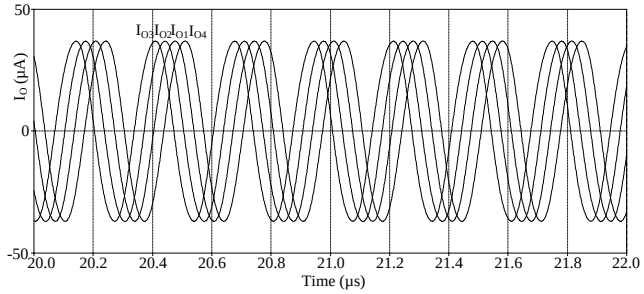

Fig. 10. Current outputs of the proposed MSO (n=4)

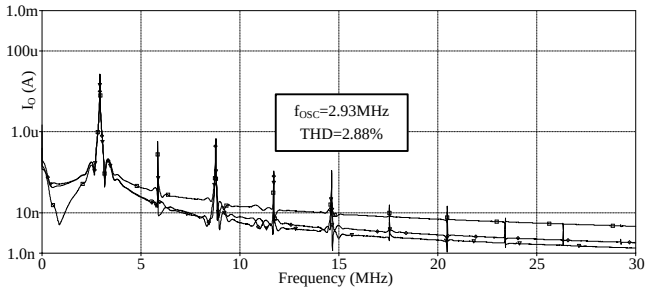

Fig. 8. Spectrum of Current outputs of the proposed MSO (n=3)

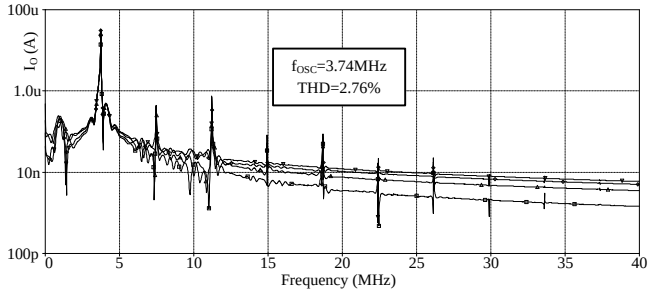

Fig. 11. Spctrum of Current outputs of the proposed MSO (n=4)

Secondly, an even four-phase sinusoidal oscillator (n=4) based on the structure in Fig. 2 has been designed on the basis of Fig. 4. The component values are as follows: I_{B1}=110μA, I_{B2}=62μA, C=0.1nF and R=1kΩ. The simulated output waveforms, I_{O1}, I_{O2}, I_{O3} and I_{O4} are shown in Figs. 9 and 10. The frequency of oscillation achieved was 3.74MHz. The frequency spectrum of output currents are shown in Fig.11. The total harmonic distortion is about 2.76%.

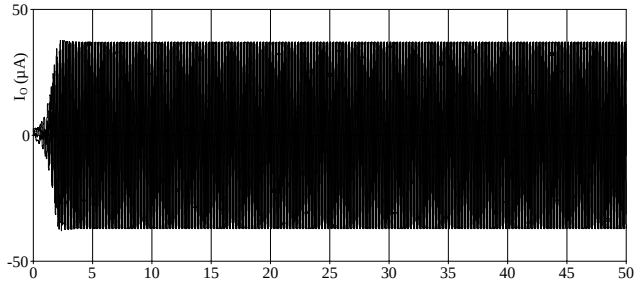

Fig. 9. Output waveforms during initial state (n=4)

IV. CONCLUSION

A new current-mode multiphase sinusoidal oscillatos using CDCTA-based lossy integrators with grounded capacitors have been presented. The features of the proposed circuit are that: oscillation frequency and oscillation condition can be independently tuned; the proposed oscillator consists of merely 1 CDCTA and 1 grounded capacitor for each phase and no additional current amplifier and availability of explicit current outputs from high-output impedance terminals. PSPICE simulation results agree well with the theoretical anticipation..

REFERENCES

[1] J. Dunlop and D.G.Smith, “Telecommunications Engineering,” 3rd ed. CRC Press, 1994.
[2] W. Tomasi, “Electronic Communications System,” New Jersey: Prentice- Hall Inc., 1998.
[3] Anritsu Emea Limited, “MG3700A vector signal generator datasheet,” Availableat:http://www.eu.anritsu.com/files/ MEG3700A_El17301.pdf..
[4] G. Eirea, and S.R. Sanders, “Phase current unbalance estimation in multiphase buck converters,” IEEE Transactions on Power Electronics, vol. 23, pp. 137-143,2008.
[5] C. Toumazou, F.J. Lidgey and D.G.Haigh, “Analogue IC design: the current-mode approach,” Peter Peregrinus: London, (1990).
[6] R. Prokop and V.Musil, “New modern circuit block CCTA and some its applications,” The Fourteenth International Scientific and Applied Science Conference - Electronics ET'2005, (Sofia: TU Sofia), Book 5, pp.93-98,2005.
[7] M. Siripruchyanun and W.Jaikla, “Current controlled current convey or transconductance amplifier (CCCCTA): a building block for analog signal processing,” Electrical Engineering, vol. 90, pp. 443–453,2008.
[8] M.T. Abuelma'Atti, “Current-mode multiphase oscillator using current followers” Microelectronics Journal, vol. 25, 457–461,1994.

[9] G D.Skotis, and C. Psychalinos, "Multiphase sinusodal oscillators using second generation current conveyors," Int. J. Electron.Commu.(AEU), vol.64,pp.1178-1181,2010.

[10] M.T. Abuelma'atti, and M.A.Al-Qahtani, "A new current- controlled multiphase sinusoidal oscillator using translinear current conveyor," IEEE Transactions on Circuits and Systems, vol. 45, 881–885,1998.

[11] C. Loescharataramdee, W.Kiranon, W.Sangpisit and W.Yadum, "Multiphase sinusoidal oscillators using translinear current conveyors and only grounded passive components," Proceeding of Southeastern Symposium on System Theory, 2004, 59-63.

[12] W. Tangsrirat and W. Tanjaroen, "Current-mode multiphase sinusoidal oscillator using current differencing transconductance amplifiers," Circuits, Systems and Signal Processing, vol. 27, pp. 81- 93,2008..

[13] W. Tangsrirat, W. Tanjaroen, and T. Pukkalanun, "Current-mode multiphase sinusoidal oscillator using CDTA-based allpass sections," International Journal of Electronics and Communications (AEU), vol. 63, pp. 616- 622, 2009.

[14] W. Jaikla, M. Siripruchyanun, D. Biolek, and V. Biolkova, "Highoutput-impedance current-mode multiphase sinusoidal oscillator employing current differencing transconductance amplifier-based allpass filters," International Journal of Electronics, vol. 97, pp. 811–826, 2010.

[15] K.Klahan, W.Tangsrirat, and W. Surakampontorn, "Realization of multiphase sinusodal oscillator using CDBAs," IEEE Asia-Pacific Conf. Circ. Sys., pp. 725-728, 2004.

[16] D.-S. Wu, S.-I. Liu, Y.-S. Hwang, and Y.-P. Wu, "Multiphase sinusoidal oscillator using the CFOA pole," IEE Proc. Circuits Devices Syst,vol.142,pp. 37-40, 1995.

[17] P. Uttaphut, "New Current-mode Multiphase Sinusodal Oscillators Based on CCCCTA-based Lossy Integrators,"Electrical Review, pp. 291-295, 2012.

[18] M. Kumngern, "Current-mode multiphase sinusoidal oscillator using current-controlled current differencing transconductance amplifiers," 2010 IEEE International Conference of Electron Devices and Solid-State Circuits (EDSSC), 2010.

[19] W. Jaikla, and P. Prommee, "Electronically tunable current-mode multiphase sinusoidal oscillator employing CCCDTA-base allpass filters with only grounded passive elements," Radioengineering, vol.20, no.3, pp. 594-599,2011.

[20] X. Jun, W. Chunhua, and J. Jie, "Current Differencing CascadedTransconductance Amplifier(CDCTA) and Its Applications on Current-Mode nth-Order Filters,"Circuits,System, and Signal Processing, Springer Science+Business Media New York 2013.

[21] Frey D., Log-domain filtering: an approach to current-mode filtering, IEE Proceedings-Circuits, Devices and Systems, pp. 406-416, 1993.

[22] W. Tangsirrat and w. Tanjaroen,"Current-mode sinusoidal quadrature oscillator with independent control of oscillation frequency and condition using CDTAs," Indian Journal of Pure &Applied Physics,vol48, ,pp.363-366, May, 2010.

First A. Author (M'76–SM'81–F'87) and the other authors may include biographies at the end of regular papers. Biographies are often not included in conference-related papers. This author became a Member (M) of **EUROPMENT** in 1976, a Senior Member (SM) in 1981, and a Fellow (F) in 1987. The first paragraph may contain a place and/or date of birth (list place, then date). Next, the author's educational background is listed. The degrees should be listed with type of degree in what field, which institution, city, state or country, and year degree was earned. The author's major field of study should be lower-cased.

The second paragraph uses the pronoun of the person (he or she) and not the author's last name. It lists military and work experience, including summer and fellowship jobs. Job titles are capitalized. The current job must have a location; previous positions may be listed without one. Information concerning previous publications may be included. Try not to list more than three books or published articles. The format for listing publishers of a book within the biography is: title of book (city, state: publisher name, year) similar to a reference. Current and previous research interests ends the paragraph.

The third paragraph begins with the author's title and last name (e.g., Dr. Smith, Prof. Jones, Mr. Kajor, Ms. Hunter). List any memberships in professional societies other than the **EUROPMENT**. Finally, list any awards and work for **EUROPMENT** committees and publications. If a photograph is provided, the biography will be indented around it. The photograph is placed at the top left of the biography. Personal hobbies will be deleted from the biography.

Artificial Intelligence Control Applied in Wind Energy Conversion System

F.Arama, A.Dahbi, B.Mazari, N.Nait Saiid

Bechar University, USTO Oran University, Batna University, Batna University
{fatmaarama@yahoo.fr; Dahbi_j@yahoo.fr, mazari_dz@yahoo.fr, n_naitsaid@yahoo.com}

***Abstract*—** This work presents a field oriented control (FOC) of active and reactive power applied on Doubly Fed Induction Machine (DFIM) integrated in wind energy conversion system (WECS). The main objective of this work is to compare the performances of energy produced by the use of two types of controllers (PI regulator and the neural network regulator (NN)) in order to control the wind power conversion system to compare their precision & robustness against the wind fluctuation and the impact on the quality of produced energy .A field oriented control of DEFIG stator is also presented to control the active and reactive power.To show the efficiency of the performances and the robustness of the two control methods those were analyzed and compared by simulation using Matlab/Simulink software. The results described the favoured method.

***Keywords*—** field oriented control (FOC), wind energy conversion system (WECS), Doubly Fed Induction Machine (DFIM), PI regulator and the neural network regulator (NN).

I. Introduction

The wind power is one of renewable energies which news fast growth in the world due to clean and nonpolluting nature [1]. Several machines were used in WECS, but the range of wind speed was limited in classical machines, the advanced technology created DFIM witch solves this problem and makes it more powerful [2].

Several control methods of the DFIM appeared, among them, the vector control [3]. The principle of this control is to make DFIM similar to separate excitation. DC machine. These last years, a big interest is given to the use of neural network in identification and control of the nonlinear systems; this is mainly due to their capacities of training and generalization[4]. This paper presents a comparison of performance in vector control using PI and controllers NN in WECS. The first regulator is PI which is simple and easy in implementation and gives acceptable performances [5], but it hasn't robustness in case of parameter variations .Then, a control device by neural network is used. This type of controller proved to be an interesting method for the design of controllers and was applied in many fields because of its excellent properties, such as insensitivity to external disturbances and variation of the parameters. It can present fast dynamic responses if the switching devices support a high frequency. The studied system is presented in (Fig. 1).

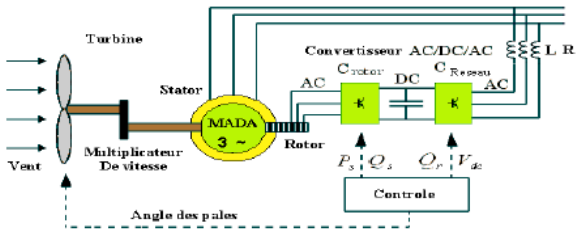

Fig. 1. Scheme of the studied system.

II. Modeling and Control of DFIM

A. Modeling of DFIM

The of Park transformation on electrical equations of DFIM in field reference frame gives the following equations [6][7][8]:

$$\begin{cases} V_{sd}=R_s i_{sd}+\dfrac{d\Phi_{sd}}{dt}-\omega_s\Phi_{sq} \\ V_{sq}=R_s i_{sq}+\dfrac{d\Phi_{sq}}{dt}+\omega_s\Phi_{sd} \\ V_{rd}=R_r i_{rd}+\dfrac{d\Phi_{rd}}{dt}-\omega_r\Phi_{rq} \\ V_{rq}=R_r i_{rq}+\dfrac{d\Phi_{rq}}{dt}+\omega_r\Phi_{rd} \end{cases} \quad (1)$$

The fields are given by:

$$\begin{cases} \Phi_{sd}=L_s i_{sd}+M_{sr} i_{rd} \\ \Phi_{sq}=L_s i_{sq}+M_{sr} i_{rq} \\ \Phi_{rd}=L_r i_{rd}+M_{sr} i_{sd} \\ \Phi_{rq}=L_r i_{rq}+M_{sr} i_{sq} \end{cases} \quad (2)$$

The electromagnetic torque is given by:

$$C_{em} = P\frac{M_{sr}}{L_s}\left(\Phi_{sq} i_{rd}-\Phi_{sd} i_{rq}\right) \quad (3)$$

$$J\frac{d\Omega_{mec}}{dt} = C_{em} - C_r - f.\Omega_{mec} \quad (4)$$

B. Power Control

In order to control easily the electrical power produced by the WECS, we applied an independent control of the active and reactive powers by FOC of stator The principle consists in aligning stator field along the d axis of Park reference frame (Fig.2) [3][9]. This choice is to eliminate the coupling between powers.

We have: $\Phi_{sq} = 0$ then $\Phi sd = \Phi s$.

ISBN: 978-1-61804-216-3

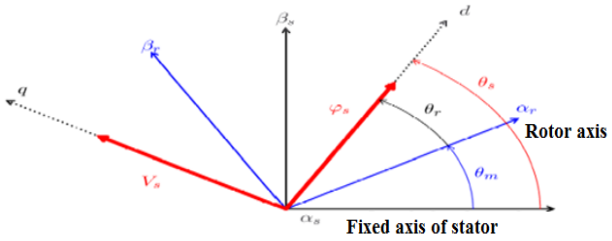

Fig. 2. Position of the stator flux.

The systems of equation (1) and (2) can be simplified as the following form:

$$\begin{cases} V_{sd}=R_s i_{sd} \\ V_{sq}=R_s i_{sq}+\omega_s \Phi_s \\ V_{rd}=R_r i_{rd}+\dfrac{d\Phi_{rd}}{dt}-\omega_r \Phi_{rq} \\ V_{rq}=R_r i_{rq}+\dfrac{d\Phi_{rq}}{dt}+\omega_r \Phi_{rd} \end{cases} \quad (5)$$

For high power machines we can neglect the resistance of the stator windings, so:

$$\begin{cases} V_{sd}=0 \\ V_{sq}=V_s=\omega_s \Phi_s \\ V_{rd}=R_r i_{rd}+\dfrac{d\Phi_{rd}}{dt}-\omega_r \Phi_{rq} \\ V_{rq}=R_r i_{rq}+\dfrac{d\Phi_{rq}}{dt}+\omega_r \Phi_{rd} \end{cases} \quad (6)$$

$$\begin{cases} \Phi_s=L_s i_{sd}+M_{sr} i_{rd} \\ 0=L_s i_{sq}+M_{sr} i_{rq} \\ \Phi_{rd}=L_r i_{rd}+M_{sr} i_{sd} \\ \Phi_{rq}=L_r i_{rq}+M_{sr} i_{sq} \end{cases} \quad (7)$$

$$Cem=-P\frac{Msr}{Ls}\Phi s\, irq \quad (8)$$

The active and reactive stator power in the Park reference, are written:

$$\begin{cases} P=v_{sd} i_{sd}+v_{sq} i_{sq} \\ Q=v_{sq} i_{sd}-v_{sd} i_{sq} \end{cases} \quad (9)$$

According to FOC, this system of equations can be simplified as:

$$\begin{cases} P=v_s i_{sq} \\ Q=v_s i_{sd} \end{cases} \quad (10)$$

$$\begin{cases} i_{sd}=\dfrac{V_s}{\omega_s L_s}-\dfrac{Msr}{L_s}.i_{rd} \\ i_{sq}=-\dfrac{Msr}{L_s}.i_{rq} \end{cases} \quad (11)$$

$$\begin{cases} P=-\dfrac{V_s M_{sr}}{L_s} i_{rq} \\ Q=-\dfrac{V_s M_{sr}}{L_s} i_{rd}+\dfrac{V_s^2}{L_s \omega_s} \end{cases} \quad (12)$$

$$\begin{cases} \Phi_{rd}=\left(L_r-\dfrac{M_{sr}^2}{L_s}\right) i_{rd}+\dfrac{M_{sr} V_s}{\omega_s L_s} \\ \Phi_{rq}=\left(L_r-\dfrac{M_{sr}^2}{L_s}\right) i_{rq} \end{cases} \quad (13)$$

$$\begin{cases} V_{rd}=R_r i_{rd}+\left(L_r-\dfrac{M_{sr}^2}{L_s}\right)\dfrac{di_{rd}}{dt}-g\omega_s\left(L_r-\dfrac{M_{sr}^2}{L_s}\right) i_{rq} \\ V_{rq}=R_r i_{rq}+\left(L_r-\dfrac{M_{sr}^2}{L_s}\right)\dfrac{di_{rq}}{dt}+g\omega_s\left(L_r-\dfrac{M_{sr}^2}{L_s}\right) i_{rd}+g\dfrac{M_{sr} V_s}{L_s} \end{cases} \quad (14)$$

III. Control of Active and Reactive Power of DFIM

In this FOC in open loop we neither measured nor estimated. The decoupling is due to voltages and currents which are evaluated using transient equations of the machine [5][6]. This method is favored with microprocessors, but it is very sensitive to parameter variations of the machine.

The this method in DFIM, the voltages are calculated by using power equations according to the following equations [5].

$$\begin{cases} V_{dr}=g\omega_s \dfrac{\left(L_r-\dfrac{L_m^2}{L_s}\right)}{\dfrac{V_s L_m}{L_s}} * P-\left(\dfrac{R_r\left(L_r-\dfrac{L_m^2}{L_s}\right)}{\dfrac{V_s L_m}{L_s}} p\right) * Q+\left(\dfrac{R_r V_s}{\omega_s L_m}+\left(L_r-\dfrac{L_m^2}{L_s}\right)\dfrac{V_s}{\omega_s L_m} p\right) \\ V_{qr}=-\left(\dfrac{R_r+\left(L_r-\dfrac{L_m^2}{L_s}\right) p}{\dfrac{V_s L_m}{L_s}}\right) * P-g\omega_s \dfrac{\left(L_r-\dfrac{L_m^2}{L_s}\right)}{\dfrac{V_s L_m}{L_s}} * Q+g\omega_s\left(L_r-\dfrac{L_m^2}{L_s}\right)\dfrac{V_s}{\omega_s L_m} \end{cases} \quad (15)$$

In this method, we power is controlled using two cascade controllers, te first is for power control, the second is for current control, the coupling terms appeared after this last, fig.3.

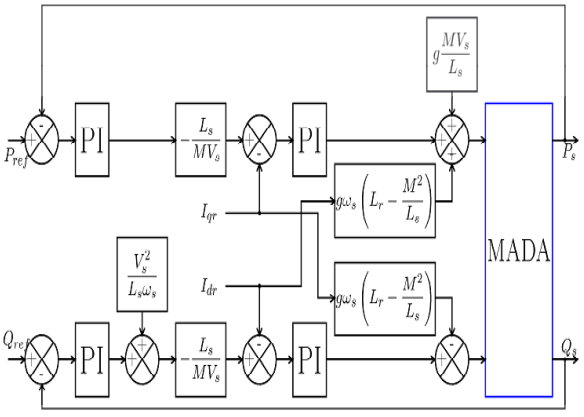

Fig. 3 Control scheme of DFIM

IV. Neural Network Control

The use of an analogical controller leads to performance degradation in nonlinear and uncertain process or parametric variation of the system [10][11]. Many intelligent controls

have been applied on DFIM. Fuzzy control, neural networks [12]. The use of neural networks is a technique for controlling complex systems can be justified by its simplicity of implementation (some preliminary mathematical analysis) [13]. Considering the process as a black box and the ability to control the minimum of process information [14]. The use of neural networks is valid to control DFIM.

The idea is to replace the four PI regulators of FOC by neural regulators (RN) simple. For the training of the neural weights from PI regulators we uses an algorithm of back-propagation called the algorithm of Levenberg-Marquardt (LM) [15][16].

Each neural network has a well defined function depending on selected architecture (hidden layers number and neural number in each hidden layer). The problem is to find that which gives better results. In our case we take a structure of neural network with only one hidden layer containing three neurals using the sigmoid transfer function of.

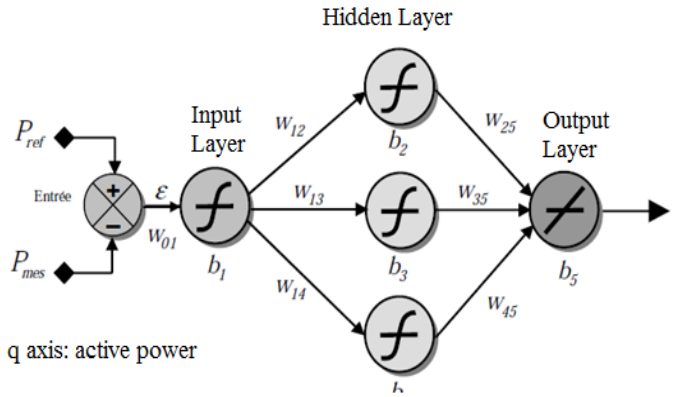

Fig. 4 Multilevel perceptrons: (1-3-1) configuration.

The total diagram of FOC control with neural regulators is presented in (Fig.5).

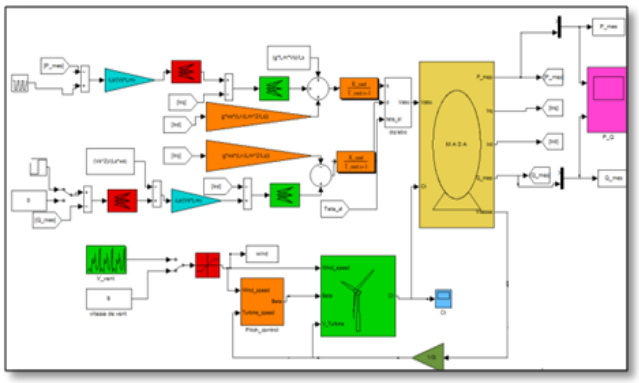

Fig. 5 Global scheme of FOC control with neural regulators

V. Simulation Results

To analyze the system and the efficienncy of proposed controller, some simulation tests were done at 0,8 s, using Matlab/Simulink. PWM Inverter control the rotor of DFIM. PI and NN Regulators are tested by two different ways, the following of the reference, and the robustness while varying the parameters of DFIM used in simulation those are presented in (table .I).

A. The following of reference

In this test, simulation was made with keeping the same parameters of the DFIM. We apply steps of active and reactivate power in order to observe well the behavior of this control. The obtained results are illustrated in (fig.6) .

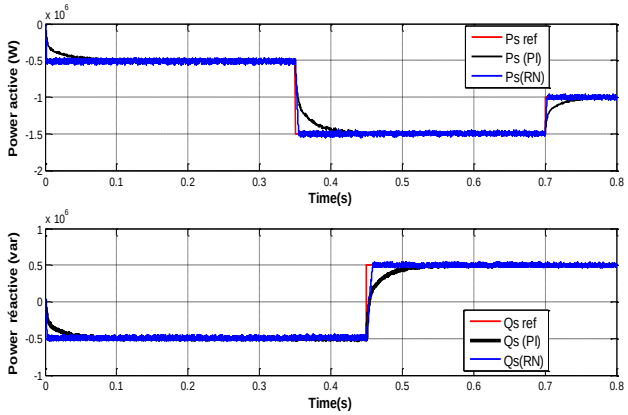

Fig. 6 Simulation results tests of reference tracking using PI and NN regulators.

The simulation results obtained show good performances in following the active and reactive power.

When the reference when changes, it is noticed that the oscillations decrease and the response time is smaller in the case of neural networks regulator.

B. Robustness

In order to test the robustness of PI and NN regulators, the value of the resistor of rotor is 1.5 of its nominal value, the stator and rotor winding values increased by 10% of their nominal values, the value of the mutual is decreased by 10 % of its nominal value.

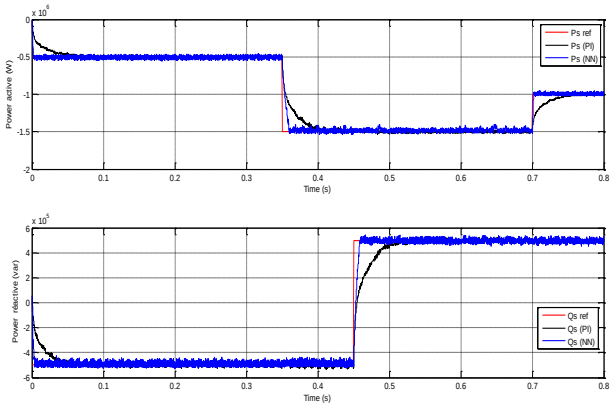

Fig. 7 Influence of rotor resistor variation *Rr* of +50 %.

ISBN: 978-1-61804-216-3

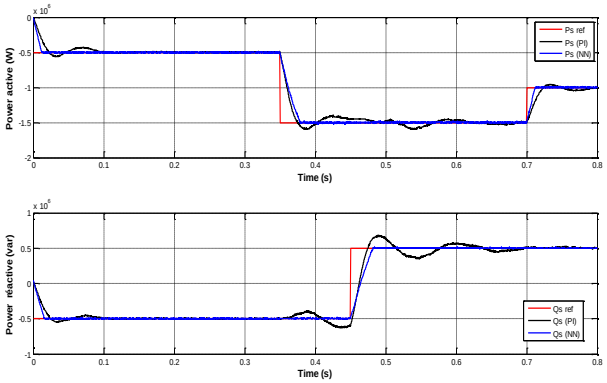

Fig.8 Influence of stator winding variation *Ls* of +10 %.

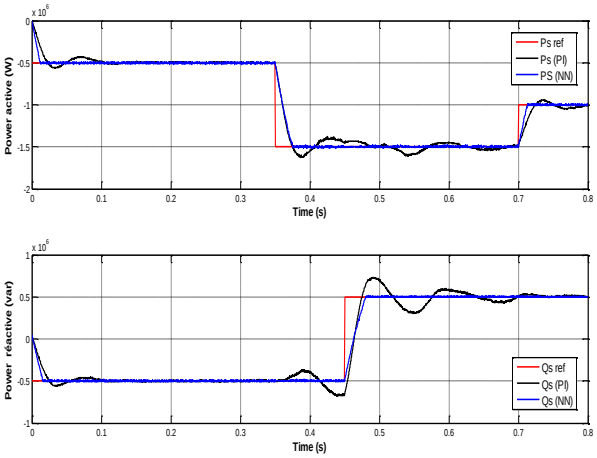

Fig. 9 Influence of rotor winding variation *Lr* of +10 %.

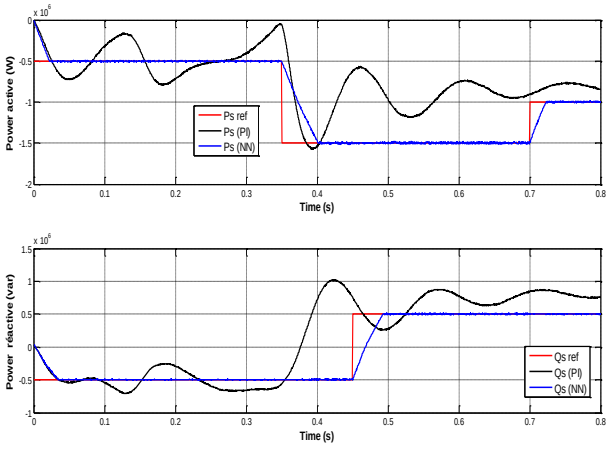

Fig. 10 Influence of mutual winding variation *Lm* of -10 %.

The comparisons between the two controllers' show that the neural network presents good performances, but PI controller performances are deteriorate.

VI. Conclusion

This work enabled us to study FOC of DFIM which makes it possible to have a decoupling and an independent control of the active and reactive power. Then we studied the WECS. Firstly, the regulation is made with PI regulators. Secondly, is with neural networks.

The architecture of the neural network corrector retained is 1-3-1. It enabled us to improve the dynamic and static performances of the DFIM.

The simulation results obtained leads us to conclude that the neural network regulator, is better in robustness with a fast response time, a good following to reference and it does not present oscillation or goings beyond at the time of the transient state.

VII. References

[1] T. Ackermann and Soder, L. " An Overview of Wind Energy-Status 2002 ". Renewable and Sustainable Energy Reviews 6(1-2), 67-127 (2002).

[2] GE Wind Energy. GE Wind brochure: http://www.gepower.com/prod_serv/products/wind_turbines/en/index.html

[3] B. Hopfensperger, D. J. Atkinson, and R. Lakin, "Stator-flux-oriented control of a doubly-fed induction machine with and without position encoder", IEE Proc.-Electr. Power Applications, vol. 147, no. 4, July 2000, pp. 241-250

[4] E.M. Petriu; "Neural Networks for Modelling Application", University of Ottawa, 1998

[5] S. El Aimani, B. François, B. Robyns, "Modélisation de générateurs éoliens à vitesse variable connectés à un bus continu commun". International forum on Renewable Energies,FIER 2002, Tétouan, Maroc.

[6] S. DRID, S.M-S.NAIT, M. TADJINE, " The Doubly Fed Induction Machine Modeling In The Separate Reference Frames", Journal of Electrical Engineering, JEE. Vol.4, N°1, pp: 11-16, 2004

[7] F. Poitiers M. Machmoum R. Le Daeufiand M.E. aim, "Control of a doubly-fed induction generator for wind energy conversion systems,"IEEE Trans .Renewable Energy, Vol. 3, N°. 3, December 2001 pp.373-378.

[8] M. Machmoum, F. Poitiers, C. Darengosse and A. Queric, "Dynamic Performances of a Doubly-fed Induction Machine for a Variable-speed Wind Energy Generation,"IEEE Trans. Power System Technology, vol. 4, Dec. 2002,pp. 2431-2436.

[9] Arantxa Tapia, Gerardo Tapia, J. Xabier Ostolaza, Jose Ramon Saenz, "Modeling and control of a wind turbine driven doubly fed induction generator", IEEE Trans. on Energy Conversion, Vol.18, no.2, 194-204, June, 2003.

[10] J. François Jodouin, "Les Réseaux de Neurones : Principes et Application", Hermès Sciences Publicat, 21sept1994.

[11] K. Warwick, A. Ekwure, R. Aggarwal, Artificial Intelligence Techniques in Power Systems, IEE Power Engineering Series 22, Bookcratt Printed, pp. 17-19, 1997.

[12] Y.H. Song and A.T. Johns, "Applications of Fuzzy Logic in Power Systems: Part 2. Comparison and Integration with Expert Systems, Neural Networks and Genetic Algorithms", IEE Power Engineering Journal, Vol. 12, No. 4, 1998, pp. 185-

[13] Qiao W, Venayagamoorthy GK, Harley RG. "Design of optimal PI controllers for doubly fed induction generators driven by wind turbines using particle swarm optimization". In: Proc. International Joint Conference on Neural Networks, Sheraton VancouverWallCentreHotel, Vancouver,BC, Canada. July 2006: p.1982–1987.

[14] Swati A. Barbade, Prabha. Kasliwal "Neural network based control of Doubly Fed Induction Generator in wind power generation".International Journal of Advancements in Research & Technology, Volume 1, Issue2, July-2012
[15] D. Yathley, "Back Propagation Neural Networks for Non-Linear Self Tuning Adaptive Control", IEEE, Control Systems Magazine, Vol. 10, N°3, pp 44 - 48, January 1990.
[16] J. J. Brey, Castro, A, E. Moreno, and C. Garcia, "Integration of renewable energy sources as an optimised solution for distributed generation," IECON 02 [Industrial Electronics Society, IEEE 2002 28th Annual Conference of the, Vol. 4, 5-8 Nov., pp.:3355 – 3359,2002.

APPENDIX

Table 1. Parameters of DFIM

Symbol	Value
Rated Power P_N	1.5 MW
Stator resistance R_s	0.012 Ω
Rotor resistance R_r	0.021Ω
Stator inductance L_s	0.0137 H
Rotor inductance L_r	0.0136 H
Mutual inductance L_m	0.0135 H
The friction coefficient f_r	0.0024 N.m.s^1
Slip g	0.03
Pole Pairs p	2

Table 2. Parameters of Turbine

Symbol	Value
Radius of the wind turbine R	35.25 m
Gear box G	90
inertia J	1000 kg.m ^{2}
Surface swept by rotor S	$\pi \cdot R^2$ m ^{2}
Air density ρ	1.22 kg/ m ^{3}

Table 3. Parameters of Feed

Symbol	Value
Stator rated voltage V_s	*398 / 690 V*
Rated frequency stator f	*50 Hz*
Rotor rated voltage V_r	*225 / 389 V*
Rated frequency stator f_2	*14 Hz*

Comparison of Quadrotor Performance Using Backstepping and Sliding Mode Control

A. Swarup and Sudhir

Abstract: A quadrotor is nonlinear, coupled and unstable system. Two control schemes, namely backstepping and sliding mode, have been applied to obtain desired trajectory tracking by quadrotor. This paper presents the comparative performance results of quadrotor under two control schemes.

***Keywords*:** Micro Quadrotor; Backstepping Control; Sliding Mode Control

I. INTRODUCTION

There are numerous applications of Unmanned Aerial Vehicles (UAVs) in defence and civil areas for monitoring, remote sensing, surveillance, dangerous environment etc. Quadrotor helicopter is an emerging rotor craft concept for UAV that consist of four rotors, with two pair of counter rotating, fixed pitch blades located at the four corners of the aircraft. A quadrotor is a dynamic vehicle with four input forces, six output coordinators, highly coupled and unstable dynamics [1-2]. Hence the design of a control law is an interesting challenge. Several linear methods, such as PID and LQR control method have been applied to control a quadrotor [3-4]. Since the quadrotor is a nonlinear system and for a good performance the nonlinear control methods have been attempted such as feedback linearization, sliding mode and backstepping control [9-11]. This paper presents two nonlinear control techniques applied to a micro quadrotor for developing a reliable control system for stabilization and trajectory tracking.

Nonlinear backstepping control technique forces the system to follow the desired trajectory [5-8]. A backstepping control algorithm was purposed [7] to stabilize the whole system and able to drive a quadrotor to the desired trajectory of Cartesian position and yaw angle. The backstepping control has been modified [9-11] to reduce the control parameters by half compared with the classical backstepping approach as given in [9]. A sliding mode controller was developed to ensure Lyapunov stability, and follow the desired trajectories [18].

The dynamical model of micro quadrotor is presented in section II. Backstepping control is explained in section III. Section IV describes the sliding mode control. The simulation results for quadrotor performance have been presented in section V. The control performance comparison is discussion in section VI.

II. DYNAMICAL MODEL OF QUADROTOR

The full order Quadrotor dynamical modelling has been presented in [5-11]. A quadrotor is an under actuated aircraft with fixed pitch angle four rotors as shown in fig. 1. These four rotors represent four input forces that are basically the thrust generated by each propeller. The collective input (u_1) is the sum of the thrusts of each motor. Pitch moment is obtained by increasing (reducing) the speed of the rear motor while reducing (increasing) the speed of the front motor. The roll movement is obtained similarly by increasing (reducing) the speed of the right motor while reducing (increasing) the speed of the left motor. The yaw movement is obtained by increasing (decreasing) the speed of the front and rear motors together while decreasing (increasing) the speed of the lateral motors together. The outputs of the system are *x*, *y* and *z*, which denote the position of the vehicle with respect to the earth frame, and *p*, *q* and *r*, which denote the angular velocity of the vehicle with respect to body frame.

The dynamic model is derived using Euler-Lagrange formalism [1], [5], [13]. The equations describing the dynamics of the micro quadrotor are [5],

$$\ddot{\emptyset} = \dot{\theta}\dot{\varphi}\left(\frac{I_y - I_z}{I_x}\right) - \frac{J_r}{I_x}\dot{\theta}\Omega + \frac{l}{I_x}U_2$$

$$\ddot{\theta} = \dot{\emptyset}\dot{\varphi}\left(\frac{I_z - I_x}{I_y}\right) - \frac{J_r}{I_y}\dot{\emptyset}\Omega + \frac{l}{I_y}U_3$$

$$\ddot{\varphi} = \dot{\emptyset}\dot{\theta}\left(\frac{I_x - I_y}{I_z}\right) + \frac{l}{I_z}U_4$$

$$\ddot{z} = -g + (cos\emptyset\ cos\theta)\frac{1}{m}U_1$$

$$\ddot{x} = (cos\emptyset\ sin\theta\ cos\varphi + sin\emptyset\ sin\varphi)\frac{1}{m}U_1$$

$$\ddot{y} = (cos\emptyset\ sin\theta\ sin\varphi - sin\emptyset\ sin\varphi)\frac{1}{m}U_1 \quad \text{..... (1)}$$

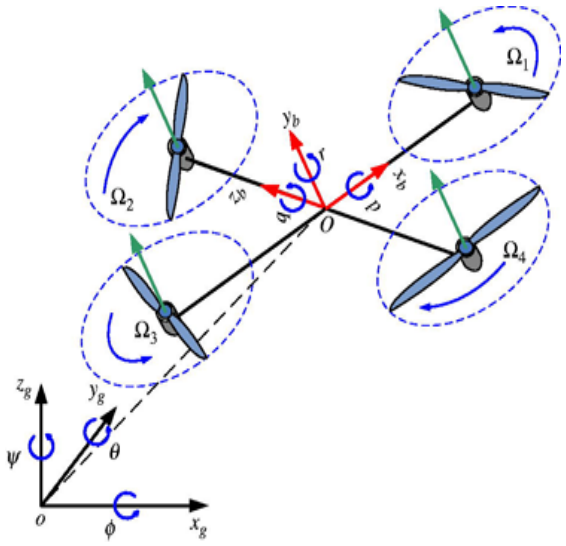

Fig.1:- Scheme of quadrotor helicopter

The first term in the orientation subsystem $(\emptyset, \theta, \varphi)$ is the gyroscopic effect resulting from the rigid body rotation in space and the second one is due to the propulsion group rotation. The system's input are expressed as U_1, U_2, U_3, U_4 and Ω a disturbance, obtaining:

A. Swarup and Sudhir are with Electrical Engineering Department, National Institute of Technology Kurukshetra, India-136119. (Emails: a.swarup@ieee.org, sudhir.nadda87@gmail.com)

$U_1 = b(\Omega_1^2 + \Omega_2^2 + \Omega_3^2 + \Omega_4^2)$
$U_2 = b(\Omega_4^2 - \Omega_2^2)$
$U_3 = b(\Omega_3^2 - \Omega_1^2)$
$U_4 = d(\Omega_2^2 + \Omega_4^2 - \Omega_1^2 - \Omega_3^2)$
$\Omega = \Omega_2 + \Omega_4 - \Omega_1 - \Omega_3$

The dynamic model presented in equation set (1) can be written in state space form as, $\dot{X} = f(X, U)$ by introducing state vector as

$X^T = [\emptyset, \dot{\emptyset}, \theta, \dot{\theta}, \theta, \varphi, \dot{\varphi}, z, \dot{z}, x, \dot{x}, y, \dot{y}]$
$x_1 = \emptyset$, $x_2 = \dot{x}_1 = \dot{\emptyset}$, $x_3 = \theta$, $x_4 = \dot{x}_3 = \dot{\theta}$, $x_5 = \varphi$, $x_6 = \dot{x}_5 = \dot{\varphi}$, $x_7 = z$, $x_8 = \dot{x}_7 = \dot{z}$, $x_9 = x$, $x_{10} = \dot{x}_9 = \dot{x}$, $x_{11} = y$, $x_{12} = \dot{x}_{11} = \dot{y}$ .....(2)

From (1) and (2) we obtained

$$\dot{x} = f(X,U) = \begin{pmatrix} x_2 \\ x_4 x_6 a_1 + x_4 a_2 \Omega + b_1 U_2 \\ x_4 \\ x_2 x_6 a_3 + x_2 a_4 \Omega + b_2 U_3 \\ x_6 \\ x_4 x_6 a_5 + b_3 U_4 \\ x_8 \\ -g + (cosx_1\ cosx_3)\frac{1}{m}U_1 \\ x_{10} \\ u_x \frac{1}{m} U_1 \\ x_{12} \\ u_y \frac{1}{m} U_1 \end{pmatrix} \quad .....(3)$$

where
$a_1 = (I_y - I_z)/I_x$ $a_2 = -J_R/I_x$ $a_3 = (I_z - I_x)/I_y$, $a_4 = -J_R/I_y$ $a_5 = (I_x - I_y)/I_z$
and
$b_1 = l/I_x$ $b_2 = l/I_y$ $b_3 = l/I_z$
and
$u_x = cosx_1\ sinx_3\ cosx_5 + sinx_1\ sinx_5$
$u_y = cosx_1\ sinx_3\ cosx_5 - sinx_1\ cosx_5$
The physical parameters of the model have been taken from [1].

Table 1.1

Symbol	Definition	Value
m	Mass	.650kg
I_x	Inertia on x axis	7.5e-3 kgm^2
I_y	Inertia on y axis	7.5e-3 kgm^2
I_z	Inertia on z axis	1.3e-2 kgm^2
b	Thrust coefficient	3.13e-5 Ns^2
d	Drag coefficient	7.5e-7 Nms^2
J_r	Rotor inertia	6e-5 kgm^2
L	Arm length	.23 m

The overall system described by (3) has two subsystems, the angular rotations and the linear translations [2]. The control scheme for the overall system is then logically divided in a position controller and a rotational controller.

III BACKSTEPPING CONTROL

In backstepping approach, the control law is synthesized to force the system to follow the desired trajectory [5-8]. Due to its complete independence from the other subsystem, firstly consider the control input for angular rotations subsystem and then the position control input is derived. The tracking error is defined as
$z_1 = x_{1d} - x_1$, and the Lyapunov function

$$V(z_1) = \frac{1}{2} z_1^2$$

Therefore

$$\dot{V}(z_1) = z_1(\dot{x}_{1d} - x_2)$$

Introducing the virtual control input x_2 for stabilization of z_1
$x_2 = \dot{x}_{1d} + \alpha_1 z_1$ with α_1>0
Then $\dot{V}(Z_1) = -\alpha_1 z_1^2$
Making the variable change

$$z_2 = x_2 - \dot{x}_{1d} - \alpha_1 z_1$$
$$V(z_1, z_2) = \frac{1}{2}(z_1^2 + z_2^2)$$

It follows,
$\dot{V}(z_1, z_2) = z_2(a_1 x_4 x_6 + a_2 x_4 \Omega + b_1 U_2) - z_2(\ddot{x}_{1d} - \alpha_1(z_2 + \alpha_1 z_1)) - z_1 z_2 - \alpha_1 z_1^2$
$\ddot{x}_{1,2,3d} = 0$, satisfying $\dot{V}(z_1, z_2) < 0$

So U_2 can be extracted as

$$U_2 = \frac{1}{b_1}(z_1 - a_1 x_4 x_6 - a_2 x_4 \Omega - \alpha_1(z_2 + \alpha_1 z_1) - \alpha_2 z_2)$$

U_3, U_4 and U_1 can be calculated with the same procedure

$$U_3 = \frac{1}{b_2}(z_3 - a_3 x_2 x_6 - a_4 x_2 \Omega - \alpha_3(z_4 + \alpha_3 z_3) - \alpha_4 z_4)$$

$$U_4 = \frac{1}{b_3}(z_5 - a_5 x_2 x_4 - \alpha_5(z_2 + \alpha_1 z_1) - \alpha_6 z_6)$$

and control input for translation subsystem is [4],

$$U_1 = \frac{m}{cosx_1 cosx_3}(z_7 + g - \alpha_7(z_8 + \alpha_7 z_7) - \alpha_8 z_8)$$
$$u_x = (m/U_1)(z_9 - \alpha_9(z_{10} + \alpha_9 z_9) - \alpha_{10} z_{10})$$
$$u_y = (m/U_1)(z_{11} - \alpha_{11}(z_{12} + \alpha_{11} z_{11}) - \alpha_{12} z_{12})$$
..... (4)

where
$z_3 = x_{3d} - x_3$
$z_4 = x_4 - \dot{x}_{3d} - \alpha_3 z_3$
$z_5 = x_{5d} - x_5$
$z_6 = x_6 - \dot{x}_{5d} - \alpha_5 z_5$
$z_7 = x_{7d} - x_7$
$z_8 = x_8 - \dot{x}_{7d} - \alpha_7 z_7$
$z_9 = x_{9d} - x_9$
$z_{10} = x_{10} - \dot{x}_{9d} - \alpha_9 z_9$
$z_{11} = x_{11d} - x_{11}$
$z_{12} = x_{12} - \dot{x}_{11d} - \alpha_{11} z_7$

IV SLIDING MODE CONTROL

The basic sliding mode controller design procedure is performed in two steps. Firstly, choice of sliding surface (S) is made according to the tracking error, while the second step consist the design of Lyapunov function which can satisfy the necessary sliding condition $(S\dot{S} < 0)$[9-11]. The

application of sliding mode control to quadrotor dynamic is presented here by obtaining the expression for control input. The sliding surface are define,

$$S_\emptyset = e_2 + \lambda_1 e_1$$
$$S_\theta = e_4 + \lambda_2 e_3$$
$$S_\varphi = e_6 + \lambda_3 e_5$$
$$S_x = e_8 + \lambda_4 e_7$$
$$S_y = e_{10} + \lambda_5 e_9$$
$$S_z = e_{12} + \lambda_7 e_{11}$$

Such that $\lambda_i > 0$ and $e_i = x_{id} - x_i \; e_{i+1} = \dot{e}_i \quad i \in [1,11]$

Assuming here that $V(S_\emptyset) = \frac{1}{2} S_\emptyset^2$ then, the necessary sliding condition is verified and Lyapunov stability is guaranteed. The chosen law for the attractive surface is the time derivative of (21) satisfying $(S_\emptyset \; \dot{S}_\emptyset < 0)$

$$\dot{S}_\emptyset = k_1 sign(S_\emptyset)$$
$$= \dot{e}_2 + \lambda_1 \dot{e}_1$$
$$= \ddot{x}_{1d} - \dot{x}_2 + \lambda_1 (\dot{x}_{1d} - x_2)$$
$$= -x_4 x_6 a_1 - x_4 a_2 \Omega - b_1 U_2 + \ddot{\emptyset}_d + \lambda_1 (\dot{\emptyset}_d - x_2)$$
$$U_2 = \frac{1}{b_1}(-k_1 sig(S_\emptyset) - a_1 x_4 x_6 - x_4 a_2 \Omega + \ddot{\emptyset}_d + \lambda_1 (\dot{\emptyset}_d - x_2))$$
$$= \frac{1}{b_1}(-k_1 sign(S_\emptyset) - a_1 x_4 x_6 - x_4 a_2 \Omega + \ddot{\emptyset}_d + \lambda_1 e_2)$$

The same steps are followed to extract $U_3, U_4, U_x, U_y \; and \; U_1$

$$U_3 = \frac{1}{b_2}(-k_2 sign(S_\theta) - a_3 x_2 x_6 - x_2 a_4 \Omega + \ddot{\theta}_d + \lambda_2 e_4)$$
$$U_4 = \frac{1}{b_3}(-k_3 sign(S_\varphi) - a_5 x_4 x_2 + \ddot{\varphi}_d + \lambda_3 e_6)$$
$$U_1 = \frac{m}{cosx_1 cosx_3}(-k_4 sign(S_z) + g + \ddot{z}_d + \lambda_4 e_8)$$
$$U_x = \frac{m}{U_1}(-k_5 sign(S_x) + \ddot{x}_d + \lambda_5 e_{10})$$
$$U_y = \frac{m}{U_1}(-k_6 sign(S_y) + \ddot{y}_d + \lambda_6 e_{12})$$

..... (5)

$$S_\emptyset = e_2 + \lambda_1 e_1 = \dot{x}_{1d} - x_2 + \lambda_1 (x_{1d} - x_1)$$
$$S_\theta = e_4 + \lambda_2 e_3 = \dot{x}_{3d} - x_4 + \lambda_2 (x_{3d} - x_3)$$
$$S_\varphi = e_6 + \lambda_3 e_5 = \dot{x}_{5d} - x_6 + \lambda_3 (x_{5d} - x_5)$$
$$S_z = e_8 + \lambda_4 e_7 = \dot{x}_{7d} - x_8 + \lambda_4 (x_{7d} - x_7)$$
$$S_x = e_{10} + \lambda_5 e_9 = \dot{x}_{9d} - x_{10} + \lambda_5 (x_{9d} - x_9)$$
$$S_y = e_{12} + \lambda_6 e_{11} = \dot{x}_{11d} - x_{12} + \lambda_6 (x_{11d} - x_{11})$$

IV SIMULATION RESULTS

Two nonlinear control techniques i.e. “Backstepping” and “Sliding Mode Control” have been exercised on nonlinear model of micro quadrotor to demonstrate the control performance. Several simulations are done in Matlab using model (3) with 12 parameters $(\alpha_1, \alpha_2 \ldots., \alpha_{12})$ controller and to reach the position $x_d = y_d = z_d = 2m$, with the initial condition $\frac{\pi}{4}$ rad for the three angles.

a) Backstepping control: The control inputs as derived equation (4) have been implemented to the nonlinear model in (3) and responses shown in fig. (3). Simulation have been performed for a desired position tracking from (0, 0, 0) to (2, 2, 2) given in fig. (2).

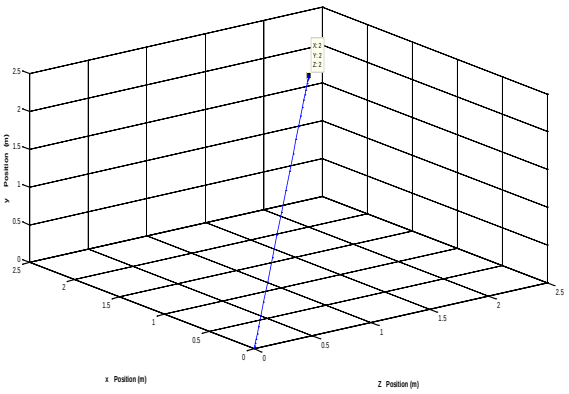

Fig. 2: Plot of position (*z*, *x*, *y*)

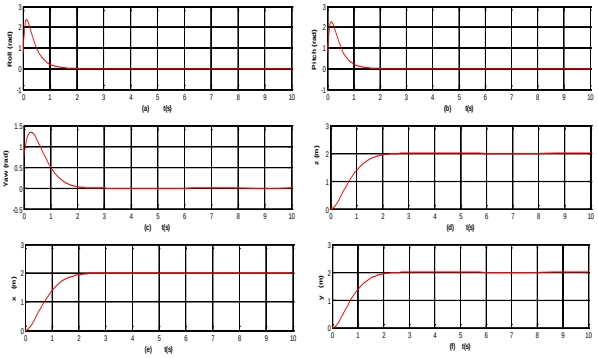

Fig. 3: Plot of roll, pitch, yaw and position (*x*,*y*,*z*) w.r.t. time

b) Sliding Mode Control: The sliding mode control inputs which were derived and expressed in equation (5) were applied to the nonlinear model in (3) and responses are shown in fig. (4). Quadrotor dynamics is stabilised following the given position.

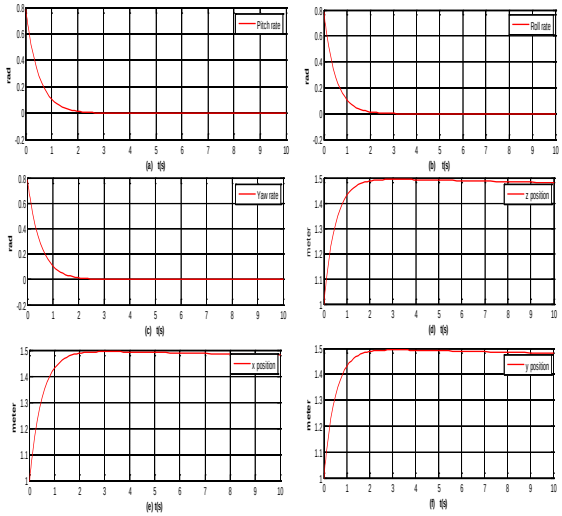

Fig. 4: Plot of roll, pitch, yaw and position (*x*,*y*,*z*) w.r.t. time

VI. CONCLUSION

This paper has considered two nonlinear control techniques (a. Backstepping Control, b. Sliding Mode Control) and a nonlinear unstable system, quadrotor which has several applications. The control equations have been derived for quadrotor dynamics. The control implementation has been exercised through simulation in MATLAB. The results have been presented here. Both the schemes stabilize the quadrotor as they are based on Lyapunov theory. Both the

ISBN: 978-1-61804-216-3

schemes are robust up to 10% change in parameters. However performance with sliding mode control is smooth and faster. This study has motivated to modify these schemes for further improvement in performance which is under study.

References

[1]. G.M. Hoffmann, H. Huang, S.L.Waslander, C.J.Tomlin, "Quadrotor Helicopter Flight Dynamics and Control: Theory and Experiment", American Institute of Aeronautics and Astronautics, pp. 01-20, 2007.

[2]. S. Bouabdallah P. Murrieri and R. Siegwart, "Design and control of an Indoor Micro Quadrotor", Proceeding of IEEE International Conference on Robotics and Automation New Orieans, pp. 4393-4398, April 2004.

[3]. B.Erginer and E. Altug, "Modelling and PD Control of a Quadrotor VTOL Vehicle", Intelligent Vehicle Symposium, pp. 1931-0587, 2007.

[4]. S. Bouabdallah, A.Noth and R. Siegwart, "PID vs LQ Control Techniques applies to an Indoor Micro Quadrotor", International Conference on Intelligent Robots and Systems, vol.3, pp. 2451 – 2456, 2004.

[5]. S. Bouabdallah and R. Siegwart, "Backstepping and Sliding-mode Techniques Applied to an Indoor Micro Quadrotor", Proceeding of IEEE International Conference on Robotics and Automation Barcelona, Spain, pp. 2259-2264, April 2005.

[6]. A.A. Main, W. Daobo, "Modeling and Backstepping-based Nonlinear Control Strategy for a 6 DOF Quadrotor Helicopter", Chinese Journal of Aeronautics 21, pp. 261-268, 2008.

[7]. T. Madani and A. Benallegue, "Backstepping Contol for a Quadrotor Helicopter", Proceeding of International Conference on Intelligent Robots and System, pp. 3255-3260, October 9-15, 2006.

[8]. A.W.A. Saif, M. Dhaifullah, M.A.Malki and M.E. Shafie, "Modiffied Backstepping Control of Quadrotor", International Multi-Conference on System, Signal and Devices, 2012.

[9]. V.G. Adir, A.M.Stoica and J.F. Whidborne, "Sliding Mode Control of 4Y Octorotor", U.P.B. Sci. Bull., Series D, Vol.74, Iss. 4, pp. 37-51,2012.

[10]. H. Bouadi, M. Bouchoucha and M. Tadjine, "Sliding Mode Control Based on Backstepping approach for an UAV Type-Quadrotor", World Academy of Science, Engineering and Technology 2, pp. 22-27, 2007.

[11]. K. Runcharoon and V. Srichatrapimuk, "Sliding Mode Control of Quadrotor" International Conference of Technological Advances in Electrical, Electronics and Computer Engineering, pp. 552-556 May 9-11, 2013.

[12]. Z.T. Dydek, A.M. Annaswamy and E. Lavretsky, "Adaptive Control of Quadrotor UAVs: A design Trade Study With Flight Evaluation", IEEE Trans. on Control Systems Tech., Vol. 21, No.4, pp. 1400-1406, July 2013.

[13]. Y.M.Younes, M.A.A.Jarrah and A.A.Jhemi, "Linear vs Nonlinear Control Technology for a Quadrotor Vehicle", Proceeding of the 7th International Symposium on Mechatronics and its Application, Shajah,UAE, April 20-22, 2010.

[14]. I.C. Dikmen, A.Arisoy and H.Temeltas, "Attitude Control of a Quadrotor", Proceeding of: Recent Advances in Space Technologies, pp. 722-727, 2009.

[15]. Y.Yali, S. Feng and W. Yuanxi, "Controller Design of Quadrotor Aerial Robot", International Conference on Medical Physics and Biomedical Engineering, pp. 1254-1260, 2012.

[16]. Z. Fang, X.Y. Wang and J. Sun, "Design and Nonlinear Control of an Indoor Quadrotor Flying Robot", Proceeding of the 8th World Congress on Intelligent Control and Automaton, pp. 429-434, China, July 6-9, 2010.

[17]. J.J.E. Slotine and W.li, "Applied Nonlinear Control", Prentice-Hall, Inc.,USA, 1991.

[18]. H.Bouadi, M.Bouchouha and M. Tadjine, "Sliding Mode Control based on Backstepping Approach for an UAV Typed-Quadrotor", World Academy of Science, Engineering and Technology, pp. 22-27, 2007.

Dr. Akhilesh Swarup received his Ph.D. in 1993 from the Indian Institute of Technology (IIT), New Delhi, India. He is currently working as Professor in the Department of Electrical Engineering at the National Institute of Technology (N.I.T), Kurukshetra, India. He is a Senior Member of the Institute of Electrical and Electronics Engineers (IEEE). His research interests include robotics and artificial intelligence, system identification and control systems.

Sudhir had received the Masters in Technology (M.Tech.) in the field of Electrical Engineering with specialization "Signal Processing and Control" from National Institute of Technology, Hamirpur (India) in 2011, he is pursuing research in the field of Nonlinear System Analysis and Control from National Institute of Technology, Kurukshetra (India). His fields of interest are Nonlinear Control Systems, Optimal Control Technique and Robust Control.

An Experimental Simulation of a Design Three-Port DC-DC Converter

Samir M. Shariff, Ahmad M. Harb, Hu Haibing, and Issa E. Batarseh

***Abstract*—**Traditional dc-dc converter topologies interface two power terminals: a source and a load. The construction of diverse and flexible power management and distribution (PMAD) systems with such topologies is governed by a tight compromise between converter count, efficiency, and control complexity. The broader impact of the current research activity is the development of enhanced power converter systems suitable for a wide range of applications. Potential users of this technology include the designers of portable and stand-alone systems such as laptops, hand-held electronics, and communication repeater stations. High power topology options support the evolution of clean power technologies such as hybrid-electric vehicles (HEV's) and solar vehicles. DC-DC converter is considered as an advanced environmental issue; since it is a greenhouse emission eliminator. By utilizing the advancement of these renewable energy sources, we minimize the use of fossil fuel. Thus, we will have a cleaner and pollution free environment. In this paper, a three-port DC-DC converter have been designed and discussed. The converter was built and tested at the energy research laboratory at Taibah University, Al Madinah, KSA.

.

***Keywords*—**Three port DC-DC Converter; Power Management and Distribution; Clean Power; buck-boost; Zero volt switching; Power Storage.

I. Introduction

The integrated power electronic converters are important for systems that are capable of harvesting power from solar sources, fuel cells and mechanical vibrations used in applications such as communication repeater stations, sensor networks, hybrid electric vehicles and laptops [1-10]. Moreover, multi-terminal interface is important since such systems require mass energy storage to compensate for the mismatch between the sourcing and loading power patterns over a regular operational cycle. For example, a solar system, consisting of a regulated load interfaced to a solar array, requires storage batteries for storing excess power and re-supplying it to the load when needed. Limited research activities on multi-terminal converter topologies have been reported in open literature, with very few commercially installed systems in industry. Interesting ideas for multi-sourced converters with multiple control variables have been introduced based on the fly back (buck-boost) converter topology.

An investigation of conventional system architectures, composed of two-terminal converters, emphasizes the significance of the advent of practical and flexible single-stage multi-terminal converters. Following on the battery-backed solar system example, the main candidate architectures are [11-17]:

1. *Two stage interface:* The solar array is interfaced to an intermediate battery-dominated bus allowing MPPT, as shown in
2. Fig. **1**, with another converter stage interfaces that bus to the load. The main disadvantage of this scheme is that solar power goes through two loosely conversion stages, before reaching the load.
3. *Independent charge and discharge:* The battery bidirectional converter can be split into two unidirectional converters: a charger interfaced to the input bus, and a discharge converter interfaced to the load bus, as seen in Fig. 2. This assures that power goes through one conversion stage when traveling between any two terminals, allowing for higher efficiency. The price paid is an additional converter, increasing the size, weight, cost, component count, and control complexity of the system.

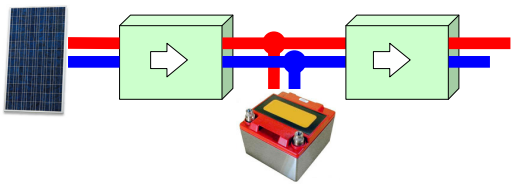

Fig. 1 Two stage solar power system.

We would like to acknowledge the funding of this project (08-ENE416-5) by the Science and Technology Unit at Taibah University through the National Science, Technology and Innovation Plan for Saudi Arabia.

S. M. Shariff is with Taibha University Electrical Engineering Dept and the Science and Technology Unit, Medinah, Saudi Arabia. (Phone: 00966503710195; e-mail: samshariff@ yahoo.com).

Ahmad M. Harb is with German Jordanian University, Aman, Jordan (e-mail: author@lamar. colostate.edu).

Hu Haibing, and Issa E. Batarseh are both with the Electrical Engineering Department, University Central Florida, USA, (e-mail: author@nrim.go.jp).

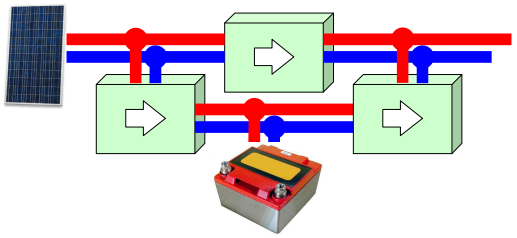

Fig. 2 Three-converter solar power system.

We believe that due to the added complexity, together with increased losses, size, weight, and cost, as well as decreased reliability, has impeded wide-spread adoption of such architectures for many applications. The potentially profitable MPPT technology has been very difficult to justify in many applications given the cost and control complexity overhead. An integrated three-terminal converter that performs the functions of the three-converter structure using a single power stage can overcome these challenges, and is thus very attractive. The proposed three-ports DC-DC converter will be used in so many real applications such as hybrid cars, communication towers and solar arrays.

Innovation in the Power Stage

Single converter stage interface of three power terminals is targeted: a source, a load, and a bidirectional terminal for power storage. Isolation through a transformer is required for the load terminal for:

1. Design flexibility with high voltage step-up/down ratios
2. Flexible series/parallel converter connection in modular designs, and compatibility with NASA's Series Connected Boost Regulator (SCBR) concept, [10], as well as the Power Electronics Building Blocks (PEBB's) approach [11].
3. User/operator safety

Achieving the power management objectives using a two-converter approach requires a minimum of one non-isolated and one isolated topology. The addition of a third converter helps increase efficiency, and requires an additional isolated converter. Options for converter selection are summarized below. Note that buck-boost and fly-back converters are not considered since they are not practically suitable for medium and high power applications due to large inductor/transformer current values, and high output capacitor current ripple.

The use of a buck or a boost, together with a push-pull converter, allows a small switch and diode count, but requires too many magnetic components. The transformer required has a center-tapped input, reducing the utilization efficiency of the core. Replacing the push-pull with a half-bridge or an active clamp forward circuit simplifies the transformer, but requires the addition of a storage capacitor. The full-bridge option is more suitable for higher power levels and lower input voltages at the cost of a high active switch count.

II. Analysis, Modeling and Control of Three-Prot DC-DC Converter of Use

The three-port DC-DC Converter, shown in Fig. 3, is the modified version of PWM half bridge converter that includes three basic circuit stages within a constant-frequency switching cycle to provide two independent control variables. The switching sequence shown in the figure ensures a clamping path for the energy of the leakage inductance of the transformer at all times. This energy is further utilized to achieve zero-voltage switching (ZVS) for all primary switches for a wide range of source and load conditions.

Full-bridge converters are more suitable for higher power applications, typically above 1kW. Applying the same concept of dual use of the phase legs, a three-terminal topology can be derived from the full-bridge circuit. The bidirectional terminal of this topology is controlled by changing the duty cycle of the phase legs to achieve the target voltage ratio. The two phase legs need to maintain equal duty cycles. The load terminal is controlled by phase shifting the driving waveforms of these two phase legs relative to each other, just like the ZVT full-bridge topology.

The steady-state voltage relationships, assuming CCM operation of the load filter inductor, are given by:

$$V_{bi} = D \cdot V_{in} \qquad (1)$$

$$V_o = 2 \cdot n \cdot \phi \cdot V_{in}, \qquad (2)$$

given that $0 \le \phi \le \min(D, 1-D)$

where: D is the duty cycle of each phase leg

ϕ is the phase shift between the two phase leg waveforms

This topology operates as boost-derived push-pull converter when supplying energy from the bidirectional terminal to the load. This topology is thus an attractive alternative for low voltage storage devices since it saves on the turns-ratio of the transformer and simplifies its design. The center-tapped transformer and the bidirectional terminal inductor assembly are suitable for being wound on a single core, in an integrated magnetic fashion.

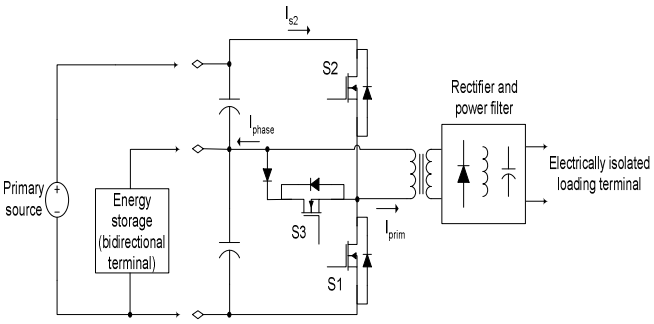

Fig. 3Three-port DC-DC converter topology.

ISBN: 978-1-61804-216-3

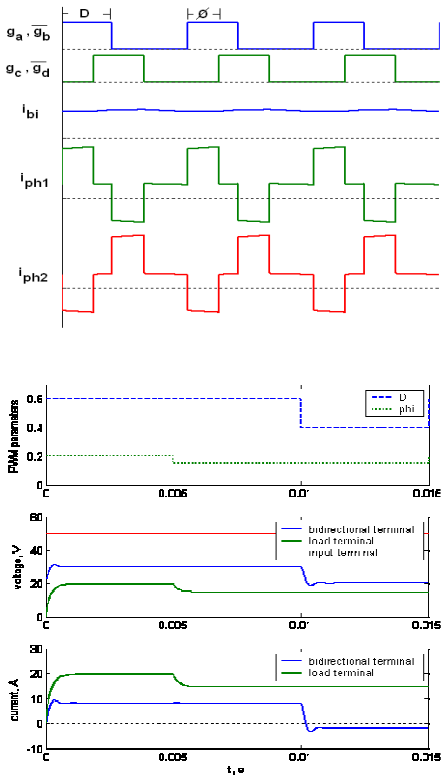

Fig. 4 Simulation waveforms (a) basic switching waveforms (b) terminal voltages and currents.

PLECS simulation results are shown in Fig4. Again, control was adjusted at t=5ms and at 10ms to independently control the voltages of the load and bidirectional terminals. Converter ability to handle negative current in the bidirectional terminal was verified. The small signal model is tailored for deriving multi-port DC-DC converters under different modes of operation. It is difficult to define different modes since there are various modes of operation. After we define the mode, a competitive method is used to realize smooth and seamless mode transition.

As we mentioned before, the converter topologies proposed in this work present new control challenges to the power electronics community. The proposed topologies call for a PWM that creates switching waveforms that have two independent variables, based on two error signals, derived by two feedback controllers, each tightly regulating a different control variable. Also we mentioned that digital control is a strong candidate for such topologies because of its flexibility, and the ability to perform complicated feed-forward and loop decoupling functions. Digital control is an indispensable tool for the development phase, since it is capable of realizing a variety of customized modulator structures. The digital control architecture that is used to regulate different power ports is shown in Fig. 5. There are many control loops named as follows;

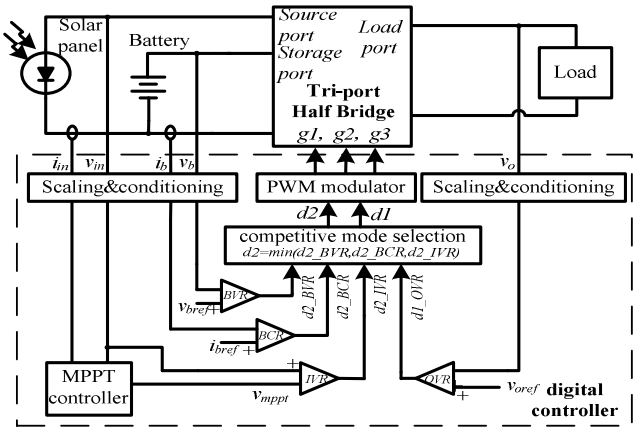

Fig. 5. Digital Controller of Multi-port Converter for MPPT.

1- Input voltage regulation (IVR),
2- Output voltage regulation (OVR),
3- Battery voltage regulation (BVR), and
4- Battery current regulation (BCR).

III. Experimental Results

Fig. 6 illustrates a 200 W prototype. Power stage's input port, battery port and output port are marked as in the prototype photo. It consists of two boards, power stage board and controller board.

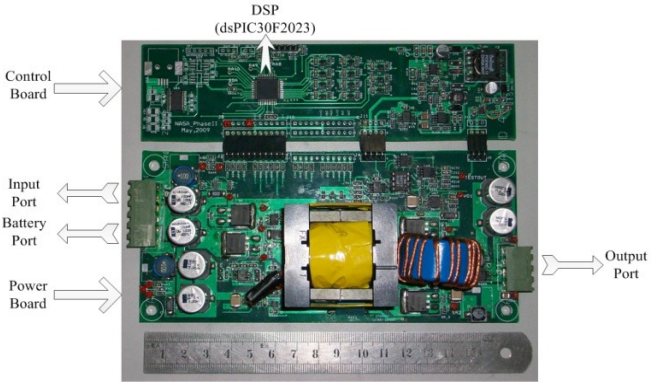

Fig. 6 Prototype photo of three-port converter which consists of one controller board and one power board.

The values of circuit parameters used in the simulation and experimental circuit are listed in the following table I.

TABLE I: VALUES OF CIRCUIT PARAMETERS

output inductor	Lo	65μH	output voltage	Vo	24V
magnetizing inductor	Lm	45μH	input voltage	Vin	60V
output filter capacitor	Co	680μF	battery voltage	Vb	28V
battery port filter capacitor	C1	680μF	input port filter capacitor	C2	210μF

The mode transition and control structure for both operational modes are tested through a 200 W prototype.

ISBN: 978-1-61804-216-3

Power stage's input port, battery port and output port are marked as in the prototype photo. It consists of two boards, power stage board and controller board. All feed-back control loops' compensators are implemented by a direct digital design method.

Fig. 7 shows the waveforms when the power is transferred from input port to the output load port, while battery port is chosen to be open. Output inductor current ILo has four stages, and transformer magnetizing average current Ipri is zero, implying no battery power. Fig. 8 shows the waveforms when the most power is transferred from input port to the battery port. Output inductor current ILo average represents the load current, which is zero. Therefore, negative ILo is observed. Ipri average value represents the battery current, which is 7A.

Fig. 9, Fig. 10 and Fig. 11 show the gating signal Vgs and switching node Vsw wave forms of the switches S1, S2 and S3, respectively. The conclusion is that all three main switches can achieve ZVS, because they all turn on after their Vds go to zero.

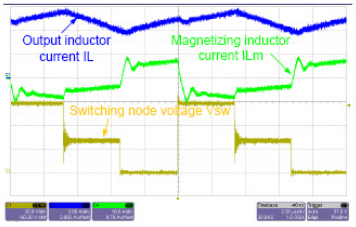

Fig. 7 Loading output port when the battery current is zero.

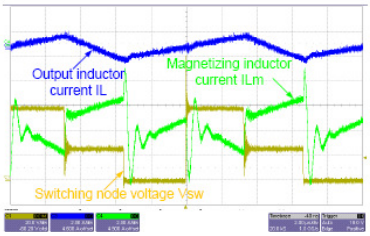

Fig. 8 Loading battery port when the output current is zero.

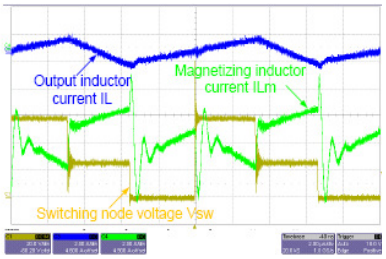

Fig. 9 ZVS for S1.

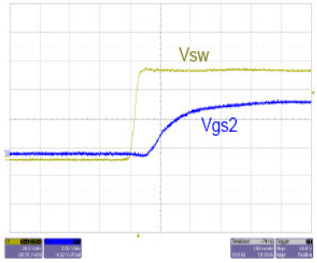

Fig. 10 ZVS for S2.

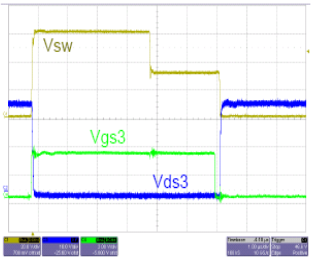

Fig. 11 ZVS for S3.

Fig. 12, Fig. 13 and Fig. 14 show the efficiency curves when the power is transferred from one port to the other port. The highest efficiency is observed when the power is transferred from solar port to battery port. The reason is that this operation has minimal transformer losses, since the power is exchanged within the primary side.

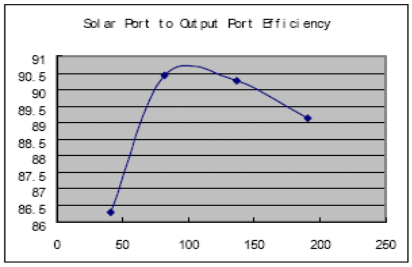

Fig. 12 The efficiency when the power is transferred from solar port to output port.

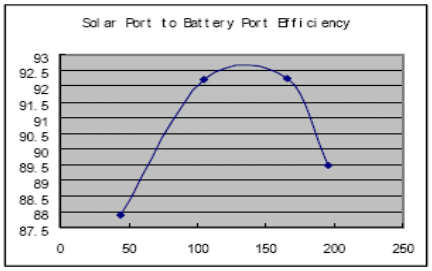

Fig. 13 The efficiency when the power is transferred from solar port to battery port.

ISBN: 978-1-61804-216-3

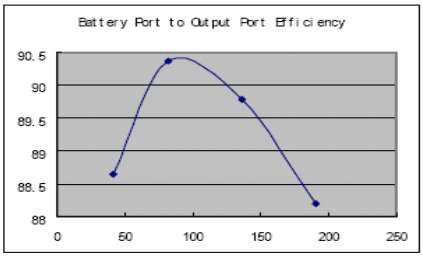

Fig. 14 The efficiency when the power is transferred from battery port to output port.

Fig. 15(a) shows mode transition from Battery-balanced Mode (Mode 1) to Battery regulation Mode (Mode 2) when battery maximum voltage setting of 29 V is reached. Solar panel first works under IVR control with MPPT to maximize solar power, then it is forced to operate in solar panel's voltage source region when IVR loses control and BVR takes control over d2, so the input port provides power balance after the transition into battery regulation mode. It can be seen that the transition of the proposed competitive method is smooth and causes no oscillation that is experienced with the sudden transition of duty cycles. The battery voltage has 0.5V overshoot, and input voltage has 2.5V overshoot, both are within acceptable range according to specifications.

Fig. 15(b) gives Mode 2 to Mode 1 transition when load level suddenly increases to force the battery to source instead of sink. Since battery voltage setting cannot be met during discharging, d2 will be controlled by IVR since BVR quickly loses control, and solar panel quickly reacts to work under MPPT control so as to harvest maximum available solar power, and battery becomes to provide the power balance in Mode 1.

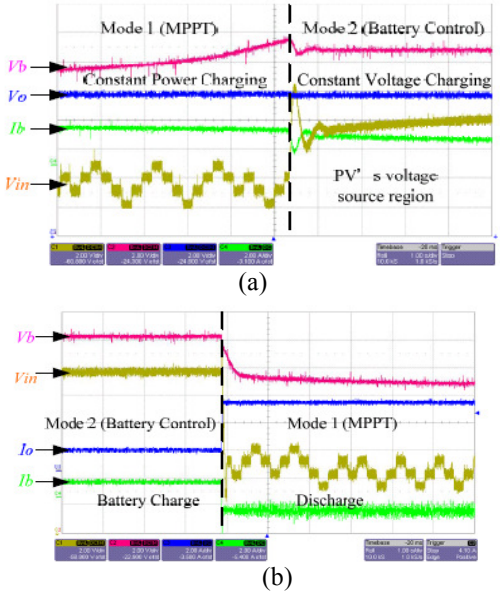

Fig15 Autonomous mode transition, (a) Mode 1 to Mode 2; (b) Mode 2 to Mode 1.

Fig. 16(a) shows the input voltage, battery voltage and output voltage response to a load transient between 1A and 3A in Battery-regulation Mode. Output voltage transient response of 500us settling time is much faster than battery voltage settling time of 40ms because OVR bandwidth is ten times larger than that of BVR. Input voltage changes according to load level changes because input port provides power balance. Fig. 16(b) demonstrates the system transient response in Battery-balanced Mode when MPPT is active. The load step is from 1A to5A. Input voltage response to load transient of 20ms settling time is much slower than output voltage settling time of 500us because IVR crossover frequency is set at one tenth of that of OVR. Input voltage remains uninterrupted at around MPP even during load changes, which is the unique feature of three-port converters, because MPPT and load regulation cannot be achieved simultaneously by conventional two-port converter.

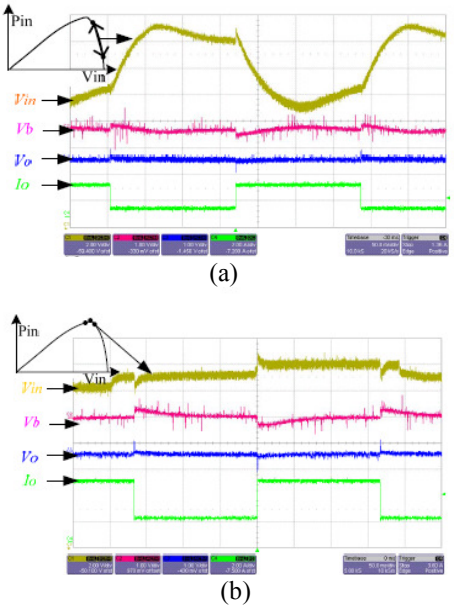

Fig. 15 (a) Battery-regulation Mode load step response, (b) Battery-balanced Mode load step response.

IV. Conclusions

In this paper, a new three-port converter interfacing the renewable energy input, battery terminal as well as output terminal is proposed. Its operation principle is analyzed in details and a small signal model is derived to guide the controller design. Simulation was carried out to verify the proposed converter. Experimental results show that the proposed converter has the capability of regulating the output voltage while maintaining the power balance between inputs and output power, which is very suitable for renewable energy applications.

ISBN: 978-1-61804-216-3

REFERENCES

[1] A. Capel, "The power system of the multimedia constellation satellite for the Skybridge Missions," in Proc. IEEE Power Electronics Specialists Conf., 1998, pp. 1913-1930.

[2] H.W. Brandhorst, M.J. O'Neill, M. Eskenazi, "Photovoltaic options for increased satellite power at lower cost," in Proc. IEEE Photovoltaic Energy Conversion, 2003, pp. 849 - 852.

[3] S. Jang, J. Choi, "Energy balance analysis of small satellite in Low Earth Orbit (LEO)," in Proc. IEEE Power and Energy Conference, 2008, pp. 967 - 971.

[4] R. D. Middlebrook and S. Cuk, "A General Unified Approach to Modeling Switching-Converter Power Stages," International Journal of Electronics, vol. 42, pp.521 - 550, June 1977.

[5] S. Cuk, "Modeling, Analysis, and Design of Switching Converters," Ph.D. thesis, California Institute of Technology, November 1976.

[6] A. Di Napoli, F. Crescimbini, L. Solero, F. Caricchi and F.G. Capponi, "Multiple-input DC-DC Power Converter for Power-flow Management in Hybrid Vehicles," in Proc. IEEE Industry Application Conf., 2002, pp. 1578 - 1585.

[7] W. Jiang, B. Fahimi, "Multi-port Power Electric Interface for Renewable Energy Sources," in IEEE 2009 Applied Power Electronics Conference, 2009, pp.347-352.

[8] W. G. Imes, and F. D. Rodriguez, "A Two-Input Tri-State Converter for Spacecraft Power Conditioning," in Proc. AIAA International Energy Conversion Engineering Conf., 1994, pp. 163 - 168.

[9] F. D. Rodriguez, and W. G. Imes, "Analysis and Modeling of A Two-Input DC/DC Converter with Two Controlled Variables and Four Switched Networks," in Proc. AIAA International Energy Conversion Engineering Conf., 1994, pp. 322 - 327.

[10] B. G. Dobbs, and P. L. Chapman, "A Multiple-Input DC-DC Converter Topology, " in IEEE Power Electronics Letters, vol. 1, pp. 6-9, March 2003.

[11] N. D. Benavides, and P. L. Chapman, "Power Budgeting of a Multiple-Input Buck-Boost Converter, " IEEE Trans. Power Electronics, vol. 20, pp. 1303-1309, November 2005.

[12] H. Matsuo, W. Lin, F. Kurokawa, T. Shigemizu and N. Watanabe, "Characteristics of the Multiple-Input DC–DC Converter, " IEEE Trans. Industrial Applications, vol. 51, pp. 625 - 631, June 2004.

[13] L. Solero, F. Caricchi, F. Crescimbini, O. Honorati, and F. Mezzetti, "Performance of A 10 kW Power Electronic Interface for Combined Wind/PV Isolated Generating Systems," in Proc. IEEE Power Electronics Specialists Conf., 1996, pp. 1027-1032.

[14] L. Solero, A. Lidozzi, and J.A. Pomilio, "Design of Multiple-Input Power Converter for Hybrid Vehicles," in Proc. IEEE Applied Power Electronics Conf., 2004, pp. 1145 - 1151.

[15] Gui-jia Su, and F.Z. Peng, "A Low Cost, Triple-Voltage Bus DC-DC Converter for Automotive Applications," in Proc. IEEE Applied Power Electronics Conf., 2005, pp.1015 - 1021.

[16] F. Z. Peng, H. Li, G. J. Su and J. S. Lawler, "A New ZVS Bidirectional dc-dc Converter for Fuel Cell and Battery Applications, " IEEE Trans. Power Electronics, vol. 19, pp. 54-65, January 2004.

[17] H. Tao, A. Kotsopoulos, J.L. Duarte, M.A.M Hendrix, "Multi-Input Bidirectional DC-DC Converter Combining DC-link and Magnetic-coupling for Fuel Cell Systems," in Proc. IEEE Industry Applications Conf., 2005, pp. 2021- 2028.

[18] Nayfeh, A. H., and Balachandran B., Applied Nonlinear Dynamics, John Willy, New York, 1995.

[19] K. Chakrabarty, G. Poddar, and S. Banerjee, "Bifurcation behavior of the buck converter,"IEEE Trans. Power Electron., vol. 11, no. 3, pp. 439–447, May 1996.

[20] S. Maity, D. Tripathy, T. K. Bhattacharya, S.Banerjee, "Bifurcation Analysis of PWM-1 Voltage-Mode-Controlled Buck Converter Using the Exact Discrete Model", IEEE Trans. Circuits and systems, vol.54, no. 5, May 2007.

Samir M. Shariff. Born in London 1972, Ph.D. EE Wichita State University, Wichita KS, USA, 2000, M.S.E.E and B.S.EE both from Washington University – St. Louis MO, USA, 1996/1994.

He is currently working at Tahibah University, Head of the Strategic Research Unit, Head of Binladin Scientific Chair on Operation and Maintenance, and Faculty member at the electrical engineering department, Medinah, Saudi Arabia; Dr. Shariff was working at Saudi Aramco till 2004 at the PMT department; before that he was employed at Saudi Binladin Group-Operation and Maintenance Co. as a Project Manger in Makkah Haram Project till 2002. He is interested in the area of Renewable Energy, Control Theory, Power Systems, Electromagnetics, Cold Plasma and Engineering Education. Dr. Shariff is a member of the IEEE and is working on several funded mega projects.

Ahmad M. Harb receive the B.S. degree from Yarmouk University, Irbid-Jordan, in 1987, M.S. degree from the Jordan University of Science & Technology, Irbid-Jordan, in 1990, and the Ph.D. degree from Virginia Polytechnic Institute and State University, Blacksburg, Virginia, USA, in 1996, all in Electrical Engineering. Dr. Harb is an Associate Professor at Jordan University of Science & Technology, Electrical Engineering Department. Dr. Harb is IEEE senior member. His research interests include power system analysis and control, modern nonlinear theory (bifurcation & chaos), linear systems, power system planning, electric machines, optimal control, and power electronics.

Hu Haibing is a Professor of electrical engineering at School of Automation Engineering Nanjing University of Aeronautics and Astronautics, Nanjing, China. He got his B.E from Industrial Automation, Hunan University of Technology, Jul.1995, his MS from Power electronics and electric drive, Zhejiang University, Mar.2003 and his PhD from Power electronics and electric drive, Zhejiang University, Mar.2007. His research interests power electronics DC-DC converter and AC-DC inverter.

Issa Batarseh is a Professor and Director of the School of Electrical Engineering and Computer Science at the University of Central Florida (UCF). He received the Ph.D., and M.S. in Electrical Engineering and the B.S. in Electrical and Computer Engineering from the University of Illinois at Chicago in 1983, '85 and '90, respectively. Dr. Batarseh was a visiting Assistant Professor at Purdue University, Calumet, from 1989 to 1990 before joining UCF in 1991.
Dr. Batarseh's power electronics research focuses on the development of high frequency power converters for solar energy conversion, and to improve power density, power factor, efficiency and performance. The research includes the analysis and design of high frequency dc-to-dc resonant converter topologies; dc-ac inverters, low-voltage dc-dc converters, small signal modeling and control of PWM and resonant converters; power factor correction techniques; power electronic circuits for distributed power systems applications. His has published many journal and conference papers and a textbook entitled "Power Electronic Circuits" in 2003.
Dr. Batarseh is a co-founder for two start-up companies: Advanced Power Electronics Corp. (APECOR) and Petra Solar.

Design of Neural Network for Rehabilitation Robotics

Bassant M. Elbagoury, Thomas Schrader, Meteb M. Altaf,SayedA.Banawan,Mohamed Roushdy

***Abstract*—** *Rehabilitation robotics systems are a very important problem, especially in the therapeutic domain of stroke patients. This is due to the complexities of patients' treatments procedures such as physiotherapy and the dealing with Electromyography (EMG) signals, which provides significant source of information for identification of neuromuscular disorders. This paper presents a new rehabilitation robotics control design that depends on neural networks and real-time EMG Analysis. The neural network robot control design along with EMG performance analysis is presented in this paper. It also presents a comparison between the performances of Levenberg – Marquardt based neural network classifier and Support Vector Machine Classifier (SVM) in classification of EMG signal. This is designed for Rehabilitation robotic system.*

Keywords— Rehabilitation robotics, Real-time EMG signalanalysis,Levenberg – Marquardt neural network

I. Introduction

Rehabilitation robotics is directed to improve mobility and independence in daily life of patients. It uses specific ex-cises related to the therapeutic problem and patients practice movements. The rehabilitation robotics controls this automatically. The pattern of movements follows a theoretical concept developed and disseminated by respected authorities. However, now the proof of evidence for each concept is missing. Especially, no validated data to compare different therapeutic strategies are missed. The health economical demand is to demonstrate the effectiveness of robotics and rehabilitative procedures [1].

F.A. ***Bassant M. Elbagoury*** is Assistant Professor of Computer Science, Faculty of Computers & Information Sciences, Ain Shams University, Cairo, Egypt. She is also visiting assistant professor of computer science, college of computers & information technology, taif university, taif, KSA. Email: bassantai@yahoo.com

S.A. ***ThomasSchrader*** is IEEE member and with the Department of Informatics and Media, University of Applied Sciences Brandenburg, D-14770 Brandenburg, Germany, e-mail: thomas.schrader@computer.org.

T.A. ***Meteb M. Altaf*** is assistant professor of mechanical engineering and director of national robotics and intelligent systems, KACST, Riyad, KSA.

Fourth A. ***Sayed A. Banawan*** is associate professor of computer science, college of computers & information technology, Taif University, taif, KSA. banawan@outlook.com

Fifth Author ***Mohamed Roushdy***is Professor of Computer Science & Dean of Faculty of Computers & Information Sciences, Ain Shams University, Cairo, Egypt. miroushdy@hotmail.com3

Many neuromuscular disorders that affect the nerves and muscles are hereditary and cause death need early detection and diagnosis by clinical investigations. This in turns will help in finding out the best method of treatment of these disorders. These investigations may include biochemical and DNA analysis in order to identify the defected cells.

A stroke is a medical emergency. It occurs when the blood supply to part of the brain is suddenly interrupted or when a blood vessel in the brain bursts, spilling blood into the spaces surrounding brain cells. Brain cells die when they no longer receive oxygen and nutrients from the blood or there is sudden bleeding into or around the brain. The symptoms of a stroke include sudden numbness or weakness, especially on one side of the body; sudden confusion or trouble speaking or understanding speech; sudden trouble seeing in one or both eyes; sudden trouble with walking, dizziness, or loss of balance or coordination; or sudden severe headache with no known cause. There are two forms of stroke: ischemic - blockage of a blood vessel supplying the brain, and hemorrhagic - bleeding into or around the brain.

Although stroke is a disease of the brain, it can affect the entire body. A common disability that results from stroke is complete paralysis on one side of the body, called hemiplegic. A related disability that is not as debilitating as paralysis is one-sided weakness or hemi paresis. Stroke may cause problems with thinking, awareness, attention, learning, judgment, and memory. Stroke survivors often have problems understanding or forming speech. A stroke can lead to emotional problems. Stroke patients may have difficulty controlling their emotions or may express inappropriate emotions. Many stroke patients experience depression. Stroke survivors may also have numbness or strange sensations. The pain is often worse in the hands and feet and is made worse by movement and temperature changes, especially cold temperatures.

Since Electromyography (EMG) detects muscle response during different actions, it gives useful identification of the symptoms' causes. Such disorders that can be identified by EMG are neuromuscular diseases, Nerve injury, and Muscle degeneration.

II. Previous Work

Many researches were made in the field of EMG signal classification using different techniques. In [4] we applied support vector machine with different kernel functions (Polynomial, Quadratic, RBF) on the same dataset and compared between their classification accuracies and we

ISBN: 978-1-61804-216-3

found out that the best of them was RBF kernel function with sigma = 1.

In [2], [5] and [6] the EMG signal classified using ANN with different learning algorithms to recognize different hand movements. The two back-propagation algorithms used are Levenberg-Marquardt and Scaled Conjugate Gradient. Levenberg-Marquardt showed better classification performance. The outcomes of the research show that the optimal design of Levenberg-Marquardt based neural network classifier can perform well with an average classification success rate of 88.4%.

Features of the MUAP clusters extracted then classified the MUAPs according to pathology using multi-class support vector machine (SVM) classifier. The classification accuracy of multi-class SVM with AR features was 100% [7].

In [8] one against all method multi-class SVM with Gaussian kernel function was implemented to identify six degree of freedom. During the training, the classifier was able to adapt each subject's motion of the forearm. During testing with the untrained data, the multi class support vector machine was unaffected by little variations in the feature values. The overall rate of correct class testing was 97%.

In [9] Support Vector Machines (SVM) was employed to extract classes of different force intensity from the EMG signals. The average accuracy in the case of thirteen classes reached about 96%.

In [10] four electromyography (EMG) sensors were used. They placed at the thigh and two force sensing resistors (FSR) placed below the heel and the toe. Support vector machine was used to detect muscular activity changes. This system has reached accuracies of roughly 67% for an amputee and of 75% for a non-amputee individual.

The feed-forward ANN with Levenberg-Marquedt back-propagation training algorithm was used in [11] with two other classification methods in constructing a learning scheme for the EMG-based teleoperation of a robotic arm-hand system in reach-to-grasp movements in 3D space.

Levenberg-Marquedt back-propagation training algorithm was also used in [12] as a part of a control system for a robotic hand to predict the grasping forces according to the multisensory signals. This network showed good convergence to the experimental results.

This algorithm was also used in [13] side by side with adaptive neuro-fuzzy inference system (ANFIS) in the classification of EEG signals. The experiments showed that both classifiers with the proposed approach resulted in satisfactory classification accuracy rates.

It also used in [14] in comparing different classifiers based on EEG mu and beta rhythm recording.

III. Rehabilitation Robotics System Architecture

Rehabilitation robotics refers to the use of robotic devices (sometimes called "rehabilitators") that physically-interact with patients in order to assist in movement therapy [16][17]. Figure 1. Shows robot system, as shown, it consists of EEG, ECG and EMG sensors, signal processing unit & robotic controller unit along with wireless sensor network (WSN) module. In this paper, we focus only on neural network controller part of the robotics system and the EMG sensor analysis. Each is presented in details in coming sections.

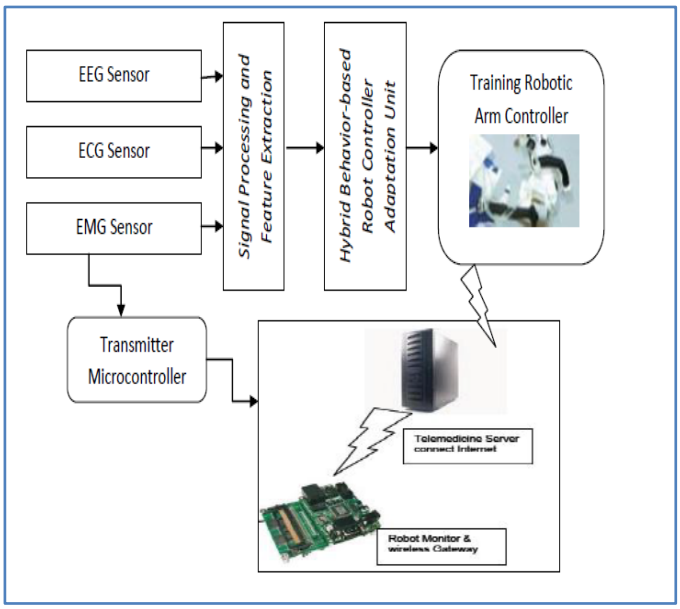

Fig.1 Architecture of Rehabilitation Robotics Systems

IV. Architectural Design of ANN

In this paper we used Multilayer perceptron Neural Network which consists of 3 layers: input layer, tan-sigmoid hidden layer and a linear output layer. The basic architecture of feed-forward back-propagation based network is shown in Fig.1. Each layer of hidden and output layer has a weight matrix W, a bias vector b as inputs and an output vector a. The weight vectors associated with inputs are called input weights (IW) and weight vectors which are inputs to hidden layer are called layer weights (LW). Additionally, superscripts are used to denote the source (second index) and the destination (first index) for the various weights, biases, and other elements of the network. *P* is the input vector, *n* is the layer output before transfer function and *a* is the actual output vector of a layer.

The designed ANN was found to perform well when it designed with 8 inputs, 10 tan-sigmoid neurons in the hidden layer and one neuron in the output layer. Deciding the number of neurons in the hidden layers is a very important part of deciding the overall neural network architecture. It is confirmed in the simulation that the hidden-output connection weights become small as the number of hidden neurons becomes large, and also that the trade-off in the learning stability between input-hidden and hidden-output connections exists. Using too few neurons in the hidden layers results in that the network cannot adjust the weights and biases properly during training which result in something called under-fitting. Under-fitting occurs when there are too few neurons in the hidden layers to adequately detect the signals in a complicated data set. Using a large number of hidden neurons may deteriorate the performance of the network. It essentially

ISBN: 978-1-61804-216-3

requires huge memory to store huge numbers of network variables and hence training becomes complicated [3].

The next step after designing the ANN and selecting the number of neurons in the hidden layer is to determine the back-propagation learning algorithm which is required to adjust weights and biases at different layers. Back-propagation training algorithm basically sets the weights and biases to minimize the performance (Mean Square Error - MSE) by using the gradient of the performance function. The classification efficiency of ANN depended on the selection of proper feature set, network structure, and training algorithm. For this research, Levenberg – Marquardt (trainlm) learning algorithm was applied. The numerical optimization techniques based Levenberg-Marquardt is the fastest and powerful method for training of moderate-sized feed-forward neural networks [2].

The Levenberg-Marquedt (LM) algorithm is very simple, but robust, method for approximating a function. It is an iterative technique that locates the minimum of a multivariate function that is expressed as the sum of squares of non-linear real-valued functions. LM can be thought of as a combination of steepest descent and the Gauss-Newton method. The update rule of the steepest descent algorithm could be written as [15]:

$$w_{k+i} = w_k - \alpha g_k \quad (1)$$

Where α is the learning constant (step size).
From Newton's method we have:

$$\Delta w = -H^{-1} g \quad (2)$$

Where H is the Hessian matrix, then from (1) and (2) the update rule for Newton's can be represented by:

$$w_{k+1} = w_k - H_k^{-1} g_k \quad (3)$$

Hessian matrix H can be obtained using Jacobian matrix J using the following function:

$$H \approx J^t J \quad (4)$$

And the relationship between Jacobian matrix J and gradient vector g would be represented by:

$$g = Je \quad (5)$$

From (3), (4) and (5) the update rule of LM algorithm can be presented as:

$$w_{k+1} = w_k - \left(J_k{}^t J_k\right)^{-1} J_k e_k \quad (6)$$

Where e is the error vector containing the output errors for each input vector used on training the network. In order to make sure that the approximated Hessian matrix$J^t J$is invertible, LM algorithm introduces another approximation to Hessian matrix:

$$H \approx J^t J + \lambda I \quad (7)$$

Where λ is the combination coefficient and I is the identity matrix. From equations (6) and (7) the update rule of LM algorithm can be presented as:

$$w_{k+1} = w_k - \left(J_k{}^t J_k + \lambda I\right)^{-1} J_k e_k \quad (8)$$

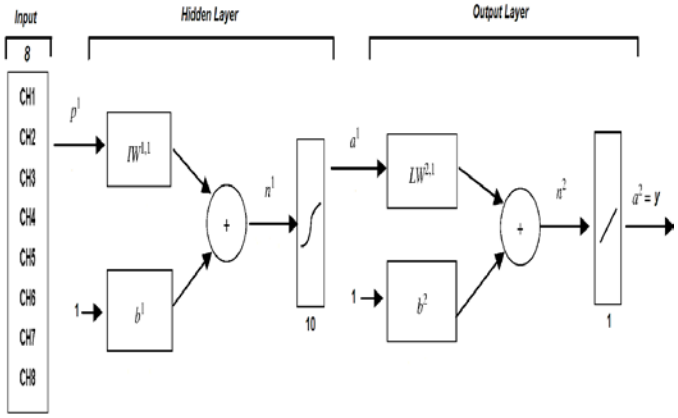

Fig.2 Architecture of Artificial Neural Network

V. MATERIALS AND METHODS

A. Sensors & Wireless Sensor Network

The Wireless Sensor Network was build up by usage of commercial available Shimmer-Sensors (Figure 3). A sensor consists of a motherboard with a Class 2 Bluetooth radio module and can be added by a daughterboard for various applications.

The EMG sensor is combined with a motion detector consisting of a gyroscope and an accelerometer for angular and linear velocity. The EMG provides pre-amplification of the signal with a sampling rate of 512 or 1024 Hz. The signal range lies between 4mV and +4mV.

Fig.3 The EMG-Shimmer Commercial Sensor

The EMG sensors were placed on eight muscles. M. biceps, femoris, M. vastuslateralis and M. titbialisanteriors. The sensor node data were collected by teMultisync-software by shimmer with a sampling rate of 512 Hz. This means for EMG signals the signal acquisition covered frequencies up to max.

VI. EMG FEATURES EXTRACTION

The analytical process of EMG covers three different aspects: time-analysis, frequency-analysis and dynamical analysis. Task of time analysis is the detection of activity and rest state, the duration and characteristics of these states (amplitudes, mean of activity, standard deviation). The meanwhile standard procedure in EMG-signal processing is [18], [19]:

- rectification of the signal
- decorrelation EMG from DC
- creation of envelope curve of EMG (we used a low pass, equiripple FIR-filter at 10 Hz (different frequencies are reported in literature [19]–[20]) The envelope curve increases the possibility to differentiate between activity and rest phases and can be used to detect these phases automatically by application of a threshold. In this study a separate rest EMG was measured as basis EMG. The threshold was calculated by the mean of rectified signal + 3 x standard deviation.

A. Time Domain Analysis

The time analysis evaluates the behavior of the emg signal over time: e.g. frequency of activity phases, their duration and intensity. The following parameter can be calculated easily [6],[7]:

- Amplitude of each activity state and mean of a set ofactivity states including their standard deviation
- Duration of activity states
- Area under the curve in activity states
- Velocity of onset and onset of activity state
- Comparison between different types of efforts and theiractivity states in contrast to the rest state and betweenthem.
- Time related pattern of activity states in case of multichannel measurements.

B. Frequency domain analysis

The frequency analysis can be used to detect various aspects of the signal. Intensity of activation and fatigue of muscle correlate with pattern of frequency and their changes. Two main frequency domain parameter in EMG signals are [18], [19], [21], [23]:

- Mean Frequency (MNF)

$$MNF = \frac{\sum_{i=1}^{N} f_i P_i}{\sum_{i=1}^{N} P_i} \tag{9}$$

- Median Frequency (MDF)

$$MDF = \frac{1}{2}\sum_{i=1}^{N} P_i \tag{10}$$

Other parameter can be derived from the frequency domain

- Total Power the aggregation of power spectrum (TTP) corresponds to the zero statistical moment [9], [10]

$$TTP = \sum_{i=1}^{N} P_i \tag{11}$$

- Mean Average Power of EMG signal (MNP) [9], [10]

$$MNP = \frac{\sum_{i=1}^{N} P_i}{N}$$

- Peak Frequency the frequency with the maximum ofpower [6], [7]
- Spectral Moments of power spectrum [9], [10]
  - SM0 corresponds to TTP
  - SM1

$$SM1 = \sum_{i=1}^{N} f_i P_i$$

  - SM2

$$SM2 = \sum_{i=1}^{N} f_i^2 P_i$$

  - SM3

$$SM3 = \sum_{i=1}^{N} f_i^3 P_i \tag{15}$$

Beside the frequency analysis based on Fourier Transformation, the wavelet transformation can be quite useful in noise reduction , detecting very fast as well as very slow changes and self-similarity [23], [24].

C. Dynamic System Analysis

The methods described until now based on assumption of a linear system model. However, the effects of the neurological signal transduction at the neuromuscular junction and the recruitment of muscle fibers maybe not linear. The Recurrence Quantification Analysis (RQA) is a nonlinear method to analysis surface EMG signals and was used in many other biosignal analysis domains such as electrocardiogram and encephalogram analysis. The result of RQU is a visualization of a square matrix representing system states over the time [13]. In a first step, the mono-channel EMG signal is transformed into the phase space by means of time delay procedure. The signal is shifted by a number of samples. The calculation of the shifting number can be done

by first zero of autocorrelation. Same states in phase space are visualized in the recurrence plot, can be quantified by histograms and expressed as:

- Recurrence Rate

$$RR = \frac{1}{N}\sum_{i,j=1}^{N} R_{i,j}$$

- Determinism diagonal lines is the recurrence plots express a deterministic behavior and is calculated as:

$$DET = \frac{\sum_{l=l_{min}}^{N} lP(l)}{\sum_{l=1}^{N} lP(l)}$$

The surface EMG is a summation of many single muscleunit action potentials (MUAP). MUAPS are repeating events for each muscle fiber. It is expected that more MUAPS are activated synchronously and create a deterministic pattern at RQA analysis [19].
For this analysis the RQA was calculated using algorithms of Hasson et al. [26].

VI. EXPERIMENTAL RESUTLS

A. *EMG data and information*

EMG data analysis allows the identification of activity and rest states, their properties (duration, amplitudes, area under the curve etc.) and their dynamical behavior. In the course of experiment with different tasks (eyes open, eyes closed, throw back a ball), the activity states have different durations and amplitudes indicating different level of stress. Especially the phase of closed eyes increased the frequency and duration of activity states. Changes of MDF and MNF can indicate an increase offatigue. Nevertheless, these observed changes in MDF andMNF do not correlate to changes of fatigue but rather they arelinked to the stress of experimental situation. The dynamicalanalysis shows an increase of determinism depending on the duration of the activity state. Shorter activity states have a lower determinism. It seems that the synchronization of MUAPS takes some time. For an activity shorter than 0.5 sec the percentage of determinism is lower than 0.1, for an activity state longer than 1.5 sec the percentage of determinism reach 0.6.

B. *DATASET DESCRIPTION*

EMG Normal activities to be classified by our work are clapping, handshaking, hugging, running, while aggressive activities are elbowing, hammering, header, kneeing, pulling, and slapping.TABLE Ishows samples of data of actions used in our study.
8 electrodes are used for the 8 input time series (one for each muscle channel (ch1–8)): right bicep (ch1), right triceps (ch2), left bicep (ch3), left triceps (ch4), right thigh (ch5), right hamstring (ch6), left thigh (ch7), and left hamstring (ch8).

TABLE 1: Different EMG Muscles Channels Processed Values

Actions	***Ch1***	***Ch2***	***Ch3***	***Ch4***	***Ch5***	***Ch6***	***Ch7***	***Ch8***
Kneeing	299	79	606	-790	1185	-63	809	-1009
Pulling	667	-1078	-1077	921	1016	658	-833	955
Hammer	48	-911	2077	1343	2120	884	-556	-1514
Header	-292	-69	-20	114	-1030	-63	53	18
Clapping	-85	22	-259	-68	282	-37	-33	-175
Handshaking	-51	2	-9	-3	-72	24	47	10
Running	131	-91	2018	-75	4000	-4000	-1999	267
Hugging	129	85	1507	-81	0	64	54	62
Elbow	-245	266	2615	-29	-4000	-549	-4000	4000
Slap	-1194	1185	-40	426	-321	1118	3103	-610

In this work, we divided EMG dataset into five groups each group has two actions kneeing and pulling, Hammering and Header, Clapping and Handshaking and Elbowing and Slapping. Each group consists of 348 training and 116 testing instances. For each group of actions a different neural network has been designed and trained and its performance has been measured with the help of statistical analysis of mean squared normalized error performance function. Each designed ANN structure has been trained by Levenberg – Marquardt training algorithm and then tested for classifying completely unknown EMG signals of the same actions. Graphical presentations in (Fig. 4., Fig. 5., Fig. 6., Fig. 7., Fig. 8.) shows the error histogram and training validation and test errors during training (clapping and handshaking, kneeing and pulling, hammering and headering, for running and hugging, elbowing and slapping) datasets consequently using Levenberg – Marquardt training algorithm. The extracted feature vectors for different actions are fed into the trained network without the corresponding target vectors. Classification accuracy of Levenberg – Marquardt based neural network classifier was 90% for clapping and handshaking, 91% for kneeing and pulling, 75% for hammering and headering, 98% for running and hugging and 88% for elbowing and slapping. Table 2 presents a comparison between performances of support vector machine with RBF kernel function and the Levenberg – Marquardt based ANN applied to train and classify the same dataset.

ISBN: 978-1-61804-216-3

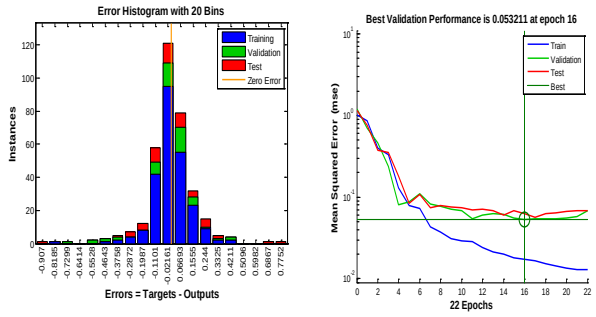

Fig.4 (a) Error histogram and (b) Training Validation and Test errors for Clapping and Handshaking

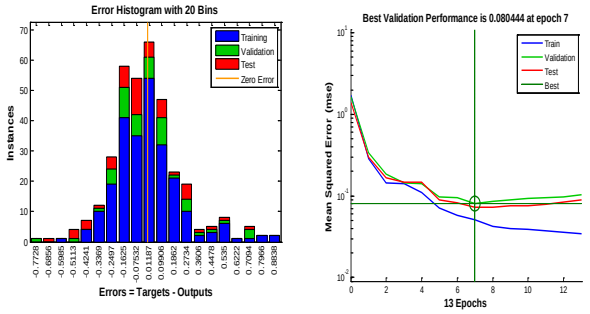

Fig.5 (a) Error histogram and (b) Training Validation and Test errors for Kneeing and Pulling

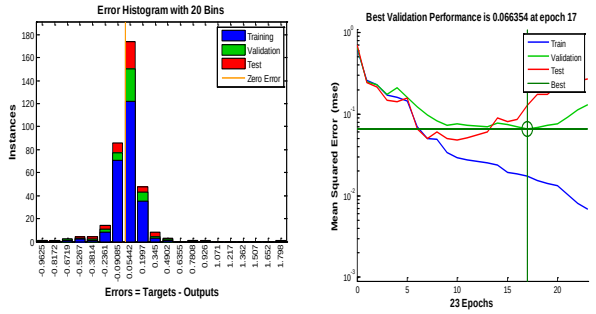

Fig.6 (a) Error histogram and (b) Training Validation and Test errors for Hammering and Headering

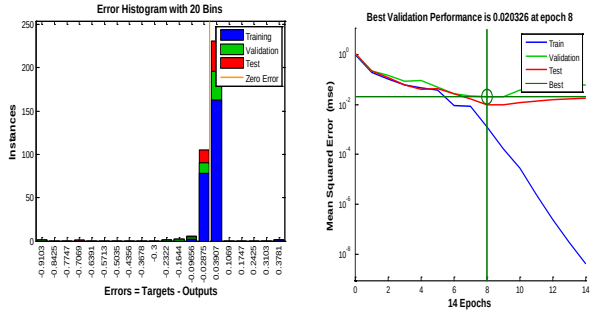

Fig.7 (a) Error histogram and (b) Training Validation and Test errors for Running and Hugging

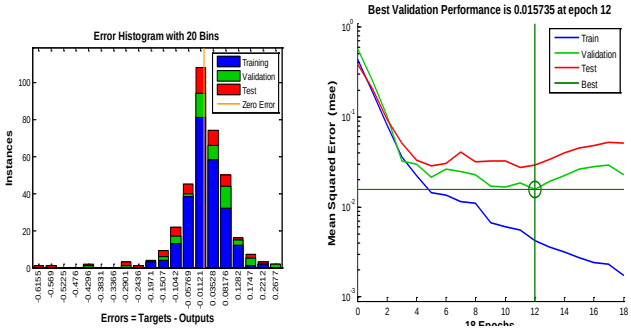

Fig.8 (a) Error histogram and (b) Training Validation and Test errors for Elbowing and Slapping

TABLE 2: Comparison of Classification performance for different techniques

Methodology	Actions				
	Knee /Pull	Hammer / Header	Clapp / Handshake	Run/ Hug	Elbow / Slap
SVM RBF sigma=1	90%	82%	94%	98%	83%
LM-ANN	91%	75%	90%	98%	88%

III. CONCLUSIONS

Rehabilitation robotics systems can facilitate and help stroke patients to move about almost without restrictions. However, the analysis of real-time EMG sensors in very complex. Also, the selection of accurate neural network classifier is very hard. In this paper,Thefeed-forward ANN with Levenberg-Marquadt back-propagation algorithm has been trained with 8 real-time features extracted from 8-channel EMG signal to classify different normal and Auto-aggressive actions. The performance of the application of this algorithm shows better accuracy in most of actions groups. The designed ANN structure has not yet been tested for the EMG signals from disabled people. Also, the overall robotics controller will be further investigated within European union research.

REFERENCES

[1] UCI homepage, [Online], Available: http://archive.ics.uci.edu/ml/datasets/

[2] M.I. Ibrahimy and Md. RezwanulAhsan, *Design and Optimization of Levenberg-Marquardt based Neural Network Classifier for EMG Signals to Identify Hand Motions*, MEASUREMENT SCIENCE REVIEW, Vol. 13, No. 3, 2013.

[3] http://www.heatonresearch.com/node/707

[4] NahlaFarid, BassantElbagoury, M.Roushdy and Abdel BadeehM.Salem, *A Comparative Analysis for Support Vector Machines for Stroke Patients*, WSEAS, Recent Advances in Information Science, ISBN: 978-960-474-304-9, 2013.

[5] Md. R. Ahsan, M.I. Ibrahimy, and O.O. Khalifa, *Neural Network Classifier for Hand Motion Detection from EMG Signal*, BIOMED 2011, IFMBE Proceedings 35, pp. 536–541, 2011.

[6] M.I. Ibrahimy, M.R. Ahsan and O.O. Khalifa, *Design and Performance Analysis of Artificial Neural Network for Hand Motion Detection from EMG Signals*, World Applied Sciences Journal 23 (6): 751-758, ISSN 1818-4952, 2013.

[7] GurmanikKaur, AjatShatruArora and V.K. Jain, *Multi-Class Support Vector Machine Classifier in EMG Diagnosis*, WSEAS Transactions on Signal Processing, Vol.5, No.12, pp. 1790-5052, 2009.

[8] Navleen Singh Rekhi, A S Arora, Sukhwinder Singh and Dilbag Singh, *Multi-Class SVM Classification of Surface EMG signal for Upper Limb Function*, Indian Journal of Biomechanics, 2009.

[9] Zeeshan O Khokhar, Zhen G Xiao and Carlo Menon, *Surface EMG pattern recognition for real-time control of a wrist exoskeleton*, BioMedical Engineering OnLine, 2010.

[10] Alexander Boschmann, Paul Kaufmann, and Marco Platzner, *Accurate Gait Phase Detection using Surface Electromyographic Signals and Support Vector Machines*, 2011.

[11] Minas V. Liarokapis andPanagiotis K. Artemiadis, *Learning Task-Specific Models for Reach to Grasp Movements: Towards EMG-based Teleoperation of Robotic Arm-Hand Systems*, 2012.

[12] Somer M. Nacy, Mauwafak A. Tawfik andIhsan A. Baqer,*Grasping Force Prediction for Underactuated Multi-Fingered Hand by Using Artificial Neural Network*, Control Theory and Informatics, ISSN 2224-5774, Vol 3, No.1, 2013.

[13] Mahmut HEKIM, *ANN-based classification of EEG signals using the average power based on rectangle approximation window*, PRZEGLĄD ELEKTROTECHNICZNY (Electrical Review), ISSN 0033-2097, R. 88 NR 8/2012

[14] Richard Nordstrom and Annika Tangmark, *Classification of Electroencephalographic Signals For Brain-Computer Interface*, [Online], 2013, Available :http://www.csc.kth.se/utbildning/kth/kurser/DD143X/dkand13/Group10Pawel/report/RichardN_report.pdf

[15] http://www.eng.auburn.edu/~wilambm/pap/2011/K10149_C012.pdf

[16] Yasuhisa Hasegawa and SaoriOura, "Exoskeletal meal assistancesystem (emas ii) for progressive muscle dystrophy patient", in *Proc.IEEE Int Rehabilitation Robotics (ICORR) Conf*, 2011, pp. 1–6.

[17] Masatoshi Nakamura, "Meal assistance system operated by electromyogram (emg) movement onset detection with adaptive threshold", *International Journal of Control, Automation, and Systems*, vol. 8, no. 2, pp.392–397, 2010.

[18] L. Sornmo, Bioelectrical signal processing in cardiac and neurologicalapplications. Elsevier Academic Press.

[19] Electromyography: physiology, engineering, and noninvasive applications,ser. IEEE Press series in biomedical engineering. IEEE/JohnWiley& Sons.

[20] A. Phinyomark, S. Thongpanja, H. Hu, P. Phukpattaranont, and C. Limsakul, "The usefulness of mean and median frequencies in electromyography analysis," in Computational Intelligence in Electromyography Analysis - A Perspective on Current Applications and Future Challenges, G. R. Naik, Ed. InTech. [Online]. Available: http://www.intechopen.com/books/computationalintelligence-in-electromyography- analysis-a-perspective-on-currentapplications-and-future-challenges/the-usefulness-of-mean-and-medianfrequencies-in-electromyography-analysis

[21] A. Phinyomark, P. Phukpattaranont, and C. Limsakul, "Feature reduction and selection for EMG signal classification," vol. 39, no. 8, p. 74207431. [Online]. Available: http://dx.doi.org/10.1016/j.eswa.2012.01.102

[22] W. Kuniszyk-Jzkowiak, J. Jaszczuk, T. Sacewicz, and I. Codello, "Time-frequency analysis of the EMG digital signals." vol. 12, no. 2, p. 1925.[Online]. Available: http://dblp.unitrier. de/db/journals/umcs/umcs12.html.Kuniszyk-JozkowiakJSC12

[23] A. Attenberger and K. Buchenrieder, "Wavelet-based detrending for EMG noise removal." in ECBS, J. W. Rozenblit, Ed. IEEE, p. 196202. [Online]. Available: http://dblp.unitrier. de/db/conf/ecbs/ecbs2013.html.AttenbergerB13

[24] A. Subasi, "Classification of EMG signals using PSO optimized SVM for diagnosis of neuromuscular disorders," vol. 43, no. 5, p. 576586.[Online]. Available: http://dx.doi.org/10.1016/j.compbiomed.2013.01.020

[25] S. Wallot, R. Fusaroli, K. Tyln, and E.-M.Jegind, "Using complexity metrics with r-r intervals and BPM heart rate measures," vol. 4. [Online]. Available: http://www.frontiersin.org/Computational Physiology and Medicine/10.3389/ fphys.2013.00211/abstract

[26] C. Hasson, R. Van Emmerik, G. Caldwell, J. Haddad, J. Gagnon, and J. Hamill, "Influence of embedding parameters and noise in center of pressure recurrence quantification analysis," vol. 27, pp. 416–422.

A Novel Programmable Current Reference with FGMOSFETs

V. Suresh Babu, Varun P. Gopi, Salini Thankachan, and M. R. Baiju

***Abstract*—High performance analog, digital and power electronic systems need stable, temperature and supply independent reference current. This paper proposes a programmable current reference using floating gate MOSFETs (FGMOSFETs). Multiple reference current can be obtained from the same circuit by programming FGMOSFETs. Subtraction technique is used to compensate the effects of variation in supply voltage and temperature. The proposed circuit has an output current varying from 473.09 nA to 15.71 μA. The circuit performs well over a temperature range of 0°C to 100°C and supply voltage range of 0.5 V to 2.5 V. The circuit has a very low temperature dependency of 1.9 nA/°C and supply voltage dependency of 10.28 nA/V respectively. This circuit avoids the need for re-design and re-fabrication for different values of output current.**

***Keywords*—Floating gate MOSFET(FGMOSFET), bias voltage, subtraction technique, temperature dependency, supply voltage dependency**

I. Introduction

Present day mixed signal circuits become very much attractive as the integrated system gets larger and complex. Highly stable current reference is needed for proper working of analog, digital and power systems. More often band gap reference (BGR) is used to obtain reference current. The positive temperature coefficient of BGR is compensated to obtain stable output current [1]-[3]. In standard CMOS process, only lateral parasitic bipolar transistors are available. So these circuits have poor performance. Temperature effect can be reduced by mutual cancellation of mobility and threshold voltage [4], [5]. But the circuits using on-chip resistors and bipolar junction transistors are heavily affected by the process variation. Off-chip resistors increase cost and area [2]. Sub-threshold design and body effects are also used for temperature compensation. Cascaded and feedback structure provides better power supply rejection ratio [6] -[8]. By multiplying a current source which is proportional to mobility and one which is inversely proportional to mobility, temperature dependence can be reduced [9].

FGMOS based circuits are suitable for low voltage applications. The programmability of FGMOS provides post fabrication adjustment of output [10]-[14]. The threshold voltage of FGMOS is programmable by varying one of the control voltage (V_{bias}). A temperature compensated programmable reference voltage is obtained by the charge difference between two Floating Gate transistors [15]. A simple method to obtain supply and temperature compensation is the subtraction technique. By subtracting two current outputs with the same dependencies on the supply voltage and temperature, stable reference current can be obtained [16], [17].

This paper presents a FGMOS based programmable current reference with temperature and supply voltage compensation. The circuit works with a supply voltage as low as 0.5 V. This paper is organized as follows: in section II, the FGMOSFET structure and its principle of operation is explained. Section III describes the proposed programmable current reference circuit. Section IV presents the mathematical analysis of the proposed circuit. In section V, simulation results are presented and conclusion is made in section VI.

II. FLOATING GATE MOSFET (FGMOS)

The FGMOS differs from a conventional MOSFET in that it has one more gate called the floating gate (FG). A Floating Gate MOS Transistor consists of a conventional MOS transistor with its gate surrounded by SiO_2. Since the gate surrounded by SiO_2 has no DC path to a fixed potential, it is known as Floating Gate. The floating gate is formed by the first poly-silicon layer, while the multiple-input gates are formed by the second poly-silicon layer located above the floating gate. Layout and symbol of FGMOSFET is shown in Fig. 1.

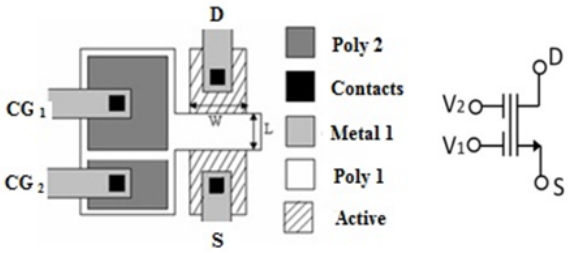

Fig. 1: Layout and symbol of FGMOS

Fig. 2 shows the equivalent schematic of a typical n-channel, N-input FGMOS. The inputs are only capacitively connected to the Floating Gate (FG), since the FG is completely surrounded by highly resistive material. So, in terms of its DC operating point, the FG is a floating node. The conduction of the FGMOS transistor is different from that of conventional MOS transistor having the same terminal potential, due to

V. Suresh Babu is with the Department of Electronics and Communication Engineering, Government Engineering College, Painavu, Idukki, Kerala, India (e-mail: vsbsreeragam@gmail.com.)

Varun P. Gopi is with the Department of Electronics and Communication Engineering, Government Engineering College, Mananthavady, Wayanad, Kerala, India (e-mail: vpgcet@gmail.com.)

Salini Thankachan is with the Department of Electronics and Communication Engineering, St. Joseph's College of Engineering, Palai, Kerala, India (e-mail: salini003@gmail.com.)

M. R. Baiju is with the Department of Electronics and Communication Engineering, Government Engineering College, Thiruvananthapuram, Kerala, India (e-mail: mrbaiju@gmail.com.)

ISBN: 978-1-61804-216-3

the capacitive coupling between the Floating Gate and control gates. When a voltage is applied to the control gates, capacitive coupling between the control gate and Floating Gate induces an electrical field on the FG. The induced field on the Floating Gate modifies the conductance of underlying channel region [10]-[14], [18].

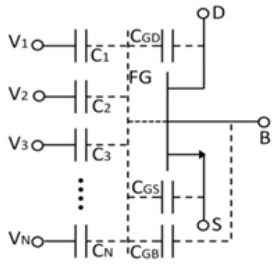

Fig. 2: Equivalent circuit of N input FGMOSFET

The voltage on FG for a two-input FGMOS [10] with $V_S = V_D = 0$ V is given by

$$V_{FG} = \frac{C_1}{C_T}V_1 + \frac{C_2}{C_T}V_2 + \frac{C_{fgd}}{C_T}V_D \tag{1}$$

where $C_T = C_1 + C_2 + C_{fgs} + C_{fgd} + C_{fgb}$ is the total FG capacitance. C_1, C_2 represents the input capacitances and V_1, V_2 represents the voltages applied on the input gates. C_{fgs}, C_{fgd} and C_{fgb} denote the capacitances from FG to source, drain and bulk respectively.

The drain current of the FGMOS in saturation region is given by (2)

$$I_D = \frac{\beta}{2}\left[\left(\frac{C_1}{C_T}V_1 + \frac{C_2}{C_T}V_2 + \frac{C_{fgd}}{C_T}V_{DS}\right) - V_T\right]^2 \tag{2}$$

Where $\beta = \mu C_{OX}\frac{W}{L}$ is the transconductance parameter. C_{OX} is the gate-oxide capacitance per unit area, μ is the mobility, $\frac{W}{L}$ is the width to length ratio of MOSFET and V_T is the threshold voltage.

III. THE PROPOSED PROGRAMMABLE CURRENT REFERENCE CIRCUIT

The proposed current reference is a voltage controlled current source, where the output current (I_{out}) varies according to the bias voltage (V_{bias}). The circuit diagram of the proposed FGMOS based programmable current source is shown in Fig. 3. The circuit is made programmable by FGMOS F_1 and F_2. Programming the charge on the FG transistors provides the flexibility of a programmable reference with the advantage of a single design providing multiple reference output [15]. The current reference consists of two circuits having same dependency on supply and temperature, and a subtractor. F_1 and M_7 forms the current mirror in stage I. M_3 provides suitable bias to F_1. M_1, M_2, M_4 and M_5 provide a variable bias to M_3.

In stage II, F_2 and M_{14} forms the current mirror and M_{10} provide suitable bias to F_2. M_8, M_9, M_{11} and M_{12} provide a variable bias to M_{10}. M_{15} scales the output current from stage I and M_{16} scales the output current from stage II. The output current of M_{16} is subtracted from the output current of M_{15} to obtain the supply and temperature compensated reference current.

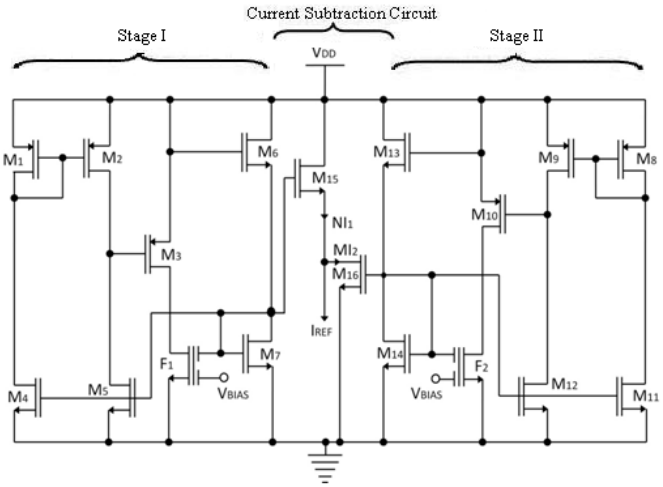

Fig. 3: Proposed circuit for FGMOS based programmable current source

IV. MATHEMATICAL ANALYSIS

Applying Kirchoffs voltage law in the output loop of stage I in Fig. 3

$$V_{SD3} + V_{DSF1} - V_{DS7} - V_{GS6} = 0 \tag{3}$$

$$V_{SG3} - V_{TP} + V_{GSF1} - V_{TN} - (V_{GS7} - V_{TN}) - V_{GS6} = 0 \tag{4}$$

In saturation region the drain current [19] is given by

$$I_D = \frac{\beta}{2}(V_{GS} - V_T)^2 \tag{5}$$

Substituting (2) and (5) in (4) results

$$\sqrt{\frac{2I_1}{\beta_P}} + \left(\frac{C_2}{C_T}\right)V_{bias} + \left(\frac{C_1}{C_T} - 1\right)\left(\sqrt{\frac{2I_1}{\beta_N}} + V_{TN}\right) = \left(\sqrt{\frac{2I_1}{\beta_N}} + V_{TN}\right) \tag{6}$$

where I_1 is the output current of stage I. On rearranging (6) becomes

$$I_1 = \frac{1}{2}\frac{\left(\left(\frac{C_1}{C_T} - 2\right)V_{TN} + \frac{C_2}{C_T}V_{bias}\right)^2}{\left(\frac{1}{\sqrt{\beta_P}} + \left(\frac{C_1}{C_T} - 2\right)\frac{1}{\sqrt{\beta_N}}\right)^2} \tag{7}$$

The transconductance parameter (β) is directly proportional to mobility (μ), the temperature dependent terms in (7) are threshold voltage (V_{TN}) and transconductance parameter (β) [3], [4]. The relationship between threshold voltage and temperature is given by (8)

$$V_T(T) = V_T(T_0) + \alpha_{VT}(T - T_0) \tag{8}$$

where $\alpha_{VT} = \partial V_T/\partial T$ is a negative constant

The relationship between mobility and temperature is given by (9)

$$\mu(T) = \mu(T_0)\left(\frac{T}{T_0}\right)^{\alpha_\mu} \tag{9}$$

where α_μ is a negative constant [3], [4].

Applying subtraction technique to voltage controlled current source circuit, it is possible to remove temperature and supply voltage effects in the reference current [16], [17]. The reference current is obtained by taking the difference of the output currents from the two stages with scaling factors N, M and it can be expressed as in (10)

$$I_{REF} = NI_1 - MI_2 \tag{10}$$

where I_2 is the output current of stage II, which is equal to I_1 . Using (7) I_{REF} can be expressed as in (11)

$$I_{REF} = \frac{(N-M)}{2}\frac{\left(\left(\frac{C_1}{C_T}-2\right)V_{TN} + \frac{C_2}{C_T}V_{bias}\right)^2}{\left(\frac{1}{\sqrt{\beta_P}} + \left(\frac{C_1}{C_T}-2\right)\frac{1}{\sqrt{\beta_N}}\right)^2} \tag{11}$$

From (11) it is observed that the reference current does not depend on supply voltage.

V. SIMULATION RESULTS

The simulation of the proposed programmable current reference is carried out using TSPICE provided by TANNER EDA with BSIM model file. Fig. 4 shows the variation of reference current with supply voltage and bias voltage. The supply voltage varies from 0 V to 2.5 V. The reference current varies from 473.09 nA to 15.71 μA as bias voltage varies from 0.6 V to 0.9 V. Fig.4 shows that the output current is almost independent of supply voltage in the range of 0.5 V to 2.5 V.

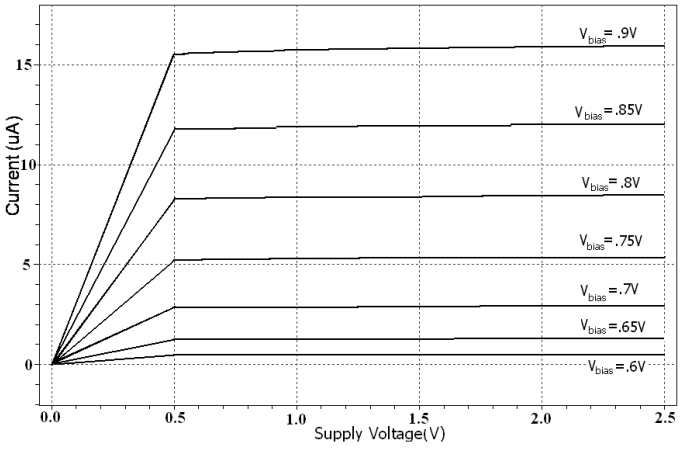

Fig. 4: Variation of reference current with supply voltage for different values of bias voltage

Fig. 5 (a) and Fig. 5 (b) show the variation of reference current with supply voltage and temperature for V_{bias}=0.9 V. For V_{bias}=0.9 V the circuit has a supply dependency of 0.175 nA/V and a temperature dependency of 1.9 nA/°C is obtained.

Fig. 6 (a) and Fig. 6 (b) shows the variation of reference current with supply voltage and temperature for V_{bias}=0.6 V.

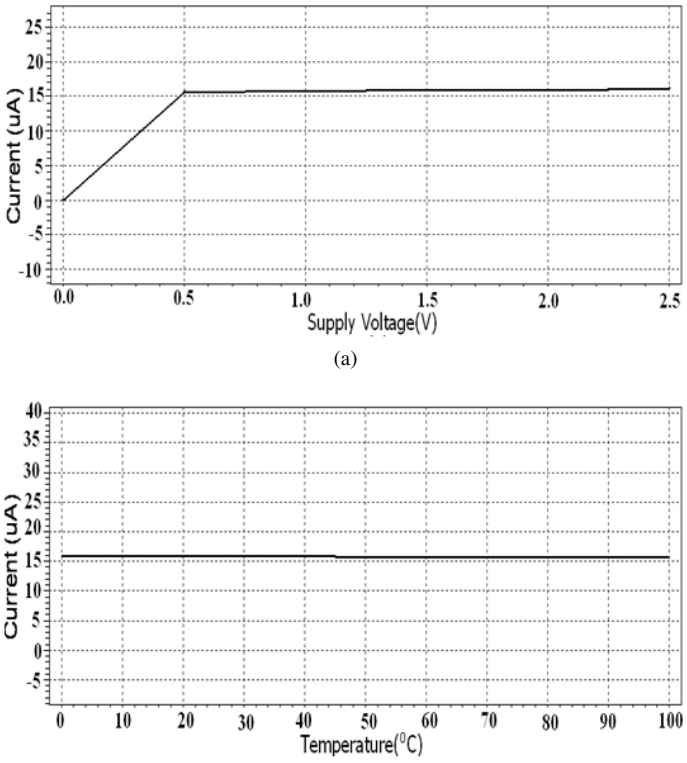

Fig. 5: Variation of reference current with (a) supply voltage (b) temperature for V_{bias}=0.9V

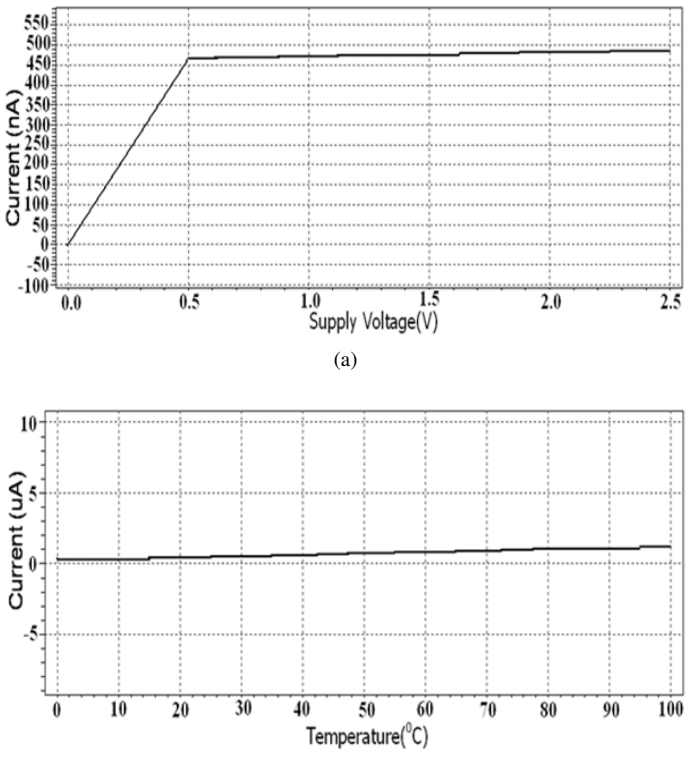

Fig. 6: Variation of reference current with (a) supply voltage (b) temperature for V_{bias}=0.6V

For V_{bias}=0.6V the supply voltage dependency is 10.28 nA/V and temperature dependency is 8.36 nA/°C. The variation of output current with bias voltage is shown in Fig. 7. It closely matches with the analytical model given by (11). As the bias voltage is changed from 0.6 V to 0.9 V the reference current varies from 473.09 nA to 15.71 μA.

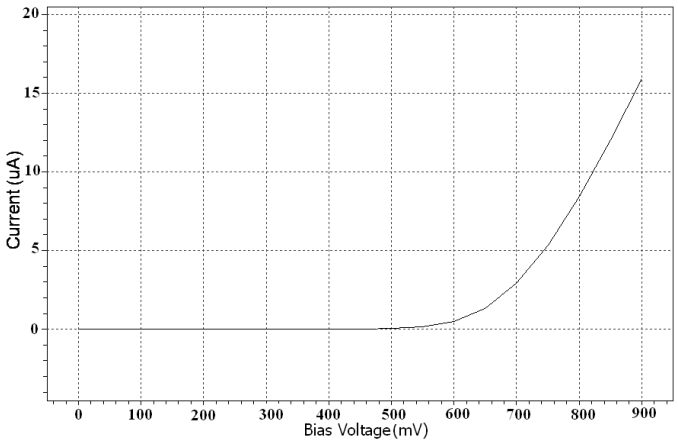

Fig. 7: Variation of reference current with bias voltage

VI. Conclusion

A programmable current reference using FGMOS with temperature and supply voltage compensation is presented. Subtraction technique is used to compensate the dependency of current reference on supply voltage and temperature. The reference current can be varied from 473.09 nA to 15.71 μA. Programmability avoids the need for re-design and re-fabrication for different values of output current. It also facilitates post-fabrication adjustments for tuning and error correction. The circuit can operate with a supply voltage as low as 0.5 V, with no passive components. The circuit performs well over the temperature range of 0°C to 100°C and supply voltage range of 0.5 V to 2.5 V. The circuit has a temperature dependency of as low as 1.9 nA/°C and a supply voltage dependency as low as 10.28 nA/V, which are better than that for reported circuits.

References

[1] J. Chen and B. Shi, "1V CMOS current reference with 50 ppm/°C temperature coefficient", *Electron. Lett.* vol. 39, pp. 209-210, Jan. 2003.

[2] R. Dehghani and S. M. Atarodi, "A new low voltage precision CMOS current reference with no external components", *IEEE Trans. Circuits Syst. II*, vol. 50, no. 12, pp. 928-932, December 2003.

[3] Bendali A. and Audet Y., "A 1-V CMOS current reference with temperature and process compensation", *IEEE Trans. Circuits Syst. I*, vol. 54, no. 2, pp. 1424-1429, 2007.

[4] M. Filanovsky and A. Allam, "Mutual compensation of mobility and threshold voltage temperature effects with applications in CMOS", *IEEE Trans. Circuits Syst. I, Fundam. Theory Appl.*, vol. 48, no. 7, pp. 876-884, Jul. 2001.

[5] F. Fiori and P. S. Crovetti, "A new compact temperature-compensated CMOS current reference", *IEEE Trans. Circuits Syst. II: Exp. Briefs*, vol.52, no. 11, pp. 724-728, Nov. 2005.

[6] Wang Yi, He Lenain and Yan Xiaolang, "All CMOS Temperature, Supply Voltage and Process Independent Current Reference", *Proceedings of IEEE*, 2007.

[7] T. Matsuda, R. minami, A. Kanamori, H. Iwata, T. Ohzone, S. Yamamoto, T. Ihara and S. Nakajima, "A VDD and Temperature Independent CMOS Voltage Reference Circuit", *Proceedings of the Asia and South Pacific Design Conference(ASP-DAC0 04), IEEE Computer Society*, 2004.

[8] Yu Guoyi and ZouXuecheng, "A novel current reference based on sub-threshold MOSFETs with high PSRR", *Microelectronics Jour.*, Vol.39, pp. 1874-1879, 2008.

[9] C. H. Lee and H. J. Park, "All CMOS temperature independent current reference", *Electronic letters, IET Jour.* Vol. 32, Issue 14, July 1996.

[10] Susheel Sharma, S. S. Jamuar and S. S. Rajput, "Floating-gate MOS Structures and Applications", *IETE Technical Review*, Vol.25, Issue 6, Dec. 2008.

[11] Maneesha Gupta and Rishikesh Pandey, "FGMOS based voltage-controlled resistor and it's applications", *Microelectronics Jour.*, Vol.41, pp. 25-32, 2010.

[12] Maneesha Gupta and Rishikesh Pandey, "A Novel Voltage-Controlled Ground Resistor Using FGMOS Technique", *IMPACT, IEEE*, 2009.

[13] Parshotam S. Manhas, Susheel Sharma, K. Pal, L. K. Mangotra and S. S. Jamuar, "High performance FGMOS-based low voltage current mirror", *Indian Jour.of Pure and applied Physics*, Vol. 46, pp. 355-358, May 2008.

[14] Axel Thomsen and Martin A.Brooke, "A temperature stable current reference source with programmable output", *IEEE Trans.*, 1992.

[15] Venkatesh Srinivasan, G. Serrano, C. M. Twigg and Paul Hasler, "A Floating gate Based Programmable CMOS reference", *IEEE Trans. Circuits Syst. I*, vol. 55, no. 11, pp. 3448-3456, Dec. 2008.

[16] C. Yoo, J. Park, "CMOS current reference with supply and temperature compensation", *Electronic letters, IET Jour.* Vol. 43, Issue 25, Dec. 2007.

[17] Haseena P. S., Suresh Babu V. and M. R. Baiju, "A Floating Gate MOSFET Based Current Reference with Subtraction Technique", *IEEE Computer Society Annual Symposium on VLSI(ISVLSI)*, pp. 206-209, July 2010.

[18] Esther Roderiguez-Villegas, "Low Power and Low Voltage Circuit Design with The FGMOS Transistor", *IET Circuits, Devices and system Series 20, British Library Cataloguing In. Pub.*, pp. 6-7 and 16-19, 2006.

[19] Paul R. Grey, Paul J. Hurst, Stephen H. Lewis and Robert G. Mayer, "Analysis and Design of Analog Integrated Circuits", *Fourth ed., John Wiley and Sons, Inc. New York*, pp. 257-336, 2000.

Easy Way to Learn Robotic Using Microcontrollers

Mohamed FEZARI, Ali Al-Dahoud

***Abstract*—** This paper presents a work to improve microprocessor and microcontroller education for robotic master students at the (BMAU) Badji Mokhtar Annaba University.. The paper examines the hardware and software used for microprocessor/microcontroller learning in robotic field, Examples are given for the PIC16F876 microcontroller and the different evaluation boards used for (a) code generation and development; (b) embedded systems applications. Then, attention is given to the software used in microcontroller education. The MPLAB comprehensive simulation and interfacing software is described. Finally, the paper discusses the interfacing between the microcontroller and the various electro-mechanical sensing and actuation components used in a mobile robot applications or project. The use of functional modules for teaching interfacing skills to EE students is described. We finish the paper with a conclusion and pointing further work.

***Keywords*—** Microcontroller education; PIC16F876; Evaluation boards; Embedded applications; Interfacing software, Simulation; Electro-mechanical; Sensing;

I . INTRODUCTION

Due to the accelerated growth of electronics, computers, and information technology industries, a gap has emerged between the traditional methods of teaching Electrical Engineering courses (e.g., robotic Engineering, biomedical Engineering, instrumentation engineering, etc.) and the skills expected of EE graduates entering the job market. A deluge of embedded systems, sensors, microcontrollers, wireless transmission, actuators have emerged present-day society. Microcontroller-based devices and appliances (in embedded systems) are found in all aspects of our everyday life. Even the automobile industry, a traditional Electro-mechanical engineering field, is putting tens of microcontrollers in a modern automobile, and plans to increase this number multifold as new technologies for security and comfort are being introduced.

New automobile technology using, hybrid propulsion, 42-Volts wiring bus, ‘‘steer-by-wire’’, ‘‘brake-by-wire’’, collision avoidance, autopilot, etc. are being currently developed, and automobiles with such capabilities will hit the market in the near future.

However, traditional EE education of students covers only minimal electrical, electronics, and information technology instruction. The ‘‘high-tech’’ components of a EE education are much below expectations, in spite of clear demand. Because of this demand in the job field, the EE engineering graduates entering the job market are at a considerable handicap. To acquire the high-tech skills required in the job market, some Robotic and Automatic Master or engineering students try to register in upper-division advanced electronic courses. However, lacking the proper lower-division background, this practice puts them at a disadvantage, and negatively affects their GPA and course load. In response to this situation, an interdisciplinary engineering branch, that spans robotic engineering, electronics, embedded microcontrollers/digital signal processing, controls, and information technology, has emerged under the name of mobile robotic. Nationwide, efforts to introduce robotics in university education have sprung in over ten Algerian universities, and several worldwide [1..8].

1.1. The need for robotics education in Algeria

At our University BMAU, the EE engineering and Master students also have an acute need for education in the interdisciplinary field of mecatronics/microcontrollers. The Algerian government is going through an intense economical development effort focused on high-tech businesses and companies. This effort is aimed at bridging the technological divide that has placed Algeria among the last in the nation in a high-tech economy. Critical to this statewide effort, is the development of an adequate cadre of well trained personnel that can ‘‘hit the ground running’’ in the growing technology-oriented job market. Akin to similar efforts going on in other places (e.g., France Italy), this will permit the building of ‘‘a critical mass of talent that local companies can draw from’’ [1]. Because of that, many universities in Algeria are introducing the course of microcontrollers and programmable circuits in their Master program for different disciplines such as: automatic, telecommunication, biomedical, mechatronics, and instrumentation.

1.2. Microcontroller education in the department of EE

The Department of EE Engineering at the BMAU Annaba is well positioned to participate in promoting and developing this emerging engineering education field. EE department at BMAU established many courses for teaching microcontrollers to Master students in Robotics, Automatic, Biomedical and instrumentation Engineering students. The course consists of four major components:

(a) courses and exercises at classroom ; (b) homework; (c) laboratory; (d) project. The classroom work is focused on instilling in students the basic knowledge related to programming and using the microcontroller. Part of the

classroom instruction is performed in a computer laboratory, where the students interact with simulation software on a one-on-one basis. The homework is focused on the students_ understanding and retention of the concepts in a self-teaching style, and it consists of examples that students follow and exercises that the students perform and return to the Teaching Assistants via email. The laboratory consists of nine sessions that gradually take the students from simple microcontroller programming through the usage of its various functions such as parallel ports, serial communication, internal timer programming (detection and generation), Analog-to-Digital Conversion, DC motor and stepper motor control, internal EEPROM read and write, and Digital to Analog conversion. The capstone of the course is a three-month project in which the students work in pairs to achieve the development, design, coding and programming, construction of PCB and wiring components, and demonstration of an embedded system project of their own choice.

The project culminates with a written report including the assembly program, an oral presentation, and a hands-on demonstration with test on hardware design. The syllabus for this course has been discussed and presented to students , final grade is as follow:50% for the final exam, 15% for homework and 35% for project and lab work.

The masters students at the EE Department at BMAU, of which 40% are women and 10% are minority from Sub-Saharian Africa countries (mainly : Niger, Mali and Senegal), are in need of support to expand and enhance the Robotics/microcontroller education. The project currently undertaken with some Laboratories support will empower the BMAU Master students with the knowledge and hands-on experience required for success in today's technologically competitive economy and market place.

II ARDWARE FOR MICROCONTROLLER IN ROBOTIC EDUCATION

The hardware issue is also challenging because of the large variety of microcontroller options available on the market . Our objective in developing this course has been to find a microcontroller that is widely used and accepted in the industry and well documented in robotic applications (Mobil robots, robot arm and robotic applications).

Another criterion in our selection was to choose a microcontroller that has the essential functions that need to be conveyed to the students (internal memories, timers, converters, parallel and serial ports). The third selection criterion was cost, i.e., an inexpensive microcontroller. There are many microcontrollers available on the market today. However, none is better than the PIC series microcontrollers for the classroom atmosphere. Many OTP microcontrollers may give a better solution in a particular application, but their computer architectures and instruction set are not suitable to a general educational purpose, moreover the OTP controllers are one time programming they are not suited for education where the student can make many tests before succeeding in the realization of the project. The PIC16F876 offers a powerful and easy-to-memorize instruction set and has been around for more than 8 years. Once you have built your solid foundation of PIC microcontroller expertise, you can easily apply the PIC16F876/628 knowledge to the more developed family of microchip PIC18F or DSPIC30 series or other family of microcontrollers in the future. Plus, there is a lot of application software that can be downloaded from the web and Electronic review. Therefore, the final choice was for the PIC16F876 from Microchip as microcontroller. Figure 1 illustrates the internal architecture of PIC16F628 witch is close in hardware and software to PIC16F876.

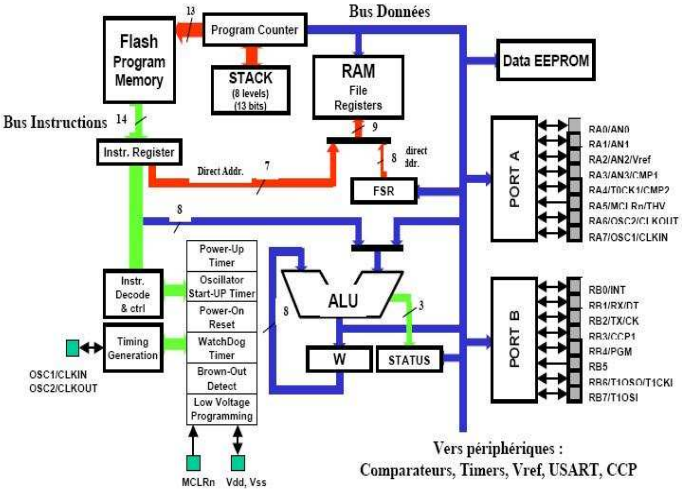

Figure 1 illustrates the internal architecture of PIC16F628

A.1. PIC-A microcontroller evaluation and development board

For embedded applications, the microcontroller is usually used in single chip mode. In embedded applications, the microcontroller comes with the program already ''burned'' into its ROM or EEPROM memory. The user only has to place the microcontroller in its intended location, to power it up and initiate the program for the OTP type , however our type of microcontroller PIC16F876 has a Flash program memory of 8K bytes. Then, the microcontroller will run by itself. There are many types of evaluation and development board in the market, in would be better to have a solid , adapted and upgradable board from microchip company (designer of PIC microcontrollers)

For code development applications, the microcontroller must be used in connection with a host computer (PC) and/or a terminal. The programmer can develop the program on the host computer and then test it on the microcontroller. Alternatively, the programmer can develop the program directly on the microcontroller using the terminal interface. The electronic circuitry and IC chips associated with this process are placed on an evaluation board (EVB). The EVB contains expanded memory chips, a port replacement unit, as well as IC chips for servicing the connection to the host computer and/or a terminal. The EVB is essential for program development, since it allows the software programmer to develop and test the microcontroller application software. Once the microcontroller application software is developed and tested, then it will be ''Flashed'' into the program memory of the mass production microcontrollers. By using the EVB expanded system containing an PIC16F876/8777 and aPC, the

ISBN: 978-1-61804-216-3

user can develop software intended for either single-chip mode or expanded mode microcontroller applications. Several microcontroller evaluation boards are commercially available. They range from the simplest to the most complex. For our lab, we have selected two types, one for code development (Easypic http://www.docshut.com/ikvmmn/easypic2-manual.html), the other for embedded applications (PIA-A microcontroller DVB,

B. PIC-A microcontroller evaluation and development board

PIC-A development board is a new type designed to develop good e-multifunctional PIC microcontroller development platform. MCU integrates commonly used external devices, such as, DS1302 clock chip, DS18B20 temperature sensor, an external EEPROM chip 24C02, MAX232, beep horn, matrix keyboard, separate keyboard, dynamic digital control, marquees, LCD1602, LCD12864, 2003 motor drive, etc. The PIC microcontroller development platform provides a great deal of learning materials, including routines, instructions, e-books, user's examples. PIC-A development board uses typically the most widely used chip PIC16F877A.

To easily study and develop all series of PIC Microcontroller's, only a set of PIC-A demo system and a computer are needed. Based on programming functions, abundant on-board hardware resources, flexible expansion, free resource distribution, and ICSP download function for customer target board, PIC-A can not only satisfy the demands of a beginner in Microcontroller study, but also meet the requirements of engineers in development of Microcontroller. In addition to a study & experimental board, PIC-A is also a demo board of Microcontroller integrated with multiple resources.

Characteristics:
Abundant on-board resources: LED, digital tube, key-press, keyboard matrix, character LCD, A/D converter, D/A converter,, USART serial communication
Open modular design: All I/O ports are open externally with output socket. Expansion is easily accomplished..

1. 8 LED lights
2. 6 Clock digital tube (do counter, voltmeter, stopwatch, electronic clock, frequency counter, etc. display);
3. 4 Independent keys (do button scanning);
4. 4 * 4 ranks of the keyboard (buttons do scan);
5. MAX232 serial port (RS232 and Computer Communication can do experiments);
6. AT24C02 (EEPROM can do experiments);
7. Buzzer sound output (do music-related sound experiments);
8. DS18B20 temperature sensor (temperature measurement do thermometers and other related experiments);
9. DS1302 real time clock circuit (tube or LCD display can be used to do digital electronic clock);
10. 1602 LCD display interface (2 lines of 16 characters per line, with backlight); (not including lcd)
11. 128 * 64 LCD display interface (4 lines of 16 characters per line, with backlight); (not including lcd)
12. Stepper motor interface (do stepper motor Reversible experimental) (not including motor)
13. All the way 10-bit A / D converter (DAC testing DC voltage, tube or LCD display with digital display);
14. DC power input (DC voltage :6-15V);
15. USB power input interface (direct access to computer power supply);
16.40 PIN Block the programming (which can replace the chip);
include: - a development board; - USB cable; - serial line; - PIC16F877A

C. . EasyPic-2 development board

Presented in figure 2, the hardware system supports 8,14, 18, 28, and40-pin microcontrollers Each jumper, element and pins clearly marked on the board. Most of the industrial applications can be tested on the board: temperature controllers, counters, timers etc. EasyPIC2 also includes practical examples in PASCAL, BASIC, C, and assembly. Port A is connected to the resistor network, if switch is not in ON position, the appropriate pin has neither pull-up or pull-down resistor attached. This is very important, because it enables using A port in Analog mode as AD Converter, and yet it can be used as ordinary digital I/O port. Setting PORT jumper to the upper position sets the pins of the appropriate port to logical one(pull-up). If jumper is set to the lower position, pins are set to logical zero (pull-down). It is very important to put pin on pull-up if you expect logical zero on input and vice versa. Prototype area in which we can place our additional components. The back side of the board has pin marks to make the connectingeasier.32 buttons allows us to control every pin on the microcontroller. we can chose how pressing the button will affect the pin, high state or low state. See all the signals - each pin has LEDs. Seven segment digits in multiplex mode for displaying the results.

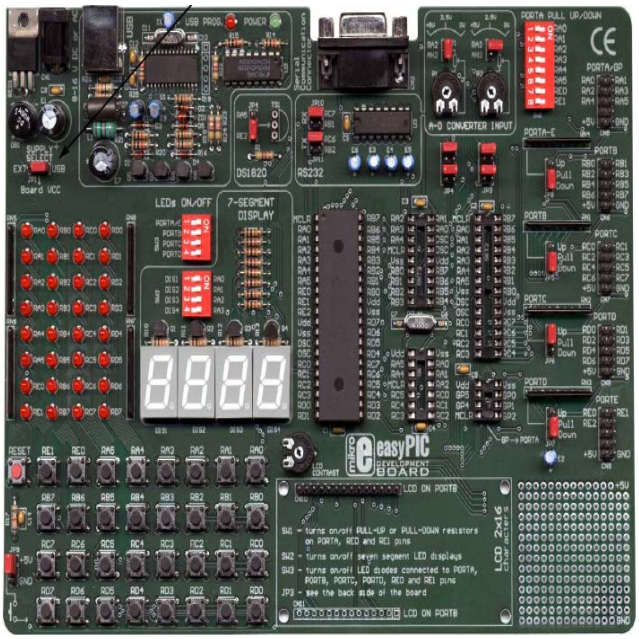

Fig. 2. Easy Pic -2 development board
http://www.docshut.com/ikvmmn/easypic2-manual.html

ISBN: 978-1-61804-216-3

III Software for Microcontroller Education in Robotics

The software issue is particularly challenging since the robotic master students receive instruction in high level programming without getting involved in assembly programming until they enter the microcontroller course. Today, most of the programming education of EE students is done in visual languages such as MathLab and LabView, for which the EE department and some laboratories at BMAU have licenses. Hence, the teaching of a script language such as Assembly or C++ for programming the microcontroller has to done from basic principles. We found that the use of microcontroller simulation software greatly enhances the students ability to climb this steep learning curve. We selected an inexpensive microcontroller simulation software based on the assembly language, MPLAB by microchip[13],[14], http://www.microchip.com.

And at http://ww1.microchip.com/downloads/en/DeviceDoc/MPLAB_User_Guide_51519c.pdf

MPLAB Integrated Development Environment (IDE), as presented in figure 3, is a free, integrated toolset for the development of embedded applications employing Microchip's PIC® and dsPIC® microcontrollers. MPLAB IDE runs as a 32-bit application on MS Windows®, is easy to use and includes a host of free software components for fast application development and super-charged debugging. MPLAB IDE also serves as a single, unified graphical user interface for additional Microchip and third party software and hardware development tools. Moving between tools is a snap, and upgrading from the free software simulator to hardware debug and programming tools is done in a flash because MPLAB IDE has the same user interface for all tools.

MPLAB IDE supports many language Toolsuites. Integrated into MPLAB IDE is the Microchip MPASM Toolsuite, but many others can be used, including the Microchip C18, C30 and C32 Toolsuites, as well as language tools from HI-TECH, IAR, CCS, Micro Engineering Labs and Byte Craft. These are integrated into MPLAB IDE in two ways: using “plug-ins” designed by the manufacturer, and by older style “.MTC” files that can be customized for any language Toolsuite.

A. STEPS for Program development

In order to create code that is executable by the target PIC MCU, source files need to be put into a project. The code can then be built into executable code using selected language tools (assemblers, compilers, linkers, etc.). In MPLAB IDE, the project manager controls this process. All projects will have these basic steps:

a) Select Device: The capabilities of MPLAB IDE vary according to which device is selected. Device selection should be completed before starting a project.

b) Create Project : MPLAB IDE Project Wizard will be used to Create a Project.

c) Select Language Tools : In the Project Wizard the language tools will be selected. For this tutorial, the built-in assembler and linker will be used. For other projects, one of the Microchip compilers or other third party tools might be selected.

d) Put Files in Project : Two files will be put into the project, a template file and a linker script. Both of these files exist in sub-folders within the MPLAB IDE folder. It is easy to get started using these two files.

e) Create Code : Some code will be added to the template file to send an incrementing value out an I/O port.

f) Build Project : The project will be built – causing the source files to be assembled and linked into machine code that can run on the selected PIC MCU.

g) Test Code with Simulator :Finally, the code will be tested with the simulator.

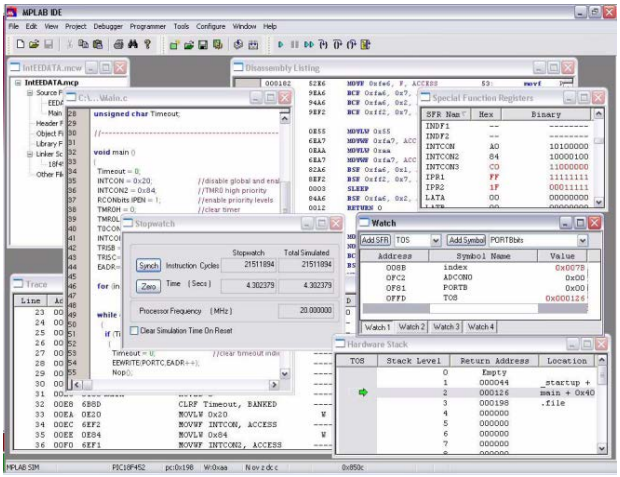

Fig. 3. Screen capture of the MPLAB IDE simulation and emulation software for PIC16F876/877 microcontroller.

B. Simulation and Debugging

The simulator visualizes the CPU, Flash memory for program, RAM, EEPROM and all memory mapped I/O ports (Figure 3). It also simulates the on board peripherals such as :

- timer (including pulse accumulator),
- analog to digital converter,
- parallel ports (including handshake),
- serial port,
- I/O pins (including analog and interrupt pins).

While debugging, the graphical user interface makes it possible to view and control every register (CPU registers and I/O registers), memory location (data, program, and stack), and pin of the simulated microcontroller. Even when the program is running! It is possible to stop the simulation at any combination of events. For example, stop when stack calls function 1 and RAM location $003F contains $BD or I/O register TCNT is greater than $2578.

A number of (simulated) external components can be connected to the pins of the simulated PIC16F876 while debugging. For example:

• LED’s, • switches, • analog sliders (variable voltage potential), • serial transmitter and receiver,

The MPLAB can communicate with the EasyPIC Development Boards and different tools for emulation and

ISBN: 978-1-61804-216-3

programming developed by Micronchip. This MPLAB program can be downloaded (for free) from the microchip website. When the assembly program is compiled it produces a HEX file which is loaded into the target board the graphical user interface makes it possible to view and control every register (CPU registers and I/O registers) and memory location (data, program, and stack) of the real microcontroller. It is possible to stop the execution at any address and inspect or change the registers and memory.

IV. Interfacing of ROBOT microcontroller projects

Finally, we are addressing the interfacing between the microcontroller and the various electro-mechanical sensing and actuation components used in a Mobil robot or robot arm project as in figure 4. These issues are very important, especially with EE engineering students that have little or no previous experience with interfacing electronics with mechanical engineering hardware. We treated this aspect using a suite of functional modules. These functional modules are used for teaching hands-on skills related to the interfacing of mechanical, electrical, and electronic components of a Mobil robot design.

EE engineering students have the need for hands-on experience to increase their ability and confidance in tackling mechanical, electrical and electronics concepts, especially during the realization phase of a Mobil robot project. To address this need, we started developing a suite of functional teaching modules. These functional modules are intended as bolt-on building blocks with clearly defined inputs and outputs, and an explanation of the underlying operational principles. The students are expected to use the functional modules as a learning tool. After understanding their functionality, they are expected to duplicate the circuitry on their own breadboards to be incorporated into their robots and automatic class projects, as well as into other hands-on projects, as appropriate. The modules that have been developed include:

- Opto-electronic sensor,
- temperature sensor LM135,
- humidity sensor,
- H-bridge for DC motor (relay and transistor),
- Stepper motor controller, stepper motor drive unit
- pulse-width modulation dc motor drive unit,
- open collector buffer, latches and LED's
- Relay and transistor commutation module.
- Ultra-sonic sensor (MSU-08).

Accompanying the functional modules are full reports containing electrical and component schematics, applicable equations, and a full experimental results during calibration tests results. These reports play an important role in the functional modules education. Several graduate students and undergraduate students composed these reports for every functional module when they first built these modules. The goals of these reports are helping the readers to understand the functional module component and facilitating repairing these functional modules. The students are provided with a bag of components and asked to reproduce the functional module circuit following the circuit diagram and observing the physical realization in the functional module box. Using this approach, the students know what to expect when using the functional module by reading the report, and acquire the hands-on experience by building the physical object. As an example, Fig. 5 shows the appearance of port information using LED's circuit containing LED's to simulates ports and Fig. 6 presents the Mobil robot project using POB-Bot that include a module called "Pob-Proto", this module uses PIC16F877 as microcontroller to interface actuators and sensors which are presented in the functional module report[19]. Machine Science in www.machinescience.com,Offers an expandable metal robot base, which includes motors, wheels,microcontroller, and other electronics. were presented in site [8] ,Giurgiutiu and Liu presented other modules for michatronics [9].

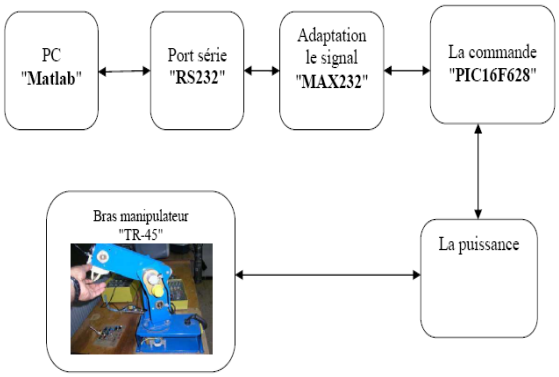

Fig.4. : synoptic of realized as project: robot arm control via Pc through microcontroller PIC16F628.

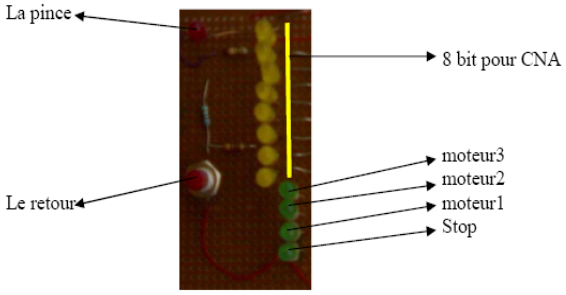

figure5.6 : carte émulation.

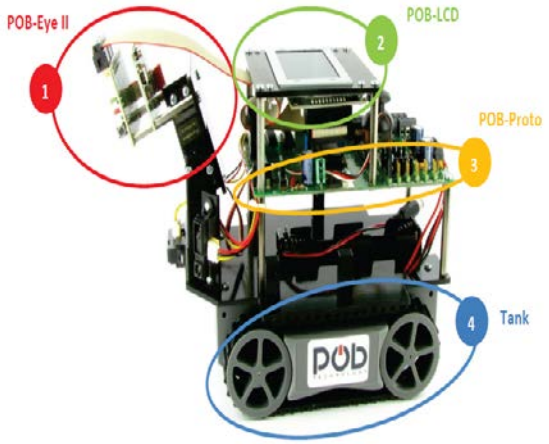

Fig 6. Pob-Bot robot with sensors for navigation, I/O interfaces are controlled via PIC16F877.

V. Conclusions

Many universities have started disposing courses on robotics to undergraduate and graduate students. Such courses, cutting across departmental boundaries and combining theory, hands-on experiments, and technology applications, greatly benefit the undergraduate students, graduate students, and even faculty. They propel the curriculum towards the forefront of engineering education and directly answer the training and education challenges of the coming years.

The Department of EE at BMAU Algeria has embarked upon a project to enhance the robotic and mechanic education of EE engineer and master students. This project is to prepare these students for jobs in industrial factory at Annaba city. Annaba City is a big industrial area with companies like ARCELOR MITAl and FERTIAL. Our approach will help expand the students understand microcontrollers from both analysis and hands-on viewpoints. Our instruction has focused on using the microcontroller in various applications in robotic sensors network and automatic, rather then how the microcontroller is built inside. This is considered most applicable for electrical engineering and other non-electrical engineering students. The work on this project is continuing. Further developments will be reported in future publications.

References

[1]. Billard: Robota,(2003), clever toy and educational tool, Robot. Autonom. Syst. **42**, 259–269 (2003).
[2] Garcia Robo, (2007)t: http://www.acroname.com (Acroname Robotics, Boulder 2007)
[3] ER1, (2007): http://www.evolution.com (Evolution Robotics, Pasadena 2007)
[4] KHR-1, (2007): http://www.kondo-robot.com (Kondo Kagaku, 2007)
[5] Robsapien: http://www.robosapien.com (WowWee, Quebec 2007)
[6] Roomba: http://www.irobot.com (iRobot Corp., Burlington 2007)
[7] iRobot Corp(2005),: *iRobot Roomba Serial Command Interface (SCI) Specification* (iRobot, Burlington 2005)
[8] Machine Science in www.machinescience.com
[9] Giurgiutiu V, Liu W. (2004),The use of functional modules in the mechatronics education of non-electrical engineering students. In: ICEER-2004 International Conference on Engineering Education and Research ‘‘Progress Through Partnership’’, Omolouc, Czech Republic, 2004.
[10] Hargrove JB. (2000),Student projects for mechatronics education in the core curriculum at Kettering University. In: Mechatronics 2000—7th Mechatronics Forum International Conference, Georgia, USA, 2000.
[11] Stein C.: Botball: (2003),Autonomous students engineering autonomous robots, Comput. Educ. J. **13**(2), 72–80 (2003)
[12] Beer R.D., Chiel H.J., Drushel R.F.:(1999), Using Autonomous Robotics to teach science and engineering, Commun. ACM **42**(6), 85–92 (1999)
[13] Development system for PIC microcontroller (2008), .http://www.mikroe.com/chapters/view/13/appendix-c-development-systems/.
[14] ABB Robotics, (2002),The RAPID Language, in the SC4Plus Controller Manual, ABB, Robotics, 2002.
[15] Asada H. and Youcef-Toumj K.,(1987), Direct-Drive Robots—Theory and Practice, MIT
Press, Cambridge, MA, 1987.
[16] http://www.mikroe.com/products/view/11/book-pic-microcontrollers/
[17] pic microncon,troller application sites http://www.best-microcontroller-projects.com/pic-microcontroller.html
[18] http://www.microchip.com/pagehandler/en-us/products/picmicrocontrollers
[19] POB-Tools is an IDE which allows users to develop with high-end langage .http://education.awabot.com/en/downloads/view/8

Mohamed FEZARI (MS’87-PHD’2010) is associate Prof. at BMAU , he is currently in LASA laboratory, he has many publications in different journals and participated in many conferences as author , reviewer and TCP.

Ali AL-DAHOUD is Professor at Zaytoonah University of Amman Jordan, Senior Member of IEEE , conference chair of ICIT’09 ICIt’11 and ICIT’13, has many Publications in different journals well indexed and actually he is in the faculty of IT.

Continuous-time Markov-Chain-based control for SIS epidemics in complex networks

A. Schaum, L. Alarcon-Ramos, R. Bernal, C. Rodriguez Lucatero, J. Alvarez

***Abstract*—The problem of robustly controlling dynamics in complex networks is addressed for the case of a multi-agent distributed SIS epidemics. The recovery rate of the agents is considered as a uniform global parameter which is employed as manipulated input, in order to steer the mean probability of infection to zero. A passivity-based constructive Output-Feedback control scheme is designed which (i) is independent of the (possibly time-varying) system parameters, as e.g. connectivity values and infection rates, and (ii) attains global stability of the extinction steady-state.**

***Index Terms*—Complex network dynamics, passivity-based control, SIS epidemics**

I. Introduction

COMPLEX network-based dynamical system represent hard-to-control applications given the complex underlying, possibly time-varying, interconnections of the agents, and the particular nonlinear dynamics associated to each agent [2], [3], [4], [6], [15]. A primer problem consists in determining input variables which can be manipulated for control purposes. Some recent works exploit this question with respect to controlling agents, taking into account the underlying network structure [12]. Unless, the corresponding studies yield important information about controllability of networks with time-invariant topology, in the case of time-varying topologies (as is the case in many real-world applications, like social networks and the internet), global variables are more likely to yield good control performance. Nevertheless, it is hard to identify adequate control variables without having at hand adequate control design approaches for these kind of problems.

A. Schaum, R. Bernal, and L. Alarcon-Ramos are with the Departamento de Matematicas Aplicadas y Sistemas, Universidad Autonoma Metropolitana (UAM)-Cuajimalpa, e-mail: aschaum correo.cua.uam.mx.

C. Rodriguez Lucatero is with the Departamento de Tecnologias de la Informacion, UAM-Cuajimalpa.

J. Alvarez is with the Departamento de Procesos e Hidraulica, UAM-Iztapalapa

An adequate framework to deal with the uncertainty and time-variance problems present in these kind of systems, consists in robustness-oriented constructive control design based on the passivity property [5].

In the present paper, a first inductive step towards an adequate design methodology for these kind of problems is presented. The constructive control approach is employed to design robust, stabilizing controllers for a particular class of nonlinear network dynamics given by epidemic spreading. A preliminary model for continuous-time virus spreading in complex networks is used, based on previous reported ones for discrete-time systems [3], [4], in order to identify the main difficulties inherent to these kind of systems, and explain how the constructive control approach can be employed to achieve good control performance. For this purpose it is assumed that the recovery rate can be continuously manipulated in real time and without delays. This work is in the same line of reasoning as a previously reported one for the discrete-time case [13], and the study of relative-degree two nonlinear network systems using PD control schemes [14].

II. Problem statement

Consider a continuous time Markov-Chain dynamics for epidemic spreading in a complex network given by

$$\begin{aligned} &\dot{p}_i(t) = -\mu p_i(t) + [1 - p_i(t)]\varphi_i[t, p(t)], \\ &p_i(0) = p_{i0}, \quad i = 1, \ldots, N \end{aligned} \tag{1}$$

with $p_i \in [0, 1]$ being the probability of node i of being infected, $p = [p_1, \ldots, p_N]' \in [0, 1]^N$ the associated probability vector for all nodes, μ being the mean recovery rate from infection, φ_i being the infection rate in function of the probability p_j of all its neighbors (i.e., adjacent nodes), and N being the total number of nodes in the network (i.e., the cardinality of the underlying vertex set V). The

ISBN: 978-1-61804-216-3

model (1) is a continuous-time adaptation of the classical SIS model for virus spread in complex networks used in previous studies [16], [4], and represents the main effects present in such kind of virus transmission processes.

According to (1) the probability of node i to be infected decreases with rate μ, and increases with the probability of being infected by its neighbors (according to the underlying graph structure). The function φ monotonically increases with the neighboring p_j, and depends on the interconnection strengths $r_{ij}(t)$, and the constant uniform infection rate β. A suitable model proposed in [16], [4] for this behavior is given by [3]

$$\varphi_i[t, p(t)] = 1 - \Pi_{j \neq i}[1 - r_{ij}(t)\beta p_j(t)]. \quad (2)$$

The control problem addressed in this study consists in designing a suitable control strategy for the recovery rate μ in function of the measured mean probability of being infected, or probability density, given by

$$z(t) = \frac{1}{N}\sum_{i=1}^{N} p_i(t), \quad y(t) = z(t). \quad (3)$$

Introducing the state vector $x(t) = [p_1(t), \cdots, p_N(t)]'$, the dynamics (1) can be written in the compact time-varying input-affine form

$$\begin{aligned} \dot{p}(t) &= f[t, p(t)] + g[p(t)]\mu, \quad p(0) = p_0, \\ y(t) &= z(t) \end{aligned} \quad (4)$$

and the control problem consists in designing functions $\psi(y, \chi)$, with χ being a dynamic controller state, and $\eta(y, \chi, \mu)$, such that the closed-loop dynamics

$$\begin{aligned} \dot{p}(t) &= f[t, p(t)] + g[p(t)]\psi[\chi(t), y(t)], \\ \dot{\chi}(t) &= \eta[y(t), \chi(t)] \end{aligned} \quad (5)$$

has the partial (global) asymptotic stability property

$$\lim_{t\to\infty} ||p(t)|| = 0, \quad \forall\, p_0 \in [0, 1]^N. \quad (6)$$

III. Control design

In this section a robust feedback control scheme is designed which, on the basis of the mean probability measurement $y = z$, determines an optimal variation of the mean recovery rate μ in the light of a suitable compromise between response speed and control effort.

A. Passivity-based control design

As a methodological step, assume for the moment that the infection rate β, the fluctuating connectivity coefficients r_{ij}, and the probability p_i of any node of being infected are known. This is a mere methodological assumption that will be removed in the next subsection.

Write the dynamics of the mean probability z of being infected on the basis of the (Lur'e-type) representation

$$\begin{aligned} \dot{z} &= -\mu z + \nu, \\ \nu &= \frac{1}{N}\sum_{i=1}^{N} \left((1 - p_i)\varphi_i[t, p(t)]\right). \end{aligned} \quad (7)$$

Note that the *relative degree* between the output z and the control input μ is 1, as long as $z \neq 0$. Given that $z = 0$ is the control objective, this implies that at the desired operation point the system has no well-defined relative degree. This fact has to be taken into account carefully in the control design because it may introduce singularity problems.

The associated *zero-dynamics* are given by $z = 0$, implying $p_i = 0$, $\forall i = 1, \ldots, N$, and are trivial, and hence asymptotically stable.

The combination of relative degree one and asymptotic stability of the zero dynamics implies that the system is feedback equivalent to a passive system [1], [5]. To design a passive controller it suffices to impose the linear exponentially stable dynamics

$$\dot{z} = -kz \quad (8)$$

on the dynamics (7) associated to the feedback law

$$\mu = k + \nu/z \quad (9)$$

with ν defined in (7). Given the particular form of the function ν it can be seen that

$$\begin{aligned} \lim_{z\to 0} \frac{\nu}{z} &= \lim_{z\to 0} \frac{\sum_{i=1}^{N}\left[(1 - p_i)\sum_{j\neq i}\beta r_{ij}p_j + \mathcal{O}^2(p)\right]}{\sum_{i=1}^{N} p_i} \\ &= \lim_{z\to 0} \frac{\sum_{i=1}^{N}\sum_{j\neq i}\beta r_{ij}p_j}{\sum_{i=1}^{N} p_i} < \infty, \end{aligned}$$

implying that there are no singularity problems with the feedback law close to the operation point $z = 0$.

With this controller the argumentation for the closed-loop stability assessment for the network

ISBN: 978-1-61804-216-3

dynamics (1) results rather simple:

$$\begin{aligned}&\dot{z} = -kz,\ z(0) = z_0\\ &\Rightarrow \lim_{t\to\infty} z(t) = \lim_{t\to\infty} \frac{1}{N}\sum_{i=1}^{N} p_i(t) = 0,\\ &\Rightarrow \lim_{t\to\infty} ||p(t)|| = 0.\end{aligned} \tag{10}$$

This result is summarized in the next Proposition.

Proposition 1: The complex network SIS dynamics (1) with the passivity-based controller (9) with gain $k > 0$ has the origin $x = 0$ as unique asymptotically stable equilibrium.

B. Robustness-based Output-Feedback Control

The preceding SF control design establishes the point of departure for the design of a robustness-based OF controller, addressed in this subsection. Given that in real complex transmission networks the function φ with time-varying the connectivity parameters r_{ij}, and unknown β a kind of unknown input framework has to be employed.

Recently, in the context of the design problem of OF (saturated and unsaturated) controllers for chemical reactors [9], [10], distillation columns [17], and biological reactors [7], [8], a simplified model was used for OF control design which retains only the main influence dependency of the control input on the output dynamics. It was shown in these studies that this simplified model-based approach leads to simple controller structures with convincing robustness properties due to the independence of a detailed mathematical model and exact knowledge on system parameters. Employing this approach to the present problem, the following simplified model is introduced

$$\begin{aligned}&\dot{z} = -a\mu + \upsilon,\ z(0) = z_0\\ &\upsilon = \upsilon(p,\mu) = \nu + (a - z)\mu.\end{aligned} \tag{11}$$

with ν given in (7).

In terms of the model (11), the passivity-based globally stabilizing controller (9) is written in implicit form as

$$\mu = \frac{kz + \upsilon}{a}, \quad \upsilon = \upsilon(p,\mu). \tag{12}$$

The value υ of υ can be easily obtained based on the change over time $\dot{y}$ of the measured output $y = z$, and the input value μ, according to the expression

$$\upsilon = \dot{z} + a\mu. \tag{13}$$

Accordingly, the value υ is observable and can be estimated by means of a reduced order observer [11].

Given that the rate of change of υ is bounded (all state variables are bounded between 0 and 1) it holds that

$$\left|\frac{\dot{\upsilon}}{\upsilon}\right| < L_\upsilon. \tag{14}$$

Thus, the reduced order observer [11]

$$\begin{aligned}&\dot{\chi} = -\omega\chi + \omega[-a\mu + \omega y],\ \chi(0) = \chi_0,\\ &y = z, \quad \hat{\upsilon} = \chi + \omega y\end{aligned} \tag{15}$$

can effectively recover the value υ of υ (11), if endowed with sufficiently fast recovery rate $\omega > L_\upsilon$.

Substituting the estimate $\hat{\upsilon} = \chi + \omega y$ in the controller (12), and combining the controller (12) with the observer (15), yields the linear dynamic OF controller

$$\begin{aligned}&\mu = \frac{kz + \chi + \omega y}{a}\\ &\dot{\chi} = -\omega\chi + \omega[-a\mu + \omega y],\ \chi(0) = \chi_0.\end{aligned} \tag{16}$$

Convergence conditions for the estimator have been drawn in [18] for a class of general purpose nonlinear systems

$$\begin{aligned}&\dot{x} = f(x,u), \quad x(0) = x_0 \in \mathcal{D},\\ &y = h(x), \quad f(0,\bar{u}) = 0.\end{aligned} \tag{17}$$

There, it was shown that the estimator asymptotically converges over the region $\mathcal{D}$ about the SS $x = 0$, if the estimator gain ω satisfies

$$\omega \in \Omega = \left(\omega^-(L_f(\mathcal{D}), \omega^+(L_f(\mathcal{D}))\right), \tag{18}$$

with $L_f(\mathcal{D})$ being the Lipschitz constant associated to the dynamics (17) and the domain $\mathcal{D}$. Note that the for very large Lipschitz constants L_f (or large domains $\mathcal{D}$), the interval set Ω (18) may be empty. Thus, the observer convergence condition represents a trade-off between attraction domain and convergence speed. Based on this preliminary result, the following proposition states sufficient conditions for the closed-loop stability of the SIS epidemics in the complex network (1) with the linear dynamic OF controller (16). The proof follows by combining the statement of Proposition 1 with the general convergence result presented in [18].

Proposition 2: Consider the SIS epidemics in the complex network (1) with the linear dynamic OF controller (16). The extinction SS $p = 0$ is robustly

and non-locally stable in the domain $\mathcal{D}$ if the controller gains k and ω satisfy

$$k > 0, \quad \omega^-[L_v(k,\mathcal{D})] < \omega < \omega^+[L_v(k,\mathcal{D})], \quad (19)$$

with ω^- and ω^+ being the boundaries of the set Ω (18) and $L_v(k,\mathcal{D})$ being the Lipschitz constant (14) associated to the dynamics of v. If (19) is satisfied for $\mathcal{D} = \mathcal{P} = [0,1]^N$, the extinction SS $p = 0$ is globally asymptotically stable.

Note that the OF controller (16) does not depend on the particular model employed. In particular it is independent of the function φ and its unknown and time-varying parameters $r_{ij}(t)$ (the connectivity weights), and the infection probability β.

Remark: As has been shown in [9], [10], [7], [8], the considered control scheme (16) can be written in proportional-integral (PI) form by an adequate state transformation. Thus, this result is in the line of reasoning of [14], where PD controllers were employed to stabilize a class of relative-degree two network dynamics.

IV. Simulation results

In this section, simulation results are presented to verify the theoretic assessments presented in the preceding sections. First, the open-loop dynamics of the dynamics (1) is analyzed, and second, the closed-loop performance of the proposed linear dynamic OF controller is tested in presence of considerable measurement noise.

For numerical implementation the numeric environment *Octave* was employed with the Runge-Kutta method *ode45* with variable step size for solving the associated set of 20 nonlinearly coupled odes. The uniform distribution of the connectivity rates r_{ij} was obtained with the *Octave*-internal method *rand*.

A. Open-loop dynamics

To analyze the open-loop behavior of the complex network epidemics, a total population of $N = 20$ was considered with connectivity (r_{ij}) changing 10 times the day according to a uniform distribution. The infection characteristic time was set as

$$\tau_\beta = \frac{1}{\beta} = 2 \text{ days}, \quad (20)$$

and the recovery characteristic time twice as fast

$$\tau_\mu = \frac{1}{\mu} = .5 \text{ days}. \quad (21)$$

From the associated discrete-time dynamics (see e.g. [16], [4], [13]) it is known that the threshold value μ_c for μ for endemic behavior (i.e., without open-loop virus extinction) is given by

$$\mu_c = \beta \max \text{eig}(R), \quad R = \{r_{ij}\}_{i,j=1,\ldots,N} \quad (22)$$

and depends on the maximum eigenvalue of the connectivity matrix R. Given that R varies with time, so do its eigenvalues. Numerically the threshold value μ_c has been determined as

$$\mu_c \approx 4 \text{ days}^{-1}, \quad \tau_c = \frac{1}{\mu_c} \approx 0.25\text{days}. \quad (23)$$

From the simulation study presented in Figure 1 it can be seen that $\mu < \mu_c$, and thus the virus does not extinct in open-loop regime. For the simulation

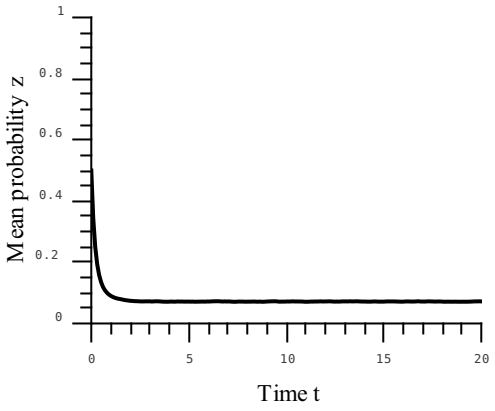

Fig. 1. Open-loop response to initial 50% population infection with infection rate $\beta = 0.5$, and recovery rate $\mu = 2$.

an initial population with 50 % infection probability was employed. As it can be seen, the mean probability of being infected decreases according to the fact that the recovery rate is four times faster than the infection rate, but converges asymptotically to a value of about 0.1, showing that unless low mean probability can be maintained without additional control effort, no global extinction of virus is achieved.

B. Closed-loop behavior

The application of the linear dynamic OF controller (16) to the scenario presented in the last subsection, is presented next. In order to achieve global stability without requiring large recovery rates, intermediate closed-loop response times where set according to the gains

$$k = 1 \text{ days}^{-1}, \quad \omega = 2.5\text{days}^{-1}. \quad (24)$$

ISBN: 978-1-61804-216-3

In order to take into account the fact the the mean probability can not be measured exactly, high-frequency measurement noise with a considerable amplitude of 10% was employed in the simulations.

The corresponding results are presented in Figure 2, showing that the initial infection mean probability of 0.5 is compensated and the extinction SS $p = 0$ is approximately reached in about 10 days. The measurement noise affects the regulated recovery rate but not the convergence feature. The recovery rate attains a final value about $\mu_c \approx 4$, showing that the critical value (23) which has to be attained for extinction of the virus is automatically reached without any *a priory* knowledge about β and $\max \text{eig}[R(t)]$. This verifies the robust convergence properties theoretically assessed in Proposition 2.

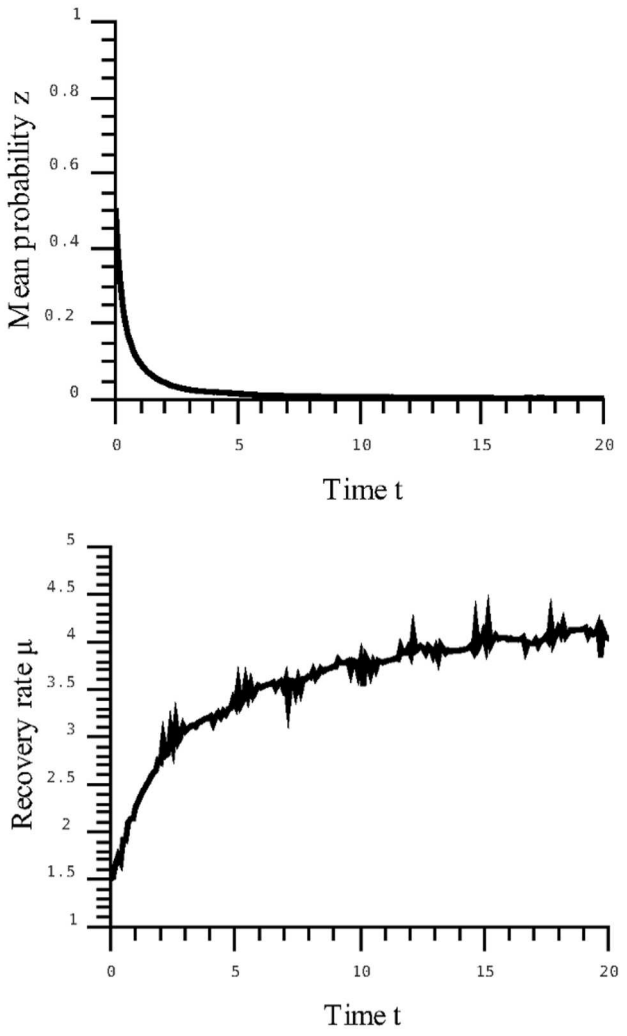

Fig. 2. Closed-loop response to initial 50% population infection with infection rate $\beta = 0.5$, and recovery rate μ manipulated according to the dynamic control law (16) and high-frequency measurement noise with 10% amplitude.

V. Conclusions

The problem of controlling SIS epidemics in complex networks was addressed. The recovery rate was considered as manipulated input, and the mean probability of infection as measured output. A passivity-based linear model-independent output-feedback control scheme was employed to globally stabilize the extinction SS. Sufficient closed-loop stability conditions were drawn for the proposed controller in terms of the controller gains and limits.

In future studies the proposed control scheme should consider saturation features due to recovery limitations, and more complex dynamics of the network nodes, including quarantine states, etc.

References

[1] C. I. Byrnes, A. Isidori, J. C. Willems, Passivity, Feedback Equivalence, and the Global Stabilization of Minimum Phase Nonlinear Systems, IEEE Trans. Aut. Cont. 36 (11), p. 1228 - 1240 ,1991.

[2] M. Mesbahi, M. Egerstedt, Graph Theoretic Methods in Multi-agent Networks, Princeton University Press, 2010.

[3] Y. Moreno, R. Pastor-Satorras, and A. Vespignani. Epidemic outbreaks in complex heterogeneous networks. The European Physical Journal B, 26(26):521529, February 2002.

[4] J. Leskovec, D. Chakrabarti, C. Floutsos, S. Madden, C. Cuestrin, M. Faloutsos, Information survival threshold in sensor and p2p networks. In IEEE Infocom, 2007.

[5] R. Sepulchre, M. Jankovic, P. Kokotovic, Constructive Nonlinear Control, Springer-Verlag, London, 1997.

[6] R. Pastor-Satorras and A. Vespignani. Epidemic dynamics and endemic states in complex networks. Physical Review E, (Volume 63, Issue 2):06611710661178, 2001.

[7] A. Schaum, J. Alvarez, T. Lopez, Saturated PI control for continuous bioreactors with Haldane kinetics, Chemical Engineering Science 68 (1) (2012) 520529.

[8] A. Schaum, J. Alvarez, T. Lopez, Saturated linear dynamic output-feedback control for a class of three-state continuous bioreactors with inhibited kinetics, Journal of Process Control 23, p. 332 350, 2013.

[9] P. Gonzalez, J. Alvarez, Combined PI-inventory control of solution homopolymerization reactors, Industrial and Engineering Chemistry Research 44 (2005) 71477163.

[10] J. Diaz-Salgado, J. Alvarez, A. Schaum, J.A. Moreno, Feedforward output-feedback control for continuous exothermic reactors with isotonic kinetics, Journal of Process Control 22 (1) (2011) 303320.

[11] R.T. Stefani, C.J. Savant Jr., B. Shahian, G.H. Hostetter, Feedback Control Systems, 3rd ed., Saunders College Publishing, Florida, 1994.

[12] Y.-Y. Liu, J.-J. Slotine, A. Barabasi, Controllability of complex networks, Nature, Vol. 473, p. 167-173, 2011.

[13] A. Schaum, L. Alarcon Ramos, R. Bernal Jaquez, C. Rodriguez Lucatero, Markov process-based saturated output-feedback control design for virus extinction in complex networks, Conferencia Internacional de Robotica y Control, Mexico, p. 74-79, 2013.

[14] A. Schaum, Optimality and stability properties of PD-controllers for a class of nonlinear SISO network systems, Proceedings of the 2013 International Conference on Systems, Control and Informatics, p. 232-236, 2013.

[15] Lucatero, C.R. and Jaquez, R.B., Virus and warning spread in dynamical networks. Advances in Complex Systems, 14(03), 341358, 2011.
[16] S. Gomez, A. Arenas, J. Borge-Holthoefer, S. Meloni, and Y. Moreno. Discrete-time Markov chain approach to contact-based disease spreading in complex networks. EPL, 89(26):38009, p. 16, 2010.
[17] E. Castellanos-Sahagun, J. Alvarez, Synthesis of two-point linear controllers for binary distillation columns, Chem. Eng. Commun. 193, p.206232, 2006.
[18] J. Alvarez, C. Fernandez, Geometric estimation of nonlinear process systems, J. Process Control 19 (2), p. 247260, 2009.

Alexander Schaum received his Diplom-Ingenieur in Technical Cybernetics from the University of Stuttgart (2006), and his PhD in Engineering from Universidad Nacional Autonoma de Mexico (UNAM, 2009). He was postdoc at the Departamento de Procesos e Ingenieria of the Universidad Autonoma Metropolitana (UAM)-Iztapalapa in Mexico from 2010-2011. Actually he is visiting profesor at the Departamento de Matematicas Aplicadas y Sistemas, of the UAM-Cuajimalpa in Mexico.

His research interests consist in nonlinear dynamics and control of biological and chemical processes, distributed parameter systems, and complex networks.

Luis Alarcon Ramos received the B.S. degree in electronical engineering from the Universidad Autonoma Metropolitana (UAM) Iztapalapa. He received the M.S. degree in information technology science from the UAM-Iztapalapa. Actually he is associate professor, and PhD student at the UAM-Cuajimalpa in Mexico. His research interests consist in nonlinear dynamics, control theory, complex networks and parallel and distributed computing.

Roberto Bernal received his Bachelor in Science in Physics from Universidad Nacional Autonoma de Mexico (UNAM), and his his PhD in Physics from Universidad Autonoma del Estado de Morelos-ICN (UNAM) Mexico (2006). He was postdoc at the Departamento de Fisica of the UAEM (2006-2007) and in the Theoretical Chemistry Group - University of Turin in Italy from 2007-2009. Actually he is full professor at the Departamento de Matematicas Aplicadas y Sistemas, of the UAM-Cuajimalpa in Mexico.

His research interests are mainly focus on algebraic methods in chemical-physics, mathematical-physics, nonlinear dynamics, and complex networks.

Carlos Rodriguez Lucatero received his Bachelor on Computer Engineering from Universidad Nacional Autonoma de Mexico (UNAM, 1987) , and his PhD in Computer Science from Université Pierre et Marie Curie (Paris VI, 1994). Actually he is researcher and profesor at the Departamento de Tecnologías de la Información, of the UAM-Cuajimalpa in Mexico.

His research interests consist in Theoretical Computer Science, Markov processes, Robot motion planning, Multi-agent systems, and complex networks.

Jesus Alvarez received his Bachelor of Science in Chemical Engineering from the University of Guadalajara in 1976, M.Sc. in Chemical Engineering from Minnesota University in 1979, Ph.D. in Chemical Engineering in 1982. He is actually a full professor at the Universidad Autonoma Metropolitana Iztapalapa.

His research interest consist in Dynamics and Control of chemical and biochemical processes, polymerization reactor engineering, and mathematical process modeling.

ISBN: 978-1-61804-216-3

Acoustic Analysis for Detection of Voice Disorders Using Adaptive Features and Classifiers

Mohamed FEZARI, Fethi AMARA and Ibrahim M. M. El-EMARY

***Abstract*—**Voice diseases are increasing dramatically, due mainly to unhealthy social habits and voice abuse. In this paper, we investigate the methods of acoustic voice analysis (AVA) with adaptive features to develop a system for voice pathologies detection, where the models correspond to classes of patients who share the same diagnostic. One essential part in this topic is the database (described later), the samples voices (healthy and pathological) are chosen from a German database which contains many diseases, non-neurological pathologies (such as chronical laryngitis and Vocal fold nodules), is proposed for this study. A supervised algorithm is used to accomplish this task, Mel frequency cepstral coefficients (MFCCs with variation of Jitter & shimmer), and modeled by weighted Gaussian mixture model (GMM) as it is used in AVA. The work is simulated using MATLAB, for features extraction, for training and testing steps. The results are encouraging for further improvement of combining classifiers and investigation multi-pathologies classifier.

Keywords- Voice disorders, Acoustic voice analysis, classifiction techniques, Jitter and Shimmer, laryngeal deseases**.**

I. INTRODUCTION

Acoustic analysis may provide a useful means to quantitatively characterize the tremulous voice. Assessment voice quality is an important tool for dysphonia evaluation, vocal fold polyp, voice Trimor and other voice pathologies; it is based on perceptual analysis [1] and instrumental evaluation which comprise acoustic and aerodynamic measure [2] [17], the first one is subjective because of the variability between listeners, although the second is objective it is invasive for one hand, on the other hand it has a limited reliability. It is well known that vocal fold pathologies alter the mechanisms of speech production; such disturbance is reflected in voice quality deterioration. Human speech production under both healthy and vocal fold pathology conditions suggests that alternative production models other than traditional may be more accurate [18].

Pitch and Formants Analysis gives many information concerning speaker identification, speaker emotions and voice disorders of speaker. Figure 1.a illustrates the pitch variation by application of the cestrum method analysis of normal and pathological female sounds (32 years).

Mohamed Fezari Author is with Badji Mokhtar Annaba University,Faculty of engineering, bp:12, 23000 Algeria. , Email:mohamed.fezari@uwe.ac.uk
Amara Fethi Autthor is with Badji Mokhtar Annaba University,Faculty of engineering, bp:12, 23000 Algeria, Email:

Ibrahim M. M. El-Emary Author is with faculty of IT, King Abdulaziz University, Saudi Arabia, Email: Omary57@hotmal.com

The high distortion and the variation of the pitch around the expected value (250 Hz) demonstrate a state of the glottic signal anomaly, resulting of a laryngeal pathology.

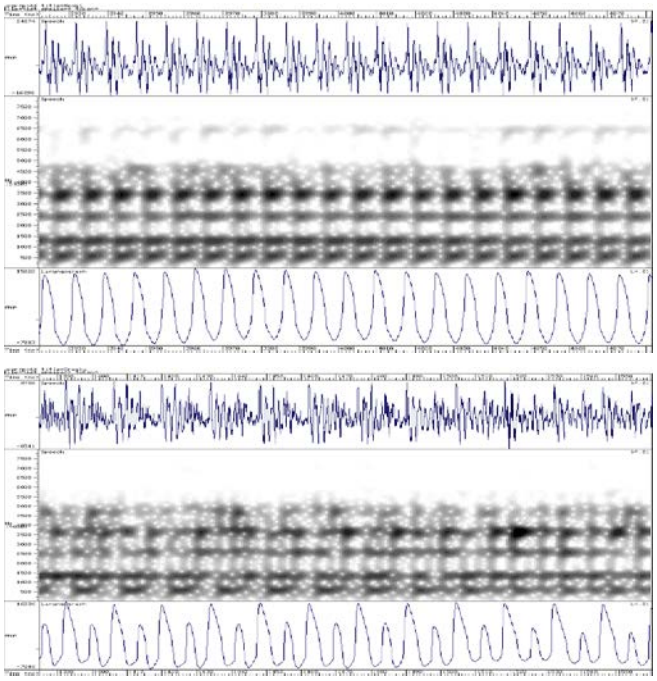

Fig 1.a : Sound of vowel /a/ normal voice and creaky voice Wav, spectrogram and pitch form [23].

Some related works are described here: Marek Wisniewski and all. in 2010 [19] developed a work on improving approach to automatic detection of speech disorders based on the HMMM technique, they apply it in Polish language. It is worth emphasizing that this method enables detection of a category of speech disturbance ie: fricative, nasal, vowels, etc… prolongation, but also provides the information about specific phoneme being disturbed.

N. Saenz-Lechon et All [9], studied the effect of audio compression in automatic detection of voice disorders, they investigated the detection of pathologies in voice when the voice samples have been compressed in MP3 format and different binary rates (160, 96, 64, 48, 24 and 8 kb/s). their detector employs cepstral and noise measurements with their derivatives, to characterize the voice signals. The classification is performed using GMM and SVM. The results between the different proposed detectors are compared by means of detector

ISBN: 978-1-61804-216-3

error tradeoff (DET), they concluded that there is no significant differences in the performance of the detector when the binary rates of the compressed data are above 64 kb/s.

In [20] Lotfi Salhi et All. Presented a new method for voice disorders classification based on multilayer network. The processing algorithm is based on hybrid technique witch uses wavelets energy coefficients as input of the multilayer neural network. The training step uses a speech database of several pathological and normal voices collected from the national hospital of "Tunis" and was conducted in a supervised mode for discrimination of normal and pathology voices. However, the database used in the tests was very short and the tests were used off line, thus the results (100%) of classification do not reflect the reality if the classifier is used on large database and in real-time.

Saenz-Lechon et All in [10], presented an overview of previous classification schemes applied to voice disorders on Massachusetts Eye & ear infirmary (MEEI) Database [11b], they described some methodological paradigms to be considered when designing an automatic pathological voice detection system. They insisted on the use of a commercially well-known databases, a cross-validation strategy based on several partitions to obtain averaged classification performances with confidence intervals, e report of the means of a detection error trade-off (DET), and an investigation of the area under receiver operating characteristic (ROC) curves.

Dean R. Hess [21], studies the effect of tracheotomy tube on voice production, the tube decreases the ability of the patient to communicate effectively, in mechanically ventilated patients, speech can be provided by the use of a talking tracheostomy tube, using a cuff-down technique with a speaking valve and using cuff-down technique without valve. They concluded that team work between the patient and the patient care team can result in effective restoration of speech in many patients with long-term tracheostomy.

This is why the development of automatic system for classification is proposed; in voice processing we distinguish three principal approaches: acoustic, parametric and non-parametric approach and statistical methods. The first approach consist to compare acoustics parameters between normal and abnormal voices such as fundamental frequency, jitter, shimmer, harmonic to noise ratio, intensity [3-6]. The evaluation of acoustic parameters depends on the fundamental frequency; the evaluation of the latter is difficult particularly in the presence of Pathology the fundamental frequency can be calculated by methods presented in [7].

Figure 1.a illustrates the main parts of the voice production system that can be affected by a pathology: throat, tongue, mouth and nasal cavity.

The second approach is the parametric and non-parametric for features selection [8-9].

The classification of voice pathology can be seen as pattern recognition so statistical methods are an important approach. We try to mimic the brain comportment where we can recognize persons from their voice. Many researches are realized for this task, Support vector machine (SVM) is applied to test the effectiveness and reliability of the short term cepstral and noise parameters [10], the same features are used with Hidden Markov Model (HMM) [11]. In [12] the MFCCs are proposed to be the input of multi-layer perceptron (MLP)

In this paper, the conception of our detector is based on AVA and inspired from a system of Automatic speech recognition [22]. 12 MFCCs, energy, dynamic parameters (first derivate and second derivate) with Jitters and Shimmers parameters are extracted to be the input of GMM. This classifier is trained with the algorithm of expectation maximization (EM) to get maximum likelihood (ML). The clustering algorithm K-mean is used for the initialization.

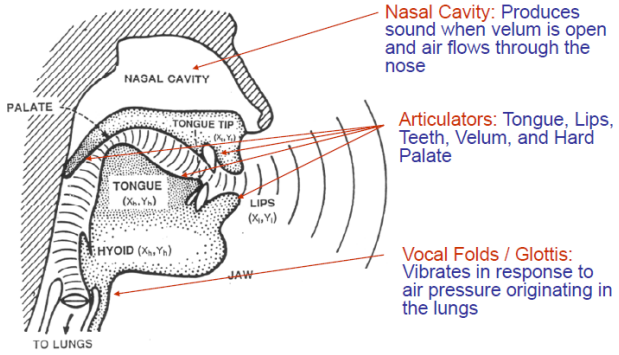

Fig 1.b Voice production system

The number of Gaussians those make up the model is chosen as power of 2 in order to test its influence on the classification rate.

•*Algorithm :*

We present in figure 1.c the principals step to develop a system for speaker recognition:

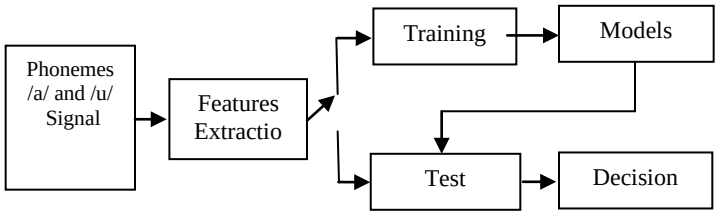

Fig 1.c: Block diagram for speaker recognition [14]

The difference between a system for ASR and a system for voce pathology detection is in two essential key points:

* In ASR the model corresponds to a speaker while the model in second system corresponds to group of patients with the same diagnostic.

* In voice pathologies detection samples used for train are different from samples used for test unlike in ASR where the two sets are used in test.

This paper is organized as a follow: in second section is dedicated to describe different steps to develop the system, the experiments are in section 3. The results are presented in section 4 and the last section is reserved for the conclusion and future work.

ISBN: 978-1-61804-216-3

II. METHODOLOGIE

Our system will pass by the same steps to concept a system for ASR, we will describe theme step by step, the block diagram in "fig2" show different steps adapted to our system.

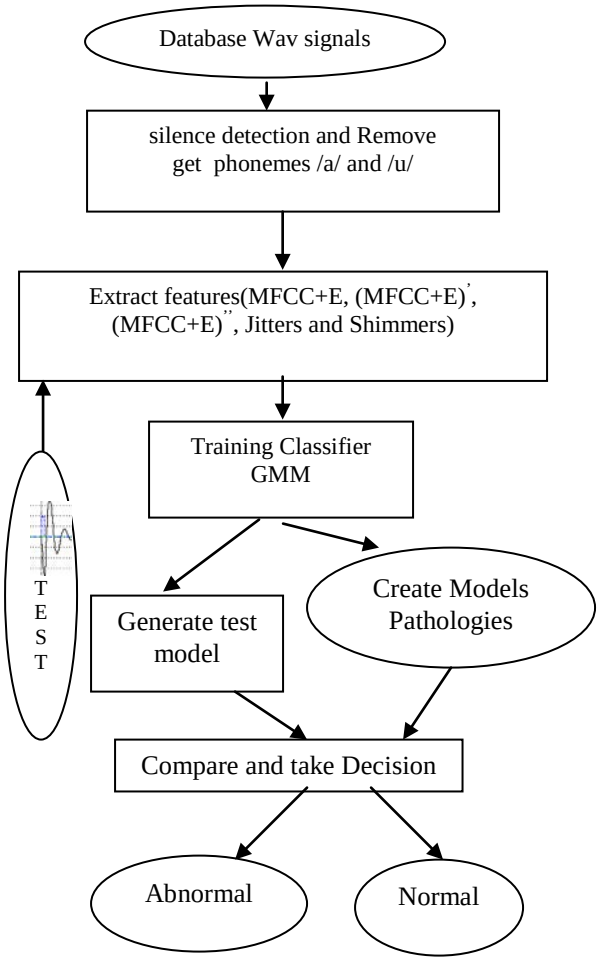

Fig. 2 Block diagram for the voice disorder detector.

A. *Speech signal:*

In this work the creation of the data base is not our goal so we will not discuss the speech acquisition but we will describe the database which the results are built around it.

The database presents an essential factor to develop a detector where the use of standard one helps to compare the obtained results in order to test the effectiveness and the reliability of methods. [12]

In this work we have choose a German database for voice disorder developed by Putzer in [15] which contain healthy and pathological voice, where each one pronounce vowels [i, a, u] /1-2 s in wav format at different pitch (low, normal, high) it contain also phrase and electroglottograph signal (EGG). All files are sampled at 50 KHz

From this large database we have select patients suffer from neurological pathology (spasmodic dysphonia), this disease affects women than men that is why we have choose a female voice for training and testing step, Table.1 show the selected samples. As mentioned above the recording files contain phrase, this study is built around the phrase "good morning how are you" pronounced in Germany. The goal to use phrase in one hand is to get more data for training where GMM need an important quantity of data particularly when use a high number of mixture (Gaussian), in other hand the diversity of data enhance the accuracy of a system.

TABLE1. DESCRIPTION OF DATASET

	Training set		**Test set**	
	Number	Age	Number	Age
Normal	52	20-60	11	20-60
Pathological	29	30-82	9	30-82

Those files are down sampled to 25 KHz in order to get optimal analysis.

B. *Pre- processing:*

Pre-processing of Speech Signal serves various purposes in any speech processing application. It includes Noise Removal, Endpoint Detection, Pre-emphasis, Framing, Windowing and silence remove. In this study we are interesting to remove silence knowing that the efficient features are included in speech portion , then we selected only vowels /a/ and /u/ for the training and tests. [16].

C. *Features extraction:*

Features extraction means finding good parameters that helps to classify between the healthy and abnormal patients, features selection make a boundary between each class.

Spasmodic dysphonia is a disorder of vocal function, characterized by spasms of the muscles of the larynx that disrupt or impede the regular flow of voice this leads us to choose the MFCCs parameters in order to split the glottal source from the effect of cavities or filter in order to have a parameters with significant difference between pathological and healthy voices. More over we added the as features variations of Jetter and Shimmer (which represent variation in frequencies, and in amplitudes of pitch) as formulated in (2) and (3).

C.1 MFCC features

Mel frequency cepstral coefficients are given by:

$$\tilde{C} = \sum_{k=1}^{K} \log(\tilde{S}) \cos[n(k-\tfrac{1}{2})]\frac{\Pi}{K} \qquad (1)$$

These parameters are extracted by 32 filter bank applied on 10 ms (256 points) Hamming windowed frames at 50% of overlap.

C.2 Jitter & shimmer Features

Jitter may occur during voice production, especially in vowel phonation, and it is defined as small fluctuations in glottal cycle lengths [3,4] and [7]. Jitter and shimmer

(amplitude perturbations) over successive speech cycles help give the vowel its naturalness in contrast to constant pitch and amplitude that can result in a machinelike sound. Moreover, jitter (and shimmer) contributes to the voice quality of a speaker. In terms of signal processing, jitter is a form of modulation noise. Specifically, jitter is a modulation of the periodicity of the voice signal. A high degree of jitter results in a voice with roughness that is usually perceived in recordings of pathological voices.

Therefore, a reliable estimation of jitter can be used to discriminate between healthy and dysphonic speakers.

Which are defined as:
Jitter : % change in cycle duration between cycles
Shimmer : % change in speech amplitude between cycles.

The equations (2) and (3) yield to determine the percentage of Jitter and Shimmer in speech signal.

$$Jitter = \frac{\frac{1}{N-1}\sum_{k=1}^{N}\left|T_k - T_{k+1}\right|}{\frac{1}{N}\sum_{k=1}^{N}\left|T_k\right|} \quad (2)$$

$$Shimer = \frac{\frac{1}{N-1}\sum_{k=1}^{N}\left|A_k - A_{k+1}\right|}{\frac{1}{N}\sum_{k=1}^{N}\left|A_k\right|} \quad (3)$$

T_i : time and A_i : Amplitude , N: number of cycles.

D. training using GMM

In pattern recognition (machine learning) the learning is supported by the statistical classifier, Gaussian mixture model (GMMs) is proposed for this task, it consist to represent the data (features) obtained at last step by a simple Gaussian curve described by:

$$P(x_i \backslash \lambda) = \sum_{j=1}^{M} p(x_i \backslash N_j) W_j \quad (4)$$

$$\sum_{j=1}^{m} W_j = 1 \quad (5)$$

λ is the model.

Each component has the general form:

$$p(x) = \frac{1}{(2\pi)^{\frac{d}{2}}|\sum|^{\frac{1}{2}}} e^{\left[-\frac{1}{2}(x-\mu)^T \sum^{-1}(x-\mu)\right]} \quad (6)$$

$\sum$ is the d-by–d covariance matrix and $|\sum|$ is its determinant it characterizes the dispersion of the data on the d-dimensions of the feature vector. The diagonal element σ_{ii} is the variance of x_i, and the non-diagonal elements are the covariances between features. Often, the assumption is made that the features are independent. Thus, $\sum$ is diagonal and p(x) can actually be written as the product of the univariate probability densities for the elements of x.

In order to get optimal model the GMMs one way to get this is the use of Maximum likelihood estimation (MLE) given by:

$$p(X\backslash\lambda) = \prod_{i=1}^{M} p(x_i \backslash \lambda) \quad (5)$$

$$X = (x_1, x_2, \ldots, x_M) \quad (6)$$

Maximizing the likelihood of observing x as being produced by the patient. Nevertheless, in the case where all the parameters are unknown, the maximum likelihood yields useless singular solutions. Thus there is a need for an alternate method.

In literature the use of Expectation Maximization (EM) is the most used solution for this problem. EM is an iterative algorithm starts from initial model; calculated here with the algorithm of clustering K-means.

E. Test step:

Once models are created and that we have managed to train the GMM, we can proceed to the classification test.

A new feature vector Xt is said to belong to an appropriate model if it maximizes p (Xt | λ) for every possible class .

In order to evaluate the performance of the system the results are presented by a confusion matrix represented in "Table 2"

TABLE 2 TYPICAL ASPECT OF A CONFUSION MATRIX

System's decision	**Actual diagnosis**	
	Pathological	**Normal**
Pathological	True positif (TP)	False positive (FP)
Normal	False negative (FN)	True negative (TN)

True positive (TP) or sensitivity, is the ratio between pathological files correctly classified and the total number of pathological voices. False negative rate (FN) is the ratio between pathological files wrongly classified and the total number of pathological files. True negative rate (TN), sometimes called specificity, is the ratio between normal files correctly classified and the total number of normal files. False positive rate (FP) is the ratio between normal files wrongly classified and the total number of normal files. The final accuracy of the system is the ratio between all the hits obtained by the system and the total number of files.

III. EXPERIMENTAL PROTOCOLS

A. Database details

The used database [16] was collected in a collaboration project of the department of phonetics and ENT at the Caritas clinic St. Theresia in Saarbrucken and the Institute of Phonetics of university of Saarland in Germany.

The collection of the database has combined research methodologies from speech science with phonetic methods. Methods from speech research which were used are Electro-glottography (EGG) and recording of the sound pressure waveform (microphone signal). Both signals were recorded onto DAT tape simultaneously in a quiet room. The signals were recorded for a read text and for the vowels /i:/, /a:/ and /u:/ at normal, high and low pitch.

As mentioned above the sample voice (normal and spasmodic) is divided in two set one for the training and one for test so we will create two model.

B. Test Scenarios

Some experiments are realized in order to evaluate the effect of different factors in our system, these experiments are described briefly:

- Change the length of segment.
- Use Mel frequency cepstral coefficients MFCCs, their first and second derivate plus Energy .
- Include Jitter and Shimmer as Features.
- Use of different number of Gaussian (power of 2).
- Change number of iteration for the EM algorithm.

IV. Result and Discussion

In our experiment we need to know the optimal model which give best classification rate, this is obtained by a model with proprieties: hamming window of 256 points, 64 centers (Gaussian), 39 MFCCs and 1000 iterations.

The results are represented in confusion matrix in table 3.

TABLE 3 CONFUSION MATRIX WITH MFCC AND ENERGY COEFFICIENTS

System's decision	Actual diagnosis (MFCCs and Energy)	
	Pathological	**Normal**
Pathological	79.92%	18.10 %
Normal	20.08%	81.90%

This recognition rate presents the percentage of the recognized frames among the total number of frames of the test set witch contain all a files of the class and then averaged.

If we test each file (normal and pathological) separately, we get an accuracy of **100%** for the two classes, by setting up a threshold to the number of classified frames. This result is based on off-line tests. If more than **70%** of the frames of a file are assigned to a certain class, then the whole file is assumed to belong to that class.

A. Discussion:

In this subsection, we discuss some experimental results obtained from the proposed analysis methods.

-The classification rate depend to the number of Gaussian and the number of parameters MFCCs as mentioned in "figures 3"

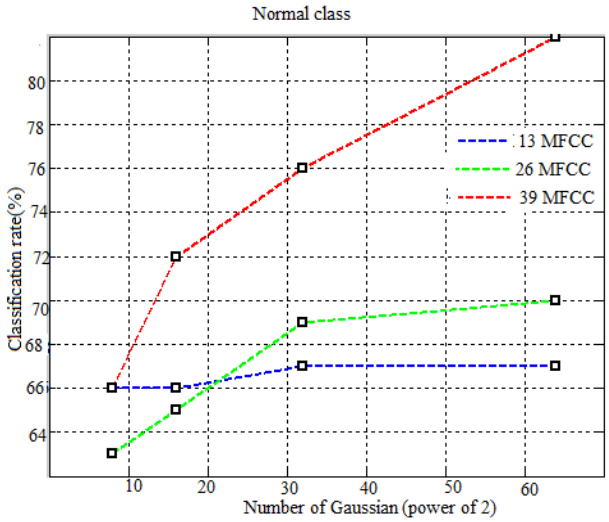

Figure3.a Classification rate for different mixtures and parameters for normal class.

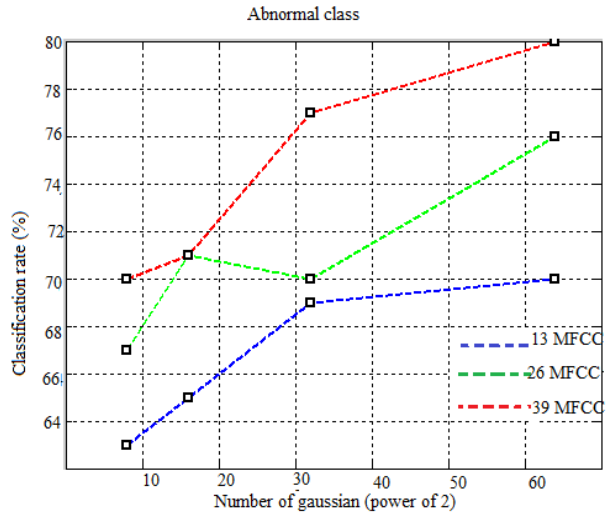

Fig3.b. Classification rate for different mixtures and parameters for abnormal class.

-From the two curve we note that when we increase the number of Gaussian with the increase of the MFCCs coefficients the classification rate improves

-Modeling by GMM requires a large number of data for the training, particularly when we use a high number of Gaussian to create a model, this prevents us to use more than 64 Gaussian particularly with the abnormal class which contains a small number of file.

TABLE 4. CONFUSION MATRIX: INCLUDING JITTER & SHIMMER COEFFICIENTS

System's decision	Actual diagnosis (MFCCs + Jitter & Shimmer)	
	Pathological	**Normal**
Pathological	82.14%	17.4 %
Normal	17.86%	82.6%

ISBN: 978-1-61804-216-3

-Including the Jitters and Shimmers as parameters in features then applying GMM has increased so how the rate of classification in both normal and pathological sets as shown in table 4.

V. CONCLUSION

This work is focused on pathological voices detection (spasmodic dysphonia) and it is built around a system for acoustic voice analysis, with automatic speaker recognition techniques, based on MFCC and variation in frequencies and amplitudes as features (Jitter & Shimmer) and GMM with multiple numbers of Gaussians as classifier.

A good classification rate needs efficient features to characterize each class, in this work, on one hand the accuracy of system increases with the number of parameters (best accuracy with 39 coefficients including Jitter & Shimmer) that means that the difference between normal and abnormal become noticeable with second derivate of MFCC and energy more than the others, on the other hand the effect of the number of Gaussian which makes up the model is important where a sufficient number of mixtures allows to represent data (features) optimally. We can deduce also that the quantity of data used for training a system is very important.

The very promising result motivates us to improve this work, the future work will be directed to the use of another database to assess the independence of the method used for the database, it must give a similar or better results. We will also validate this work with other pathologies for example organic pathologies. In order to improve the obtained classification rate we will be interested in improving the classification phase by combining a hybrid system GMM-SVM. Features selection will be investigated more to get correlated features with specific pathologies and defining more classes such as throat, nasal cavity of mouth pathologies.

REFERENCES

[1] Mirjana Petrovic-lazic et All, " Acoustic Voice Analysis of Patient With Vocal FoldPolyp", in journal of Voice Vol.25 no:1, pp. 94-97, 1997.

[2] Antoine Giovanni1, Pirng Yu2, Joana Révis1, Marie-Dominique Guarella1, Bernard Teston3, Maurice Ouaknine1 ''Analyse objective des dysphonies avec l'appareillage EVA''. Fr ORL - 2006 ; 90 : 183

[3] Miltiadis Vasilakis, Yannis Stylianou ''Voice Pathology Detection Basedeon Short-Term Jitter Estimations in Running Speech'' Folia Phoniatr Logop 2009;61:153–170.

[4] Sonu, R. K. Sharma '' Disease Detection Using Analysis of Voice Parameters'' International Journal of Computing Science and Communication Technologies, VOL.4 NO. 2, January 2012.

[5] Jacques Koremana, Manfred Pützer, Manfred Just ''Correlates of Varying Vocal Fold Adduction Deficiencies in Perception and Production: Methodological and Practical Considerations '' Folia Phoniatr Logop 2004;56:305–320

[6] Miltiadis Vasilakis, Yannis Stylianou ''Voice Pathology Detection Based eon Short-Term Jitter Estimations in Running Speech'' Folia Phoniatr Logop 2009;61:153–170.

[7] Raissa Tavares , Nathália Monteiro , Suzete Correia , Silvana C. Costa , Benedito G. Aguiar Neto (2) and Joseana Macêdo Fechine ''Optimizing laryngeal pathology detection by using combined cepstral features'' Proceedings of 20th International Congress on Acoustics, ICA 2010 23-27 August 2010, Sydney, Australia ICA 2010

[8] N. saenz-Lechon et All., "Effect of Audio Compression in Automatic Detection of Voice Pathologies", in IEEE Transaction on Biomedical Engineering , Vol. 55, no.12, dec. 2008.

[9] N. saenz-Lechon et All, "Methodological issues in the development of automatic systems for voice pathology detection", in Biomed. Signal Processing Control, vil 1 , no:2, pp. 120-128, 2006.

[10] Juan Ignacio Godino-Llorente, Pedro Gómez-Vilda,Nicolás Sáenz-Lechón1, Manuel Blanco-Velasco, Fernando Cruz-Roldán, and Miguel Angel Ferrer-Ballester" Support Vector Machines Applied to the Detection of Voice Disorders" Springer-Verlag Berlin Heidelberg pp. 219 – 230, 2005.

[11] Alireza A. Dibazar, Theodore W. Berger, and Shrikanth S. Narayanan" Pathological Voice Assessment"IEEE EMBS 2006 NEW YORK.

[12] Nicolas Saenz-Lechon, Juan I. Godino-Llorente, Vıctor Osma-Ruiz, Pedro Gomez-Vilda ''Methodological issues in the development of automatic systems for voice pathology detection'' Biomedical Signal Processing and Control 1 (2006) 120–128.

[13] G. Pouchoulin, C. Fredouille1, J.-F. Bonastre, A. Ghio, M. Azzarello, A. Giovanni ''Modélisation Statistique et Informations Pertinentes pour la Caractérisation des Voix Dysphonies'' Actes des XXVIes journ´ees d''etudes sur la parole Dinard, juin 2006.

[14] Charles pelltier "classification des son respiratoires en vue d'une detection automatique des sibllants" these november 2006.

[15] Manfred Putzer & Jacques Koreman '' A german databse for a pattern for vacal fold vibration '' Phonus 3, Institute of Phonetics, University of the Saarland, 1997, 143-153.

[16] Ayaz Keerio, Bhargav Kumar Mitra, Philip Birch, Rupert Young, and Chris Chatwin "On Preprocessing of Speech Signals" On Preprocessing of Speech Signals" World Academy of Science, Engineering and Technology 47 2008.

[17] Sanchez I, Avital A, Wong I, Tal A, Pasterkamp H. "Acoustic vs. spirometric assessment of bronchial responsiveness to methacholine in children" . Pediatr Pulmonol 1993;15(1):28-35.

[18] Darcio G. Silva, Luıs C. Oliveira and Mario Andrea ''Jitter Estimation Algorithms for Detection of Pathological Voices'' Hindawi Publishing Corporation, EURASIP Journal on Advances in Signal Processing Volume 2009, Article ID 567875, 9 pages.

[19] Hansen J. H.L. et All., « A non-linear Operator based speechFeature Analysis Method with Application to Vocal fold pathology Assessment », IEEE Transaction Biomedical Eng. 29 pgs. 1995.

[20] lotfi Salhi, Talbi Mourad and Adnene Cherif, " Voice Disorders Identification using Multilayer NeuralNetwork", in the International Arab journal of Information Technology, Vol. 7, no 2, april 2010.

[21] dean R. Hess, " Facilitating Speech in the patient With a Tracheostomy", in Journal of Respiration care , April 2005, Vol. 50 No.4, pp. 519-525.

[22] Mohamed FEZARI, Hamza Attoui & Mouldi BEDDA "Arabic Spotted Words Recognition System Based on HMM Approach to control a didactic Manipulator Arm", In Proc. MS'08, nt. Conf. On Modelling and Simulation, PETRA/ Jordan, Vol. 2008.

[23] Acoustic of speech and hearing analysis, "Lecture note 2.1: voice quality" ,of UCL/PLS/SPSC2003/WEEK2-1/110920/1, 2003.

Recent Review of Active Noise Control Systems Using DSP Based Adaptive Algorithms

S.Manikandan ,
Principal,
Ganesh College of Engineering,
Mettupatti, Salem – 636111.
drsmanikandan1978@gmail.com

Abstract—This paper represents a short review of active noise control (ANC) with the emphasis on ANC systems implemented by using DSP algorithm. The physical mechanism behind active noise control, based on which local silence zones can be created is detailed. Basic configurations for realization of ANC systems are then introduced. It is shown that FxLMS algorithm has been widely used in different types of ANC systems. Available theoretical work on analysis of FxLMS-based ANC systems is reviewed. Shortcomings of available theoretical findings are discussed. Finally, recent advances in theoretical analysis of FxLMS-based ANC systems are introduced. These advances can be considered as the recent contributions made by the authors. Simulation results are also used to demonstrate the validity of the theoretical findings.

Keywords: ANC,FxLMS,LMS,FIR,DSP,RLS.

I. INTRODUCTION

Acoustic noise problem are increased number of industrial equipment (1) Acoustic noise control using passive technique, it is high attenuation over a board frequency range, costly (2).It has a mechanical vibration in another related type of noise. It creates the problem in all the areas(3).Electromechanical system is cancels the primary (or) unwanted noise based upon superposition principle.(4)ANC system efficient attenuates low frequency noise, very expensive or bulky Acoustic ANC used in microphone and an electronically driven loudspeaker to generate a canceling sound. It was first proposed in a 1936 patent by Lueg(7). The characteristics of the acoustic noise source and environment are time varying, amplitude, phase etc, ANC system must be adaptive order system it has to minimize an error signal can be realized as (transversal) finite impulse response (FIR). (Recursive) infinite impulse responses (IIR), Lattice transform – domain filters. It has most used in least – mean – square (LMS) algorithm (17) & (18).

Electro acoustic (or) electromechanical transducers are sampled and processed in real time using (DSP) digital signal processing system(5). It was developed in 1980's low cost implementation. It has more sophisticated algorithm allow faster convergence & greater noise attenuation(6) & more robust noise is defined as most of undesirable disturbance, where it is born by electrical, acoustic, vibration and etc., ANC used for different type of noise using sensors & secondary sources.

A. Current Applications

ANC is a large amount of noise reduction in a small package, especially at low frequencies (8).

1. Automotive: Electronic muffles for exhaust, induction system and so on.
2. Appliances: Air conditioning ducts, refrigerators washing machine, head boarder and so on.
3. Industrial: Fan, air ducts wind tunnels and so on.
4. Transpiration: Airplanes, ships, boats, and so on.

B. *Performance Evaluation & Practical Considerations*

ANC performance analysis resolvers the following issues

1. The fundamental performance limitation
2. The practical constraints that limit performance
3. Performance balanced against complexity
4. How to determine practical design architecture. At each step is degree of confidence as gained and a bench mark is established for compared next level checking

C. *ANC system properties are*

1. Maximum efficiency over larger frequency to cancel a wide range of noise.
2. Autonomy it is build and reset
3. Self adaptability
4. Robustness & reliability

ANC is based on feed forward control. Input is sensed and the active noise controller attempts to cancel noise without the benefit of an "upstream" reference input.

ISBN: 978-1-61804-216-3

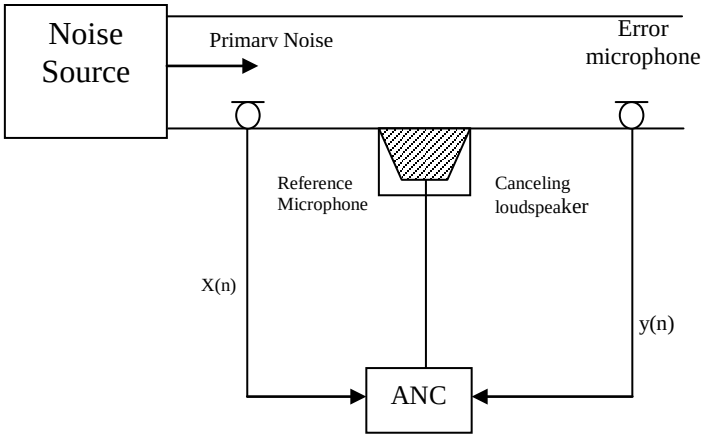

Fig1. *Signal – channel broad band feed forward ANC system in a duct*

II. BROAD – BAND FEED FORWARD ANC

It has a single reference sensor, single secondary source & signal error in this section. Single channel figure above mentioned. The error microphone used to monitor the performance of the ANC system controller is used minimize the acoustic noise (9).

The basic broad band ANC system shown in Fig.1 and the adaptive system identification framework shown in Fig.2 in which adaptive filter W(Z) and primary path P(Z) the Fig.1 and Fig.2 difference between Fig.2 using Summing junction for subtraction of electrical signals

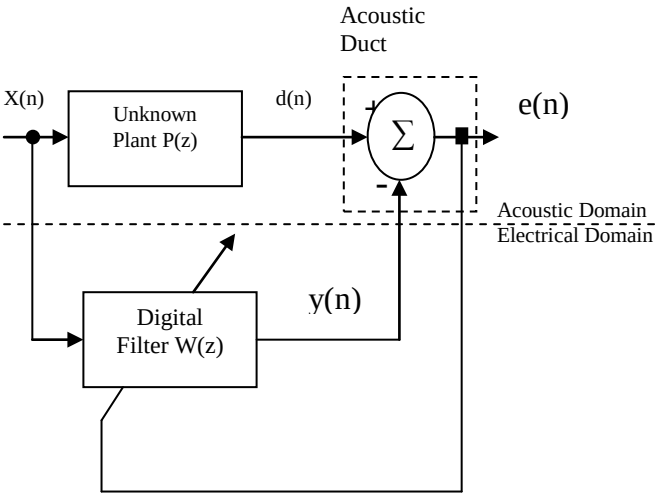

Fig.2 *system identification of Active Noise Control System*

w(z) minimize the error signal e(n) i.e e(z)=0 w(z)=p(z) for x(z) ≠0 the adaptive filter output y(n), Primary disturbance d(n).

E(n)=d(n)-y(n)=0, which result in perfect cancellation of both sounds based on superposition principals.

$$See(w) = [1-cdx(w)]sdd(w) \qquad (1)$$

Where cdx(w) is the magnitude – squared coherence function between two wide sense d(n) & x(n). sdd(w) is the auto power spectrum of d(n). [cdx(w) ≈ 1] the maximum noise reduction of an ANC systems at frequency w by $-10\log_{10}[1-cdx(w)]$ in figure.1. Causality condition is movement the ANC system is capable of canceling board band random noise. Then the causality is not possible. The system can effectively control only narrow band (or) periodic noise (10).

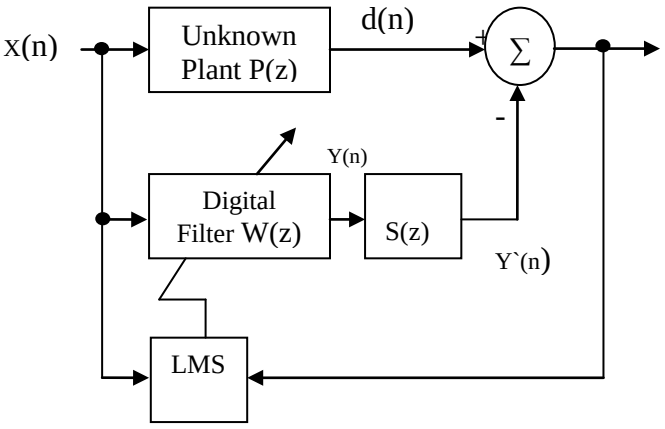

Fig.3Simplified block diagram of Active Noise Control system.

In this necessary to compensate for the secondary path transfer function S(z) from y(n) to e(n), which includes the D/A converter, reconstruction filter, power amplifier, loudspeaker, acoustic path from loudspeaker to error microphone, preamplifier, anti aliasing filter and A/D converter

$$E9X)=[P(Z)-S(Z)\ W(Z)]X(Z) \qquad (2)$$

The residual error is ideally zero i.e. E(Z)=0, The Optimal transfer function is

$$W^0(Z) = \frac{P(Z)}{S(Z)} \qquad (3)$$

It W(Z) has to simultaneously model P(Z) inversely model S(Z). it is a proper model of the plant is a key advantage change is i/p signal caused by changing in the noise sources. It is FIR filter function 1/s(z) show in fig(3) P(z) does not contain a delay of at least equal length

ISBN: 978-1-61804-216-3

III. FILTERED – XLMS ALGORITHM

Morgan(31) suggested two approaches to solving this problem, the first solution is to place an inverse filter 1/s(z), is series with s(z) to remove its effect the second solution is to place an identical filter in the reference signal(11).

E. *DERIVATION OF THE FXLMS ALGORITHM*

. $E(n)=d(n)-s(n)*[W^t(n)x(n)]$ (4)

Where n is time index s(n) is impulse response of secondary path S(Z), * denoted convolution.

$W(n)=[w_o(n),w_1(n)\ldots\ldots W_L\text{-}1(n)]^T$ (5)

$X(n)=[x(n)\ x(n-1)\ldots\ldots x(n-L+1)]^T$ L is filter order mean sequence cost function

$\sum(n=E(e^2(n)], \sum\hat{}(n)=e^2(n)$ (6)

$W(n+1)=w(n)-\mu/2\Delta\ \sum\hat{}(n)$ (7)

$\nabla\sum\hat{}(n)=\nabla e^2(n)=2[\nabla e(n)]e(n)$ have $\nabla e(n)=-s(n)*x(n)=-x^1(n)$, where $x^1(n)=[\ x^1(n)\ x^1(n-1)$ (8)

$x^1(n-L+1)\ ]^T$ and $x^1(n)=s(n)*x(n)$

$\nabla\sum\hat{}(n)=-2x^1(n)\ e(n)$ (9)

Substituting 9 in to 6 we have FXLMS Algorithm

$W(n+1)=w(n)+\mu x^1(n)\ e(n)$ (10)

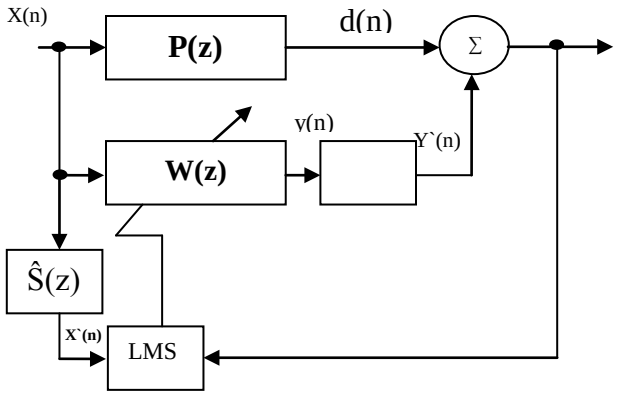

Fig4. Block Diagram of ANC system using the FLXMS algorithm.

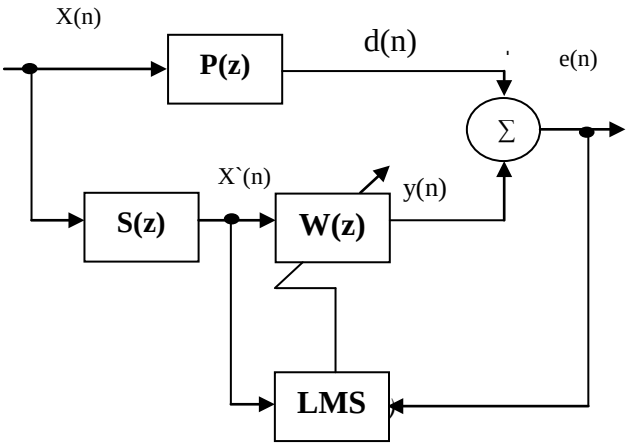

Fig.5 Equivalent diagram if Fig.4 for slow adaptation and

F. ANALYSIS OF FXLMS ALGORITHM

If $\hat{S}(z)*x(z)$, maximize step size that can be used in FXLMS Algorithm is

$$\mu max = \frac{1}{Px^1(l+\Delta)} \quad (11)$$

$Px^1=E\ (x^12(n)]$ power filtered reference signal $x^1(n)$ & is Δ no of samples.

The error is estimated is the two parts:

Amplitude error and phase errors. The optimal unconstrained transfer function $W^o(z)$,

$$W^o(z) = \frac{P(z)\ S_{xx}(z)}{[S_{xx}(z)+S_{uu}(z)} \quad (12)$$

In Fig.4 secondary part transfer function s (z) is modeled as a pure delay Δ , $\hat{S}(z)$ replaced by a delay (12).

G. LEAKY FXLMS ALGORITHM

It is a direct application of the FXLMS Algorithm

$\sum\hat{}(n)=e^2(n)+\gamma\ W^T(n)\ w(n)$ (13)

where γ is a weighting on the control effort.

$W(n+1)=Vw(n)+\mu x^1(n)\ e(n)$ (14)

where V=1-μ8 is the leakage factor 0<v<1.

If x(n) is the signal picked up by the reference sensor & F(z) if the feedback path transfer function from the output of adaptive filter w(z). the steady – state transfer function,

$$W^o(z) = \frac{P(z)}{S(Z)+P(Z)F(Z)} \quad (15)$$

$H_{OL}(z) = W(Z)F(Z)$, HOL(Z) – open loop transfer fn,

$$H_{OL}(z) = \frac{P(z)\ C(z)}{S(z)+P(Z)F(Z)} \quad (16)$$

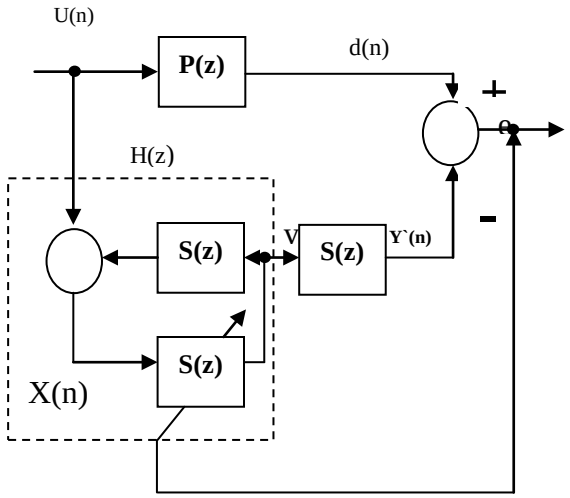

Fig.6 diagram of ANC system with feedback

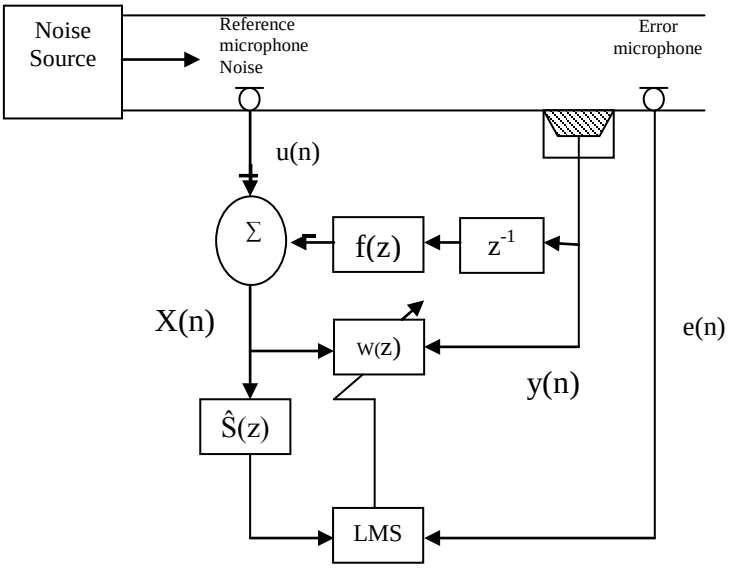

Fig.7 ANC with acoustic feedback neutralization.

The simple approach to solving the feedback problem is to use a separate feedback cancellation (or) "neutralization" filters within the controller. We are using the broad band adaptive feedback forward control with a reference sensor, in the above section we seemed (13).

IV. NARROW – BAND FEED FORWARD ANC

In this method using reference sensor, but reference sensor is not influenced by the control field ie. Tachometer.

Here using too types of the reference signals. They classifieds into.

1. An impulse train with a period equal to the fundamental frequency to the periodic noise ie. Chaplin (or) wave form synthesis
2. Originally cancelled for tonal inference is called adaptive notch filter.

G. WAVEFORM SYNTHESIS METHOD

In this method using waveform synthesizer stores canceling noise waveforms.

$$Y(n) = w_j(n)\,(n) \quad ; \; j(n) \approx n \bmod L$$

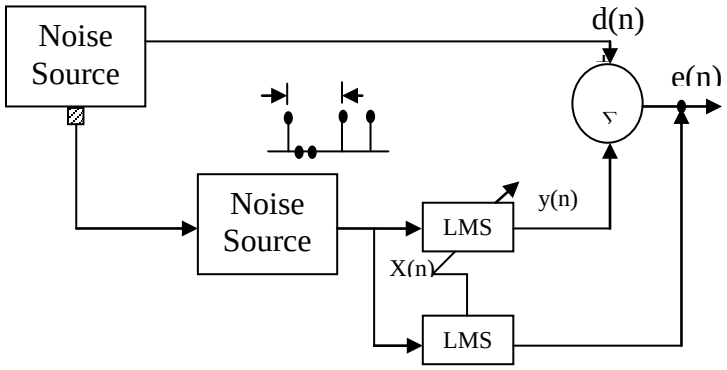

Fig.8 Equivalent diagram of waveform synthesis method using impulse train input and neglecting secondary path effects.

Here the signal will be analyzed kronecker delta function will be used.

FXLMS Algorithm used in synchronous periodic controller in the ideal environment

$$H(Z) = \frac{1-z^{-1}}{1-[1-\mu S(z)]\, z^{-L}} \qquad (17)$$

The steady – state transfer fn H(z) from D(z) to E(z) for the delayed LMS Algorithm

$$H(Z) = \frac{1-z^{-1}}{1-[1-\mu Z^{-l}\ \Delta^{/L]}L)\, z^{-L}} \qquad (18)$$

μ is increased, these out-of-band peaks become larger until the system finally becomes unstable.

H. ADAPTIVE NOTCH FILTER

In this method using narrow band adaptive noise canceller. in this method main advantage is easy to control bandwidth and infinite null. the exact frequency of the interference(14) (15).

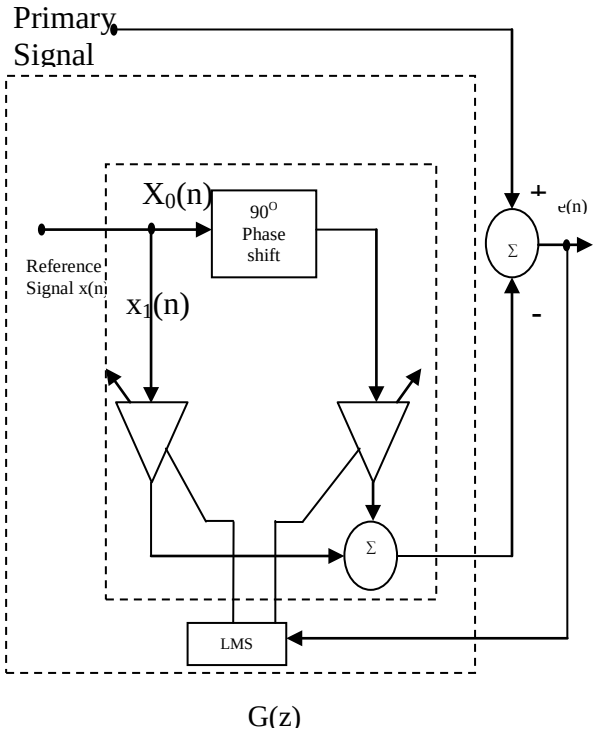

Fig.9 Signal – frequency adaptive notch filter.

$$H(Z) = \frac{E(Z)}{D(Z)} = \frac{Z^2 - 2Z\cos W_o + 1}{Z^2 - (2-\mu A^2)Z\cos W_o + 1 - \mu A^2} \quad \frac{1 - z^{-1}}{W(Z)} \qquad (19)$$

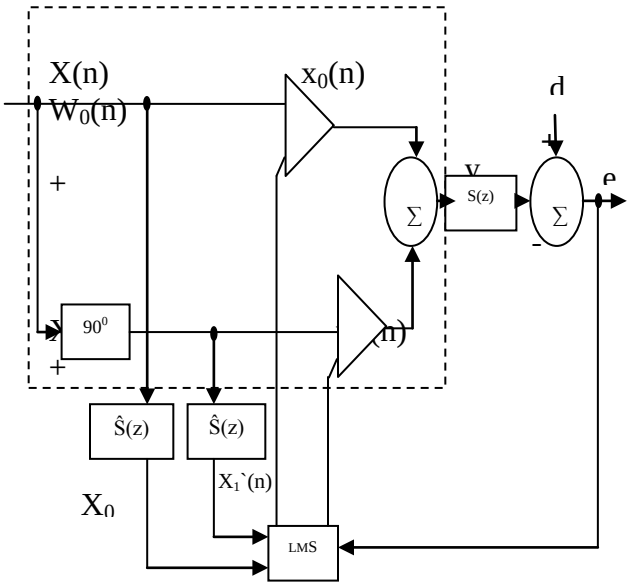

Fig.10. Single-frequency ANC system using the FXLMS algorithm.

V. CONCLUSION

ANC cancels the unwanted noise from secondary sources. In this ANC system is practically adapted algorithms and DSP implementation for real-world applications, FXLMS Algorithm based on broad band feel forward, narrow –band feel forward, adaptive feedback control. ANC signal algorithm expanded to multiple channel cases for controlling the noise field in enclosure or a larger dimension duct. Various adaptive algorithms are lattice, frequency domain, sub band and RLS algorithm were also modified for ANC application. Online secondary path modeling was provided some direction on new algorithms real world problems are demonstrated application to connect.

References

1. Ahmad N.A. and Okwonu F.Z. (2011), Least Squares Problem for Adaptive Filtering, Australian Journal of Basic and Applied Sciences, 5 No. 3, 69-74.
2. Akhtar M.T. (2007), On Active Noise Control Systems with Online Acoustic Feedback Path Modeling, IEEE Transaction on Audio, Speech and Language Processing, No. 2, 593-600.
3. Akhtar M.T. (2009), Improving Performance of Active Noise Control Systems in the Presence of Uncorrelated Periodic Disturbance at Error Microphone, IEEE Transaction on Audio, Speech and Language Processing, No. 3, 2041-2044.
4. Alves R G, Petraglia M R and Diniz P S R (2000), Convergence Analysis of an Oversampled Subband Adaptive Filtering Structure Using Global Error, Proc. ICASSP, Vol. 1, pp. 468-471.
5. Bahoura M. and Ezzaidi H. (2009), FPGA-implementation of a sequential adaptive noise canceller using Xilinx system generator, Inter. Conf. on Microelectronics ICM, Marrakech, 213-216.
6. Boucher C, Elliott S J and Nelson P A, (1990), The effect of modeling errors on the Performance and stability of active noise control systems, Proc. Recent Advances in Active Control of Sound Vibration, pp. 290-301.
7. Chaoui J, Gregorio S de, Gallisian G, Masse Y (1999), DSP-Based Solution for Ambient Noise Reduction in Mobile Phones, Proc. ICASSP, Vol. 4.
8. Das D.P. and Panda G (2004), Active mitigation of nonlinear noise processes using a novel filtereds LMS algorithm, IEEE Trans. Speech, Audio Processing, vol. 12, no. 3, p.313–322.
9. Delvecchio D, Piroddi L. (2011), A nonlinear active noise control scheme with online model structure selection, 50th IEEE Conference on Decision and Control, Orlando(FL), USA, , pp. 8014–8019.
10. Diniz P. S. R. (1997), Adaptive filtering algorithms and practical implementation, Norwell, MA: Kluwer.
11. Douglas. S, and W. Pan (1995), Exact Expectation Analysis of the LMS Adaptive Filter, IEEE Trans. Signal Process., 43: 2863-2871.
12. Elliott S J and Nelson P A (1993), Active Noise Control, IEEE Signal Processing Magazine.
13. Feintuch P F, Bershad N J and Lo A K (1993), A frequency domain model for filtered LMS algorithms stability analysis, design and elimination of the training mode, IEEE Transactions on Signal Processing, Vol. 41, pp. 1518-1531.
14. Ghafarioun E., Sharifi-Tehrani O. and Khaluei T. (2011), An Evaluation of Probability of Transmitted Pilot Bit Error on Multi- Path Fading Channels and Using it in Estimation the Mobile Station Speed, Inter. Journ. on Comm. Anten. and Prop. (IReCAP), No. 1.
15. Glentis G.O, K. Berberidis and S. Theodoridis, (1999), Efficient least squares adaptive algorithms for FIR transversal filtering, IEEE Signal Process. Mag., 16. 4. 13-41.

The control of an industrial process with PLC

Florica Petrovan, Alina Balan, Daniel Besicuta and Cristian Barz

***Abstract*—** The present paper intends to highlight the utility and importance of programmable automates in the control of the industrial processes. The paper presents the programming of a Siemens CPU 313C PLC in Ladder Diagram language and the making of a graphical interface for an interactive simulation with the help of a touch screen HMI of a concrete plant.

The application allows the control and the simulation of the production processes for some mixtures recipes, the manual control of the plant's components and the simulation of the monitoring of quantities in the silos with the help of some level sensors placed inside them.

***Keywords*—**PLC, automatic control, control systems, process interface

I. INTRODUCTION

Controlled engineering has evolved in time. Sometime, in the past, humans were the main method to control a system. Nowadays, electricity is used for control, and this control is based on relays. These relays allow turning energy on or off without using a mechanical switch.

The development of technology and implicitly of computers, which are low cost, led to revolutionizing the appearance of PLCs (programmable logic controllers). The progress of technology at large scale led to the possibility to simulate in real time many applications in the industrial field, these being very useful when a technological process is being programmed, preventing or removing possible malfunctions and/or system blockages that can destroy or temporarily affect its components. This causes the reduction of costs with the implementing of any automated technological process, because the verification through simulation does not imply a massive consumption of materials for diverse initial testing. [2], [3]

Through its conception, a programmable controller is adaptable for functioning in the industrial environment, it can operate in a large variety of temperature and humidity, it is easily adaptable to interfacing with any process and does not raise any special problems regarding the training of service personnel, due to the programming facilities it offers.

At the present, it is estimated that over 60% of the total industrial commands in the advanced countries are carried out with PLCs, and this percentage is increasing. [1]

II. THEORETICAL BACKGROUND

The Programmable Logic Controllers are programmable automates of command and adjustment which are used for industrial machinery and processes.

Their programming is done using dedicated software, developed by each PLC producer, but having as common point the use of Ladder Diagram (the electrical command schemes).
The structure of a PLC is made of:

- *the central unit*: represents the most important part of the programmable controller and it has 3 important parts: processor, memory and power source. It practically leads the entire process;
- *the programming unit*: currently, it is represented, in most cases, by a computer through which programs can be written, which then are uploaded on the central unit for running. In the case when an easier to maneuver unit is desired, most companies will supply the programmers with consoles (laptop type systems), through which programs for controllers can be written;
- *input/output modules:* they allow the interconnection with the process, receiving or giving out signals to it. These can be directly linked with the central unit or through distance control (if a certain process requires it);
- *base*: the device on which the central unit, the input/output modules and other additional functioning modules (where needed) are set.

The internal structure of a PLC is presented in Fig. 1.

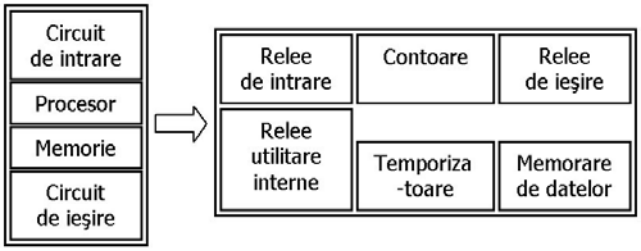

Fig. 1. The internal structure of a PLC

The programming using Ladder Diagrams appeared in the case of programmable controllers due to the necessity to have an easy programming way which allows the realization of applications without having complex programming knowledge.

The Ladder Diagrams are taken from electrical field and they inherit certain names and representations from this field. The base elements of the ladder diagrams are the contacts and coils. [4]

Siemens succeeded to bring its contribution to numerous big projects, considering that SIEMENS is a concern with a rich portfolio of products and services in the following fields: information and communications, medical technology, energy, transportation, automations and drives. The decisive criteria in

ISBN: 978-1-61804-216-3

designing are the stability and robustness of the system, without neglecting aspects such as: the easiness in operation, the monitoring and registering of errors, diagnosing possible malfunctions and also a fast and easy service. [6]

Also, an important accent is on the consistent documentation of the application. Designing a controller system implies choosing for the beginning of a standard solution, successfully implemented and tested, followed by its developing and its modifying in order to satisfy the requirements of the client for the application in question.

For the functioning of the PLC, the use of and interface is necessary in order to monitor and command the industrial process.

HMI MT8070 iH is a touch screen produced by Weintek which facilitates the creation of a graphic interface for a large number of PLCs found on the market. MT8000 series is the new generation of HMI from Weintek. This is more than a simple touch screen; it is capable of programming the PLC and of transferring data and programs among several similar devices from this producer. [7]

III. DESIGNING AND IMPLEMENTING THE APPLICATION

The project has been realized with the help of software: Simatic Step 7 Manager, software for the programming of PLCs produced by Siemens Company, and EasyBuilder 8000, software used for the realization of graphical interfaces for simulation.

The paper highlights the main functionalities that an application which simulates a concrete plant can have, thus: implementing mixture recipes, manual control of silos pumps, functioning of the agitator and of the conveyer belt, signaling the fact that a certain product has reached the maximum or minimum quota allowed by the silo.

A. Implementing the recipes

A certain debit, of kg/s, respectively of l/s, has been established for each silo and for the water pump, as follows: cement 30 kg/s, sand 20 kg/s, additive 10 kg/s, water 15 l/s. One recipe produces 1000 kg of mixture.

Each recipe is started with the 'START' button and it can be stopped by pushing the 'RESET' button. After pressing the start button, the operator has nothing else to do but supervise the functioning of the production process and to stop it in case it becomes necessary.

The production process of a recipe is the following: at the push of the start button, the cement pump, the conveyer belt and the agitator are activated; after the time set for the cement in the recipe is up, a 2 seconds break follows, after which the sand pump is activated and after the sand pump stops, there is another 2 seconds break.

The additive is also placed on the conveyer belt and after it stops, the belt functions a few more seconds to realize a complete tour in order to unload the ingredients into the agitator; when the conveyer belt stops, the water pump is activated and it unloads the necessary quantity of water for the recipe into the agitator.

After the time for the functioning of the water pump is up, the agitator runs for a while for the homogenization of the mixture; when the agitator stops, an evacuation pump is activated which unloads the obtained mixture in the cars that will transport it to the site where it is going to be used.

In the case of recipes, only two entrances are used, for start and stop, the exits being controlled with the help of time relays and intermediate relays. The intermediate relays are known in the Ladder Diagram programming language as "Markers", using the symbols M0 … Mn (Fig. 2). [5]

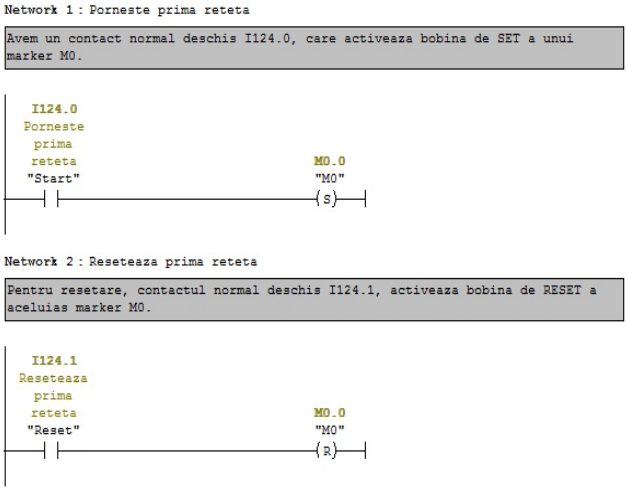

Fig. 2. Start and stop of the first recipe

Once a recipe started, the contact of the set M0 coil also activates the cement pump, the conveyer belt and the agitator, each of these having a certain functioning time counted by the time relays.

It is being proceeded analogously for the other two recipes, each having an entrance for start and one for stop, activating different markers, whose contacts activate the exits corresponding to the pumps, agitator and conveyer belt.

Stopping the pumps and the other components is done by activating the reset coil of some markers. Activating these coils is done by the time relays, after the established functioning time is up. Fig. 3 presents the time relay which counts the functioning time of the agitator.

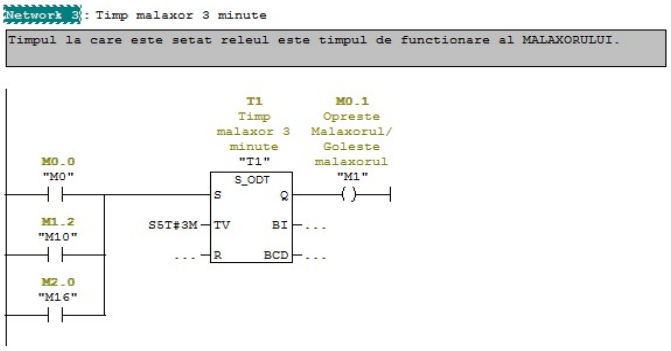

Fig. 3. Functioning time of the agitator

As it can be seen in the figure above, the functioning time of the agitator is the same for each of the implemented recipes (Fig. 4).

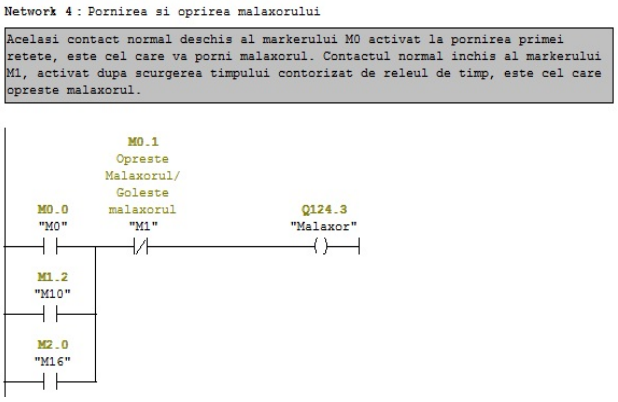

Fig. 4. The start and stop of the agitator

B. The interface in EasyBuilder 8000

The EasyBuilder 8000 program is easy to use. The interfaces are created on panels of 800x480, these being stored in a list of panels. The interface created to simulate the functioning of the concrete plant is made of 6 panels. In the time of the simulation, the switching between panels is realized with the help of some buttons. (Function Keys).

The Main Panel (Fig. 5) is the panel that opens when the simulation starts. This is totally made of buttons which help select the other screens contained in the application.

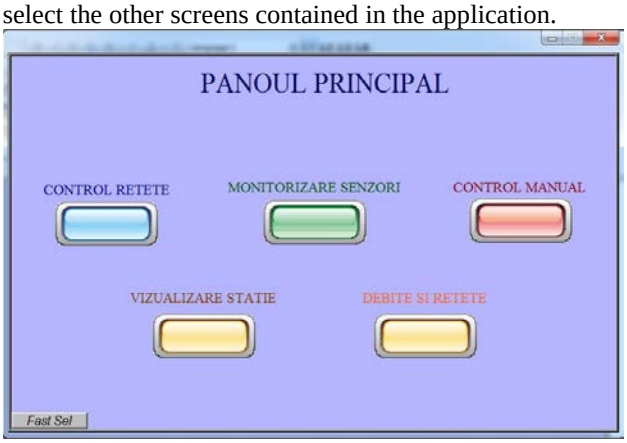

Fig. 5. The main panel

The recipe control panel: This is the panel through which the operator can start or stop the operation of processing a mixture recipe (Fig. 6). The screen contains a start button and a reset button corresponding to each recipe. These buttons have been assigned to the start and stop contacts from the scheme realized in Simatic Step 7 Manager.

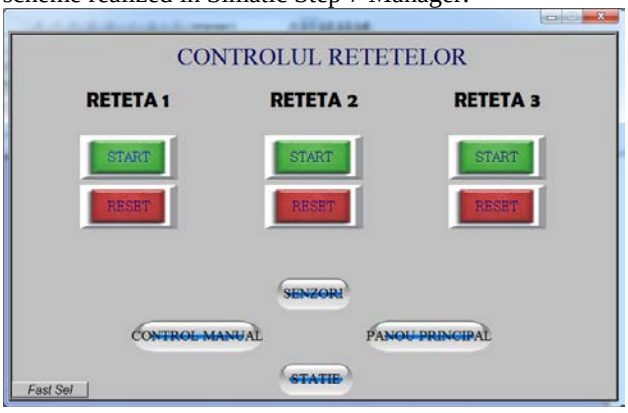

Fig. 6. The recipe control panel

The station view panel: The station view screen is made of three silos, a water tank, an agitator, the conveyer belt and a button to return to the main panel. The silos, the water tank, the metallic legs which support the belt and the agitator have been chosen from the image library of the program (Fig. 7).

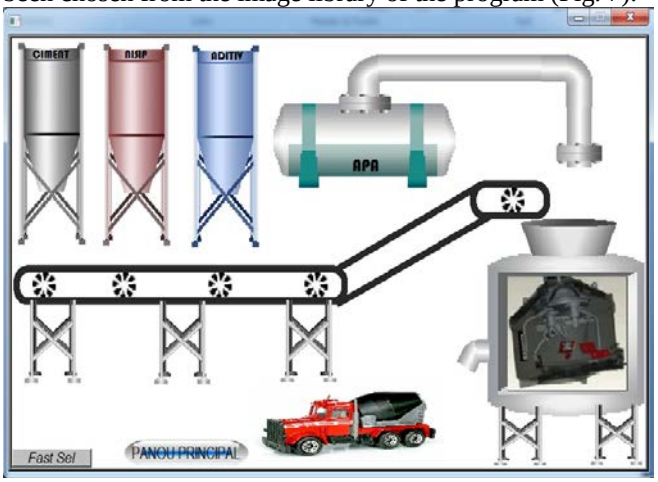

Fig. 7. The station view panel

Sensor monitoring panel: To simulate the functioning of sensors, the panel contains a button for each level, near each silo (Fig. 8). We assigned these buttons to the contacts which represent the sensors, the LEDs being assigned to the exits activated by each sensor.

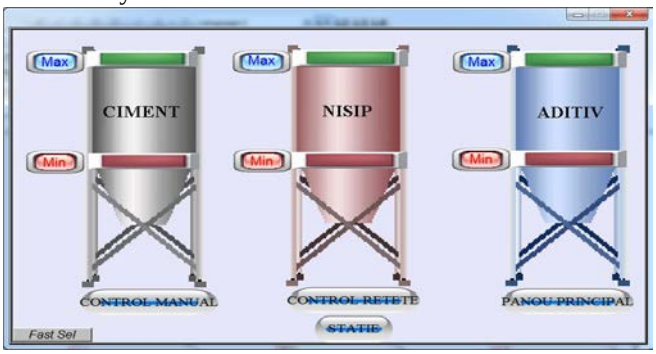

Fig. 8. The sensor monitoring panel

"Debits and Recipes" panel: This plane (Fig. 9) displays two tables, one that shows the debits of each pump and one that displays the detailed recipes, more exactly, the quantities of each ingredient.

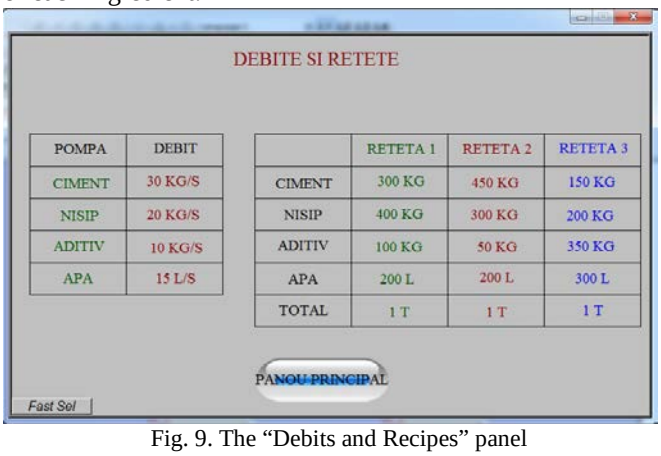

POMPA	DEBIT
CIMENT	30 KG/S
NISIP	20 KG/S
ADITIV	10 KG/S
APA	15 L/S

	RETETA 1	RETETA 2	RETETA 3
CIMENT	300 KG	450 KG	150 KG
NISIP	400 KG	300 KG	200 KG
ADITIV	100 KG	50 KG	350 KG
APA	200 L	200 L	300 L
TOTAL	1 T	1 T	1 T

Fig. 9. The "Debits and Recipes" panel

ISBN: 978-1-61804-216-3

C. Settings for interface with CPU 313C

Each added element in the Weintek panel, must have its properties set in order to have its correspondent from the CPU 313C automate program recognized in the moment of the online simulation (Fig. 10).

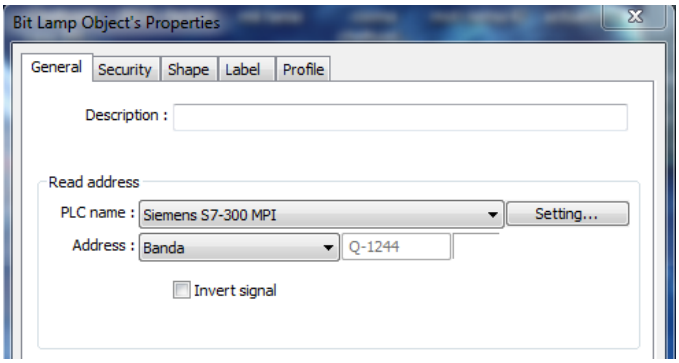

Fig. 10. Setting the bit lamp

The different buttons that can be added in the menu window can have different type correspondents in the program of the CPU 313C automate (Fig. 11).

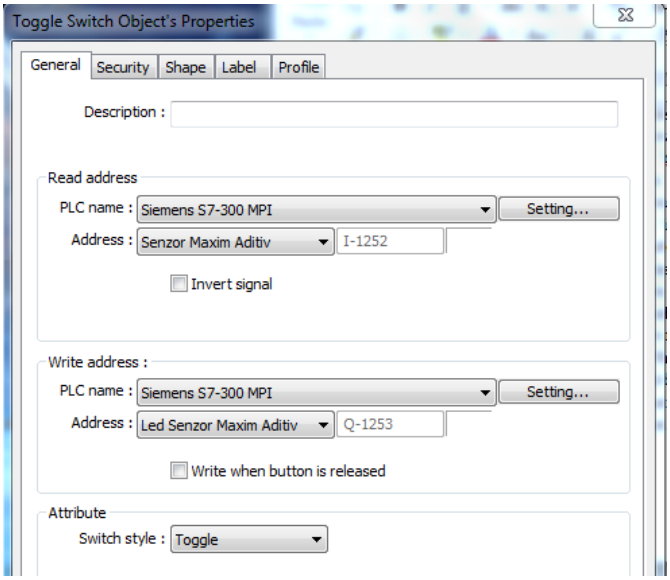

Fig. 11. Different settings for the Toggle switch

The numeric display can be set from Weintek panel and input to the PLC through the marker word (Fig. 12):

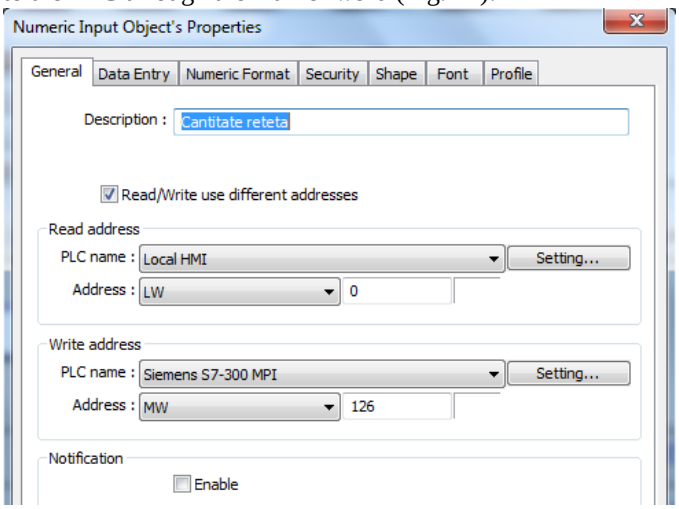

Fig. 12. Setting of the numeric display

IV. Conclusions

The paper highlights the utility and importance of programmable automates in the control of the industrial processes, simulating the functioning of a concrete plant. We watched the manufacturing process of mixtures in a plant of this type, the program makers being able to modify the recipes in order for it to function according to the requirements imposed by the process.

REFERENCES

[1] Dunning G., Introduction to Programmable Logical Controllers, Ed. TWI Press Inc 2002.
[2] Mărgineanu I., "Automate Programabile", Editura Albastră, Bucure ti 2005.
[3] Oprea Ctin, Barz C., "Elemente de inginerie electrica, reglare automata si automatizari", Ed. Risoprint, Cluj Napoca, 2011.
[4] J. W. Webb, R. I Reis, "Programmable Logic Controllers", Prentice Hall, 2000.
[5] *** - Simatic S7, Siemens documentation
[6] http://www.automation.siemens.com/
[7] http://www.weintek.com

Florica Petrovan
The place of birth is Baia Mare to the date 26.05.1991
Graduate the"George Baritiu" technical high school 2010
Student of Technical University of Cluj-Napoca, North University Center from Baia Mare, Electronical Aplied Section from 2010
Email: florica_paula@yahoo.com

Temperature control for a chemical reactor using a new Genetic Algorithm

Fayez Areed[#1], Mostafa A. El-Hosseini [*2], M S Saraya[#3]

[#]*Computer and control systems Engineering Department, Mansoura University*
Egypt - Mansoura
mohamedsabry83@mans.edu.eg

Abstract— Genetic algorithms (GAs) have been fairly successful in a diverse range of optimization problems, providing an efficient and robust way for guiding a search even in a complex system and in the absence of domain knowledge. This paper, presents a comparative study for a chemical reactor system by conventional P, PI, PID, and by using genetic algorithm for the same plant. The results obtained here, assure the actual possibility of using GA to identify and controlling plants. The major efforts are to adjust the controller in order to minimize the steady state error. GA offer, an alternative approach both for identification and control of nonlinear processes in process engineering.

Keywords— genetic algorithm, GA, PID Controllers, Stochastic systems, chemical reactor, optimization.

I. INTRODUCTION

In the last two decades, the growth in interest in heuristic search methods for optimization has been quite dramatic. Heuristics have now attained considerable respect and are extremely popular in the field of optimization. One of the most interesting developments is in the application of genetic algorithms (GAs), which has regularly been featured, in control engineering. The genetic algorithm is one of the newly developed field and one of the important topics in research of computational intelligence. Application of genetic algorithms, to research of computer architecture is not new. The algorithm is used for research of Very Large Scale Integrated Chip (VLSI) design to find the optimized area and optimized number of VIAs for the situation [1] – [5]. These references and [6] give more details for genetic algorithm, which we do not go over deeply. In this paper, we only provide the minimum knowledge to understand operations of the genetic algorithm.

I.1 General Genetic Algorithm

Genetic algorithms are rich in application across a large and growing number of disciplines. Really genetic algorithm supports computer programming. This research provides an Introduction to Genetic Algorithms and its components. A GA is a stochastic optimization method based on the biological principles of Darwinian evolution [7]. GA incorporate operators that mimic natural selection and reproduction (on a simplistic level) using a probabilistic search on a population of designs. The population 'evolves' through the application of genetic operators to determine the design that is best adapted to a fitness landscape. The fitness landscape is defined by a fitness function that is typically composed of an objective function and an appended penalty function if the problem is constrained. Unlike calculus-based methods, GAs are developed as a framework for a global search of the design space [7].

GA were formulated by Holland in 1975 as a computational technique to artificially model biological evolution [8]. GA as search and optimization routines were popularized by Goldberg's 1989 publication GA in Search, Optimization, and Machine Learning [9]. The GA and its variations, along with similarly inspired genetic programming, evolutionary programming, and evolution strategies, constitute the family of evolutionary algorithms (EA) [10]. Evolutionary algorithms are then grouped into the larger category of biologically-motivated evolutionary computation, which includes techniques such as ant colony optimization, particle swarm optimization, and differential evolution.

"Genetic Algorithms are good at taking large, potentially huge search spaces and navigating them, looking for optimal combinations of things, solutions you might not otherwise find in a lifetime." (- Salvatore Mangano Computer Design, May 1995).

Provide efficient, effective techniques for optimization and machine learning applications

- To understand the adaptive processes of natural systems
- To design artificial systems software that retains the robustness of natural systems

I.2 Components of a GA

A problem to solve, and...

- Encoding technique (gene, chromosome)
- Initialization procedure (creation)
- Evaluation function (environment)
- Selection of parents (reproduction)
- Genetic operators (mutation, recombination)
- Parameter settings (practice and art)

This way of search technique is shown in figure 1

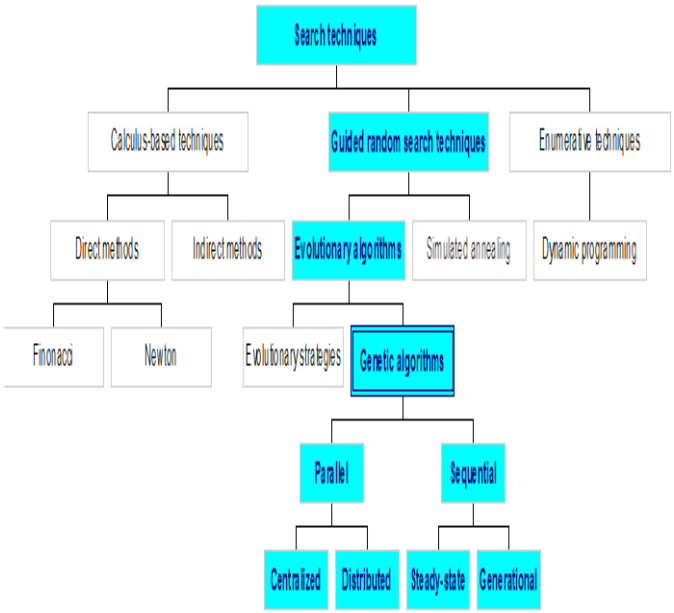

Figure1 Classes of Search Techniques

A GA for a particular problem must have the following five components as shown in figure 2:

- a genetic representation for potential solutions to problem
- a way to create an initial population of potential solutions
- an evaluation function that plays the role of the environment, rating the solutions in terms of their fitness values
- genetic operators that alter the composition of children
- Values for various parameters that the genetic algorithm uses (population size, probabilities of applying genetic operators, etc.)

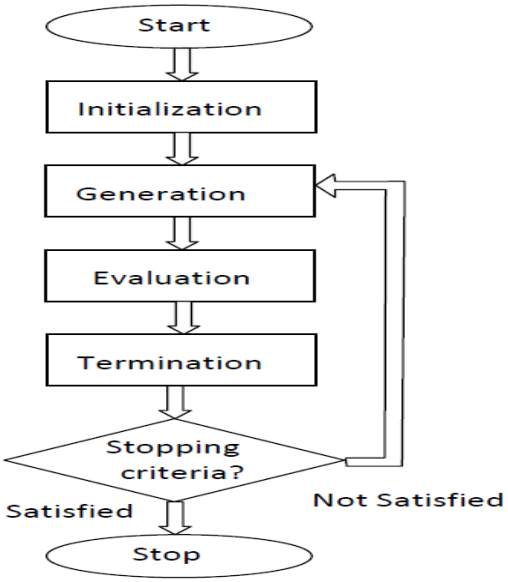

Figure2: Operation flowchart for the genetic algorithm

2.3 The GA Cycle of Reproduction

Is the biological process by which new "offspring" individual organisms are produced from their "parents". Specify how the genetic algorithm creates children for the next generation as shown in figure 3. The steps in described as follow

- Initialize population with random chromosomes
- Decode chromosome into phenotype
- Evaluate fitness
- Select new generation probabilistically based on fitness
- Crossover chromosomes of parents
- Mutate chromosomes

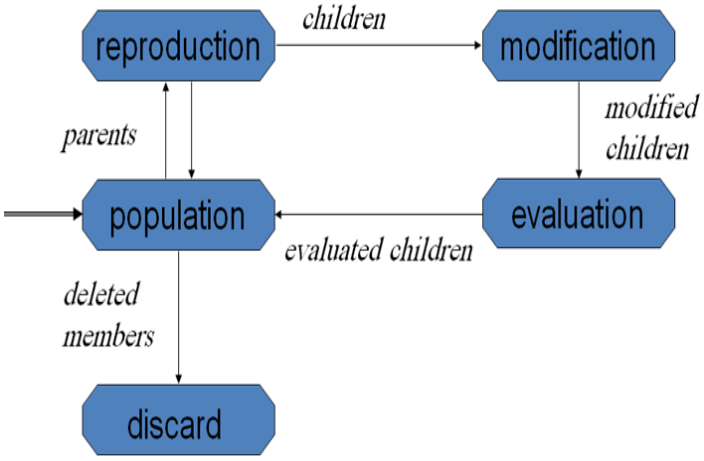

Figure 3: GA cycle of reproduction

There is significant benefit for applying the genetic algorithm as the optimization technique. The genetic algorithm is an optimization algorithm which has both global search and local search abilities. With the crossover operation, we implement the local search. With mutation operation, we implement the global search, which checks randomized candidate other than similar candidates which we produce with crossover. In conventional optimization algorithm, most algorithms have only one search method, not both. Also the conventional optimization technique uses the sequential evaluation, in which the algorithm generates only single candidate, evaluates and compares with the current system. Example of sequential optimization is simulated annealing [13] [14]. For the genetic algorithm, we use the parallel optimization, which generates multiple candidates, evaluate, and compares with the previous population. We can find better candidates more efficiently since we check more candidates simultaneously and choose better candidates.

II. Chemical Reactor

Stirred Tank Reactor (CSTR) is an important component in chemical process and offering a diverse range of researches in the area of the chemical and control engineering. Various control approaches have been applied on CSTR to control its dynamics. The problem of controlling of CSTR is considered as an attractive and controversial issue, especially for control

engineers, corresponding to its nonlinear dynamic. Most of the conventional controllers are restricted just for linear time invariant system applications [15]. However, in real environment, the nonlinear characteristics of the systems and their functional parameters changes, due to wear and tear, cannot be neglected. Furthermore, dealing the systems with uncertainties in real applications, is another subject which must be noticed. In this way, the role of the adaptive and intelligent controllers, by the capability of the overcoming the aforementioned points are of importance. A chemical reactor is adopted that finds typical applications in chemical industry. The chemical reactor is a very rich example of MIMO systems with complex nonlinear behaviour and sensitivity to parameters uncertainty.

II.1 statement of the problem

It is required to control the temperature of the reactor via adjusting the position of the control valve.

II.2 Mathematical Model of a Chemical Reactor

Continues Stirred Tank Reactor (CSTR) as shown in figure 4. It is a jacketed-type reactor, and it's assumed that:

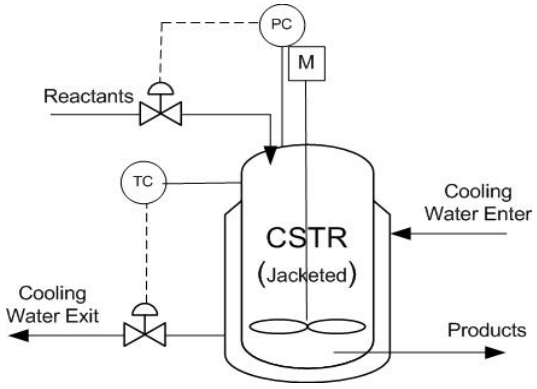

Figure 4: Continues Stirred Tank Reactor (CSTR)

1. Both the reactor and the jacket are perfectly mixed
2. The volumes and physical properties are constant

The reactor is subjected to various kinds of disturbances such as the feed rate and ambient temperature fluctuations. The valve has equal percentage dynamics that

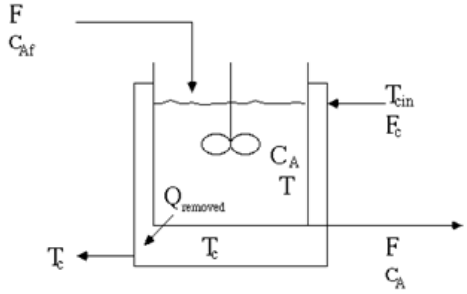

Figure 5: CSTR process

adds to the nonlinear behaviour of the model. Figure 5 illustrates the schematic of the CSTR process. In the proposed CSTR, an irreversible exothermic reaction takes place. The heat of the reaction is removed by a coolant medium that flows through a jacket around the reactor.

II.2.1 CSTR Model

The system has three states given by:

$X=[x_1\ x_2\ x_3]^T = [C_A\ T\ T_c]^T$

$Y=[0\ 1\ 0]X$

Where :

C_A is the concentrayion of the reactant in the reactor

T is the temperature of the reactor

T_c is the jacket temperature

Y is the output of the model

A Cyclopenadine (Input flow concentration of A)

B Cyclopentenol (output flow concentration of B)

A flow stream A is fed to the reactor. A catalyst is placed inside the reactor. The liquid inside the reactor is perfectly mixed and sent out through the exit valve .The jacket surrounding the reactor also has feed and exit streams. The jacket is assumed to be perfectly adjacent with the tank and at a lower temperature than the reactor [16], [17]. The mathematical model equations are obtained by a component mass balance (1), energy balance principle (2) in the reactor and energy balance principle (3) on the jacket.

- Balance of mass of reactant A:

$$\frac{dC_A}{dt} = \frac{F}{V}(C_{Ai} - C_A) - K_o e^{-\frac{E}{R(T+273.16)}} C_A^2 \quad (1)$$

- Energy balance on reactor contents:

$$\frac{dT}{dt} = \frac{F}{V}(T_i - T) - \frac{\Delta H_R}{\rho C_p} K_o e^{-\frac{E}{R(T+273.16)}} C_A^2 - \frac{UA}{V\rho C_p}(T - T_c) \quad (2)$$

- Energy balance on jacket:

$$\frac{dT_c}{dt} = \frac{UA}{V_c \rho_c C_{pc}}(T - T_c) - \frac{F_c}{V_c}(T_c - T_{ci}) \quad (3)$$

Where

C_A	Concentration of the reactant in the reactor
T	Temperature in the reactor
T_c	Jacket temperature
C_{Ai}	Concentration of the reactant in the feed
T_i	Temperature in the feed
T_{ci}	Coolant inlet temperature
F	Feed rate
V	Reactor volume
K_o	Arrhenius frequency parameter
ΔH_R	Heat reaction (assumed constant)
ρ	Density of reactor content
C_ρ	Heat capacity of the reactants
U	Overall heat transfer coefficient
A	Heat transfer area
V_c	Jacket volume
ρ_c	Density of the coolant
$C_{\rho c}$	Heat capacity of the coolant
F_c	Coolant rate
F_{cmax}	Maximum flow through the control valve

A	Valve range ability parameter
E	Activation energy of the reaction
R	Ideal gas law constant

Thus the system is seen to be third order and heavily nonlinear as shown in figure 6. The idea is to regulate the output to set point temperature using only one control signal, which is the signal applied to the control valve.

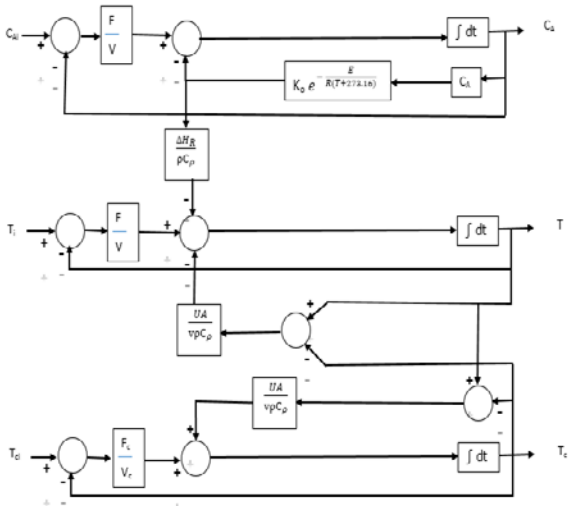

Figure 6: system description

A complete description of the parameters involved in deriving the mathematical model of the reactor, their units, as well as their nominal values is given in table 1.

Parameter	Unit	Value
C_A	Kgmole/m^3	
T	^oC	
T_c	^oC	
C_{Ai}	Kgmole/m^3	2.88
T_i	^oC	66
T_{ci}	^oC	27
F	m^3/s	7.5E-3
V	m^3	7.08
K_o	m^3/s-kgmole	7.44E-2
ΔH_R	J/kgmole	-9.86E7
ρ	Kgmole/m^3	19.2
C_ρ	J/kgmole-^oC	1.815E5
U	J/s-m^2-^oC	3.55E3
A	M^2	5.4
V_c	m^3	1.82
ρ_c	Kgmole/m^3	1000
$C_{\rho c}$	J/kgmole-^oC	4.184E3
F_c	m^3/s	
F_{cmax}	m^3/s	0.02
A		50
E	J/kgmole	1.182E7
R	J/kgmole-^oK	8314.39

Table 1: system parameters

II.3 Using noise at low temperature

In this case a low level of temperature used as an input to the chemical reactor as shown in figure 7.

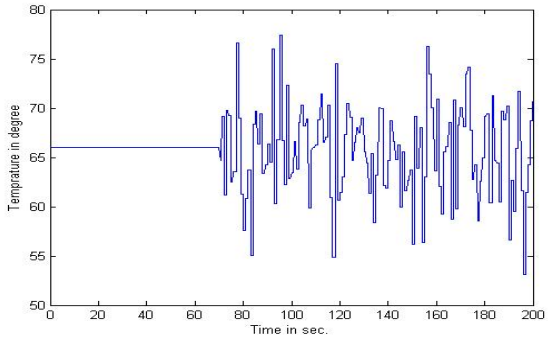

Figure 7: input signal with noise

As shown the noise is random and ripple ratio about 40% from the input value.

II.3.1 Using proportional controller

In the proportional control algorithm, the controller output

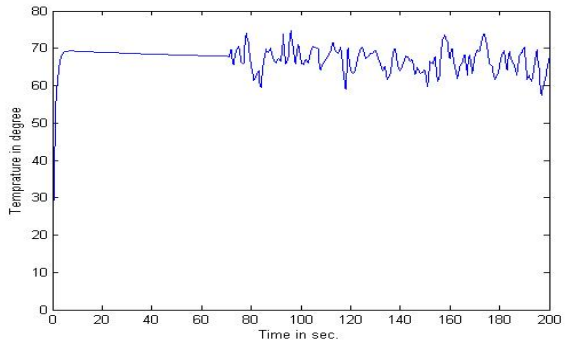

Figure 8: system with P controller

is proportional to the error signal, which is the difference between the set point and the process variable. Figure 6 show the output after using P controller.(Kp=20.8718473357658)

II.3.2 using proportional-integral controller

A PI Controller (proportional-integral controller) is a special case of the PID controller in which the derivative (D) of the error is not used. The result of using this type of controller is shown in figure 9.

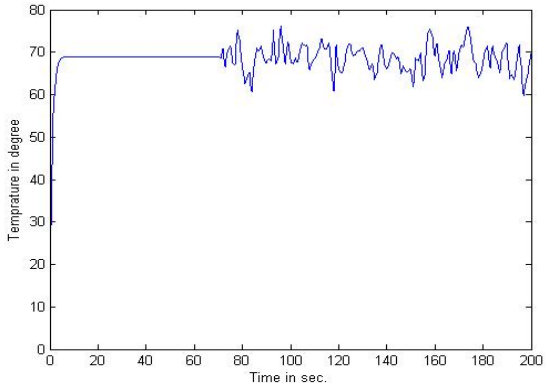

Figure 9: system with PI controller

ISBN: 978-1-61804-216-3

Where (Kp=20.87, KI=-9.8317)

II.3.3 using PID controller

Proportional-integral-derivative controller (PID controller) is a generic control loop feedback mechanism (controller) widely used in industrial. A PID controller calculates an "error" value as the difference between a measured process variable and a desired setpoint. The controller attempts to minimize the error by adjusting the process control inputs. The result of using this type of controller is shown in figure 10 as shown blow. Where (Kp=20.87, KI=-9.8317, Kd=0.183)

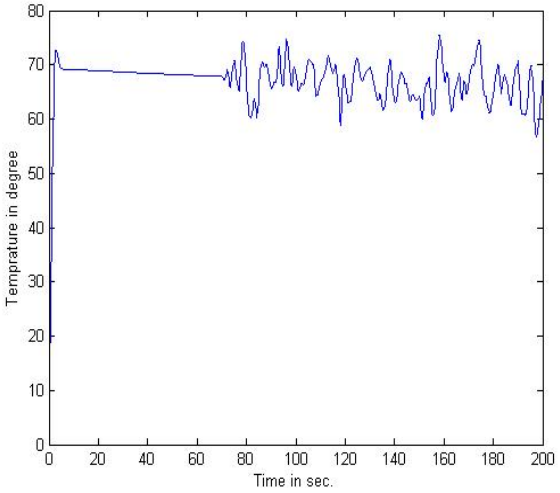

Figure 10: system with PID controller.

As a result ts =192.21 sec, and tr =1.31sec

II.3.4 using Genetic Algorithm

To describe the GA optimization process, consider the system as shown if figure 11. At the beginning of the process, the initial populations comprise a set of chromosomes

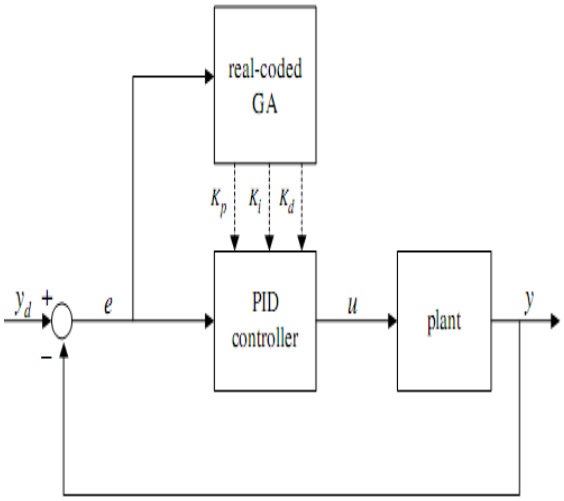

Figure 11: PID controller design using GA

that are scattered all over the search space. The initial population may be randomly generated. However, in all experiments, the population consists of 25 chromosomes which are all randomized initially. Thus, the use of heuristic knowledge of the controller is minimized.

II.3.4.1 Parameters of GA

GA has many parameters like, population size, probability of crossover, probability of mutation, the way you encode your variable, etc. as shown in figure 12

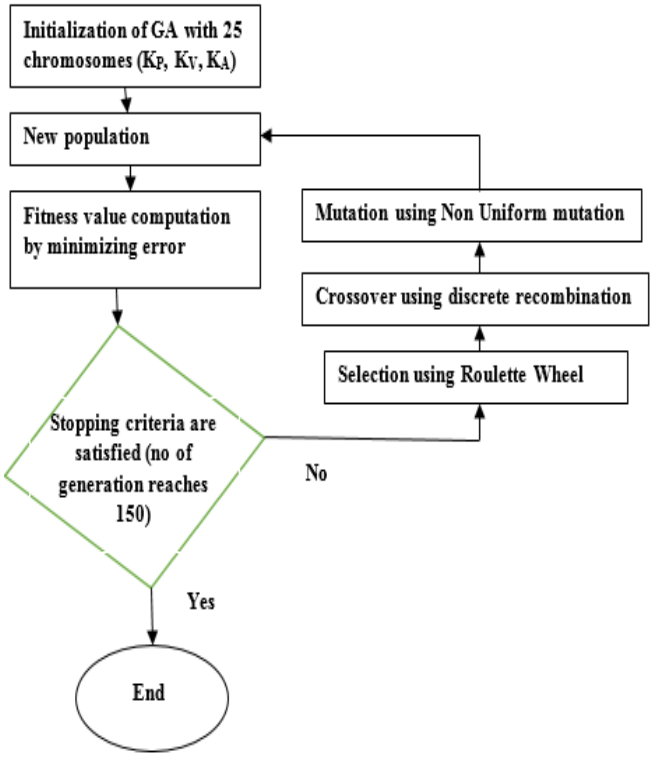

Figure 12: GA steps flowchart

II.3.4.1.1 Population size

Specifies how many individuals there are in each generation. The population consists of 25 chromosomes, each one represent a temperature.

II.3.4.1.2 Selection

Specify how the genetic algorithm chooses parents for the next generation, here the selection is Roulette Wheel, The size of the section in the roulette wheel is proportional to the value of the fitness function of every chromosome - the bigger the value is, the larger the section is.

II.3.4.1.3 Crossover

Crossover is a genetic operator that combines (mates) two chromosomes (parents) to produce a new chromosome (offspring). The idea behind crossover is that the new chromosome may be better than both of the parents if it takes the best characteristics from each of the parents. Crossover occurs during evolution according to a user-definable crossover probability. The type of crossover used here is discrete recombination

II.3.4.1.4 Mutation

Mutation is a genetic operator that alters one or more gene values in a chromosome from its initial state. This can

ISBN: 978-1-61804-216-3

result in entirely new gene values being added to the gene pool. With these new gene values, the genetic algorithm may be able to arrive at better solution than was previously possible. Mutation is an important part of the genetic search as help helps to prevent the population from stagnating at any local optima. The type of mutation that used here is Non Uniform mutation

II.3.4.1.5 stopping criteria

Stall generations: The algorithm computes the specified number of generations with no improvement in the fitness function. Here no of generations was 150.

II.3.4.1.6 Range of parameters

Range that bounded the generation of the PID parameters (Kp,Ki,Kd). here the range was from -20 to 40

Applying the GA to the system this will led to the PID parameters (Kp,Ki,Kd). And the transfer function of the PID controller.

The system is shown in figure 13 after applying the Genetic Algorithm technique to compute PID parameters

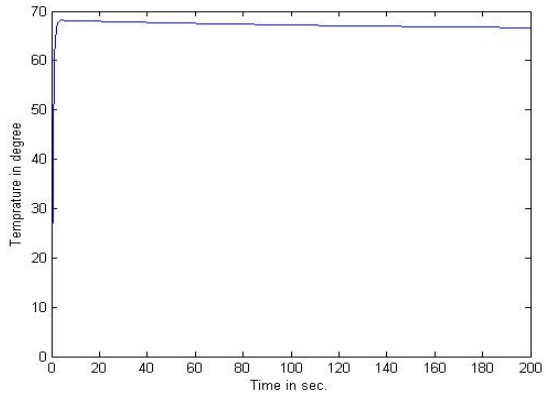

figure 13: system with GA

as shown in figure the system has less noise that is abouu 1.25% from the steady state value

II.4 Using noise at high temperature

In this case a high level of temperature used as an input to the chemical reactor as shown in figure 14.

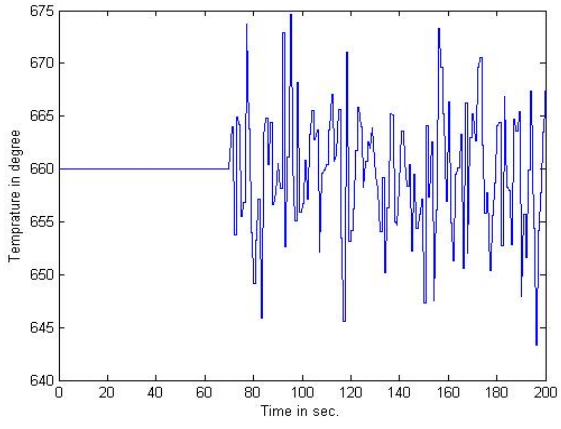

Figure 14: input signal with noise

II.4.1 Using proportional controller

The result of using this type of controller is shown in figure15.

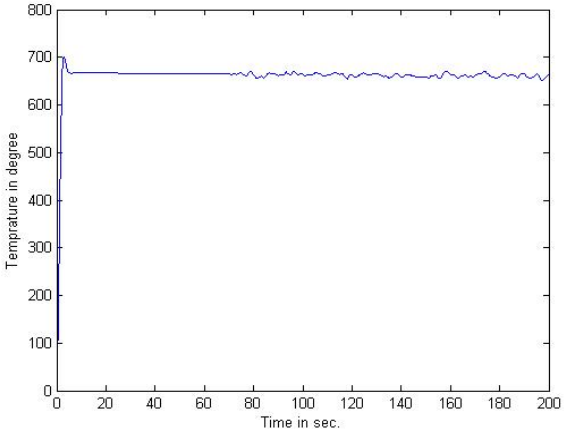

Figure 15: system with P controller

II.4.2 using PI controller

The result of using this type of controller is shown in figure16.

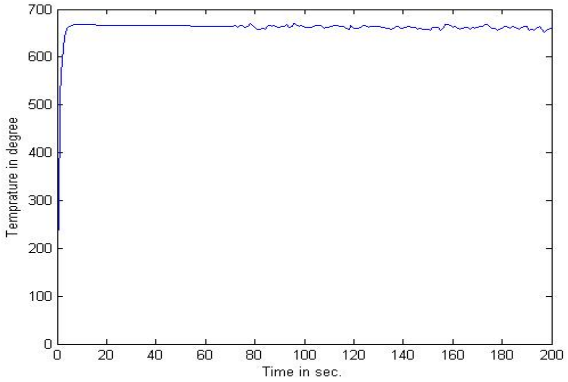

Figure 16: system with PI controller

II.4.3 using PID controller

The result of using this type of controller is shown in figure 17 as shown blow

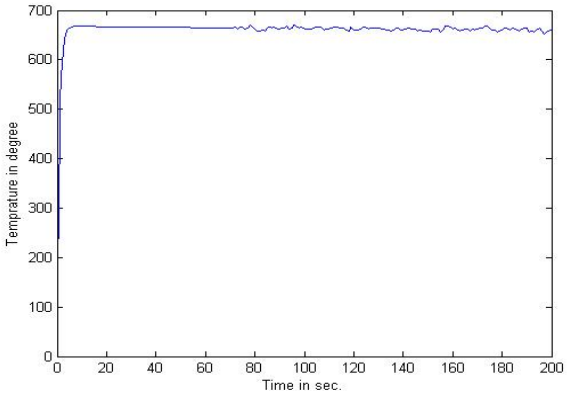

Figure 17: system with PID controller.

II.4.4 using Genetic Algorithm

The results of using genetic algorithm to control the parameter of PID is shown in figure 18 as shown blow

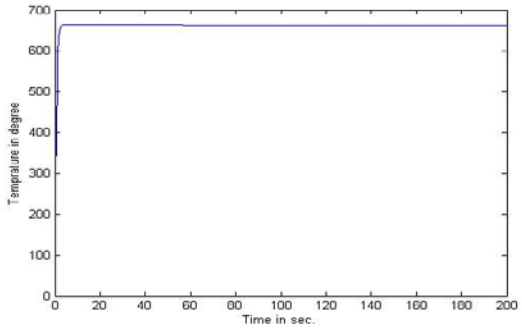

Figure 18: system with GA

II.4 Summarized Results

As a results of the above figures, the results could be compared in table 2. That shown the noise percentage of input and the ripple ratio by using different types of controllers.

Controller	Noise 40%	Noise 10 %
P	10.2%	4.34%
PI	9.74%	3.65%
PID	7.36%	2.98%
GA	1.24%	1.25%

Table 2: comparative results

Table 3 summarize the values of PID parameters (Kp, Kv, Ka)

Parameter	Kp	Kv	Ka
value	20.87185	0.183389	-9.8317

Table 3: PID values

III. CONCLUSION

The proposed GA is tested by using Math lab Simulink program and its performance is compared to a different temperature & concentration. The paper demonstrated that while the GA controller exhibits superior control in the presence of nonlinearities.

This paper illustrates the control of non-linear system CSTR (Continuous Stirred Tank Reactor). And the results prove that GA controllers are appropriate under non-linear difficulties.

REFERENCES

[1] Guo-Fang Nan, Min-Qiang Li, Dan Lin and Ji-Song Kou, "Application of evolutionary algorithm to three key problems in VLSI layout," Proceedings of 2005 International Conference on Machine Learning and Cybernetics. Volume 5, p.p. 2929 – 2933

[2] S. Coe, S. Areibi, and M. Moussa, "A hardware Memetic accelerator for VLSI circuit partitioning," Computers and Electrical Engineering, vol.33 no.4, p.p. 233- 248, July, 2007

[3] S. Coe, S. Areibi, and M. Moussa, "A genetic local search hybrid architecture for VLSI circuit partitioning," in Proceeding on 16th International Conference on Microelectronics, 2004. ICM 2004, p.p. 253-256, 6-8 Dec. 2004

[4] S. Areibi, M. Moussa, and G. Koonar, "A Genetic algorithm hardware accelerator for VLSI circuit partitioning," International Journal of Computers and Their Applications, 2005 vol. 12, no.3, p.p. 163-180.

[5] S. Areibi, and Z. Yang, "Effective memetic algorithms for VLSI design automation = genetic algorithms + local search + multi-level clustering," Evolutionary

[6] C. R. Reeves, and J. E. Rowe, "Genetic Algorithms: Principles and Perspectives: A Guide to GA Theory," Kluwer Academic Publishers, Norwell, MA, 2002

[7] Goldberg, D. E., and Richardson, J., "Genetic Algorithms with Sharing for Multimodal Function Optimization," Genetic Algorithms and their Applications: Proceedings of the Second International Conference on Genetic Algorithms, Cambridge, Massachusetts, 1987, pp. 41-49.

[8] Holland, J., Adaptation in Natural and Artificial Systems, The University of Michigan Press, Ann Arbor, Michigan, 1975.

[9] Goldberg, D. E., Genetic Algorithms in Search, Optimization, and Machine Learning, Addison Wesley, Reading, Massachusetts, 1989.

[10] Bäck, T., Evolutionary Algorithms in Theory and Practice: Evolution Strategies, Evolutionary Programming, Genetic Algorithms, Oxford University Press, Oxford, 1996.

[11] C. Darwin, "The Origin of Species," Literature.org [Online] Available at: http://www.literature.org/authors/darwin-charles/the-origin-of-species/index.html [Accessed: May. 20, 2008]

[12] J. Grefenstette, R. Gopal, B. Rosmaita, and D. Van Gucht, "Genetic Algorithms for the Traveling Salesman Problem", in Proceeding on 1st International Conference on
Genetic Algorithms and Their Applications, p.p.160 - 168, 1985.

[13] F. Zhuang, and F. D. Galiana, "Unit commitment by simulated annealing," IEEE Transactions on Power Systems, vol. 5, no. 1, February 1990, p.p. 311-318.

[14] G. G. Yen and H. Lu, "Dynamic population size in multiobjective evolutionary algorithm," in Proceeding on 9th IEEE Congress of Evolutionary Computation, p.p. 1648-1653, 2002.

[15] Mohd Fua'ad Rahmat1, Amir Mehdi Yazdani1, Mohammad Ahmadi Movahed1 and Somaiyeh Mahmoudzadeh, "TEMPERATURE CONTROL OF A CONTINUOUS STIRRED TANK REACTOR BY MEANS OF TWO DIFFERENT INTELLIGENT STRATEGIES", INTERNATIONAL JOURNAL ON SMART SENSING AND INTELLIGENT SYSTEMS VOL. 4, NO. 2, JUNE 2011

[16] U. Sabura Banu , G. Uma, "Fuzzy Gain Scheduled Pole Placement Based State Feedback Control of CSTR" , International Conference on Information and Communication Technology in Electrical Science,.2007.

[17] U. Sabura Banu , G. Uma, "ANFIS Gain Scheduled CSTR with Genetic Algorithm Based PID Minimizing Integral Square Error", International Conference on Information and Communication Technology in Electrical Science,.2007

A Proposed Case Retrieval Nets Algorithm for Hierarchical Behavior control of Humanoid Robot

Meteb M. Altaf[3], Bassant M. Elbagoury[1,2] , Fahad Alraddady[2], Said Ghoniemy[1,2]

Abstract- *Efficient retrieval of a relatively small number of relevant cases from a huge case-memory is an important task of Case-Based Reasoning. In a previous work by the author, it was found that the retrieval accuracy of the proposed behavior controller is low. This is because the case-memory storage is huge, and the used algorithm for case retrieval is the Nearest-Neighbor. Case-Retrieval Nets is a recent case-memory model that improves case retrieval from large case-memories. This paper proposes a hybrid retrieval algorithm for behavior control of robot. The main motivation is to improve the retrieval accuracy of the Hybrid Case-Based Reasoning behavior control, develop an automatic real-time hybrid CBR-Retrieval Algorithm for robot, and improve the storage capacity of the case-memory. The obtained results show that the average efficiency of the CRN_HCBR is very high. It reaches 98 % at level two, 96% at level three and 92 % at level four. This is because the cases used for querying are divided into similar sets, which increases the overall retrieval efficiency.*

Keywords: Humanoid Robotics, Artificial Intelligence, Case-Based Reasoning, RoboCup.

I. INTRODUCTION

Robot World Cup (RoboCup), [1,3,4] is an international research and education initiative. It is an attempt to foster Artificial Intelligence (AI) [2] and Robotics research by providing a standard problem where wide range of technologies can be used for an integrated project.

F.A. Author Meteb M. Altaf isAssistant Professor and Head of AI and Robotics center King Abdulaziz City for Science & Technology, Riyad, Kingdom of Saudi Arabia. *(maltaf@kacst.edu.sa)*
S.A. Author Bassant M. Elbagoury is Assistant Professor of Computer Science, College of Computers & Information Technology, Taif University, taif, kingdom of Saudi Arabia *(bassantai@yahoo.com)*
T. Author Fahad Alraddady is Dean of College of Computers & Information technology, Taif University, taif, Kingdom of Saudi Arabia. *(alraddykh@yahoo.co.uk)*
F.Author Said Ghoniemy is Professor of Computer Science, College of Computers & Information Technology, Taif University, Taif, kingdom of Saudi Arabia.(*ghoniemy@tu.edu.sa)*

The ultimate goal of the RoboCup Initiative is to be stated as follows: " By mid-21st century, a team of fully autonomous humanoid robot soccer players shall win the soccer game, in accordance with the official rule of the FIFA, against the winner of the most recent World Cup ". RoboCup has three major domains, which are RoboCup Soccer, RoboCup Rescue and RoboCup Junior.

There are many research problems that are being investigated internationally by researchers. Robotics vision and control for an autonomous humanoid robot are very complex problems, especially in the RoboCup domain. This is due to the dynamics of the environment and the complexity of behaviors that should be executed in real-time. This paper focus on developing an intellgent algorithm for robotic platform for Humanoid Robot. Especially Case-Based Reasoning technique (CBR) [6,7,8], which is an AI technique for robotics control.The main algorithm focus mainly on CBR control algorithm. CBR [5] as a paradigm for building intelligent computer systems has been applied to robot tasks such as navigation [7,8,9] and behavior control [11]. For example, Raquel [18] uses CBR for action selection in cooperative robotics soccer. Arcos et al., [7] uses CBR for autonomous mobile robot navigation. CBR has also been widely applied in RoboCup domain; Krussma et el. [8] uses CBR for high level planning strategies for robots playing in the Four- Legged RoboCup. However, in the RoboCup [1,3] domain the overall complexity increases especially in behaviour control. This is due to the complexities and dynamics of robot environment. Complex behaviors such as Goal-Score should be executed correctly in real-time. We have previously developed a CBR behavior control Platform for Humanoid Soccer RoboCup with NAO

ISBN: 978-1-61804-216-3

Team Humboldt [15]. However, still many problems are not addressed like ball localization and tracking. Moreover, adaptation in CBR engine is difficult because it needs a lot of adaptation knowledge [2].The coming sections will explain algorithm architecture in details along with experimental results and future work.

II. PROPOSED CASE-RETRIEVAL NETS HYBRID CASE-BASED REASONING (CRN_HCBR) RETREIVAL ALGORITHM FOR BEHAVIOR CONTROL

This section presents our new hybrid retrieval algorithm for behavior control of Humanoid Robot. It depends on our previous HCBR algorithm described in [17]. It also depends on the basic case retrieval nets CRN [16] structure. The coming subsections describe in detail our main architecture and the algorithm in details.

1) CRN-HCBR Behavior Control Architecture

The proposed architecture of the CRN-HCBR algorithm is shown in Figure 1. It is a modified model of our HCBR, where the previously used Nearest-Neighbor retrieval modules are replaced by four CRN's. The CRN-HCBR architecture consists of a hierarchy of four levels and each level uses a single CRN to retrieve cases from its case-memory. Its reasoning process starts from bottom to top. At level one, the robot starts building its case-query features about its real-time status. Then only the features of robot are used by CRN to determine its role. The most similar case nodes are then retrieved. There solutions are then adapted by the adaptation propagation function to determine Robot role as Goalie or Attacker.

By backward reasoning, the case-query is recalled again at level two but only features of robot skill are activated. Then by forward reasoning a second CRN is used to retrieve most similar cases to robot skill. The adaptation propagation function of level two adapts the solutions of retrieved case nodes to determine new robot skill for example as **goal-score or dribble** in case of Attacker robot. Finally, at level four the real-time robot behaviors are decided by HCBR-CRN retrieval and adaptation engines.

To formalize our CRN-HCBR structure, as shown in Figure 1, it consists of the following main modules:-

1. Case Base of Information Entities (IE's) and Case Nodes (CN's).
2. Four CRN's for IE's and cases retrieval.
3. Four Adaptation modules for Adapting Role, Adapting Skill, Adapting Behaviors and Adapting low level reactive behaviors.

Also, its reasoning path uses both backward reasoning and forward reasoning [2,5]. The coming subsections describe the modules of the CRN-HCBR in details.

2 Case-Memory and the relevance function

As discussed in previous sections, the main goal of CRN is to speed up the retrieval process. This is done mainly by introducing a new structure of case-memory. Instead of storing complete flat-cases, now the case-memory consists of IE's and it separates its cases' solutions or cases' nodes. Table 1 shows a sample example of Robot IE's stored in the case-memory of CRN. As shown, there are basic IE's such as Rx and Ry. Each IE is further extended to ten discretized IE's. This is to simplify the retrieval process.

These discretized IE's are stored as arrays with their associated case nodes, where a case node association is assigned by relevance function [16], which we redefine as a Boolean function as follows:

$$\Omega = \begin{cases} \textbf{1: IE is totally associated to case} \\ \textbf{0: IE is not associated to case node} \end{cases} \quad \textbf{(1)}$$

Table 1. Sample of the Discretized IE's and their associate case nodes as stored in the case-memory of the CRN-HCBR retrieval algorithm

Basic IE'S:	Discretized IE's	ρ =
Rx: x	Rx1 = -2200	34
	Rx2 = -1900	72
	Rx3 = -1600	12
	Rx4 = -1300	58
	Rx5 = 1560	120
	Rx6 = 1710	603
	Rx7 = 1821	701
	Rx8 = 1924	932
	Rx9 = 2013	1200
	Rx10 = 2200	1409
Ry : y	Ry1 = -900	34
	Ry2 = -700	72
	Ry3 = -500	12
	Ry4 = -300	58
	Ry5 = -100	723
	Ry6 = 200	768
	Ry7 = 500	846
	Ry8 = 700	900
	Ry9 = 800	1012

The main steps of CRN-HCBR Algorithm are described as follows:

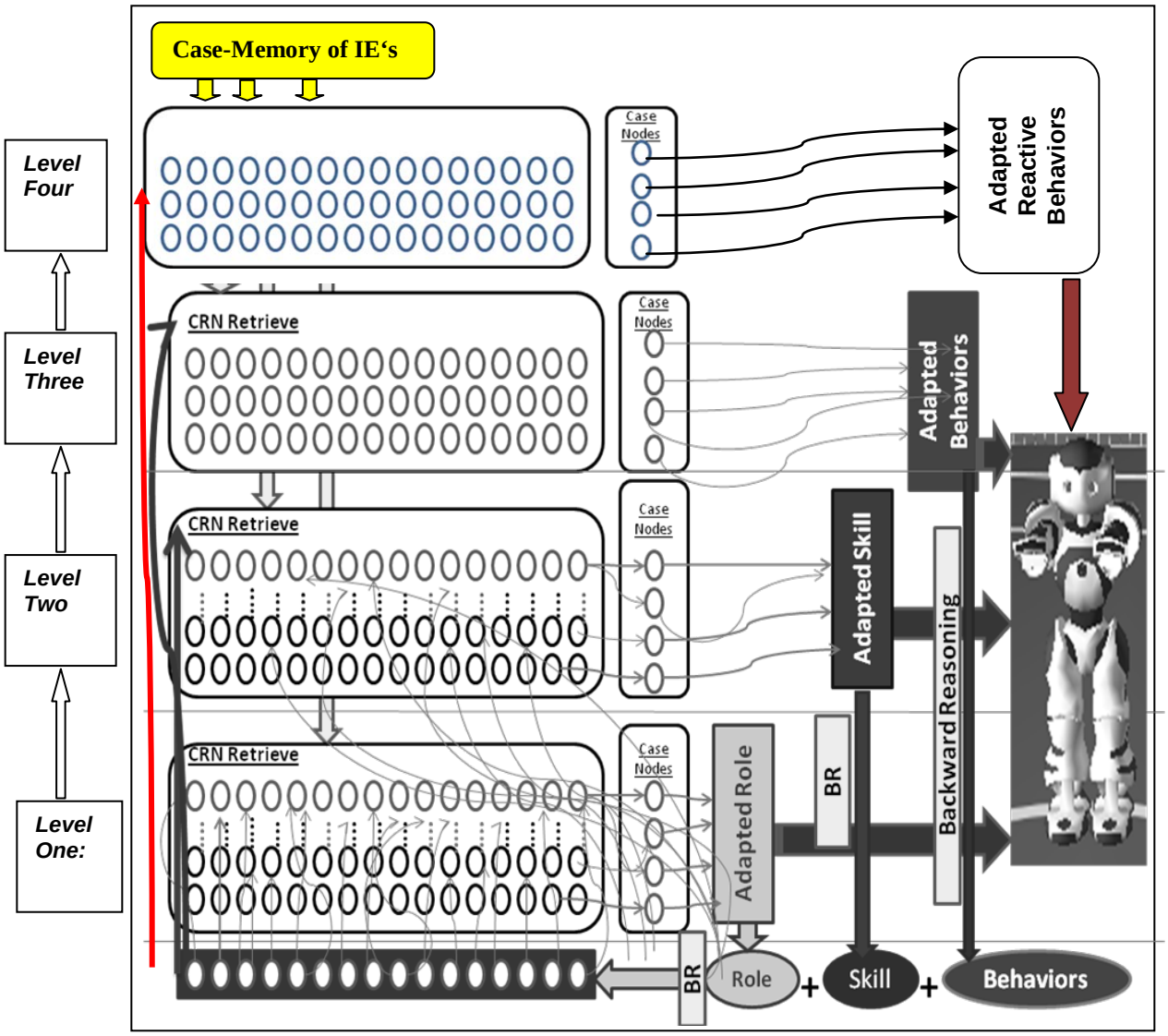

Figure 1. The proposed architecture of CRN-HCBR for Behavior control of Robot

3 CRN-HCBR Behavior Control Algorithm

This section presents the main algorithm of the CRN-HCBR behaviour control. As shown in Figure 2, it consists of 20 steps, which are classified into four levels. Each level uses a CRN to retrieve a similar sub-case and apply propagation adaptation rules to adapt its solution until the final solution of the complete case is found at level[2] four. Then the algorithm repeats again for real-time robot controller, so that new case situation is executed starting from level 1 back through level 4.

- ***Step1:*** **Activate IE's-Query of Level 1**. This is done by reading real-time sensor values of robot IE's from robot simulation environment. We define IE-Query activati

$$\lambda(IE) = \begin{cases} 1, & \text{if IE-Query} \in]-\infty, 0[\ , \ ]0, \infty[\\ 0, & \text{if IE-Query} = 0 \end{cases}$$

- **Step 2: Retrieve similar IE's and associated case nodes**. The CRN-HCBR algorithm uses two local similarity functions to retrieve its most similar IE

from the case-memory. These are Boolean similarity function [16] for Boolean IE's and a real-value similarity function.

- A list **C** of associated case nodes is also retrieved for each single retrieved IE. We formulate it as:

CRN-HCBR Algorithm:

1. **Activate** *Real-Time IE's Query of Level 1*
2. **Retrieve similar IE's and associated case nodes** *using CRN and local similarity function.*
3. **Adaptation Propagation Rules** *to adapt Abstract case nodes of Robot Role.*
4. **Output1:** *Adapted Role solution*
5. **Backward Reasoning** *Adapted Role & Append as new IE to Level 2.*
6. **Reactivate** *Real-time IE's Query of Level 2*
7. **Retrieve similar IE's and associated case nodes** *using CRN and local similarity function*
8. **Adaptation Propagation Rules** *to Abstract case nodes of Robot Skills.*
9. **Output2:** *Adapted Skills solution*
10. **Backward Adapted** *Skills & Append as new IE to Level 3.*
11. **Reactivate** *Real-time IE's Query of Level 3*
12. **Retrieve similar IE's and associated case nodes using** *CRN and local similarity function.*
13. **Adaptation Propagation Rules to** *Abstract case nodes of robot behaviors.*
14. **Output 3.** *Adapted Behaviors solution.*
15. **Backward Adapted** *Behaviors & Append as new IE to level 4.*
16. **Reactive** *Real-time IE's Query of Level 4.*
17. **Retrieve similar IE's and associated case nodes using** *CRN and local similarity function.*
18. **Adaptation Propagation Rules** *of case-based NAO reactive behaviors.*
19. **Output & Execute** *Lower Level Robot Reactive behaviors.*
20. ***Real-time Repeat* Call to step 1**

Figure 2 Main steps of the proposed CRN-HCBR Retrieval Algorithm

$$\mathbf{C} = \{C_1, C_2, \ldots, C_i, \ldots\ldots Cn\},$$

Where,

$C_i \in [0\text{-}N]$, N is the number of case nodes associated to each IE in the Case-memory. This list is computed by our relevance function **ρ**[4, 16] and stored in Case-memory of each CRN.

- ***Step3:*** **Apply Adaptation Propagation rules.** We define it as the rules to adapt the solutions of the retrieved robot role from the list of case nodes C, in order to find the solution of queried IE. An informal example of an adaptation propagation rule at this step is given as:

  "IF case node no. 34 has role solution = Attacker and case node no. 56 has role solution = Attacker and case node no.112 has role solution = Attacker and case node no. 305 has role solution = Goalie Then Adapt Role solution to Attacker "

The number of case nodes compared in each adaptation rule is not fixed. Another example is given as:

"IF case node no. 12 has role solution = Attacker and case node no. 23 has role solution = Attacker and case node no. 71 has role solution = Attacker and case node no. 112 has role solution = Attacker ..... and case node no. 879 = Attacker.... THEN Adapted Role solution = Attacker "

Our formal description of the Adaptation propagation rule at this step is represented as the vector of the form:

[n_1, n_2, n_3, ... , n_i, ... n_m, ROLE]

Where,

n_i , is the case node number

ROLE, the robot role solution either Attacker or Goalie.

- ***Step4:*** **Output 1.** Find adapted role solution. This is the first solution that results for robot role as attacker or Goalie.
- ***Step5.*** **Backward Reasoning.** This is to append Robot Role solution to case query IE's in real-

time RoboCup soccer domain. This updates the Case query IE's.

- ***Step6.*** **Activate IE's-Query of Level 2.** It uses the same activation function **λ (IE)** defined in step 1 but it is applied for new readings of sensors IE's.
- ***Step7.*** **Retrieve Similar IE's and associated case nodes.** This step is similar to step 2, but it retrieves IE's of Robot skill.
- ***Step 8.*** **Adaptation Propagation Rules.** These are the adaptation rules to adapt the retrieved solutions of Robot skills, such as goal-score or dribble. Our formal description of the Adaptation propagation rule at this step is represented as the vector of the form:

[m_1, m_2, m_3, ... , m_i, ... m_m, SKILL]

Where,

m_i , is the case node number at Level 2.

SKILL, the robot skill solution either goal-score or dribble.

- ***Step9:*** **Output 2.** Find adapted skill solution. This is the second solution that results for robot skill as goal-scorer or dribble.
- ***From Step 10 to Step 15.*** Repeat similar steps from step 1 to step 5 but we modify them to adapt the third solution ***(Output 3)*** of the CRN-HCBR algorithm, which is the Robot behavior, such as search for ball, go to ball, kick to goal or small walk and fast walk.
- ***From Step 16 to Step 19.*** Repeat similar steps from step 1 to step 5 but we modify them to adapt the fourth solution ***(Output 4)*** of the CRN-HCBR algorithm, which is the Robot low level reactive behavior, walk with speed = 20.
- ***Step 20.*** Recursive call to the algorithm after final execution of robot reactive behaviors.

III. EXPERIMENTAL RESULTS

In this section, the experimental results of the proposed hybrid CRN-HCBR algorithm are discussed. Our experiments are done in the simulation environment of *Webots* integrated with Visual Studio for programming our CBR behavior control algorithm. These are done in the framework of the project of NAO Humanoid Team Humboldt. The performance measures used are adopted from Burkhard work [6,16] and some are defined by our previous research [11,17].We define our used performance measures as:

Number of IE's in the Case-Memory of the CRN-HCBR: *Our main goal from applying CRN is the reduction of the size of case-memory. In our experiments, we measure the size of CRN memory by the number of the stored IE's but this must be independent from the overall total number of cases stored in a flat structure case-memory.*

IE's Completeness. *We redefine it from the case completeness concept defined by Burkhard [40]. In our experiments, IE's completeness means that all discretized ranges are set for each IE of the robot and its world.*

- ***CRN-HCBR Retrieval Accuracy (RA).*** *We redefined it [25, 40 ,44] as the measure that assures that the required set of IEs nodes are retrieved correctly during the execution of the retrieved process .*
- ***CRN-HCBR Retrieval Efficiency (RE).*** *It means the ability of our CRN retrieval to give the same set of retrieved case nodes at different similarity ranges, for similar test query cases. That is to access relevant cases. Access of these cases should avoid exhaustive search in memory.*

IE's completeness and CRN_HCBR Retrieval Accuracy (RA): In the second cross-validation test, we use a fixed set of well-defined and discretized IE's. These are 270 IE's. The average retrieval accuracy is very high at the three levels of our CRN-HCBR model. At level two, it reaches 97 %, at level three, it reaches 95%, while at level four it decreases to 91 %. In order to test the retrieval accuracy of our CRN_HCBR model, we calculate the retrieval accuracy of the CRN_HCBR by our formula that we define it as:

$$\mathbf{RA = IE\_C / T\_IE}$$

where,

IE_C: number of IE's nodes retrieved correctly by our algorithm.

T_IE: number of total sets of IE's nodes included in the CRN-HCBR controller.

Retrieval Efficiency (RE). In order to measure the retrieval efficiency of our algorithm, we run again the same cross-validation test but we divide the test cases into 20 sets and the case-memory is fixed to 750 stored cases. Each set of test cases consists of 750 cases. Also, we fix the number of IE_CNR to 270 IE's. As shown in Figure 7.6 the average efficiency of the CRN_HCBR is very high. It reaches 98 % at level two, 96% at level three and 92 % at level four. This is because the cases used for querying are divided into similar sets, which increases the overall retrieval efficiency. Our formula for retrieval efficiency is defined as:

$$\mathbf{RE = SC / TQ}$$

Where, RE : CRN-HCBR Retrieval Efficiency

SC = Number of sets of case nodes retrieved correctly during cases query runs. TQ = Total number of sets of case queries used for testing

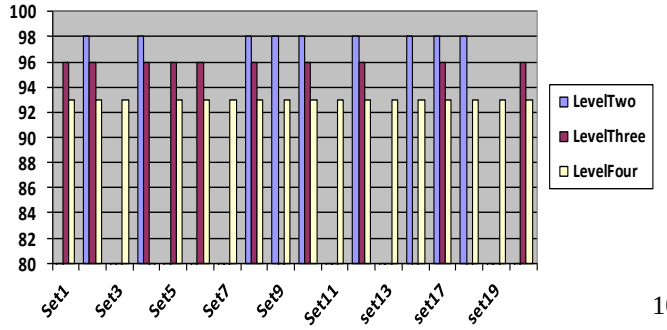

Figure 3. Case Retrieval Accuracy sets

III. CONCLUSIONS AND FUTURE WORK

This paper proposed an enhanced intelligent algorithm for behavior control of humanoid soccer . It is based on case-based reasoning . The main aim of this research is to develop a more effient retrieval algorithm for humanoid soccer robot. Thus enables the robot to be fully autonomous and adapt its behaviors to dynamic soccer game. The enhanced algorithm increases the overall performance of the robot controller. A high performance is achieved at all the levels due to the proposed hieracacal case retrieval structure. In future work, the controller will be tested using rest of soccer behaviors for goalie and defender players. Also, other similarity formulas will be tested like fuzzy similarity measures to improve case retrieval.

V. REFRENCES

1. Behnke, S.: RoboCupSoccer Humanoid League rules and setup, http://www.HumanoidSoccer.org/rules.html
2. Burkhard, H. –D.:Modern Approaches of Artificial Intelligence, HU Berlin 2006. http://www.ki.informatik.hu-berlin.de/lehre/ss06/mmki-prakt_html.
3. Burkhard, H. –D., Duhaut, D., Fujita, M., Lima, P., Murphy, R., Rojas, R.: The road to robocup 2050. In IEEE Magazine of Robotics and Automation, Volume 9, Issue 2, pp. 31-38, (2002).
4. Humanoid Team Humboldt: Homepage of Humanoid Team Humboldt, http://www.humanoidteamhumboldt.de.
5. Kolodner, J . Case-based reasoning, Morgan Kaufmann Publishers Inc. (1993).
6. Berger R. and Lämmel G. Exploiting past experience-case-based decision support for soccer agents. In KI 2007: Advances in Artificial Intelligence, Volume 4667 of Lecture Notes in Computer Science, pp 440-443, Springer, (2007).
7. Arcos, Lluis, J.,; Mantaras, L., Ramon; Sierra, Carles; Ros, Raquel.: A CBR system for Autonomous Robot Navigation. In: Proceedings of CCIA'05, Fronteries in Artificial Intelligent and Applications, pp 299—306, (2005).
8. Kruusmaa, M.: Global navigation in dynamic environments using Case-based reasoning. Autonomous Robots, Volume 14, Issue 1 , pp 71–91, (2003).
9. Urdiales, J. Vázquez-Salceda, E.J. Perez, Sànchez-Marrè, and Sandoval, F.: A CBR Based Pure Reactive Layer for Autonomous Robot Navigation. In: Proceedings of the 7th IASTED International Conference on Artificial Intelligence and Soft Computing, Canada, pp 99–-104, (2003).
10. Steffens, T.: Similarity-based Opponent Modelling using Imperfect Domain Theories. In: Proceedings of CIG'05 IEEE 2005 Symposium on Computational Intelligence and Games, Graham Kendall and Simon Lucas editions, pp 285—291, (2005).
11. Hans-Dieter Burkhard, Abdel-Badeeh Salem, Bassant M.El-Bagoury. Case-Based Motion Controller for Humanoid Robot. In Proceedings of AIPR-08, International Conference of Artificial Intelligence and Pattern Recognition, Florida, USA, pp 32-37, (2008).
12. Abdel-Badeeh M.Salem, Bassant M .El Bagoury. "A Case-Based Adaptation Model for Thyroid Cancer Diagnosis Using Neural Networks", In Proceedings of the 16th International FLAIRS conference, Florida, U.S. pp 155-159, (2003).
13. Webots simulation tool website: www.cyberbotics.com/products/webots/
14. NAO Humanoid Robot : www.aldebaran-robotics.com
15. NAO Team Humboldt: Homepage of NAO Team Humboldt http://www.naoteamhumboldt.de/index.php
16. Hans-Dieter Burkhard: Case Completion and Similarity in Case-Based Reasoning. Comput. Sci. Inf. Syst. 1(2), pp 27-55, (2004).
17. Bassant Mohamed El Bagoury, Abdel-Badeeh M-Salem, Hans-Dieter Burkhard Hierarchical Case-Based Behavior Control of Humanoid Robot. In Annals of University of Craiova, Math. Comp. Sci. Ser. Volume 36, Issue (2), ISSN: 1223-6934, pp 131-140, (2009).
18. Raquel Ros. Action Selection in Cooperative Robot Soccer using Case-Based Reasoning. http://www.iiia.csic.es/ , (2008).
19. Karol, A., Nebel, B., Stanton, C., Williams, M.: Case Based Game Play in the RoboCup Four Legged League Part I: The Theoretical Model. In: RoboCup, volume 3020 of LNCS, pp 739 – 747, (2003).
20. Ros, R.; Veloso, M.; L´opez deM`antaras, R.; Sierra, C.; and Arcos, J. Retrieving and Reusing Game Plays for Robot Soccer. In *8th European Conf. on Case-Based Reasoning*, Volume 4106 of *LNAI*, pp.47–61. Best Paper Award, (2006).

ISBN: 978-1-61804-216-3

Dynamically Adaptive AOMDV for V2V communication

Hafez Moawad, Eman Shaaban, Zaki Taha Fayed

***Abstract*—** Vehicular Ad hoc Network (VANET) is a special class of Mobile Ad hoc Network (MANET) where vehicles are considered as MANET nodes with wireless links. The design of efficient routing protocols in VANET is a key issue for supporting the smart Intelligent Transportation System ITS. Existing routing protocols of MANET are not suitable for VANET. AOMDV is the most important ad hoc on demand multipath routing protocol. Our previously proposed SD-AOMDV is an efficient AOMDV-based VANET routing protocol with good average delay and packet delivery fraction. However it has high normalized routing load due to considering speed and direction in its routing decision. This paper proposes SW-AOMDV as VANET routing protocol that dynamically switches between AOMDV and SD-AOMDV based on roads traffic condition. Simulation results show that SW-AOMDV reduces the overall network routing overhead and achieves good results with average delay and packet delivery fraction .

***Keywords*—** VANET; AOMDV; MANET; Intelligent Transportation System...

I. Introduction

Wireless communications among vehicles get the focus of research in both of the academic research community and automobile industry. Some vehicles manufacturers have equipped their new vehicles with global positioning systems (GPS), wireless interfaces. In addition, in 1999, the United States Federal Communications Commission (FCC) allocated 75 MHz of spectrum at 5.9 MHz to be used by DSRC (Dedicated Short Range Communications). DSRC is a short to medium range communications service that was developed to support vehicle-to-vehicle and vehicle-to-roadside communications. Such communications cover a wide range of applications, including vehicle-to-vehicle safety messages, traffic information, toll collection, drive-through payment, and several others. DSRC is aimed at providing high data transfers and low communication latency in small communication zones. IEEE is also working on the IEEE 1609 family of standards for wireless access in vehicular environments (WAVE), which define architecture and a complementary, standardized set of services and interfaces that collectively enable secure vehicle to vehicle (V2V) and vehicle-to-infrastructure (V2I) wireless.

The main goal of VANET is providing safety and comfort for passengers. Besides safety applications VANET also provide comfort applications to the road users. For example, weather information, mobile e-commerce, Internet access and other multimedia applications. MANET and VANET are characterized by the movement and self-organization of nodes. The key difference of VANET and MANET is the special mobility pattern and rapidly changeable topology of VANET. Also, MANET nodes cannot recharge their battery power where VANET has no power constraint for nodes.

Due to special characteristics of VANETs, traditional routing protocols in wireless ad hoc networks may not be suitable for vehicular communications.

The design of effective vehicular communications poses a series of technical challenges. Guaranteeing a stable and reliable routing mechanism over VANETs is an important step toward the realization of effective vehicular communications. One of the critical issues consists of the design of scalable routing algorithms that are robust to frequent path disruptions caused by vehicles mobility. Existing routing protocols, which are traditionally designed for MANET, do not make use of the unique characteristics of VANETs and are not suitable for vehicle-to-vehicle communications over VANETs. Topology-based and position-based routing are two strategies of data forwarding commonly adopted for multi-hop wireless networks [1], [2]. Topology-based protocols use the information of available network links for packet transmission. Every node has to maintain the routing table. Position-based protocols assume that every node is aware of the location of itself, the location of neighboring nodes, and the location of the destination node. With the increasing availability of GPS-equipped vehicles, Position based Protocol is getting more convenient. However, the position-based protocols developed for MANETs may not directly be applied to vehicular environments, due to the unique vehicular network characteristics.

One good way of data forwarding in VANET is to modify MANET routing protocols and make it suitable for vehicular environment. There are many routing protocols for ad hoc networks [3], [4], [5]. One of the most well-known is AODV [6], [7], [8], [9]. Ad-hoc On-demand Multipath Distance

.
Hafez Moawad ,Faculty of Computer and Information science Ain shams University ,Cairo, Egypt(e-mail: hafez.moawad@cis.asu.edu.eg).
Eman Shaaban, Faculty of Computer and Information science Ain shams University, Cairo, Egypt (e-mail: Eman.Shaaban@cis.asu.edu.eg).
Zaki Taha Fayed ,Faculty of Computer and Information science Ain shams University, Cairo, Egypt (e-mail: ztfayed@cis.asu.edu.eg).

Vector Routing (AOMDV) protocol is an extension to AODV protocol for computing multiple loop-free and link disjoint paths [10]. SD-AOMDV is an efficient AOMDV-based VANET routing protocol with good average delay and packet delivery fraction [11].

This paper proposes SW-AOMDV as VANET routing protocol. SW-AOMDV improves AOMDV to suit VANET characteristics. SW-AOMDV dynamically switches between AOMDV and SD-AOMDV based on roads traffic condition to reduce the overall routing overhead. Simulation results show that SW-AOMDV achieves better performance compared to AOMDV and SD-AOMDV.

The remainder of this paper is structured as follows. Section 2 introduces SD-AOMDV routing protocol. Section 3 surveys the related researches conducted in dynamically adapted routing protocols for V2V communication. Section 4 introduces the proposed scheme SW-AOMDV. Section 5 presents the simulation results and discussions. The paper is concluded in Section 6.

II. SD-AOMDV

SD-AOMDV [11] improves the most important on demand multipath routing protocol AOMDV to suit VANET characteristics. SD-AOMDV adds the mobility parameters: speed and direction to hop count as new AOMDV routing metric to select next hop during the route discovery phase. When a source node wants to send a packet to destination node, first, routing protocol gets direction and speed of source node. Then, it gets direction and speed of destination node. Based on direction and speed of both source and destination, intermediate nodes that can be participating in route between source and destination are specified.

As nodes in VANET move with high speed and different directions, their route stability is much less than MANET. In other hand, if two nodes that are moving in different direction communicate together, their link breaks sooner than state which these node move in same direction. Therefore, if source and destination are moving in same direction, the protocol must only selects intermediate nodes that move in same direction with source and destination. However, if source node and destination node are moving in different direction, the protocol must only selects intermediate nodes that move in source or destination direction. The protocol also tries to select intermediate nodes that are moving in appropriate speed between source and destination. All intermediated nodes have minimum difference between its speed and average speed of source and destination ensuring more path stability. The path satisfies the following condition will be selected to forward packets:

Minimum (Maximum (difference between (Node speed, Average speed of source and destination) [k]), hop count). Where K is the number of disjoint paths to destination node D. SD-AOMDV adds the mobility parameters: speed and direction to hop count as new AOMDV routing metrics to select next hop during the route discovery phase. Simulation results indicated better performance in general achieved by SD-AOMDV compared to AOMDV. End-to-End Delay has been decreased by 76.47%. Packet Delivery Fraction PDF has been decreased by 11.92%. However Normalized Routing Load NRL with SD-AOMDV has been increased by 29.4%.

III. Related Work

This section surveys the related researches conducted in MANET routing protocols for V2V communication. These researches proposed routing protocols that dynamically switch between routes to improve the overall network performance.

In [12] a position-based routing scheme called Connectivity-Aware Routing (CAR) why designed specifically for inter-vehicle communication in a city and/or highway environment. A distinguishing property of CAR is the ability to not only locate positions of destinations but also to find connected paths between source and destination pairs. These paths are auto-adjusted on the fly, without a new discovery process. In CAR all nodes include information about their moving directions and speeds in the periodic HELLO beacons. When a node receives a HELLO beacon, it adds the sender of that beacon in the node's neighbor table, estimates its own and the neighbor's velocity vectors, and sets the expiration time for the entry in the neighbor table. The entry expires after a time when estimated positions of the current node and the neighbor become separated by more than 80% (configurable) of the average coverage range, or after two HELLO intervals (whatever is smaller). A new HELLO beacon from the neighbor updates the entry.

ARSMA [13] an adaptive routing protocol named Adaptive Route Selection in Mobile Ad Hoc Networks (ARSMA). The aim of this work is to improve the delivery ratio and reduce the end-to-end delay. In the route request phase, source nodes will discover multiple routes to the destination node, one for primary path, and the others for the backup paths. During the discovery procedure, each node will estimate the link expire time by way of the moving speed and direction of the precursor node. When a link breakage is about to occur, source node will try to switch the transmission to the backup route.

A2OMDV [14] resolve the problem through dynamic route switching method. Based on the delay of the multiple paths, a source node selects its route dynamically and checks the quality of the alternative routes according to the change of the ad hoc network. A source node maintains a group of multiple disjoint paths to its destination and keeps monitoring the quality of the routes. If the performance of the selected route drops below a certain threshold, the source node picks another route from the group of the candidate routes considering their round trip time (RTT).

AM-AOMDV [15] Adaptive Multi-metric Ad-Hoc On-Demand Multipath Distance Vector Routing extends the AOMDV scheme by including a multiple route metrics; a novel local route updates and route maintenance algorithm. The algorithm uses the one-hop information exchange between neighboring nodes to increase the packet throughput and route

longevity, decrease the end-to-end latency, route discovery frequency and routing overhead under high mobility environments. The multiple metrics (i.e., node-to-end latency, node-to-end RSSI, and node occupancy) allow the routing scheme to converge to the most efficient route during the data transmission period and hence avoid the creation of hotspots under heavy traffic conditions.

IV. Proposed SW-AOMDV

Proposed SW-AOMDV dynamically switches between AOMDV and SD-AOMDV routing protocols based on roads traffic condition to reduce the overall routing overhead. SD-AOMDV has a good average delay but has high normalized routing load (NRL) due to considering speed and direction in routing decision. In some mobility patterns where vehicles are moving with the same speed and direction, there is no need to consider speed and direction metric. Hence switching to AOMDV protocol will be the appropriate choice for the proposed protocol. In this case AOMDV is more likely to establish stable single and multi-hop paths saving extra routing overhead associate with using SD-AOMDV as vehicles are moving together. In some other mobility patterns where vehicles are moving with different speed and direction, switching to SD-AOMDV will be the appropriate choice for the proposed protocol.

In SW-AOMDV, each vehicle detects road traffic condition by periodically sending its speed and direction to its neighbors. Based on neighbors speed and direction, each vehicle individually selects the appropriate protocol to communicate with destination.

SW-AOMDV selects between AOMDV and SD-AOMDV. After source node selects the appropriate protocol, it will send route request to get path to destination and start communication.

SW-AOMDV proposes that AOMDV has better performance than SD-AOMDV when most of neighbor's nodes move in the same direction with minimum speed differences (relative static to each other). Also, SD-AOMDV has better performance than AOMDV when most of neighbor's nodes move in different directions or different speeds.

V. SW-AOMDV Design

In SW-AOMDV, each node modifies periodically sent Hello message to its neighbors of by adding its direction and speed as new fields. These added field increase routing protocol overhead. However SD-AOMDV introduces much more routing overhead by adding speed and direction fields to route request (RREQ) and route reply (RREP) packets.

When a source node requires a route to a destination, and there are not available paths, the source node will initiate a route discovery process, and each node will check its neighbors list. If the following conditions are satisfied, then source node will switch to AOMDV:

More than 75% from its neighbor nodes have the same direction with source node.

Difference in speeds among all these 75% neighbor nodes (including source node) does not exceed 3m/s.

Otherwise it will switch to SD-AOMDV. Details of our previously proposed SD-AOMDV design explained in [11].

VI. Performance Evaluations

To evaluate the performance of SW-AOMDV relative to AOMDV and SD-AOMDV, we measure the following performance metrics: end-to-end delay, packet delivery fraction, and normalized routing load against packet rate.

Normalized Routing load (NRL): ratio of total number of routing control packets to the total number of data packet received.

End to end delay: average delay in receiving data packets generated by all traffic sources. This includes all possible delays caused by buffering during route discovery, queuing delay at the interface, retransmission delays at the MAC, propagation and transfer times.

Packet delivery ratio (PDF): ratio of total number of data packets received to the total number of data packets sent by all traffic sources.

A. Configuration

VanetMobisim [17] as a validated vehicular traffic generator. Manhattan is used as Mobility Model. 802.11 is used as MAC layer protocol with transmission range of 250 meters of each node. Traffic pattern consists of 20 CBR/UDP connections between randomly chosen source-destination pairs and Packet size of 512 Bytes. We consider a square area of 3000 x 3000 meters with 70 nodes for 500 sec simulation time. Speeds of vehicles are varying from 10km/h to 90 km/h. To compare the routing performance with different traffic loads, packet generation rate is set to 1 packet/s, 2 packet/s, 4 packet/s, and 8 packet/s, respectively. Results are averaged over five simulation runs. A snapshot of the mobility is shown in Fig 1.

B. Normalized Routing Load

Fig. 2 shows that NRL with SW-AOMDV has been increased by 11% and NRL increased by 55% for SD-AOMDV compared to AOMDV. The overall average NRL is decreased by 28% for SW-AOMDV compared to SD-AOMDV.

SD-AOMDV has higher NRL due to the increasing of route request RREQ and route reply RREP routing packet sizes. SW-AOMDV has higher NRL than AOMDV due to new added fields (speed and direction) in periodically sent hello message.

SW-AOMDV switches between AOMDV and SD-AOMDV based on roads traffic condition saving extra routing overhead associate with SD-AOMDV.

C. End-to-End delay

Fig. 3 shows average end-to-end delay against generated packet rates. Results show that overall average end-to-end delay is improved by 47% for SW-AOMDV and improved by 48% for SD-AOMDV compared to AOMDV. The overall average end-to-end delay is decreased by 1% for SW-AOMDV compared to SD-AOMDV. Though SW-AOMDV

saves extra routing load (overhead) associate with SD-AOMDV, the improvement in end-to-end delay is approximately the same for both SW-AOMDV and SD-AOMDV.

SW-AOMDV has better end-to-end delay than AOMDV as AOMDV selects the least hop count path regardless road traffic condition, and it is much less likely to select a stable path.

SW-AOMDV switches between AOMDV and SD-AOMDV. It selects AOMDV when most of neighbor's nodes move in the same direction with minimum speed differences. Also SW-AOMDV selects AOMDV when most of neighbor's nodes move in different directions or different speeds.

SD-AOMDV selects routing path based on speed and direction regardless road traffic state, and hence it will always guarantee a stable path with minimum end-to-end delay. However SD-AOMDV will add extra high routing overhead resulting from new added fields to RREQ and RREP packets.

Although SW-AOMDV saves extra high routing overhead associate with added fields to RREQ and RREP packets, it does not guarantee selecting stable path as SD-AOMDV.

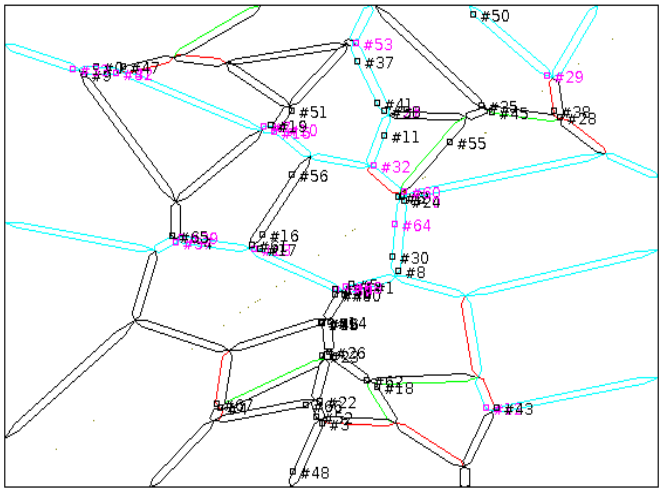

Fig. 1: A snapshot of the city scenario mobility

D. Packet Delivery Fraction

Fig. 4 shows that average packet delivery fraction is increased by 13% for SW-AOMDV and 9% for SD-AOMDV compared to AOMDV. The overall average packet delivery fraction is improved by 4% for SW-AOMDV compared to SD-AOMDV.SW-AOMDV has better PDF than AOMDV.

SW-AOMDV saves extra routing load (overhead) associate with SD-AOMDV, and its PDF is better than SD-AOMDV.

AOMDV selects the least hop count path regardless environment condition. AOMDV has much more frequent path failure than SW-AOMDV and SD-AOMDV due to ignoring mobility in its routing decision. Hence AOMDV is more likely to lose much more packets than others.

SW-AOMDV selects stable path as SD-AOMDV does with saving extra routing overhead associate with added fields to RREQ and RREP packets.

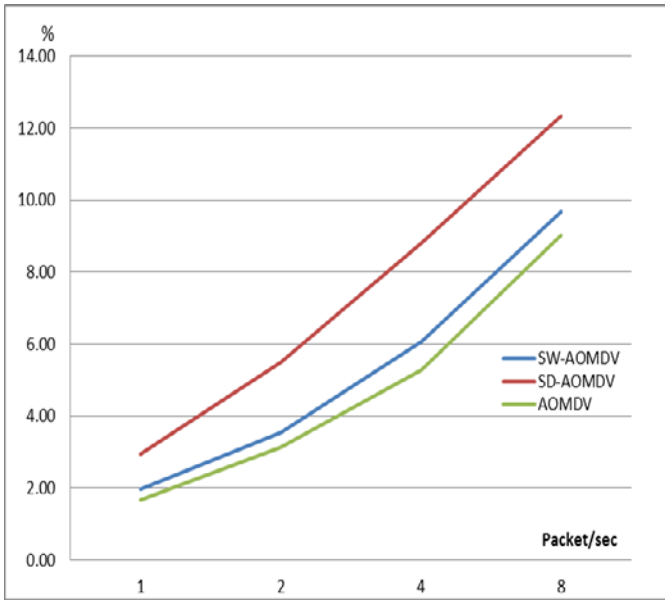

Fig. 2: Normalized Routing load

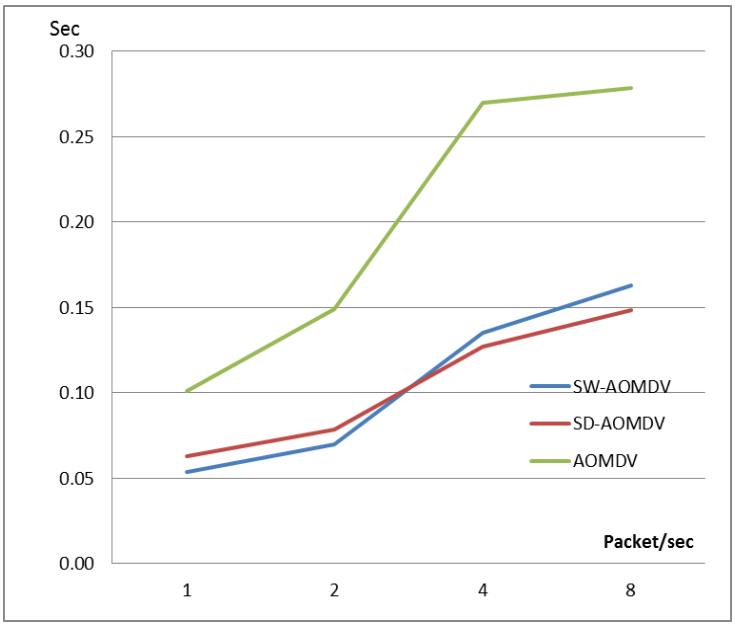

Fig. 3: End-to-End delay

ISBN: 978-1-61804-216-3

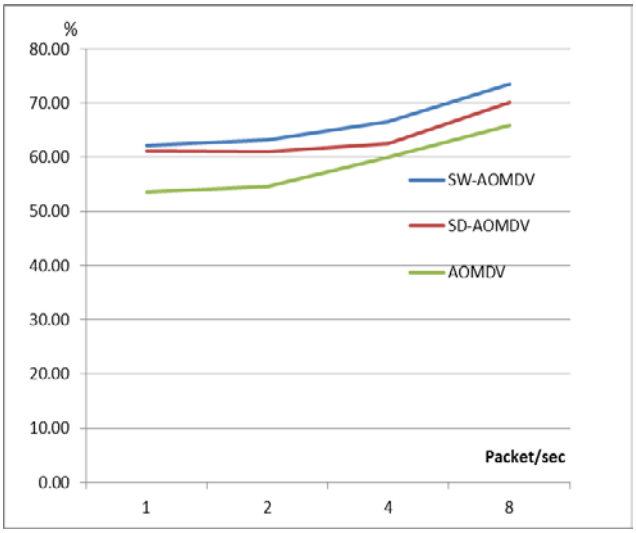

Fig. 4: Packet delivery fraction

VII. Conclusions

This paper proposes SW-AOMDV as VANET routing protocol. SW-AOMDV dynamically switches between AOMDV and SD-AOMDV based on roads traffic condition to reduce the overall routing overhead. SD-AOMDV has a good average delay and packet delivery fraction. However it has high normalized routing load due to considering speed and direction in its routing decision. SW-AOMDV proposes that AOMDV has better performance than SD-AOMDV when most of neighbor's nodes move in the same direction with minimum speed differences (relative static to each other). SW-AOMDV is designed, implemented, and compared with AOMDV and SD-AOMDV. Simulation results show that SW-AOMDV achieve good results.

References

[1] Ramakrishnan , R. S. Rajesh , R. S. Shaji,"CBVANETA Cluster Based Vehicular Adhoc Network Model for Simple Highway Communication" J. Advanced Networking and Applications Volume: 02, Issue: 04, Pages: 755-761 (2011).

[2] Yun-Wei Lin1, Yuh-Shyan Chen, and Sing-Ling Lee1," Routing Protocols in Vehicular Ad Hoc Networks: A Survey and Future Perspectives "Journal of Information Science And Engineering 26, 913-932 (2010).

[3] .J. Lou, J.P. Hubaux, " A Survey of Inter-Vehicle Communication", Technical Report, School of Computer and Communication Science, EPFL, Switzerland, 2004.

[4] D. Johnson et al., "Dynamic Source Routing for Mobile Ad Hoc Networks", IEFT MANET Draft, April 2003.

[5] Royer et al., "A review of current routing protocols for ad hoc mobile wireless networks", IEEE Personal Communications, Apr'99.

[6] C. E. Perkins and E. M. Royer, " Ad-hoc On-Demand Distance Vector Routing", In Proceedings of the 2nd IEEE Workshop on Mobile Computing Systems and Applications, pages 90–100, New Orleans, LA, 1999.

[7] C. Perkins, "Ad Hoc On Demand Distance Vector (AODV) routing", Internet-Draft, draft – ietf - MANET - aodv-00. Txt, 1997.

[8] C. Perkins, E. Royer, and S. Das., "Ad hoc on-demand distance vector (AODV) routing". Internet Draft, Internet Engineering Task Force, Mar. 2001.

[9] M. K. Marina, and S. R. Das, "On-demand multipath distance vector routing in Ad Hoc networks," Proc. 9th International Conference on Network Protocols, IEEE Press, Nov. 2001, pp. 14-23, doi: 10.1109/ICNP.2001.992756.

[10] R. Biradar, Koushik Majumder, Subir Kumar Sarkar, Puttamadappa, "Performance Evaluation and Comparison of AODV and AOMDV" S.R.Biradar et al. / (IJCSE) International Journal on Computer Science and Engineering Vol. 02, No. 02, 2010, 373-377.

[11] Hafez Moawad; Eman Shaaban "Efficient Routing Protocol for Vehicular Ad Hoc Networks " 2012 9th IEEE International Conference on Networking, Sensing and Control, China.

[12] Naumov, Valery, and Thomas R. Gross. "Connectivity-aware routing (CAR) in vehicular ad-hoc networks." INFOCOM 2007. 26th IEEE International Conference on Computer Communications. IEEE. IEEE, 2007.

[13] Lin, Yuh-Chung, and Chu-Wei Ke. "Adaptive Route Selection in mobile ad hoc networks." Fourth International Conference on Communications and Networking, pp. 1-5. IEEE, China, 2009.

[14] Shin, Ducksoo, Jonghyup Lee, Jaesung Kim, and JooSeok Song. "A2OMDV: An Adaptive Ad hoc On-demand Multipath Distance Vector Routing Protocol Using Dynamic Route Switching." Executive Development 21 (2008): 22.

[15] Abedi. O., Fathy M., Taghiloo J. "Enhancing AODV Routing Protocol Using Mobility Parameters in VANET" Computer Systems and Applications, 2008. AICCSA 2008. IEEE/ACS International Conference.

[16] http://www.isledu/nsnam/ns.

[17] http://vanet.eurecom.fr.

.

Simulation of ISFET Characteristics Using Constant Voltage Constant Current (CVCC) Readout Circuit

ROZIAH JARMIN, LEE YOOT KHUAN, HADZLI HASHIM, ABU ZAHRIN MOHD SIH AND MOHAMAD HISYAM B ABD GHANI

Faculty of Electrical Engineering
Universiti Teknologi MARA
40450 Shah Alam, Selangor
Malaysia.
leeyootkhuan@salam.uitm.edu.my

Abstract: - This paper presents a readout circuit for ion-sensitive field-effect transistor (ISFET) including study and investigation of ISFET performance using Linear Technology Simulation Program with Integrated Circuit Emphasis (LTspice) in order to identify the characteristics relationship of an ISFET variable. A macromodel of an ISFET had been created and tested using simulation program, in order to make sure the performance results of ISFET as the ion concentration (pH) changes, the current over the transistor will change accordingly. The graphs showing relationship between Id with Vd, Vref and VpH were produced, in order to make sure the macromodel function as stated characteristic. This paper also consists of analysis results before and after combining an ISFET with constant voltage constant current (CVCC) readout circuit. The results of the simulation are taken in order to monitor the behavior of ISFET variable by changing in the pH of the electrolyte which affects the voltage output at CVCC circuit.

Key-Words: - ISFET, CVCC, LTspice ,macromode.

1 Introduction

Generally ISFET is known as an ion sensitive sensor that is emerging as significant sensing devices in the areas of environmental monitoring applications, analytical chemistry, and biomedical applications such as medical diagnostics and for testing pharmaceutical. Bergveld in 1970, proposed an idea of an ion sensitive solid state device that is based on operation of field effect transistor for physiological measurement [1]. The construction of an ISFET is nearly similar with MOSFET because ISFET use an MOS (metal oxide semiconductor) transistor arrangement where the metallic gate is not a control electrode [7]. The physical variances in the ISFET structure are the substitute of the metal gate of the MOSFET by the sequence combination of the reference electrode, electrolyte and chemically sensitive insulator or membrane [2].

In general, ISFET is a sensor that can easily ensure pH and other electrolyte characteristics solution under test. The idea of an ISFET is to expose the oxide straight to the electrolyte by eliminating the metal gate electrode from a MOSFET, so the concentration of an ion can be observed. In other words, when pH sensitive oxide layer is deposited and put in contact with the electrolyte which is biased together with a reference electrode, so a change in pH of the electrolyte can be detected. Basically, changes of pH in the electrolyte can be determined by either measurement of Id (constant Vref) or Vref (constant Id) [4]. In addition, these requirements are needed to find the suitable readout circuit for an ISFET output. The main objective of readout circuit is to produce the output voltage related to the pH concentration of the electrolyte. After analysis and considering the requirement of an ISFET, suitable circuit chosen to be the readout circuit for ISFET is the conventional floating-source constant-voltage and constant-current circuit introduced by Caras & Janata,1980. Constant-voltage and constant-current (CVCC) circuit applied constant Id to an ISFET, in order to measure the response to the pH change at the electrolyte. As a results Vd and Vs (Vout) will response to the modification of Vref. This paper

also presents the analysis behavior and graph of Id, Vd and Vs after merging an ISFET with CVCC circuit. A macromodel of an ISFET and CVCC circuit is created for analysis and simulation using LTspice IV software.

2 Isfet Theory

Essentially, ISFET structure construction idea is to eliminate the standard metal-polysilicon-dielectric gate from MOSFET. The electrolyte solution will be in contact with the gate and the gate voltage will change as the concentration of the electrolyte changes. The reference electrode produced a reference potential (Vref). The construction is nearly the same with MOSFET because the metal part of electrode can be considered as the gate of the MOSFET [6]. The structure of an ISFET illustrated in Figure 1.

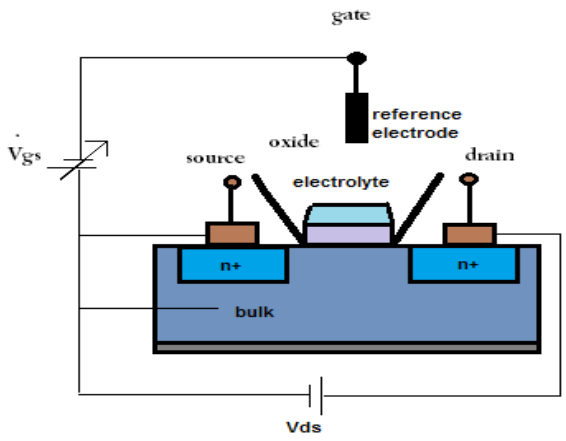

Figure 1: Structure of an ISFET

Specifically, the insulator or surface of gate oxide that is placed directly in aqueous electrolyte solution commonly used silicon as the material which contains OH-functionalities means that electrochemical equilibrium with ions in the sample solutions (H+ and OH) [6]. This resulted in which, silicon surface potential will be modified as gate potential is in contact with the electrolyte [6]. Hence, the gate potential is influenced by the ion concentration in the electrolyte solution, which cause the modification of the threshold voltage (Vth). So, changes in the pH of the electrolyte produce variations on the threshold voltage due to ionic activity at the electrolyte-insulator interface.

Using this method, the hydrogen ion concentration produces an electrostatic control on the drain-source current. Basically, pH solution will contain H^+ ions. High concentration of H^+ will give low values on pH and otherwise, that's how it will specify the values of pH. Specifically, these ions will become positively charge, thus produce electrostatic potential (electrical potential) by way of diffuse through the membrane at the silicon insulator layer and the oxide layer tend to except proton of H^+ ions. An additional gate voltage is needed to overcome the threshold voltage and create the channel for drain to source current to flow because of the electrical potential is too small. As a result, the variation of drain current (Id) due to the variation of the ion concentration in the electrolyte solution is compensated by the alteration of the reference electrode potential (Vref).

The operations of ISFET are usually worked under the constant drain current mode. In general, drain current moves from the source to the drain via the channel and it is dependent on the potential difference at the gate oxide. The selectivity and sensitivity of an ISFET depends on the selection of the gate dielectric material. Materials such as aluminum oxide and silicon nitride will have better properties than silicon, in terms of pH response, hysteresis and drift.

3 Isfet Macromodel

The macromodel specification for the ISFET to be used in combination with LTspice for simulation and analysis is based on previous work [3]. LTspice is chosen because of its capabilities, facilities and easy to create new library for new component. This paper only covers on LTspice macromodel specification.The description of ISFET macromodel subcircuit is based upon MOSFET parameter model. It is because the structure of ISFET comes from modification of MOSFET model. Specifically, ISFET macromodel is the electrochemical behavior based from equivalent circuit shown in Figure 2.

ISBN: 978-1-61804-216-3

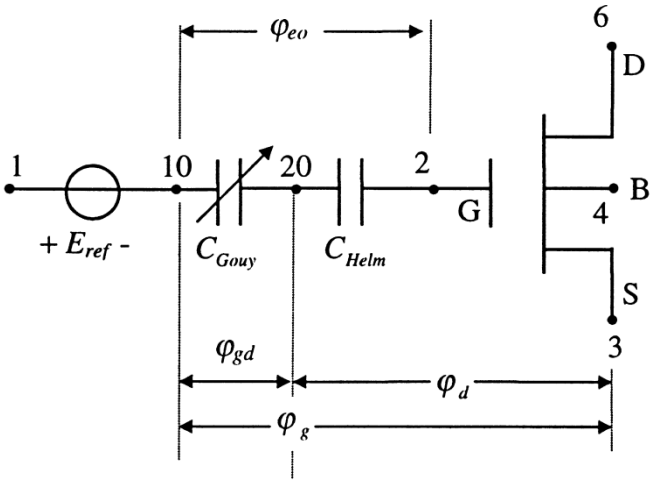

Figure 2: Equivalent circuit of an ISFET

The pH-independent source is a chemical input signal demonstrated by an independent voltage source connected to a dummy resistor [3]. This voltage is used to indicate as pH value. These macromodel was made based on n-type semiconductor and silicon nitride as the insulator [3]. The silicon nitride was placed linearly in an aqueous electrolyte solution. This macromodel was created for monitoring ISFET variable simulation in order to combine ISFET with readout circuit.

The results of the ISFET macromodel is to identify the characteristics of an ISFET. Graphs of Id versus Vd, Vref and Vph were produced in order to make sure the macromodel function as stated characteristic.

4 CVCC Readout Circuit

This readout circuit features of constant drain-source voltage (Vds) and constant draincurrent (Id) operation. The changes of pH can be obtained by the measurement of Vref (constant Id). The CVCC readout circuit in Figure 3 is used to obtain the change in voltage output in variation of the pH of the electrolyte as detected by the ISFET.

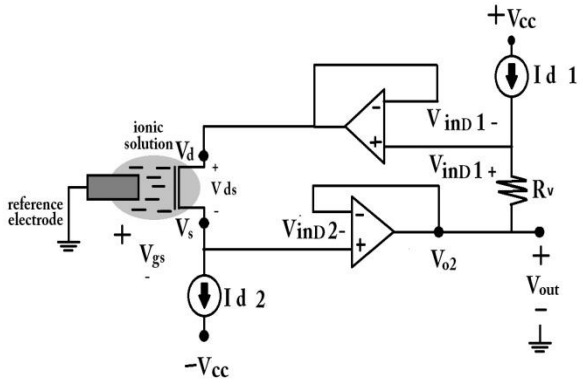

Figure 3: The CVCC readout circuit

The circuit in Figure 3 used current source and voltage follower to provide constant-voltage constant-current (CVCC) biasing. Moreover, the operational amplifiers are used to keep the voltage biasing constant. It functions like a voltage follower with unity gain. Current source (Id1) together with resistor (Rv), keeps the drain-source voltage (Vds) constant. It is because the non-inverting input of op-amp draws negligible current. So, Rv keeps Vds constant together with Id1. As the gate potential change in variation to pH electrolyte solution, Vgs changes [5]. Since Vg is grounded, Vs can be the final output since any modulation of Vgs, it also changes Vs.

5 Results and Discussion

The main objective of simulation of ISFET macromodel and readout circuit aiming on the relationship between pH electrolyte of an ISFET and output voltage from readout circuit. The simulation focused on the ISFET macromodel in order to analyse the relationship of ISFET variable and to make sure ISFET macromodel function as stated characteristics. The value pH4, pH7 and pH10 is based on the acidity, neutrality and alkaline of the electrolyte solution.

ISBN: 978-1-61804-216-3

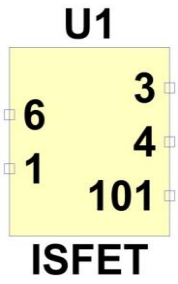

Figure 4: The ISFET capture symbol in LTspice

Figure 4 illustrated an ISFET capture symbol in LTspice schematics. The connection points of the symbol, 6 = Drain; 1 = Reference Electrode; 3 = Source; 4 = Bulk; 101 = pH input.

Before discussing on the ISFET characteristics, the results and analyzed data was based on discussion below:

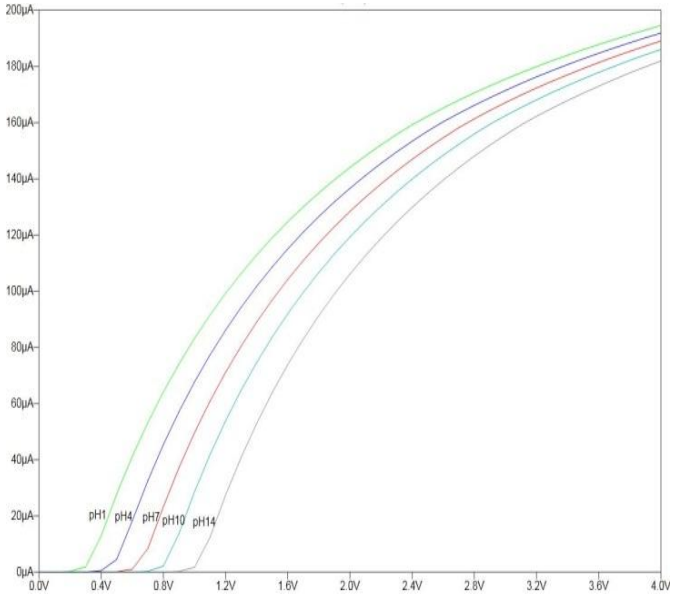

Figure 5: Graph of Id vs. Vref (Vd = 0.1V)

All these theories can apply on the Figure 5 that Id current is controlled by Vref voltage. Next, different pH gives different cut-off voltage value. Lastly, the turn ON region for all pH value are spotted at below 1V Vref (0V to< 1V).

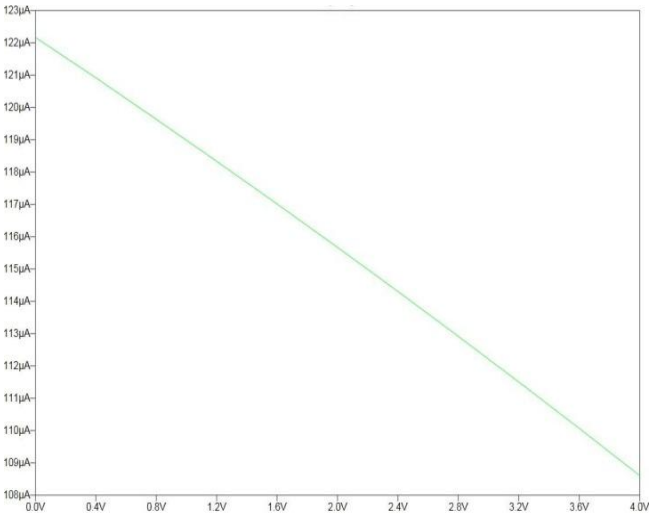

Figure 6: Graph of Id vs. VpH (Vref = 1.5V)

Figure 6 shows the relationship between linearity and sensitivity is an important characteristic of an ISFET in order to monitor the behavior against pH. Figure 6 shows a linear relationship which resulted sensitivity at 3.39µI/V. As a result, from the graph of Id versus VpH, the values of Vref are inversely proportional to the sensitivity (I/V).

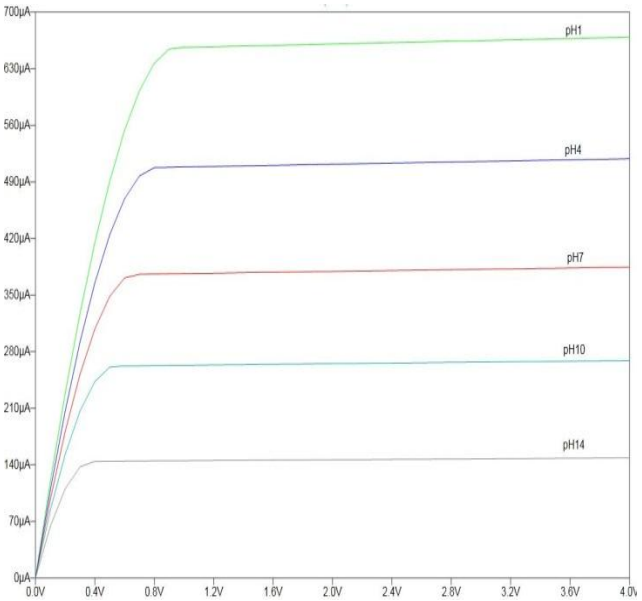

Figure 7: Graph of Id vs. Vd (Vref = 1.5V)

Lastly, for simulation ISFET macromodel the best value of Vref were used in

order to verify the behavior of Id and VpH. From the results, it can seen that both Id and Vd is proportional and the graph is linear until Id is saturated which gives values of constant Id. This also depends on the value of pH. A different value of pH indicates different values of constant Id. Moreover, lower value of pH gives high value of constant Id and continues vice versa for other values of pH. Figure 7 show a good range of output current Id. Figure7 also gives good distribution of constant Id between different pH values.

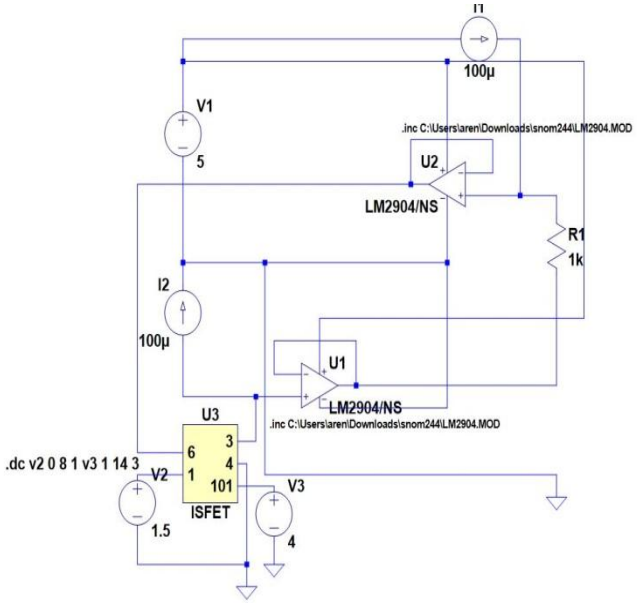

Figure 8: ISFET macromodel readout circuit schematic

Figure 8 illustrated an ISFET macromodel combined with CVCC readout circuit, it was captured from LTspice schematic. The output from ISFET macromodel that had been analyzed becomes an input for CVCC circuit. These combined circuit is aimed to identify the relationship between pH and output voltage from CVCC circuit which is Vs. Changes of pH in the electrolyte can be determined by the measurement ofV ref (constant Id). Based on theoretical of CVCC circuit, Id will be constant at 100µA. Upon to this consideration, changes of pH in the electrolyte can be determined by measurement of Vref.

Output voltage Vs shows a direct feedback to the changes of Vref. Although Vs shows same curve shape as Vd, but they had a different at starting value of voltage. As we can see output voltage Vd show 0.1V higher for all value of pH than Vs. Upon to these results, we can conclude that Vds is constant at 0.1V. Figure 10 shows both graphs of Vd and Vs as the proven for the conclusion above.

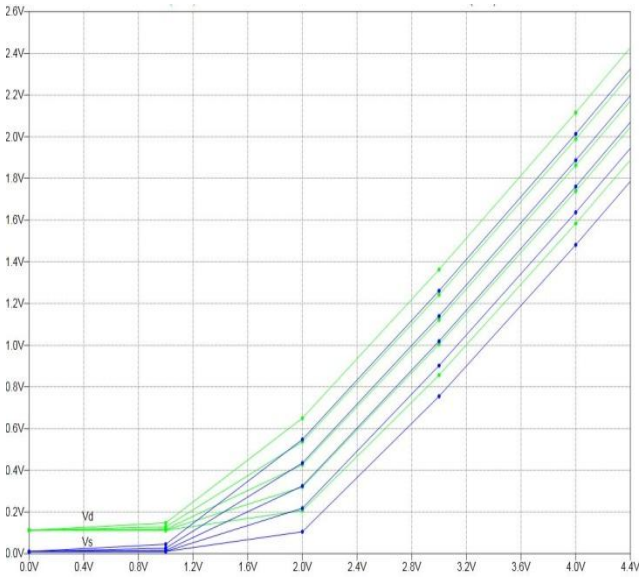

Figure 10: Graph of Vd and Vs vs. Vref

Table 1 shows data collection of output CVCC circuit after changing Vref with six different set values. It also shows the proportional change of Vd and Vs towards Vref. Furthermore, although Vd and Vs change accordingly to Vref, CVCC readout circuit will make sure that Vds is constant at 0.1V.

6. Conclusion

This paper has presented the CVCC readout circuit related to the characteristics behavior of ISFET variable. After analyzing the simulation, before and after combining ISFET macromodel with CVCC readout circuit the output voltage (Vs) of readout circuit change as pH of the electrolyte change. The “turn ON” value of Vref has been identified at 1V. At this value the Id start to be constant and Vd and Vs react towards Vref which means Id, Vd and Vs change accordingly towards changes of the electrolyte.

ISBN: 978-1-61804-216-3

Table 1 : Data collection of output ISFET macromodel and CVCC circuit

Vref(V)	Vph(V)	Vd(mV)	Vs=Vout(mV)	Vds(mV)
0.4	1	112.509	10.738	101.771
	4	112.300	10.167	102.133
	7	112.267	10.134	102.133
	10	112.260	10.116	102.144
	14	112.368	10.107	102.261
0.8	1	125.673	23.581	102.092
	4	116.119	14.013	102.106
	7	112.883	10.755	102.128
	10	112.388	10.206	102.182
	14	112.271	10.138	102.133
1.2	1	179.659	77.701	101.958
	4	151.705	49.720	101.985
	7	132.012	29.981	102.031
	10	119.261	17.173	102.088
	14	113.150	11.240	101.910
1.6	1	381.154	279.201	101.953
	4	275.083	173.134	101.949
	7	197.447	95.495	101.952
	10	162.155	60.184	101.971
	14	135.000	32.977	102.022
2	1	649.909	547.943	101.966
	4	537.157	435.196	101.961
	7	427.000	324.583	101.955
	10	319.672	217.722	101.950
	14	206.876	104.925	101.951
2.4	1	929.211	827.131	102.080
	4	812.349	710.376	101.973
	7	697.300	595.332	101.968
	10	585.295	483.332	101.963
	14	445.388	343.432	101.956

References:

[1] P. Bergveld, ISFET, Theory and Practice, IEEE Sensor Conference in Toronto (2003).

[2] S. Swaminathan, S. M. Krishnan, W. K. Lim, Z. Ahmed, and G. Chiang, "Microsensor Characterization in an integrated blood gas measurement system," IEEE, 2002.

[3] Sergio Martinoia, Giuseppe Massobrio, "A behavioral macromodel of the ISFET in SPICE" Department of Biophysical and Electronic Engineering (DIBE), University of Genova, Via all'Opera Pia 11/A, 16145 Genova, Italy, 182-189 pp, 28 OCTOBER 1999.

[4] Stephan Schmid, Ion sensitive Field Effect Transistors (ISFETs) Basics and Applications, Moscow Bavarian Joint Advanced Student School 2006

[5] Wan Fazlida Hanim Abdullah," Ion selectivity studies using supervised neural network for ion-sensitive field effect transistor sensor" pp. 38, 2011

[6] http://csrg.ch.pw.edu.pl/tutorials/isfet/

[7] Rozina Abdul Rani, Othman Sidek, "ISFET pH Sensor characterization: towards Biosensor Microchip Application," Universiti Sains Malaysia, IEEE

ISBN: 978-1-61804-216-3

Authors Index

ISBN: 978-1-61804-216-3